

SIMULATING NEUTRON BACKGROUNDS TO RARE EVENT SEARCHES

by

ALEXANDER JAMES BIFFL

B.S., Metropolitan State University of Denver, 2021

A thesis submitted to the Faculty of the
College of Liberal Arts and Sciences of
the University of Colorado in partial fulfillment
of the requirements for the degree of
Master of Integrated Sciences
Integrated Sciences Program

2023

This thesis for the Master of Integrated Sciences degree by
Alexander James Biffi
has been approved for the
Integrated Sciences Program
by

Anthony N. Villano, Chair
Tom Altman
Erin E. Austin
Martin E. Huber

Date: May 13, 2023

Biffi, Alexander James (M.I.S., Integrated Sciences)

SIMULATING NEUTRON BACKGROUNDS TO RARE EVENT SEARCHES

Thesis directed by Assistant Professor Anthony N. Villano

ABSTRACT

Neutron-induced nuclear recoils represent a substantial background to many rare-event searches. In this thesis, neutron backgrounds are investigated in the context of searches for two types of events: coherent-elastic neutrino-nucleus scatter (CENNS) searches in the vicinity of nuclear reactors, and dark matter (DM) direct detection experiments and detector calibration in underground sites.

Sensitivity of generic silicon and germanium detectors to reactor neutrino CENNS in the presence of neutron capture backgrounds is investigated by simulating detector deployment for varying energy resolutions and ambient thermal neutron fluxes. It is shown that typical reactor-adjacent fluxes must be reduced by several orders of magnitude by shielding or other means in order to make a CENNS measurement with high statistical significance. Germanium detectors are found to have higher sensitivity to the CENNS signal at finer resolutions. It is shown that unbinned and binned likelihood analyses yield similar results. The influence of an active neutron capture veto is discussed.

Next, a semianalytical method for simulating neutron-induced backgrounds in SuperCDMS (Super Cryogenic Dark Matter Search) HVeV (high-voltage, electronvolt resolution) detectors is presented. A basic model of radiogenic neutron flux is presented, and the resulting recoil spectrum in silicon is calculated analytically. A new ionization model based on the models of Lindhard and Alig is presented. The resulting neutron-induced phonon spectrum is found to be separated into rounded e/h pair peaks spaced by 120 eV. Rates of neutron induced events total 68.61 ± 13.52 (syst.) ± 0.07 (stat.) events $\text{kg}^{-1} \text{day}^{-1}$ below 1 keV, with around 0.2 events $\text{kg}^{-1} \text{day}^{-1}$ in the first few nonzero-charge e/h pair peaks. It is found that systematic errors dominate the error budget.

The form and content of this abstract are approved. I recommend its publication.

Approved: Anthony N. Villano

For my family.

ACKNOWLEDGEMENTS

First, to my advisor, Anthony Villano, thank you not just for guiding my way to the completion of this thesis, but also for agreeing to take me under your wing in the first place. I will forever be indebted to your kindness, your wisdom, and your faith in me. I couldn't have asked for a better captain.

To the rest of my committee members, firstly Martin Huber, thank you for serving on the committee and also thank you for your guidance throughout my time in the Integrated Sciences program. To Tom Altman and Erin Austin, thank you for agreeing to read this monstrosity and for providing insights and feedback when called.

To the rest of our neutrons and cryogenics family at Denver, especially Kitty Harris and Ana Gevorgian, thank you for those long sessions working in silent solidarity as we all tried to put together the pieces of this great puzzle, and for always being willing to drop what you were doing to entertain my silly questions.

To all the folks I was lucky enough to work with at CDMS, in particular Valentina Novati, Rob Calkins, Taylor Aralis, Ziqing Hong, Noah Kurinsky, Mike Kelsey, Tarek Saab, Tom Ren, Ishwita Saika, Xiao Yu, Matt Wilson, Enectali Figueroa-Feliciano, Dan Baxter, Benjamin Schmidt, and so many others, thank you for providing your valuable feedback, insight, and assistance, and for withstanding my poor mic quality. It's been an honor searching with you.

To my family, thank you for the support, for the phone calls and texts, and for pretending to listen when I started talking about neutrons. Especially to my sister Natalie, thank you for your encouragement, for forwarding me tweets of dogs in hats, and for hot-dropping Fragment with me when I needed to unwind. I couldn't have done any of this without you guys.

And last, to my D&D folks, thank you for keeping me sane.

TABLE OF CONTENTS

CHAPTER

| | |
|---|----|
| I. INTRODUCTION | 1 |
| 1.1 Backgrounds in Rare Event Searches | 1 |
| 1.1.1 Neutrons | 2 |
| 1.2 Neutrinos | 3 |
| 1.3 Dark Matter Particles | 4 |
| 1.4 Notation and Standards | 6 |
| 1.4.1 Units | 6 |
| 1.4.2 Scatters and recoils | 6 |
| 1.4.3 The cross section | 7 |
| II. CENNS SEARCHES NEAR NUCLEAR REACTORS | 10 |
| 2.1 Coherent Elastic Neutrino-Nucleus Scatter | 11 |
| 2.1.1 Cross section | 12 |
| 2.1.2 Detection | 13 |
| 2.2 Searches at Reactors | 15 |
| 2.2.1 Current experiments | 15 |
| 2.2.2 Reactor neutrinos | 16 |
| 2.2.2.1 Production mechanism | 17 |
| 2.2.2.2 Neutrino spectrum | 18 |
| 2.3 Neutron Backgrounds at Reactors | 21 |
| 2.3.1 Capture spectrum model | 23 |
| 2.4 Detector Model | 24 |
| 2.4.1 Operational parameters | 26 |
| 2.4.2 Ambient thermal neutron flux | 27 |
| 2.4.3 Irreducible background | 27 |
| 2.5 Statistical Analysis | 28 |
| 2.5.1 Unbinned likelihood analysis | 28 |

| | |
|---|----|
| 2.5.2 Binned likelihood analysis | 30 |
| 2.6 Computational Procedures | 32 |
| 2.6.1 Calculating recoil spectrum of CENNS events | 32 |
| 2.6.2 Simulating samples of events | 32 |
| 2.6.2.1 CENNS | 33 |
| 2.6.2.2 Captures | 34 |
| 2.6.2.3 Background | 35 |
| 2.6.3 Calculating measurement PDFs | 35 |
| 2.6.3.1 CENNS | 36 |
| 2.6.3.2 Captures | 37 |
| 2.6.3.3 Background | 38 |
| 2.6.4 Calculation of Likelihood Function | 38 |
| 2.7 Results | 39 |
| 2.7.1 Unbinned analysis | 40 |
| 2.7.2 Comparing binned and unbinned methods | 43 |
| 2.7.2.1 Comparing landscapes | 43 |
| 2.7.2.2 Binning methods | 44 |
| 2.7.2.3 Comparing distributions | 47 |
| 2.7.2.4 Comparing contours | 48 |
| 2.7.3 Binned analysis | 51 |
| 2.8 Capture Veto | 54 |
| 2.9 Discussion | 56 |
| 2.9.1 Scaling laws | 57 |
| 2.9.2 Silicon vs. germanium | 58 |
| 2.9.3 Uncertainties | 58 |
| III. DARK MATTER DIRECT DETECTION | 60 |
| 3.1 Dark Matter Direct Detection | 61 |

| | |
|--|-----|
| 3.1.1 WIMP Dark Matter | 61 |
| 3.1.2 Detecting WIMPs | 64 |
| 3.2 SuperCDMS | 65 |
| 3.2.1 The NEXUS facility | 66 |
| 3.3 The HVeV Detectors | 66 |
| 3.3.1 HVeV development | 68 |
| 3.4 Neutron Spectrum in NEXUS | 68 |
| 3.5 Calculation of Event Rates and Spectra | 72 |
| 3.5.1 Captures | 72 |
| 3.5.2 Scatters | 73 |
| 3.6 Treatment of Multiple Scatters | 75 |
| 3.6.1 Capture as second interaction | 80 |
| 3.7 Ionization Model | 82 |
| 3.7.1 Lindhard model | 83 |
| 3.7.2 Alig model | 86 |
| 3.7.3 Putting it together: the Alig-Lindhard model | 94 |
| 3.7.3.1 Higher-energy recoils | 95 |
| 3.7.4 Comparison with IMPACT data | 95 |
| 3.8 Simulation Procedure | 98 |
| 3.9 Results | 99 |
| 3.9.1 Generated samples | 99 |
| 3.9.2 Total event rates | 100 |
| 3.10 Error Estimation | 103 |
| 3.10.1 Neutron spectrum | 103 |
| 3.10.2 Cross sections | 104 |
| 3.10.3 Inelastic scatters | 105 |
| 3.10.4 Propagating systematic uncertainties through MC process | 106 |

| | |
|---|-----|
| 3.10.5 Statistical uncertainties | 109 |
| 3.10.6 Negligible sources of error | 110 |
| 3.10.6.1 Uncertainties in multiple scatters, second captures | 110 |
| 3.10.6.2 Numerical errors | 110 |
| 3.10.6.3 Overlapping samples | 111 |
| 3.10.7 Ionization model | 113 |
| 3.10.8 Detector efficiency | 114 |
| 3.10.8.1 Phonon collection efficiencies | 114 |
| 3.10.8.2 Charge collection efficiency | 116 |
| 3.10.8.3 Other types of efficiencies | 122 |
| 3.10.9 Miscellaneous Errors | 122 |
| 3.10.9.1 Detector shielding and neutron attenuation | 122 |
| 3.10.9.2 Event timing and timing resolution | 123 |
| 3.10.10 Summary of errors | 123 |
| 3.11 Discussion | 125 |
| IV. CONCLUSIONS | 127 |
| 4.1 Main Takeaways | 127 |
| 4.2 Where To Go From Here? | 128 |
| REFERENCES | 129 |
| APPENDIX | |
| A. Additional data for unbinned CENNS significance analysis | 141 |
| B. Supplemental figures on the similarities between binned and unbinned likelihood analyses | 142 |
| C. Sample maximum likelihood fits in binned analysis | 146 |
| D. Neutron elastic scatter cross sections with silicon | 153 |
| E. The characteristic length | 155 |
| F. Alig model high-energy, high- n limit | 158 |

LIST OF TABLES

TABLE

| | | |
|-----|--|-----|
| 2.1 | Summary of CENNS searches at reactors | 17 |
| 2.2 | Coefficients α_{pk} for Mueller model antineutrino spectra from Mueller, et al. | 21 |
| 2.3 | Capture cross sections and numbers of capture events for Si and Ge detectors. Uncertainties are given in the second column in parentheses | 27 |
| 2.4 | Summary of Z scores for variation between distributions of calculated significances for four binnings for ten surveyed points in landscape | 46 |
| 2.5 | Z scores for unbinned significances compared with distribution of significances calculated with 3k log binning. | 47 |
| 2.6 | Variance about the dense unbinned contour for the other contours plotted in Figure 2.13 | 51 |
| 2.7 | Expected effective thermal neutron flux reduction (2.8.1) in silicon and germanium detectors as a function of \bar{d} | 56 |
| 2.8 | Effective flux reduction (2.8.1) for cubic silicon and germanium detectors as a function of mass | 56 |
| 3.1 | Abundances of radioactive isotopes in rock and concrete at SNOLAB reported by D. Tiwari | 69 |
| 3.2 | Total i^{th} scatter rates up to $i = 6$. Proportions of the initial incident scattering rate given in the third column | 79 |
| 3.3 | Comparison of methods for calculating the probability of second captures | 81 |
| 3.4 | i^{th} capture rates and rates relative to initial capture rate | 82 |
| 3.5 | Event rates by type in and peak positions of each e/h pair peak. All rates in $\text{kg}^{-1} \text{day}^{-1}$. Uncertainties listed are systematics, then statistics (see Section 3.10). Note the errors listed in the peak position column are not uncertainties in the peak positions, but are the standard deviation of each peak about the listed mean | 103 |
| 3.6 | Integrated uncertainties in the total neutron-induced event rate over the region of interest ($\leq 1 \text{ keV}$) | 125 |
| B.1 | Average standard deviation of Z values for each binning method | 143 |
| B.2 | Scaled variances of unsmoothed contours | 145 |

LIST OF FIGURES

FIGURE

| | | |
|------|--|----|
| 2.1 | Flow chart showing the procedure used in this chapter to investigate neutron capture backgrounds to reactor CENNS searches. | 11 |
| 2.2 | Neutrino emission spectrum for four main fissionable isotopes. Circles show tabulated spectrum data from Mueller, et al. and solid curves show their fit parameterizations (eq. (2.2.3)). The fits are extended to a minimum neutrino energy of 0.8 MeV | 22 |
| 2.3 | Histograms of generated capture events using <code>nrCascadeSim</code> for silicon (top) and germanium (bottom). Bin widths are 10 eV | 24 |
| 2.4 | CENNS-induced recoil PDFs for silicon and germanium | 33 |
| 2.5 | Results of unbinned analysis for $\sigma_0 = 1$ eV in silicon. Dashed and dotted gray lines mark standard sea level flux and reported thermal neutron flux at MINER facility reduced by a factor of 10^9 , respectively. Black line marked “ 5σ ” represents the $Z = 5$ contour line (after smoothing) | 41 |
| 2.6 | Three example fits using the unbinned likelihood function in Si for a baseline resolution of 1 eV. Lower panes show zoomed-in views of red boxed regions. | 42 |
| 2.7 | Resulting 5σ contours in unbinned analyses for 1 eV, 5 eV, and 10 eV baseline resolutions in Si | 43 |
| 2.8 | Comparison of binned (left) and unbinned (right) Z landscapes for $\sigma_0 = 5$ eV in silicon | 44 |
| 2.9 | Histograms of generated Z values for $\sim 1.2M$ capture events with an effective resolution of 23.5 eV for the four different binnings. The Z value calculated with the unbinned methods is shown as a vertical dashed black line | 45 |
| 2.10 | Standard deviations of all 40 generated samples of Z values (confidence values) with all different binning methods. The average standard deviation was 0.989 | 47 |
| 2.11 | Comparison of original unbinned Z landscape data ($\sigma_0 = 5$ eV) and “dense unbinned” data, evaluated on a denser grid of points | 48 |
| 2.12 | 5σ contours for unbinned, dense unbinned, and 3k log binned data | 49 |
| 2.13 | Relative difference in unbinned and binned contours from dense unbinned contour | 50 |
| 2.14 | 5σ contours for flat background model in Si and Ge. Inline labels on the contours give the baseline resolution in eV. | 52 |
| 2.15 | 5σ contours for sloped background model in Si and Ge. Inline labels of contours give baseline resolution in eV | 52 |
| 2.16 | 5σ contours for combination background in Si and Ge. Inline labels of contours give baseline resolution in eV | 53 |
| 2.17 | Summary of all 5σ contours for the different background models (blue, orange, and green) and baseline resolutions (dotted, solid, dashed, and dot/dashed lines) | 53 |

| | | |
|------|--|-----|
| 3.1 | Flow chart summarizing semianalytical method used in this chapter to calculate neutron-induced phonon spectrum | 62 |
| 3.2 | Unnormalized radiogenic fast neutron fluxes simulated in the SNOLAB geometry (provided by R. Calkins) | 69 |
| 3.3 | Total radiogenic fast neutron flux spectrum (blue) and fitted power-law (orange) | 70 |
| 3.4 | Model ambient neutron flux spectrum at NEXUS | 72 |
| 3.5 | Neutron-scatter-induced recoil spectrum calculated via (3.5.8). The expected scatter rate is $146.1 \text{ kg}^{-1} \text{ day}^{-1}$. The spectrum continues almost completely flat down to the minimum energy, and drops nearly vertically to zero above one MeV. | 75 |
| 3.6 | First six i^{th} fluxes $I_i(E_n)$ | 79 |
| 3.7 | Recoil energy spectra for first six scatters. | 80 |
| 3.8 | Ionization energy vs. recoil energy according to the Lindhard model with $k = 0.15$ | 84 |
| 3.9 | Fano factor vs recoil energy data extracted from Lindhard model approximation (D) (provided by A. Villano) | 85 |
| 3.10 | First several pair-production probability curves $p_n(E)$ from the Alig model | 91 |
| 3.11 | Full Alig-model e/h pair production probability data $p_n(E)$, evaluated at 3,000 energies between 0 and 189 eV for n up to 75. Values smaller than 10^{-6} have been masked out. | 91 |
| 3.12 | Alig model probabilities for $n = 0, 3, 6,$ and 9 calculated by several integration methods. Even on a 750×750 grid, the values are noticeably and systematically smaller than the MC method. Discrepancies are negligible for $n = 0$ and worsen with growing n . Note the 25kMC curve is semi-transparent | 93 |
| 3.13 | The difference between Alig-model peaks calculated by MC method with 25,000 points vs. several other integration methods. Grid-based methods converged very slowly, but the MC method with 2,500 is consistent with the 25,000-point MC method up to statistical fluctuations at the 90% level | 94 |
| 3.14 | Distributions $\hat{p}_n = \hat{p}_n(E_r)$ for several recoil energies | 95 |
| 3.15 | Heatmap of AL model e/h pair creation probabilities $\hat{p}_n(E_r)$ for recoil energies up to 2 keV. Values smaller than 10^{-6} have been masked out. The red line marks the average number of e/h pairs predicted by the Lindhard model | 96 |
| 3.16 | Comparison of AL model (dashed curves) with IMPACT data (black circles) | 97 |
| 3.17 | Histogram of generated phonon energies for scatters and captures up to 1 keV | 100 |
| 3.18 | Neutron-induced event spectra by type | 101 |
| 3.19 | Total neutron-induced phonon energy spectrum (solid blue) with uncertainties (transparent blue shading). See Section 3.10 for description of error sources | 101 |

| | | |
|------|---|-----|
| 3.20 | Neutron spectra by amount of charge produced. Red dotted lines correspond to the NTL phonon energy produced by an integer amount of charge | 102 |
| 3.21 | Relative error in the elastic scatter cross section data for silicon from ENDF database | 105 |
| 3.22 | Elastic and inelastic cross sections for the isotopes of silicon | 107 |
| 3.23 | Effect of differing prompt and NTL phonon collection efficiencies. Plot shows original (equal) data and 95% prompt efficiency. The unrealistic case of 50% prompt efficiency is included to better illustrate the effects of $\epsilon_p < 1$ | 116 |
| 3.24 | Laser calibration data from SNOLAB HVeV Run 2. Red bands indicate estimated peak locations to calculate rate of in-between peak events (13.3%) | 117 |
| 3.25 | Spectrum of neutron-induced events with charge trapping and impact ionization as per flat trapping model | 120 |
| 3.26 | Effect of simple drift trapping model | 121 |
| 3.27 | Uncertainties relative to the final total neutron-induced phonon spectrum by source | 124 |
| 3.28 | Absolute uncertainties due to systematic uncertainties and statistical uncertainties associated with MC procedure. Original neutron spectrum plotted in dashed blue for reference. | 125 |
| A.1 | Full significance landscapes for $\sigma_0 = 5$ eV (left) and 10 eV (right) in Si. Black curves indicate 5σ contours. Gray lines indicating references fluxes are the same as in Figure 2.5. | 141 |
| B.1 | Side-by-side comparisons analogous to Figure 2.8 for 1 eV and 10 eV baseline resolutions. Behaviors of the other baselines are similar to the 5 eV case | 142 |
| B.2 | Histogram shown in Figure 2.10 broken up by binning method | 143 |
| B.3 | Z landscape evaluated on the same grid of data points as the dense unbinned data introduced in Section 2.7.2.4 | 144 |
| B.4 | Unbinned, dense unbinned, and 3k log binned 5σ contours without smoothing | 144 |
| B.5 | Relative difference in unbinned and binned contours from dense unbinned contours (analogous to Figure 2.13 without smoothing the contours) | 145 |
| C.1 | Sample fits for flat background in Si | 147 |
| C.2 | Sample fits for flat background in Ge | 148 |
| C.3 | Sample fits for sloped background in Si | 149 |
| C.4 | Sample fits for sloped background in Ge | 150 |
| C.5 | Sample fits for combination background in Si | 151 |
| C.6 | Sample fits for combination background in Ge | 152 |
| D.1 | Neutron elastic-scatter cross sections for silicon. Plots show shaded 1σ confidence intervals. Taken from ENDF/B-VIII.0 database, web interface | 154 |

E.1 Schematic of the square region of integration in (x, x') space (left) and (ν, μ) space (right).
Equations for the line segments marking the sides of the square in (μ, ν) space are labelled. . . . 156

F.1 Results of fit with $k = 3.7465$ and $\sigma_0 = 1.271$ to $n = 5, 10, 25,$ and 40 164

CHAPTER I

INTRODUCTION

Experimental particle physics today is often concerned with rare events, events caused either by uncommon particles or low-probability interactions. As a general rule, events that happen often have been studied often. There the processes are well understood, and the standard model (SM) parameters are finely-tuned with low uncertainties. Where there are still large uncertainties, and where there is room for new discoveries, is where the events are rare.

Thus, much experimental particle physics today becomes a lottery, searching for rare and hard-to-detect happenings underneath the mundane, everyday events caused by more common particles. Statistical methods become extremely important, to decipher the massive samples of collected data and extract the events of interest from the background of mundane events. This process of extraction is a vital part of any sort of rare-event search, and is only possible by careful analysis and characterization of those backgrounds.

The aim of this thesis is to study the backgrounds caused by neutrons, in the context of searches for rare interactions between atomic nuclei and two types of particles - neutrinos and dark matter particles. The rest of this chapter will introduce the particles in question, discuss some of their properties, and give some background for these types of pursuits in general and for the work contained herein. The second chapter will be a sensitivity analysis for the search for neutrino-nucleus interactions in the vicinity of nuclear reactors, and will attempt to analyze the extent to which neutron backgrounds impede such endeavors. The third chapter will be a study of the neutron backgrounds for dark matter detector calibration in the NEXUS (Northwestern Experimental Underground Site) underground facility, and will attempt to characterize the signature of neutrons in those detectors.

1.1 Backgrounds in Rare Event Searches

This thesis will be concerned with rare interactions between certain non-baryonic particles and atomic nuclei. These interactions, called "scatters" (the quantum mechanical equivalent of a direct collision), leave as their signature a *nuclear recoil* (NR), when the struck nucleus jolts as a result of the energy deposited into it. For the particles of interest in this thesis, these interactions are likely the most common, if not the only, ways that these particles interact with normal atomic matter.

Low energy nuclear recoils are extremely difficult to detect, which contributes to the rareness with which these events are studied. More will be said about their detection later, but suffice it to say here that the detection of individual NRs requires extremely sensitive detectors. Such sensitivity inevitably leads to the detection of many more events than desired. The majority of interactions with common particles

(gammas (photons), electrons, other atoms, etc.) cause *electron recoils*, which often can be discriminated from NRs. However, background events that also cause NRs cannot be immediately discriminated, and so the only method of getting rid of them is by statistical means.

1.1.1 Neutrons

A major source of NR backgrounds is free neutrons, neutrons not bound inside of a nucleus. Free neutrons predominantly interact with atomic matter through two means [1], either by scattering off of nuclei or through *radiative neutron capture*, which is where a low energy neutron is absorbed by an atomic nucleus, increasing its mass number by one. When this happens, the neutron is absorbed into an excited nuclear energy state, and as the nucleus falls to the ground state it emits gammas, and during these emissions the nucleus recoils.

Neutrons occur most often inside of atoms, but free neutrons can also be found essentially everywhere normal matter can be found. The IEEE standard sea level thermal neutron flux, a good indicator of typical amounts of environmental free neutrons in general, is 4 neutrons $\text{cm}^{-2} \text{hr}^{-1}$ [2]. This flux level changes by less than a factor of two across different positions on the surface of the Earth, and decreases gradually with depth underground (depending on radioactivity in the rocks). These ambient neutrons are almost always present in rare event searches, and so a characterization of their effects in these searches is a vital part in effectively searching.

Neutrons are generally divided into categories two ways. The first set of categories are based on energy. Low-energy neutrons ($\lesssim 0.05$ eV) are generally called “thermal” neutrons, between 0.05 eV and ~ 1 MeV are “epithermal” or “intermediate” neutrons,¹ and greater than 1 MeV are called “fast” neutrons. The exact bounds on these groups are often fluid, but the terminology is almost always consistent - thermal means the lowest energy, fast means the highest.

The other categorization is based on the source of the neutrons. Most of the time, two production types are important, cosmogenic and radiogenic neutrons. Cosmogenic neutrons are produced by cosmic rays and cosmic-ray-produced particles, most commonly cosmic-ray muons scattering off of nuclei. Radiogenic neutrons are produced by trace radioactive isotopes like uranium and thorium. The most common avenue for radiogenic neutron production is during (α, n) reactions, where an α particle produced in a decay chain collides with a nucleus and fragments into a new, heavier nucleus and a neutron [3]. These radioactive elements can also produce free neutrons during spontaneous fission events. We will also encounter *reactogenic* neutrons, neutrons produced by fissions in a nuclear reactor during operation.

¹Sometimes “epithermal” and “intermediate” are used to denote two distinct energy ranges, but the distinction won’t be important here

In the next two sections, the exotic particles that cause the rare interactions of interest in this thesis will be described.

1.2 Neutrinos

The first type of rare event that will be considered is interactions between atomic nuclei and the *neutrino* (ν), which itself is not a rare particle, but interactions between neutrinos and normal matter *are* rare.

The existence of the neutrino was first proposed by Wolfgang Pauli in 1930, in a letter to a conference of nuclear physicists (“radioactive people”) in Tübingen, Germany [4] He postulated the existence of the new particle as a solution to the apparent non-conservation of energy during β decays [5], which we now know to be the emission of an electron and an antineutrino during the decay of a neutron into a proton:

$$n^0 \rightarrow p^+ + e^- + \bar{\nu}_e \tag{1.2.1}$$

Pauli proposed that the neutrino would be a spin- $1/2$, electrically neutral particle with a small magnetic moment and a mass “of the same order of magnitude as the electron mass” (translated by K. Riesselmann [4]). The first direct experimental evidence of neutrinos came in 1953 following experiments searching for inverse beta decay (IBD; the opposite process to beta decay, $\bar{\nu}_e + p^+ \rightarrow n^0 + e^+$), at a nuclear reactor in Washington state [6]. Several experiments following in the next few years corroborated the measurement of the new particle [7]. The neutrino’s position in the standard model has since been solidified.

Neutrinos are leptons, and come in three “flavors,” corresponding to the three heavier leptons: electron (ν_e), muon (ν_μ), and tau (ν_τ), and can transition between flavors (called “neutrino oscillation”). They are indeed neutral and spin- $1/2$, as Pauli predicted, though they are far lighter than his estimate. It was thought for a while they were entirely massless, though now it is known they have nonzero mass. Their masses are estimated to be $\lesssim 0.17$ eV by astronomical observations [8] and ≈ 0.26 eV by observations of tritium (^3H) decay [9].

Interactions between neutrinos and normal matter are extremely rare. An average solar neutrino (energy 530 keV [10]) can pass through over a light year of solid lead without interacting with a single atom.² The detection of neutrinos is thus no trivial task, and many things about these elusive particles re-

²Assuming room-temperature density 11.34 g/cm³, and using the IBD cross section from [11] and the neutrino-nucleus-interaction cross section described in Section 2.1.1. By the phrase “can pass through without interacting,” we mean that the probability of the neutrino interacting with any lead nuclei or elec-

main uncertain, since observing the particles is so difficult. Many of their properties have large error bars or just plainly have never been measured. It is of great interest to measure the properties of these particles precisely, to test whether standard model predictions are accurate, or whether new physics needs to be developed. Thus there are many experiments currently seeking to measure the rare interactions between neutrinos and neutrino detectors.

1.3 Dark Matter Particles

The second rare interaction that will be considered is interactions between normal matter and dark matter (DM), a category of interactions that has never before been observed directly. Dark matter is a mysterious category of particle that is suspected to account for around 80% of the mass in the universe. The properties of dark matter are still completely unknown, and experiments searching for it rely on the current best guesses and constraints on its properties to search.

The concept of dark matter, matter invisible to the eye, goes back to the earliest days of natural philosophy. In the modern era, dark matter’s place in physics is bolstered by four main categories of evidence for its existence: the masses of large galaxy clusters, galactic rotation curves, cosmological simulations, and gravitational lensing measurements.³

Following just a few years after Hubble and Humason’s seminal work measuring the distances and redshifts of faraway galaxies at the Mount Wilson observatory [14], Fritz Zwicky published an analysis of the redshift of those galaxies, part of which involved an analysis of the relative velocities of the ~ 800 galaxies of the Coma cluster [15]. Though the numbers used by Zwicky have since been corrected by substantial amounts, his core argument still holds: the mass of galaxies in the cluster calculated by the gravitational energy binding the cluster, and the mass of the galaxies calculated by measuring their total luminosities, disagree substantially [16]. The corrected version of Zwicky’s calculation of the gravitating mass is almost an order of magnitude larger than the mass of luminous matter, suggesting those galaxies are composed of some 90% nonluminous (dark) matter [12]. In Zwicky’s (translated) words, “dark matter is present in much greater amount than luminous matter” (pg. 222).

Some four decades later, advances in radio astronomy allowed for measurements of the rotation of the Andromeda galaxy (M31) by Vera Rubin and Kent Ford Jr. with unprecedented resolution [17]. Over the years, further measurements of galactic rotation speeds as a function of distance from their center (so-called “rotation curves”) found that the mass distribution in those galaxies had to be much larger

trons during its traversal is less than 50%, calculated with the macroscopic cross section, as explained in Section 1.4. The exact 50% value is something like 1.0138 light years.

³The history of dark matter is far more complicated than recounted here, see [12], and there are several other major pieces of evidence favoring the existence of dark matter that will not be discussed here. See [13] and references within

than estimated by the amount of luminous matter, and that this extra mass had to be distributed out to far larger radii and in much larger amounts than the luminous matter.⁴

Around the same time as Rubin and Ford’s measurements of rotation curves, computers were becoming powerful enough to model the evolution of the universe as a whole. The first cosmological simulations were published in 1974 [19], and advances happened quickly (see references in [12]). It was quickly discovered that in order to replicate the features of the universe we observe (including especially the distribution of galaxies in the universe, measured early on by the CfA redshift survey [20], and the magnitude and scale of CMB (cosmic microwave background) anisotropies measured by, among others, the Planck collaboration [21, 22]), dark matter is needed. Simulations incorporating dark matter show remarkable success predicting these features, for example [23] in 1984 and more recently the Millenium [24], Millenium-II [25], and Millenium-XXL [26] simulations.

Perhaps the most direct evidence of dark matter came in the form of measurements of gravitational lensing around the Bullet Cluster, two colliding clusters of approximately 40 total galaxies ~ 1.14 billion parsecs away [27].⁵ The collision caused great disruption of the mass in the cluster, and measurements of weak gravitational lensing indicates that the distribution of the majority of mass in the cluster is little, if at all, correlated with the location of the luminous matter. A halo of dark matter makes up a substantial portion of the Bullet Cluster’s mass.

Since the earliest smoking guns, discourse around this nonluminous matter has changed substantially. Before, dark matter (in Zwicky’s original German, “dunkle materie”) could mean any form of matter not actively radiating enough light to be visible on Earth. Now, the phrase “dark matter” is unambiguously a new, heretofore undiscovered particle, with nonzero mass but invisible to electromagnetic and strong interactions. To quote Bertone and Hooper, “[when] a modern paper discusses the distribution of dark matter, or the impact of dark matter on structure formation, or the prospects for detecting dark matter with a gamma-ray telescope, one does not have to ask themselves whether the authors might have in mind white dwarfs, neutron stars, or cold clouds of gas—they do not” ([12], pg. 15). To modern science, dark matter is a *particle*, a specific type of undiscovered particle whose properties are only constrained, not known. The search for dark matter is as much a pursuit of particle physics as it is astrophysics (and in fact, an entire field of “particle astrophysics” has emerged as a result of this overlap). The search for dark

⁴An important step in the development of these ideas was the result due to Chandrasekhar [18] that one can treat the dynamics of galaxies accurately by completely neglecting the interactions between neighboring stars. Thus the orbital speeds of stars in a galaxy are completely determined by the amount of mass between them and the center of their galaxy

⁵Technically “Bullet Cluster” refers to only one of the galaxy clusters in the colliding pair, but the distinction is minor

matter nowadays involves the search for these dark matter particles, with an as-yet total measured event rate of zero interactions per second.

1.4 Notation and Standards

This section will give some necessary preamble to the particle physics concepts discussed in this work, as well as establishing standards of notation and conventions. It is likely that this section will be helpful to novice and expert in particle physics alike.

1.4.1 Units

The first point that should be mentioned is units. Except where explicitly stated, all equations and quantities will use a natural units system where c , \hbar , the elementary charge, and the Boltzmann constant are all equal to one. One way to view this unit system is that all quantities are given in units of an appropriate power of energy, i.e., the electron mass is 0.511 MeV, one Angstrom (a length) is $\approx 0.507 \text{ keV}^{-1}$, and one barn (an area) is $\approx 2568 \text{ GeV}^{-2}$.

In addition, we may occasionally use the terms “dru” and “tru” when discussing counting rates. These refer to “differential rate unit” and “total rate unit,” with typical units (counts $\text{keV}^{-1} \text{ kg}^{-1} \text{ day}^{-1}$) and (counts $\text{kg}^{-1} \text{ day}^{-1}$), respectively. A rate in dru is the height of an event *spectrum* over measured energies, while the tru rate is the integral of that spectrum.

Another somewhat uncommon unit used in this thesis is meters or kilometers *water-equivalent* (mwe or kmwe), which is the depth of water that provides the same shielding from cosmic rays as the overburden of an underground facility. Depending on the density of overlaying rock, the mwe overburden is typically 2.5 – 3 times higher than the physical depth of the facility. The conversion between meters water equivalent and meters of “standard” rock ([28], pg. 144) is 2.65. The shielding power of a bulk material is proportional to mass density, thus the conversion factor is just equal to the density of the material in g/cm^3 .

Lastly, the abbreviation “AU” will always mean “arbitrary units.”

1.4.2 Scatters and recoils

As mentioned before, *scattering* is the generic term for short-range interactions between two particles. The type of interaction, whether electromagnetic, weak, or strong, is not relevant; all of these interactions are considered scatters when the interaction is close-range, and reasonably approximates a classical “collision of cue balls.” Generally, momentum is conserved in such interactions. In *elastic* scatters, energy is conserved as well, while in *inelastic* scatters, some energy is lost (typically, that energy goes into exciting one of the particles to an elevated energy level).

A *recoil* is the motion of an initially stationary (or approximately stationary) particle as a result of a scatter; in the collision, some energy and momentum will be imparted to the stationary particle. As mentioned before, we will mainly be concerned with interactions that cause *nuclear recoils* (NRs), where one of the particles taking part in the scattering interaction is an atomic nucleus. In a solid, the interaction will cause the struck nucleus to recoil out of its position in the atomic lattice with some kinetic energy called the *recoil energy*. Occasionally, we may speak of *electron recoils* (ERs), where an electron is the particle struck in a scattering event.

In nuclear recoils, some other terminology becomes relevant. As the result of a nuclear recoil, some of the nucleus' recoil energy may be transferred into electrons, freeing those electrons from the atomic lattice and sending them into the conduction band (“ionization”). In semiconductors and metals, ejecting an electron from its position in the atomic lattice leaves behind a positively-charged gap, which itself can propagate through the material and acts in many ways as a positively-charged particle with the mass of an electron – this quasiparticle is called an “electron hole” or “hole” (h^+). Ionized electrons and electron holes always come in pairs (“e/h pairs,” “electron/hole pairs”). The total energy given to ionized electrons and holes is called the *ionization energy*, and the ratio of ionization energy to recoil energy is termed the *yield*. In the literature, the term “quenching factor” is also used in place of yield, though that term may also refer to the ratio of nuclear recoil energy and *scintillation* energy, the energy produced in the form of gammas (light) as a result of the recoil in certain materials. We will prefer to use the term “yield.” Generally, the yield is on the order of 10-50% for recoils between ~ 10 eV and 100 keV. When discussing ionization energies, values will usually be reported with units ending in “ee”, i.e., 5 keV_{ee} or 0.1 eV_{ee}, which stands for “electron-equivalent” energy – the energy given to the electrons and holes.

The processes of ionization and the dissipation of nuclear recoil energy will be discussed in further detail when we introduce the mathematical models used to describe them in Section 3.7.

1.4.3 The cross section

The quantum-mechanical formalism used to parameterize the probability of an interaction is the *cross section*. This formalism helps capture the non-deterministic nature of interactions by assigning to each particle, for each interaction, an effective cross-sectional area, an area that an equivalent purely classical object would have such that it would undergo interactions at the same rate given some uniform flux of particles. Consider a monochromatic (having a singular energy) flux of f incident particles per unit area per unit time. If E_r is the recoil energy due to an interaction, then the rate of interactions (interactions per unit time) R is:

$$R = \int_0^\infty f\sigma(E_r)dE_r \quad (1.4.1)$$

where $\sigma(E_r)$ is what we will refer to as the cross section. Normally, this is referred to as the “differential” cross section, and just “cross section” refers to the integral of $\sigma(E_r)$ over E_r . We shall instead refer to this as \mathcal{O} , the “total cross section:”

$$\mathcal{O} = \int_0^\infty \sigma(E_r)dE_r \quad (1.4.2)$$

We may also refer to the “differential cross section over x ” for some quantity x , which will denote $d\mathcal{O}/dx$ (so $\sigma(E_r) = d\mathcal{O}/dE_r$ would be the “differential cross section over E_r ”). The phrase “differential cross section” used *without* specifying a differential parameter will refer to σ , as will just “cross section.”

Note that in general, the cross section will also depend on the energy of the incident particle E_i : $\sigma = \sigma(E_r, E_i)$. Also note that we will generally refer to what may more commonly be called flux densities as “fluxes” – e.g., the number $I(E_i)$ of incident particles with energy E_i passing through a unit area in a unit time per unit energy will simply be called the “flux” of those particles. So the total number of particles hitting a unit area of a surface per unit time is $\int I(E_i)dE_i$.

We define these quantities in this way so that the number of interactions with each nucleus in some energy bin centered at an energy E_i with width dE_i , that cause recoils with energies in some energy bin of width dE_r centered at an energy E_r , is $I(E_i)\sigma(E_r, E_i)dE_idE_r$, and the total number of interactions per unit time is:

$$\iint I(E_i)\sigma(E_r, E_i)dE_idE_r \quad (1.4.3)$$

Dividing this by the nuclear mass of the detector material gives the total event rate in tru.

Another quantity that may come up is the *macroscopic* cross section Σ , which is the total cross section times the number density ρ_n of the material:

$$\Sigma(E_i) = \rho_n\mathcal{O}(E_i) = \rho_n \int \sigma(E_r, E_i)dE_r \quad (1.4.4)$$

The probability that an incident particle of energy E_i undergoes an interaction when moving an infinitesimal length dx through the material is $\Sigma(E_i)dx$. The probability that a particle travels a finite distance Δx through the material without interacting is $e^{-\Sigma(E_i)\Delta x}$. For situations where multiple different interactions are possible, one can just add the appropriate cross sections or macroscopic cross sections together.⁶

⁶This is technically an approximation, but is almost always true for finite- \mathcal{O} interactions, which includes all the interactions considered in this thesis. The relative correction is $O(p)$, where p is the probability of the less-probable interaction. See Section [3.10.6.3](#)

CHAPTER II

CENNS SEARCHES NEAR NUCLEAR REACTORS

This chapter focuses on neutron backgrounds in the context of coherent elastic neutrino-nucleus scatter (CENNS) searches, specifically at experiments looking to detect CENNS with nuclear reactor antineutrinos.⁷

In the vicinity of nuclear reactors, the capture of ambient thermal neutrons represents a substantial background to CENNS searches. The goal of the work in this chapter is to investigate what ambient thermal neutron flux is “acceptable,” that is, what flux could be present and still allow a high-significance measurement of a CENNS signal, given some detector energy resolution. This will be accomplished by simulating the collection of nuclear recoil energy data using generic low threshold silicon and germanium detectors, including both CENNS events and background events, and performing statistical analysis on the collected data to search for the component of CENNS events for a range of environmental and detector conditions.

A flow chart showing the overall procedure in this chapter is shown in Figure 2.1. The procedure starts with models for three types of events. First, the model for reactor neutrinos and CENNS events are described in Section 2.2. Next the model of neutron captures, the main background, is described in Section 2.3. Third, generic “other” background models are described in Section 2.4.3. Datasets consisting of all three types of events will be simulated. The rest of Section 2.4 describes the detector model used, which converts the simulated datasets of true recoil energies induced in the detectors into datasets of measured energies, emulating data collection with a silicon or germanium detector at a reactor site. The full simulated sample, representing the data collected by a typical reactor-CENNS search, is fed into a statistical analysis procedure described in Section 2.5, which attempts to extract the CENNS signal from the simulated sample. Section 2.6 describes the simulation and computational procedures used to sample the three types of events and analyze them in more detail. The simulation/statistical analysis procedure is repeated several times, varying the thermal neutron flux (the number of neutron capture events in simulated samples) and the detector resolution (ability to distinguish close-together event energies). Section 2.7 gives the results of the simulations, including a comparison of the two statistical methods described in Section 2.5. Section 2.8 discusses the possibility of vetoing capture events to reduce the effective neutron flux, and Section 2.9 gives an overall discussion. The chapter begins with some background on CENNS.

⁷Portions of work in this chapter were previously published in [29]

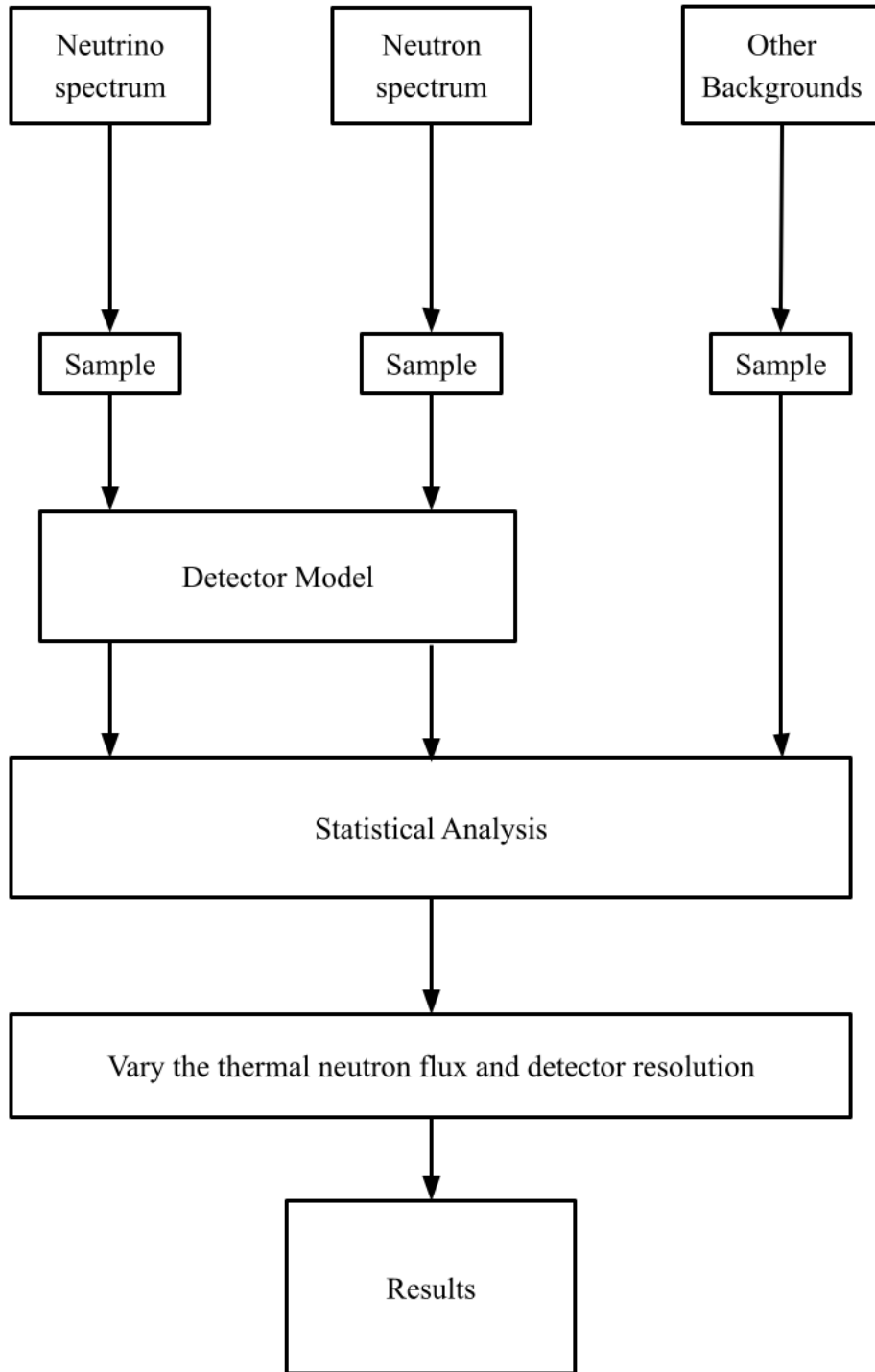


Figure 2.1: Flow chart showing the procedure used in this chapter to investigate neutron capture backgrounds to reactor CENNS searches.

2.1 Coherent Elastic Neutrino-Nucleus Scatter

Coherent elastic neutrino nucleus scatter (CENNS, also abbreviated $\text{CE}\nu\text{NS}$, CEvNS , CNNS , or ECNS) is a standard model process that was predicted in 1973 by Freedman [30]. In a CENNS event, a neutrino scatters *elastically*, meaning no energy is lost in the collision, and *coherently* off of an atomic nucleus, meaning it interacts with the nucleus as a whole as opposed to interacting with one or more of the constituent protons or neutrons individually. This happens because at lower energies ($\lesssim 10^2$ MeV), the neutrino wavelength is large compared to the size of the nucleus, too large to resolve the individual nucleons. The CENNS cross section is enhanced by this coherence – every nucleon in the nucleus contributes to the interaction probabilities. CENNS is a weak interaction that is mediated by neutral current exchange, the exchange of a Z^0 boson.

CENNS is one of the most common ways for low-energy ($\lesssim 100$ MeV) neutrinos to interact with normal matter [11, 31, 32], which makes it an incredibly valuable type of interaction for probing all sorts of neutrino-related science. Measurements of CENNS can help constrain SM parameters like the weak mixing angle [33–35], neutrino properties like the neutrino magnetic moment [36–39] and charge radius [40, 41], and can help reveal details about nuclear structure [42–46]. Experiments relying on CENNS measurements can also help expand the frontiers of particle physics. Several beyond-the-standard-model (BSM) models and hypotheses can be probed directly via CENNS measurements, including searches for a new generation of undiscovered sterile neutrinos [47–49], dark matter searches [50–52], and a whole set of generic hypotheses about interactions with new particles called non-standard interactions (NSI) [53–63]. CENNS detectors can even have applications in geophysics [64], nuclear reactor monitoring [65] and in nuclear non-proliferation [66, 67]. Understanding and measuring CENNS can also help understanding in various fields of astrophysics such as solar physics and models of the solar interior [68], and in the study of stellar evolution, including crucial aspects of supernovae, stellar collapse, and the formation of neutron stars and black holes [68–70].

2.1.1 Cross section

The coherence of CENNS means all the neutrons and protons contribute to the cross section. The cross section scales with the total weak charge \mathcal{N} of the nucleus, which is parameterized for a nucleus with atomic number Z and neutron number N as $[Z(4\sin^2\theta_W - 1) + N]$, where θ_W is the “Weinberg angle,” a measure of the mixing between photons and the Z^0 gauge boson [71]. As of 2020, the SM measured value of $\sin^2\theta_W$ is 0.23121 ± 0.00004 ([28], pg. 182-183). Since this is so close to $1/4$, $\mathcal{N} \approx N$. It is common to neglect the protonic contribution to the weak charge entirely (see, e.g., [72, 73]).

The spin-independent⁸ cross section $\sigma(E_r, E_\nu)$ for incident neutrino energy E_ν and recoil energy E_r is [30, 31]:

$$\sigma(E_r, E_\nu) = \frac{G_f^2}{4\pi} M_N \mathcal{N}^2 (F(E_r))^2 \left(1 - \frac{M_N E_r}{2E_\nu^2}\right) \quad (2.1.1)$$

where $G_f = 1.1663787 \times 10^{-5} \text{ GeV}^{-2}$ is the Fermi coupling constant [74], M_N is the mass of the nucleus, and $F(E_r)$ is the (unitless) nuclear form factor which accounts for the size of the nucleus. We adopt the form factor used by Klein and Nystrand [75], which parameterizes the distribution of nucleons as a solid sphere (“hard sphere” in the literature) of radius $R_A = A^{1/3} \times 1.2 \text{ fm}$, convoluted with a Yukawa potential, which is the potential of a force with a finite-mass force-carrying particle with range $a = 0.7 \text{ fm}$:

$$F(E_r) = \frac{3}{q^3 R_A^3} [\sin qR_A - qR_A \cos qR_A] \frac{1}{1 + q^2 a^2} \quad (2.1.2)$$

where $q = \sqrt{2M_N E_r}$ is the momentum transfer. For coherent scattering, the form factor is usually extremely close to one (corresponding to a point-mass distribution), reflecting the fact that a coherent interaction does not distinguish between individual nucleons and treats the nucleus essentially as a single point particle.

Neglecting the variation in the form factor,⁹ the total cross section $\mathcal{O}(E_\nu)$ for incident neutrinos of energy E_ν is

$$\begin{aligned} \mathcal{O}(E_\nu) &\approx \int \frac{G_f^2}{4\pi} M_N \mathcal{N}^2 \left(1 - \frac{M_N E_r}{2E_\nu^2}\right) dE_r \\ &= \frac{G_f^2}{4\pi} \mathcal{N}^2 E_\nu^2 \end{aligned} \quad (2.1.3)$$

where the integration in the first line goes from $E_r = 0$ to $E_r = 2E_\nu^2/M_N$. If the integration is taken from some finite energy E_0 instead of zero, possibly to account for a recoil energy threshold, corrections are introduced on the order of $(M_N E_0/E_\nu^2)$.

⁸The axial (spin-dependent) contribution to the cross section depends on the total spin of the nucleus as a whole, which for heavy nuclei is small compared to the total weak charge (only unpaired nucleons contribute). For even-even nuclei, e.g., ²⁸Si and ⁷²Ge, this contribution is zero.

⁹It was found that the smallest the form factor got, for interactions with Ge at a recoil energy of 1 keV, was ≈ 0.9895 , so this is a good approximation

2.1.2 Detection

Despite their relatively large cross section, CENNS events eluded detection for 43 years after they were first predicted. This large gap in time between prediction and measurement is due to the great difficulty in actually detecting whether a CENNS event has occurred. The only evidence a CENNS event leaves is a nuclear recoil with $O(\text{keV})$ energies or lower. The recoiling nucleus is extremely difficult to spot directly, and the sub-keV ionization that is then produced is only detectable by the most sensitive instruments. There is also a trade off between the cross section of the interaction, which is enhanced with larger nuclei, and a reduction in deposited recoil energy with heavier nuclei. That is, larger nuclei may interact via CENNS more often, but the signals they produce are smaller and more difficult to detect. Additionally, Hakenmüller et al. [76] point out that the requirement for close proximity to the neutrino source usually leaves detectors exposed to atmospheric and cosmic-ray-induced backgrounds, making detection that much more difficult.

The first observation of CENNS was published in 2017 by the COHERENT collaboration using neutrinos from the Spallation Neutron Source (SNS) at Oak Ridge National Laboratory [73]. The SNS generates one of the most intense neutron beams in the world, but it also functions very well as a neutrino source, for several reasons.

Spallation is the ejection of particles due to fragmentation of atomic nuclei in energetic collisions. A pulsed beam of high-energy ($O(\text{GeV})$) protons is directed at a target of usually high atomic number (in the case of the SNS, mercury). This produces (as the name suggests) neutrons, as well as pions π^\pm . The π^- are captured quickly by the mercury, but the π^+ decay into a muon μ^+ and a muon neutrino ν_μ . The muon further decays into a positron e^+ and two more neutrinos: a muon antineutrino $\bar{\nu}_\mu$ and an electron neutrino ν_e . Thus every pion produced results in three neutrinos. At the SNS, every hundred incident protons produces approximately eight neutrinos of each flavor [73] (for reference, the SNS delivers $\approx 5 \times 10^{20}$ protons per day, something like 10^{10} protons per beam pulse). At the soon-to-be-operational European Spallation Source (ESS), it is estimated that every hundred protons will produce ~ 30 neutrinos of each flavor, and the MW proton beam will deliver something like 10^{21} protons per day [31].

Since the ν_μ result from two-particle decay of the π^+ , the spectrum of ν_μ is monochromatic: all the ν_μ are produced with the same energy (roughly equal to the difference between the π^+ and μ^+ masses, ≈ 29.79 MeV). The energy spectra of the other two neutrinos, resulting from the well-understood process of muon decay, are known exactly (see [31]). Thus the energy spectrum of neutrinos produced by spallation sources is known very precisely.

Another major benefit of using a spallation source for neutrinos is that these sources produce particles in rapid, finely-controlled pulses. The SNS' pulsed proton beam has a full width at half maximum

(FWHM) of only 380 ns, and the pulses are run at 60 Hz. This allows data-takers to separate environmental backgrounds from events associated with the beam very easily, which is hugely beneficial for statistical analyses trying to infer the detection of any beam-related events.

A third benefit of spallation sources for CENNS searches is that the produced neutrinos are all in an appropriate energy range to undergo CENNS, higher energy than reactor neutrinos but low-enough energy so as not to scatter off of individual nucleons. The largest possible neutrino energy is half the difference between the μ^+ and e^+ masses, a little under 53 MeV. Neutrinos in this energy regime easily satisfy the coherence criterion, $qR_A \lesssim 1$ (momentum transfer q). For silicon, $qR_A \sim 0.5$ for these energies, and is never bigger than ≈ 1.04 , meaning essentially all the produced neutrinos contribute to the possibility of a CENNS event.¹⁰

A good description of the operation of the SNS, and spallation sources in general, is given by Scholz [77]. Suffice it to say further here that spallation sources are incredibly fertile ground for CENNS searches, and these searches are only limited by the sources' power output (total neutrino production rate) and ease of access to them. Thus, it makes sense that the first confirmed measurement of CENNS utilized one of these sources. However, these limitations are not going away any time soon, and alternative neutrino sources are currently being considered, and new experiments are underway.

2.2 Searches at Reactors

Nuclear reactors have a rich history in neutrino science, and were the source of the first neutrinos ever detected [6, 7]. Several experiments have been proposed in the past few years with the goal of detecting CENNS using nuclear reactor neutrinos. Nuclear reactors naturally generate large fluxes of electron antineutrinos, approximately 2×10^{20} ν /sec per GW reactor power [78] (compared to $\sim 3.5 \times 10^{15}$ ν /sec at ESS). These huge fluxes give an opportunity for high-statistics (high-counts, high-significance) experiments in relatively short time, in theory. In addition, ambient environmental backgrounds can be characterized fairly easily by taking data when the reactor is refueling or otherwise not in operation. These factors make reactors an extremely enticing source of neutrinos for CENNS searches.

2.2.1 Current experiments

Several experiments to search for CENNS at nuclear reactors have either been proposed or are currently underway. These experiments take many forms. The MINER [55, 79, 80] and RICOCHET [81–84] experiments use research reactors as their neutrino sources, while the CONNIE [85–88], CONUS [39, 76, 89], Dresden-II [90, 91], NUCLEUS [92–95], NuGeN [96], RED-100 [97–99], and TEXONO [100–103]

¹⁰The CENNS differential cross section over q scales approximately as $\sigma \sim q(1 - q^2/q_{\max}^2)$, ignoring the form factor. The maximum momentum transfer $q_{\max} = 2E_\nu$. The mean value of q is then $\frac{8}{15}q_{\max} = \frac{16}{15}E_\nu$

experiments use commercial power reactors. The power reactors tend to have much higher thermal power output (and thus create more neutrinos), but the research reactors generally allow access closer to the reactor core for experiments, with the tradeoff of an accompanying increase in the uncertainty in reactor-generated (reactor-created) backgrounds [92].

The detector technologies used in these experiments are also highly diverse. The most common detector type is called a “p-type point contact” (PPC) semiconductor detector [89, 90, 96, 102]. The active detection material in PPCs is a semiconductor crystal, most commonly Ge, held at low temperature, and hooked up to high-voltage electrodes to produce a large, nonuniform electric field in the crystal. NRs in the crystal ionize e/h pairs, and the e^- are focused into the actual ‘point contact,’ the cathode terminal of the electrodes, which takes the form of a small single-point connection to the high-voltage (HV) circuit. The ionized charge is detected by the minute bumps in current in the HV circuit, allowing a reconstruction of NR events (and other types of events) in the crystal.

The second most common detector type are cryogenic calorimeters [80, 93], which also consist of low-temperature ($O(10\text{ mK})$) semiconductor crystals at their core. NRs in the crystals cause optical (nondispersive) phonons which propagate through the crystal and are picked up at the surface, to be transferred to a transition-edge-sensor (TES), a low-heat-capacity component held very close to its superconducting transition temperature (where the resistance of the component changes extremely rapidly under small changes in temperature). There the phonons thermalize (dissipate), increasing the temperature of the component and drastically changing its resistance, which in turn causes a drop in electrical current through it. The drop in current allows one to reconstruct the energy deposited into the crystal.

A related detector type is a bolometer [81], which combines the target semiconductor crystal and TES into a single component. Here, the target crystal acts as TES as well, with particle interactions changing the temperature/resistance of the crystal directly, which is measured by a drop in current through the crystal.

Two other detector types are used in CENNS searches at reactors: two-phase noble gas scintillators [97, 104] and charge-coupled devices (CCDs) [85]. Two-phase noble gas scintillators look for interactions in a large volume of liquid noble gas. Charges freed by NRs in the liquid are transferred to a liquid-gas interface, where they cause scintillation (production of light) in the gas. CCDs are arrays of semiconductor crystals called ‘pixels’ that are coupled to each other. When an NR happens in one, causing a small ionization, the charge flows from pixel to pixel and can be measured.

These detectors all share the ability to detect extremely low-energy NRs, as are produced in CENNS events with reactor neutrinos. A summary of current experiments, including their locations and specifications of the experimental sites, reactors, and detectors, are given in Table 2.1.

Table 2.1: Summary of CENNS searches at reactors

| Experiment | Location | Reactor, Type, Thermal Power, Baseline Distance ^a | Detector Mass/Type | Detector Threshold/Resolution ^h |
|----------------------------|--------------------------------|--|--|---|
| CONNIE | Angra Dos Reis, Brazil | Angra 2 PR, ^d 3.8 GW, 30 m | 47.6 g Si CCD array | 28 eVee, ^c 5.5 eVee ^c |
| CONUS | Brokdorf, Germany | KBR PR, 3.9 GW, 17.1 m | 3.73 kg Ge PPCs | 0.2 keVee, ^c ~25 eVee ^c |
| Dresden-II | Morris, IL, USA | Dresden-II PR, 2.96 GW, 8 m | 2.924 kg Ge PPCs | 0.2 keVee, ^c ~33 eVee ^b |
| MINER | Texas A&M University, USA | NSC RR ^e , 1 MW, ~ 1 m | 100 kg Si & Ge calorimeters | ~ 20 eV, ^b 5 eV ^{c,f} |
| NUCLEUS (ν -cleus) | Ardennes, France | Chooz B PR, 4.25 GW, 72 m | 10 g CaWO ₄ /Al ₂ O ₃ calorimeters | 19.7 eV, ^c 3.7-3.8 eV ^c |
| NuGen (ν GeN) | Udomlya, Russia | Kalinin PR, ~1 GW ^g , 10 m | ~1.6 kg Ge PPCs | 350 eV, ^c ~93 eV ^c |
| RED-100 | Udomlya, Russia | Kalinin PR, ~1 GW ^g , 10 m | ~240 kg Xe two- phase scintillator | 300 eV, ^b not listed |
| RICOCHET | Institut Laue-Langevin, France | ILL-H7 RR, 58.3 MW, 8 m | ~1 kg Ge & Si bolometers | ~ 50 eV, ^b 17 eV ^c |
| TEXONO | Jinshan, Taiwan | Kuo-Sheng PR, 2.9 GW, 28 m | ~1.5 kg Ge PPCs | 300-400 eVee, ^b ~45 eVee ^c |

^aminimum distance allowed by reactor facility or minimum distance considered by authors (if multiple reactor cores, distance to closest)

^btarget

^cbest achieved

^dPR = Power Reactor

^eRR = Research Reactor

^fdata taken from [105]

^gdata found online

^hbaseline resolution

2.2.2 Reactor neutrinos

From here, now that the background of CENNS searches at reactors has been established, the procedure outlined in Figure 2.1 begins. This subsection describes reactor antineutrinos and the model used to describe their emission, which in turn will be used to simulate CENNS events in our detector.

2.2.2.1 Production mechanism

Neutrinos are produced in nuclear reactors during beta-decay, the decay of a neutron into a proton, an electron, and an electron antineutrino:

$$n^0 \rightarrow p^+ + e^- + \bar{\nu}_e \quad (2.2.1)$$

As this happens inside of atomic nuclei, the reaction looks like:

$${}^A(Z) \rightarrow {}^A(Z-1) + e^- + \bar{\nu}_e \quad (2.2.2)$$

where the notation ${}^A(Z)$ indicates a nucleus with atomic number Z and mass number A .

A nuclear reactor generates energy from the neutron-induced fission of four main isotopes of uranium and plutonium: ${}^{238}\text{U}$, ${}^{235}\text{U}$, ${}^{239}\text{Pu}$, and ${}^{241}\text{Pu}$. Each of these fissile isotopes is parent to a different branching decay chain that produces neutrinos in different amounts and with different energy spectra (“ β -branches” or “beta branches”). For example, the dominant fission chain is described by Hayes and Vogel [106]: ${}^{235}\text{U}$ decays into two unstable fragments most commonly with mass numbers 94 and 140. The stable nuclei with those masses are ${}^{94}\text{Zr}$ and ${}^{140}\text{Cr}$, with a total 98 protons and 136 neutrons between them. However, the initial system has 92 protons and 142 neutrons, meaning that in order to reach the stable configuration six neutrons must undergo beta decay, in the process emitting six neutrinos.

The average number of neutrinos emitted in a fission decay chain is six [32]. Following neutron capture on ${}^{238}\text{U}$, the beta decays carrying ${}^{239}\text{U}$ to ${}^{239}\text{Pu}$ also release low-energy neutrinos. Further neutron captures on ${}^{239}\text{Pu}$ produce ${}^{241}\text{Pu}$. These all contribute to reactor neutrino emissions, which in total amount to approximately 2×10^{20} neutrinos per second per gigawatt of reactor thermal power [78].

2.2.2.2 Neutrino spectrum

The spectrum of neutrinos emitted by nuclear reactors in the manner described in the previous section has been the subject of considerable study. There are two main approaches to calculating reactor neutrino emissions [32, 106]. The first is called the *ab initio* approach. This approach constructs the neutrino emission spectra of each fissile isotope from the ground up, calculating the neutrino spectra for each β -branch of each fission product and summing them all up. The neutrino spectrum of each branch is obtained theoretically, based on the properties of the parent isotope in the transition and the energy of the transition, and weights to each β -branch are given according to the branching ratios of the branch and the “activity” (also called “fission yield”) of the daughter fission product (proportion of fissions that form the product), both of which are either measured or, if unmeasured, estimated using computational models of the nucleus. Uncertainties associated with this method are largest for branching ratios, fission yields, and endpoint energies of short-lived fragments that release larger energies. For these transitions, the shape of the neutrino spectra of each branch is less certain, as factors governing the shape and corrections due to radiation effects and the finite size of the nucleus are much more complicated. There is likewise a large un-

certainty associated with “missing info,” β -branches that are completely missing from nuclear databases because too little information about them is known ($\sim 30\%$ of contributing transitions are known to be forbidden,¹¹ and a substantial fraction of these constitute “missing info” [106]). The overall error in the estimated neutrino spectrum can be as large as 10 – 20% [32, 78].

The second approach consists of electron spectrum conversion methods, wherein the measured electron emission spectrum from each fission fuel isotope is used to infer the neutrino spectrum. Most approaches of this sort rely on measurements of the electron spectrum of ^{235}U , ^{239}Pu , and ^{241}Pu taken at the Institut Laue-Langevin (ILL) in the 80’s [107–109], and the spectrum of ^{238}U taken at the FRM II neutron source in Garching, Germany in 2014 [110]. This method divides the measured electron spectrum into an energy grid, with each point in the grid defining the endpoint of a virtual (effective) beta decay branch. High-energy slices of the electron spectrum are used to estimate the rates of the high-energy virtual branches, and the rates of successive virtual branches (branching ratios of each branch) are fitted in sequence. The spectra of electrons and neutrinos from any one branch are correlated, as the total energy in the decay along the branch is split between the emitted electron and the neutrino (recoil energy of the nucleus and energy of any emitted gammas are considered negligible), allowing one to estimate the neutrino spectrum.

This method has the benefit of, by definition, predicting β -branch branching ratios that yield the correct electron spectrum – however, the method has been shown to distort the predicted neutrino spectrum around the endpoint energies on the energy grid, and assumptions about the average nuclear charge of the virtual branches can bias the shape of the spectrum [111]. Additionally, there are systematic uncertainties on the order of 4% in the normalization of antineutrino emissions, caused by uncertainty in the structure of forbidden transitions along the β -branches [112].¹² The total uncertainties in this method are on the order of $\sim 5\%$ [32].

Mueller et al. [78] uses a “mixed approach” (that we will refer to as the *Mueller model*) that combines the best of both methods. This is the model we use to describe reactor neutrino emissions. The mixed approach begins with the *ab initio* approach, fully calculating the neutrino spectrum based on combined data from four main sources. The activity of each fission fragment is calculated using a custom fuel burnup code built on the neutron transport code MCNP (Monte-Carlo N-Particle transport code), Version 4C [113]. For branching ratios, the majority of their data was taken from the Evaluated Nuclear Struc-

¹¹“forbidden transitions” are transitions between nuclear states that violate rules for conservation of spin and angular momentum assuming simple single-particle interactions – these transitions are more complicated, and computational models are difficult to use because of the complexity of the nuclei in question

¹²These uncertainties apply to both *ab initio* and electron spectrum conversion methods, and revolve around changes to models based on the assumed form of the forbidden transitions.

ture Data File (ENSDF) library [114], a large-scope database compiling together all kinds of evaluated nuclear structure data. Another substantial portion of their data, some 67 isotopes’ worth, was taken from a collection of (anti-)neutrino- and beta-spectrum measurements taken jointly at OSIRIS (On-line Separation of Isotopes at a Reactor In Studsvik) in Sweden, and at ISOLDE (Isotope mass separator on-line facility) at CERN in Switzerland [115, 116]. These measurements used isotope-separator-on-line (ISOL) methods to isolate short-lived fission fragments by irradiating targets made of uranium or thorium (at ISOLDE) or uranium carbide (at OSIRIS) with high-energy protons and rapidly pumping the resulting fission-fragmented material through a mass separator and into measurement apparatus, where β and ν spectra could be observed [117]. The last important collection of data they used were estimates of contributions from high-energy transitions of exotic nuclei not included in the ENSDF files, from the Japanese Evaluated Nuclear Data Library (JENDL) [118], which uses predictions of the “gross theory” of beta decay to estimate these contributions based on gross (aggregate) properties of the final states of these rare (but highly significant at high neutrino energy) decay chains [119].

This collection of data substantially minimizes the discrepancy between the *ab initio* approach and the ILL data, compared to using the ENSDF data alone. The ISOL-measurement data helped alleviate systematic errors from what is called the “pandemonium” effect [120], wherein photons emitted by higher-energy transitions are more likely to be missed by common germanium-based gamma detectors when measuring branching ratios. This has the effect of over-estimating high-endpoint branches that release more photons at lower energy, the range where the Ge detectors have highest efficiency. Directly measuring electron and neutrino spectra eliminates this error. The inclusion of exotic decay branches from JENDL helps fill in some, but not all, of the “missing data” that would otherwise cause underestimation of (especially high-energy parts of) the spectrum. In total, this part of the Mueller model includes 845 nuclei and $\sim 10^4$ β -branches.

At this point, the electron spectrum emitted by the predicted β -branch configuration only accounts for between $\sim 80\%$ and $\sim 90\%$ of the ILL electron spectra. The last phase of the Mueller model calculation is to fill in those remaining few percent using essentially identical methods to the electron-spectrum conversion method alone. That is, they fit a system of five virtual branches with unknown endpoint energies to the difference between the ILL measurements and their *ab initio*-predicted electron spectra. The neutrino spectra associated with those five virtual branches are then added to the neutrino spectra of the *ab initio* calculations to yield the full neutrino spectrum. The intrinsic errors associated with the electron-spectrum conversion procedure are reduced by nearly an order of magnitude since they are only responsible for a fraction of the total spectra, and errors associated with “missing information” are decreased by the inclusion of the extra beta branches. The overall resulting uncertainties in the neutrino

spectrum are around 2-3% below 5 MeV neutrino energy, and then climb to $\sim 5\%$ for ^{235}U and ^{241}Pu . The errors for ^{239}Pu are higher at high energies, reaching 20% at the highest neutrino energies. The errors associated with the ^{238}U spectrum, for which there were no electron-spectrum measurements made at ILL (and the measurements at FRM II had not yet been made), are the errors of the original *ab initio* calculations, maximum $\sim 20\%$.¹³

Mueller and collaborators [78] tabulate the results of these calculations for the neutrino spectrum on an energy grid between 2 and 8 MeV neutrino energy with spacing of 0.25 MeV (the “12 h” data in Table 3, and Tables 4 and 5). They also provide a useful parameterization of their data, fits of the form

$$S_k(E_\nu) = \exp\left(\sum_{p=0}^5 \alpha_{pk} E_\nu^p\right) \quad (2.2.3)$$

for the emitted neutrino spectrum (neutrinos per fission per MeV) S_k for isotope k at neutrino energy E_ν . The α_{pk} are fitted parameters, determined by a least-squares fit of a fifth-order polynomial to the log-spectrum data (energy vs log of the spectrum data tabulated in their tables). The reported values of α_{pk} are given in Table 2.2. The Mueller model’s tabulated data and their fitted functions are plotted in Figure 2.2.

Table 2.2: Coefficients α_{pk} for Mueller model antineutrino spectra from Mueller, et al.

| p | ^{235}U | ^{238}U | ^{239}Pu | ^{241}Pu |
|-----|------------------|------------------|-------------------|-------------------|
| 0 | 3.2170 | 0.4833 | 6.4130 | 3.2510 |
| 1 | -3.1110 | 0.1927 | -7.4320 | -3.2040 |
| 2 | 1.3950 | -0.1283 | 3.5350 | 1.4280 |
| 3 | -0.3690 | -0.0068 | -0.8820 | -0.3675 |
| 4 | 0.0445 | 0.0022 | 0.1025 | 0.0425 |
| 5 | -0.0021 | -0.0002 | -0.0046 | -0.0019 |

We emulate the neutrino emissions of a typical low-enriched research reactor, whose emitted neutrino spectrum is dominated by the fission of ^{235}U . The relative strengths of the different isotopes in the spectrum of the MINER reactor are adopted here: 96.7% ^{235}U , 1.3% ^{238}U , and 2% ^{239}Pu [55].

The Mueller model fit truncates at a lower bound of 1.8 MeV. We extend the fits to 0.8 MeV, approximately the lowest neutrino energy that can produce a recoil of 50 eV in silicon, and consider the spectrum to drop to zero below that. A peak position of 0.8 MeV is in moderate agreement with the peaks of the spectra calculated by Vogel and Engel [122].

¹³For comparison, uncertainties in measured antineutrino spectra from the Daya Bay reactor complex in 2017 [121] (one of the most recent such measurements) are on the order of 3% between 2.5 and 6 MeV, and climb to $\sim 9\%$ at low energies and past 30% above 9 MeV.

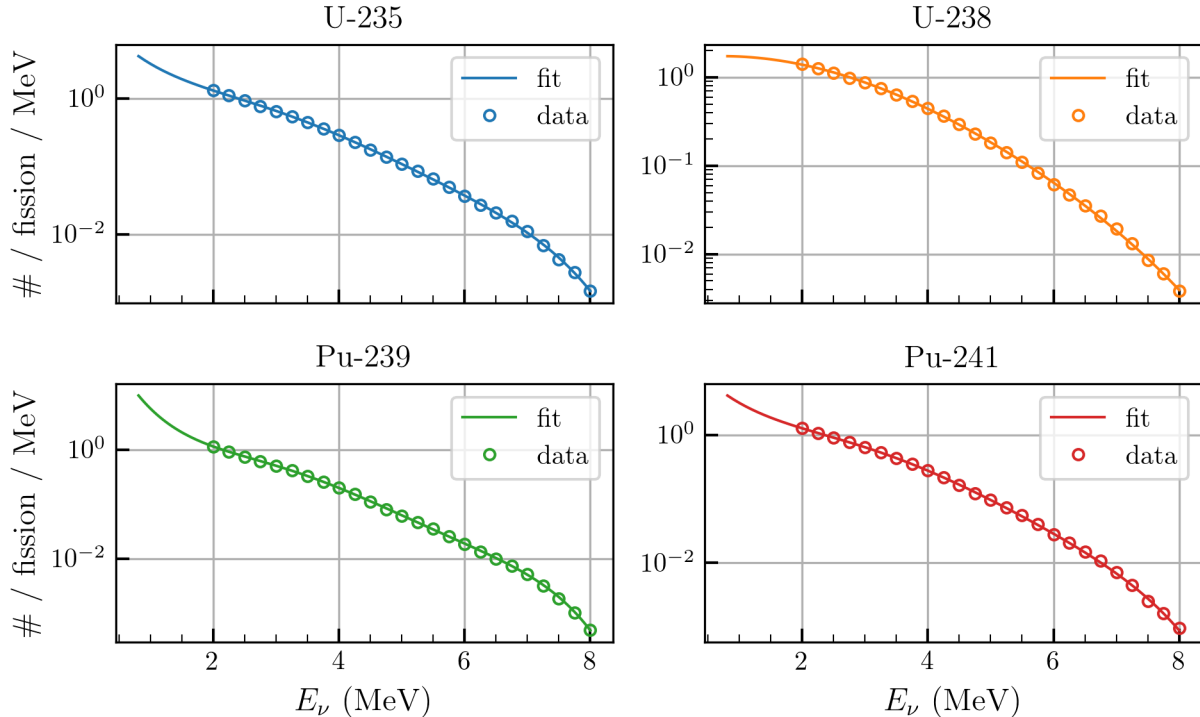


Figure 2.2: Neutrino emission spectrum for four main fissionable isotopes. Circles show tabulated spectrum data from Mueller, et al. and solid curves show their fit parameterizations (eq. (2.2.3)). The fits are extended to a minimum neutrino energy of 0.8 MeV

2.3 Neutron Backgrounds at Reactors

One of the biggest obstacles to CENNS searches near nuclear reactors is reactogenic backgrounds. Among the sources of backgrounds, reactor neutrons are one of the most difficult types of background to deal with. The main reason for this difficulty is that neutrons cause NRs that cannot be distinguished from NRs caused by CENNS events.¹⁴ This section describes the model of neutron captures used to simulate capture events. These events are the main background to the CENNS signal considered, as shown in Figure 2.1.

Background studies at CONUS [76], MINER [79], and RICOCHET [83] all identified neutrons as a major source of backgrounds. However, for the most part they focus on NRs produced by elastic scatters with fast neutrons, and none of them explicitly consider captures of thermal neutrons. Scatters caused by thermal neutrons are generally extremely low-energy, below the detection thresholds of essentially all modern detectors, and so can be safely ignored. However, neutron captures can cause NRs of hundreds of

¹⁴Depending on the type of detector and the location of the experiment, backgrounds from cosmic-ray muons may be the dominant source of backgrounds (e.g., [87]). However, these experiments commonly have the ability to dependably discriminate between ERs and NRs, of which muons produce the latter, which effectively reduces the rate of these backgrounds to almost zero.

eV in the case of Ge, and up to 2 keV in the case of Si, firmly within the parameter space of interest for CENNS searches. Furthermore, thermal neutron fluxes are generally much larger than their fast counterparts, and increase relative to high energy neutrons with distance from the reactor due to thermalization in the air and when passing through shielding and building materials (see, e.g., [123]). Some experiments at commercial reactors [92, 102] actually ignore reactogenic neutrons entirely since they expect the fast neutron flux to drop so much between their reactor core and their detectors. However, the background studies for CONUS [76] and RICOCHET [83] find highly thermalized neutron fluxes at detector sites 17.1 and 7 m from the reactor cores, respectively, which indicates that a strong thermal component of reactogenic neutrons can reach even several rooms away from the reactor core. The capture of these neutrons therefore represents a significant background to these experiments.

2.3.1 Capture spectrum model

To investigate the influence of neutron captures on CENNS searches, samples of neutron capture events were simulated using `nrCascadeSim` [124], an open-source software package dedicated to the simulation of radiative neutron captures.¹⁵ The code simulates nuclear cascades following a neutron capture by choosing from the most common decay paths from the neutron separation energy (the energy level of the nucleus upon capturing a free neutron) down to the nucleus’ ground state energy, using nuclear energy level data from ENSDF [114]. The output of this code is, among other things, an array of recoil energies corresponding to the energy released in each capture event.

Samples of $O(10^5)$ events were simulated in silicon and germanium.¹⁶ The resulting spectra of capture-induced recoil energies are shown in Figure 2.3.

Some features of the capture spectra are of note. First, both spectra clearly extend to recoil energies of several hundreds of eV, firmly in the region of interest for CENNS searches. Second, both spectra exhibit a series of narrow peaks. These peaks are caused by high-probability cascades involving either “straight-to-ground” transitions from the neutron separation energies of the naturally-occurring isotopes in the material, or transitions that act similar to the “straight to ground” transitions due to large lifetimes of intermediate states. In these cascades, all of the extra energy of the nucleus is released from rest in a single gamma, eliminating “smearing out” effects from decay-in-flight of shorter lived intermediate states, resulting in nearly monoenergetic spikes in the recoil energy spectra.

¹⁵Version 1.0.6 was used to generate events in Si, version 1.4.6 for Ge

¹⁶The actual number is somewhat less than 10^5 , because of a quirk in how `nrCascadeSim` handles the random generation of decay cascades

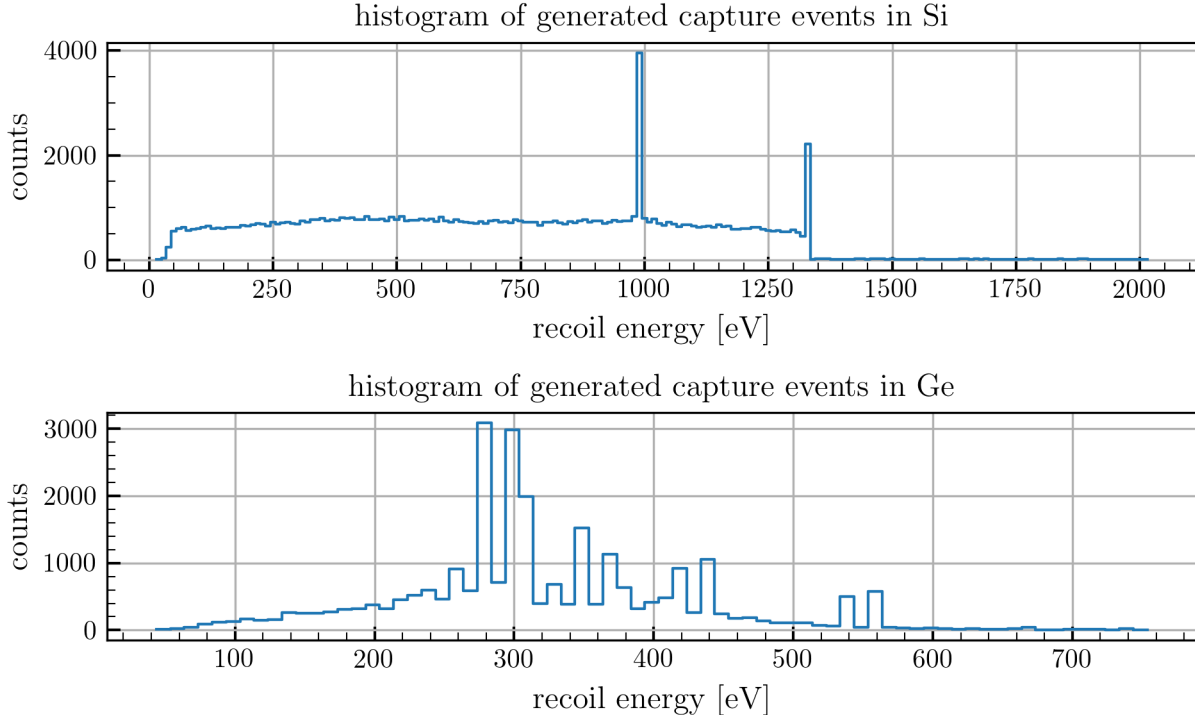


Figure 2.3: Histograms of generated capture events using `nrCascadeSim` for silicon (top) and germanium (bottom). Bin widths are 10 eV

To simulate samples of capture events, the desired number of events are selected from the events generated by `nrCascadeSim` with repetitions (i.e., selections are made from the samples of recoil events plotted in Figure 2.3).

2.4 Detector Model

This section describes the detector models used, which convert between datasets of true recoil energy for CENNS and capture events to measured recoil energy. As mentioned above, the detector models used here will attempt to emulate generic low-background silicon and germanium detectors. In order to be agnostic about the exact type of detector used, we will only consider the direct measurement of recoil energy. In reality, very few detector types measure recoil energy directly, but instead measure ionization energy or some combination of ionization and recoil energy as a proxy for direct measurements. We reason however that statistical comparisons of such collections of data will be roughly equivalent whether the collected data is expressed in terms of distributions over recoil energy or distributions over ionization energy or other measured quantities. Since both CENNS and neutron captures produce NRs, conversions between these measured quantities will be the same regardless of the source of the event.¹⁷

¹⁷We make this assumption of equivalence because in theory, the actual physical processes converting recoil energy to other forms of measured data are one-to-one and invertible, though of course in reality

The operation of these generic detectors is described completely by two parameters: the energy threshold and the energy-dependent energy resolution. The threshold energy is the minimum recoil energy that can be detected, and the energy resolution is a measure of how precisely the detector can measure an event of a given energy. Specifically, the energy resolution is the standard deviation of the energy measured by the detector with respect to the actual energy of an event due to random noise effects in the detector. That is, for an event with “actual” recoil energy E_r and an energy resolution $\sigma(E)$, the energy that is recorded is a normally-distributed random variate with mean E_r and standard deviation $\sigma(E_r)$.

A common parameterization of the detector resolution takes the form (see, e.g., [87, 125, 126]):

$$\sigma(E_r) = \sqrt{\sigma_0^2 + CE_r} \quad (2.4.1)$$

where σ_0 is the baseline resolution, the resolution at zero energy, and C is a constant combining detector-specific effects and the intrinsic variance in e/h pair production (more on this in Section 3.7). To test the effects of detector resolution, we sweep different values of σ_0 and C . For a given baseline resolution, the full resolution function (2.4.1) is characterized by the *effective resolution*, $\sigma_{\text{eff}} \equiv \sigma(50 \text{ eV})$, the resolution at a recoil energy of 50 eV. Rewriting (2.4.1) in terms of the effective resolution yields:

$$\sigma(E_r) = \sqrt{\sigma_0^2 + \left(\frac{\sigma_{\text{eff}}^2 - \sigma_0^2}{50 \text{ eV}}\right) E_r} \quad (2.4.2)$$

The 50 eV value was chosen arbitrarily as a typical low-energy value where measurements of resolution might be made.

The threshold energy of the detector is taken to be $5\sigma_0$. The reasoning behind this is that ~ 0 energy “events” caused by random thermal fluctuations will be measured with energies up to and including $\sim 5\sigma_0$, and so any events that can be dependably observed by the detector must clearly rise above this thermal noise (assuming a normally-distributed noise population, only approximately 1 in 1.7 million zero-

these processes are often chaotic and unobservable, and are often themselves parameterized by stochastic processes (see, e.g., Section 3.7). We find it sufficient to reason that stochastic processes carrying recoil energies into other measured data are identical for both event types, and so the resulting transformations of the event distributions will also be identical.

energy noise events will appear higher than $5\sigma_0$). A factor of five relating baseline resolution and threshold is consistent with [39, 81, 85, 87, 90, 93, 96, 99, 102, 103].

2.4.1 Operational parameters

The simulated experiment here attempts to approximately emulate a 100 kg yr exposure of a detector 10 m from a research reactor with similar neutrino emissions to the reactor used in the MINER experiment. In a study of detector response [80], the MINER collaborators estimate an event rate of ~ 7.83 CENNS events/day in a 100 kg Si detector. This yields approximately 2,860 CENNS events in a 100 kg yr exposure, which we round up to 3,000.

To convert these CENNS rates to Ge detectors for an identical exposure, we note that the number of interactions per energy bin n in a detector for an exposure Q (mass \times time), composed of particles with nuclear mass m and total cross section \mathcal{O} in an ambient flux I (particles per unit area per unit energy per unit time) is:

$$n = \frac{Q}{m} \mathcal{O} I \quad (2.4.3)$$

Solving for the flux

$$I = \frac{nm}{Q\mathcal{O}} \quad (2.4.4)$$

Thus, for two detectors (primed and unprimed) in the same fluxes, the relationship between the number of events is:

$$n' = n \frac{\mathcal{O}'}{\mathcal{O}} \frac{m}{m'} \frac{Q'}{Q} \quad (2.4.5)$$

For CENNS, the ratio of cross sections \mathcal{O}'/\mathcal{O} is approximately $(\mathcal{N}'/\mathcal{N})^2$, the ratio of the weak charges squared.

For identical exposures $Q = Q'$ we get $n' = n(\mathcal{N}'/\mathcal{N})^2(A/A')$ where A is the mass number of the nucleus. For detectors composed of multiple materials or isotopes, the expressions include summations over materials i with relative abundances p_i :

$$n' = n \left(\sum_{i'} p'_{i'} \frac{(\mathcal{N}'_{i'})^2}{A'_{i'}} \right) \left(\sum_i p_i \frac{\mathcal{N}_i^2}{A_i} \right)^{-1} \quad (2.4.6)$$

Taking the unprimed parameters to be those for silicon, and the primed to be for germanium, we get $n' \approx (20/6)n$. For our selected CENNS event rate, $n = 3,000$ in Si over the whole energy range, which yields $n' = 10^4$ in Ge. The MINER detector response paper [80] estimates a rate for Ge that's about 60% larger than this value, but attempts to repeat these calculations have been unsuccessful. Thus 3,000 and 10,000 are the numbers of CENNS events included in each simulated sample for Si and Ge detectors, respectively.

2.4.2 Ambient thermal neutron flux

Ambient thermal neutron fluxes were tested between $\approx 2.7 \times 10^{-7}$ and 2.7×10^{-3} neutrons per cm^2 per second. To translate these fluxes into numbers of capture events, we use radiative capture cross section data taken from the EGAF (Evaluated Gamma-Ray Activation File) database [127, 128]. The values of the capture cross sections and their corresponding uncertainties for Si and Ge are given in Table 2.3. The number of capture events corresponding to the lowest/highest neutron fluxes considered are also given.

Table 2.3: Capture cross sections and numbers of capture events for Si and Ge detectors. Uncertainties are given in the second column in parentheses

| Detector material | Capture cross section (barns) | Events at minimum flux ($2.7 \times 10^{-7} \text{ cm}^{-2} \text{ s}^{-1}$) | Events at maximum flux ($2.7 \times 10^{-3} \text{ cm}^{-2} \text{ s}^{-1}$) |
|-------------------|-------------------------------|--|--|
| Si | 0.171 (3) | 3,162 | 3.162×10^7 |
| Ge | 2.2 (1) | 15,849 | 1.5849×10^8 |

2.4.3 Irreducible background

In addition to the CENNS and capture events simulated, we also add in a number of “background” events meant to emulate the leftover NR events that remain from outside sources (e.g., environmental radioactivity, cosmogenic neutrons, etc.) after background vetos and subtractions. Some of these background events will evade vetos and discriminations and will remain in any typical “final” dataset of NR events. We choose two extremely rudimentary models for these backgrounds, mainly in order to emulate uncertainty in other types of backgrounds rather than to actually emulate the effect of those backgrounds themselves.

The first is uniformly distributed at 10% the CENNS rate (300 events in Si, 1000 in Ge). This “flat background” is meant to approximately emulate a flat uncertainty in a background subtraction, leaving behind approximately 1% of a background with a rate $\sim 10 \times$ the CENNS rate (see, e.g., [79]). The second background is slightly more realistic in form. Its probability density function takes the form $P_b(E) \propto$

$E^{-0.9}$, which is the result of a rough fitting of the neutron background data given by [79]. The normalization of this spectrum is set at 60% the CENNS rate, similar to the rate of fast-neutron-induced events at the Chooz reactor site [82] and about 50% larger than the target NR background rate published by the RICOCHET collaboration on the arXiv [84]. This rate is also consistent with assuming an $\sim 80\%$ reduction in the backgrounds at TEXONO with shielding [102], which is a plausible (if pessimistic) reduction. This will be referred to as the “sloped background.” We will also consider a “combination background” consisting of both components.

Note that this “other” background component circumvents the detector model in Figure 2.1. This is because we are not interested in how the over-simplified PDFs for these events are affected by the detector resolution. The PDFs are considered to represent distributions over measured energies, rather than true recoil energies. This assumption makes simulating these events much easier, and it will be seen later that the resulting uncertainties are very minor, as the results for the different background models are very similar.

2.5 Statistical Analysis

This section outlines the statistical procedure used to determine whether the CENNS signal can be detected in a given simulated sample. The input to this procedure is the simulated sample of CENNS, capture, and background events, and the output will be a number measuring the probability there is a CENNS component in the sample. In this way we will determine whether the CENNS component can be discerned in the data in the simulated environmental conditions.

This procedure went through two distinct phases over the course of developing our methodologies. Both phases are described here.

2.5.1 Unbinned likelihood analysis

At first, an unbinned likelihood analysis, analogous to ones used in the context of searching for a dark matter signal [125, 129, 130], was used. This form of likelihood analysis has also been used in the context of CENNS searches by the NUCLEUS collaboration [92, 94]. The form of the likelihood function used is analogous to the form given in [125]:

$$\mathcal{L} = \frac{e^{-n_{\text{total}}}}{N!} \prod_{i=1}^N [n_{\nu} P_{\nu}(E_i) + n_c P_c(E_i) + n_b P_b(E_i)] \quad (2.5.1)$$

Here, the set $\{E_i\}$ is the dataset of N measured recoil energies, and $P_\nu(E)$, $P_c(E)$, and $P_b(E)$ are the probability density functions (PDFs) at energy E for CENNS, capture, and background events, respectively. n_ν , n_c , and n_b are the number of each corresponding type of event, and n_{total} is the sum of these.

If we factor out n_{total} from the term in brackets, we get:

$$\mathcal{L} = \frac{n_{\text{total}}^N e^{-n_{\text{total}}}}{N!} \prod_{i=1}^N P_{\text{true}}(E_i) \quad (2.5.2)$$

where $P_{\text{true}}(E)$ is the “true” probability distribution of the events in the dataset, a weighted sum of the PDFs for the individual event types with weights given by the numbers of each event:

$$P_{\text{true}}(E) = \frac{n_\nu}{n_{\text{total}}} P_\nu(E) + \frac{n_c}{n_{\text{total}}} P_c(E) + \frac{n_b}{n_{\text{total}}} P_b(E) \quad (2.5.3)$$

Written this way, we can understand the likelihood function as being the joint probability of the N measurements $\{E_i\}$, which is just the probability densities for each individual measurement $P_{\text{true}}(E_i)$ multiplied together, times the Poisson-distributed probability of making n_{total} measurements, $n_{\text{total}}^N e^{-n_{\text{total}}}/N!$.

For a given dataset $\{E_i\}$, the likelihood \mathcal{L} is a function of the $\{n_k\}$ (where the index k runs over CENNS, capture, and background events). We thus estimate the numbers of each event type composing a sample $\{E_i\}$ by maximizing the likelihood \mathcal{L} with respect to the $\{n_k\}$. We refer to the maximized likelihood as \mathcal{L}_1 .

The maximized likelihood \mathcal{L}_1 for a sample including all three event types (CENNS, captures, and backgrounds) is contrasted with a maximized likelihood \mathcal{L}_2 with only capture and background events, that is, a likelihood that is the maximized value of a modified likelihood function \mathcal{L}' , which is \mathcal{L} with n_ν constrained to be zero:

$$\mathcal{L}' = \frac{e^{-(n_b+n_c)}}{N!} \prod_{i=1}^N [n_c P_c(E_i) + n_b P_b(E_i)] \quad (2.5.4)$$

The two likelihoods \mathcal{L}_1 and \mathcal{L}_2 can be compared using Wilks’ theorem [131], which states that the quantity $\chi_0^2 = 2 \ln(\mathcal{L}_1/\mathcal{L}_2)$ is distributed as a χ^2 random variate with one degree of freedom.

In general, for a first maximized likelihood L_Ω over an h -dimensional parameter space Ω and a second maximized likelihood L_ω over a subset $\omega \subseteq \Omega$ with m free parameters and $h - m$ parameters con-

strained, Wilks’ theorem states that up to $O(N^{-1/2})$, the quantity $2 \ln(L_\Omega/L_\omega)$ is distributed as a χ^2 random variate with $h - m$ degrees of freedom. The condition must also be met that the likelihood function over Ω is smooth and differentiable with respect to the parameters and there must exist a true maximum likelihood somewhere in Ω (the likelihood function must be finite everywhere and have a peak). Since we consider samples of minimum size $\sim 6,000$, we don’t worry about the $O(N^{-1/2})$ error terms. The two additional conditions are met by (2.5.1), which is a smooth function of the $\{n_k\}$.

Wilks’ theorem allows us to immediately calculate and characterize the confidence with which the CENNS signal can be detected. Since χ_0^2 is a χ^2 variate with one degree of freedom, $\sqrt{\chi_0^2}$ is distributed as a standard normal variate. This allows us to immediately calculate the probability that we measure some value of $\sqrt{\chi_0^2}$ purely as a result of randomness in our sample, using the normal error integral.¹⁸ The most common way to report this confidence is to simply report the value of $\sqrt{\chi_0^2}$, the “statistical significance” of the measurement [133] (see, e.g., [92]). This can also be called a sigma-value, sigma-level, or Z value, and we will often refer to it as the “confidence” or “confidence level.” For example, a sample with $\sqrt{\chi_0^2} = 2$ is a 2σ sample, and the probability that the sample only consists of capture and background events, and the preference for \mathcal{L} over \mathcal{L}' is the result of random chance, is 4.55%. A 3σ sample or $Z = 3$ sample doesn’t have CENNS events only 0.27% of the time. A common threshold for affirmative confidence in a measurement is a confidence level of 5σ , where the probability of the measurement being the result of random chance is only 0.00006% (so the confidence in the presence of CENNS is 99.99994%).

This likelihood analysis thus allows us to quantify the confidence in a CENNS measurement for some simulated dataset by calculating the sigma value. High confidence values indicate experimental conditions favorable to measuring reactor CENNS, while low significance values indicate the conditions of the simulated experiment are not favorable to measuring CENNS; a real experiment in such conditions would likely not be able to confidently claim a CENNS measurement in a 100 kg yr exposure time.

2.5.2 Binned likelihood analysis

Over the course of this work, it was found that the unbinned likelihood analysis was extremely slow and resource-intensive. Its storage requirements scaled linearly with N , the sample size – for the largest samples considered (Ge at maximum flux), this translated to several gigabytes of storage for each array of data, and three such arrays had to be kept in memory: one for the energy values $\{E_i\}$ and one each for the CENNS and capture PDFs.

¹⁸Reference on the normal error integral can be found in [132]. Note we must use the symmetric (two-tailed) error integral because the probability mass of both positive and negative values of a normal variate get folded into the probability mass of the chi-squared variate. The normal error integral is calculable using the `scipy.special.erf()` and `erfc()` functions in Python.

Binned methods, on the other hand, only need to keep track of data corresponding to each bin, rather than to each event. A batched-generation method can be used to generate the N events, where a smaller number of events is generated at once, the histogram-counts added to a running total, and the sample overwritten with another sample of the same size, repeating until the desired number of samples is reached. It was found that this method was around 1,000 times faster than the unbinned analysis, and yielded extremely similar results (see Section 2.7.2).

Binned analyses are much more common in CENNS searches than unbinned analyses (see [37, 39, 73, 82, 89] for binned likelihood functions or [31, 81] for binned chi-squared fits). The binned likelihood function takes the form [133]:

$$\mathcal{L} = e^{-n_{\text{total}}} \prod_{j=1}^{N_{\text{bins}}} \frac{1}{C_j!} [n_{\nu} A_{\nu,j} + n_c A_{c,j} + n_b A_{b,j}]^{C_j} \quad (2.5.5)$$

where C_j is the counted number of data points in bin j and $A_{k,j}$ is the expected proportion of events of type k in bin j (the area under $P_k(E)$ in the bin). Defining n_j for the fitted number of events in bin j , $n_j = n_{\nu} A_{\nu,j} + n_c A_{c,j} + n_b A_{b,j}$, and noting that $\sum_j n_j = n_{\text{total}}$, we can rewrite this as:

$$\mathcal{L} = \prod_{j=1}^{N_{\text{bins}}} \frac{e^{-n_j} n_j^{C_j}}{C_j!} \quad (2.5.6)$$

which can be understood as the joint probability of n_j Poisson-distributed events winding up in each bin j with averages C_j .

This binned likelihood can be approximately derived from the unbinned likelihood by partitioning the full sample of data $\{E_i\}$ into sets j where, for all E_i in a set j , the E_i are “close enough” to a central value of the set E_j that $P_k(E_i) \approx P_k(E_j)$. Then, if each set j contains C_j data points, our original likelihood function becomes

$$\mathcal{L} = \frac{e^{-n_{\text{total}}}}{N!} \prod_{j=1}^{N_{\text{bins}}} [n_{\nu} P_{\nu}(E_j) + n_c P_c(E_j) + n_b P_b(E_j)]^{C_j} \quad (2.5.7)$$

However, we need to account for the size of the range of energies that gets grouped up into each set j , so each $P_k(E_j)$ should become $P_k(E_j)\Delta E_j$, where ΔE_j is the width of bin j . We can see then that in the appropriate limit, this is really the area under $P_k(E)$ in bin j , hence we arrive at (2.5.5) up to some factor of

$N!/\prod_j C_j!$. We should also mention that (2.5.1) should have a factor of dE^N somewhere, to translate the product of probability *densities* into *probabilities*, but in the likelihood ratio test such factors (including the $N!$ and $\prod_j C_j!$) will all cancel out, and we can see the likelihood ratios calculated will be roughly the same so long as the bins are small enough.

The rest of our likelihood analysis proceeds in exactly the same way as the unbinned version, with a modified \mathcal{L}' with n_ν constrained at zero:

$$\mathcal{L}' = e^{-(n_c+n_b)} \prod_{j=1}^{N_{bins}} \frac{1}{C_j!} [n_c A_{c,j} + n_b A_{b,j}]^{C_j} \quad (2.5.8)$$

Note that for the mixed background model, terms for both flat and sloped backgrounds are included in (2.5.5) and (2.5.8) and the two background components are treated as separate values of k .

2.6 Computational Procedures

This section will outline the computational procedures used in calculating sampling spectra, simulating events, and calculating (and maximizing) the likelihood function.

2.6.1 Calculating recoil spectrum of CENNS events

As we saw in Section 1.4.3, the rate of CENNS events due to neutrinos of energy E_ν that cause recoils of energy E_r is $I(E_\nu)\sigma(E_r, E_\nu)$, where $I(E_\nu)$ is the flux of neutrinos with energy E_ν and $\sigma(E_r, E_\nu)$ is the CENNS cross section (2.1.1). We can integrate this product to get the total rate per unit energy $R(E_r)$ of CENNS events that cause recoils with energy E_r for a single nucleus:

$$R(E_r) = \int_0^\infty I(E_\nu)\sigma(E_r, E_\nu)dE_\nu \quad (2.6.1)$$

We perform this integration numerically using `scipy.integrate.quad_vec()` for each isotope of Si and Ge and add them together (weighted by the natural abundances [134]), for a grid of recoil energies spaced by 1 eV between zero and 1 keV. So the total average CENNS rate per atom $R_\nu(E_r)$ of material with natural abundance p_A of isotope A is $R_\nu(E_r) = \sum_A p_A R_A(E_r)$, where $R_A(E_r)$ is the rate (2.6.1) corresponding to the isotope A . We then normalize the spectra to a PDF of CENNS events $\rho_\nu(E_r) = R_\nu(E_r)/\int R_\nu(E_r)dE_r$, where the integral is calculated via trapezoidal integration.

The resulting PDFs of CENNS-induced recoil energies are shown in Figure 2.4. To simulate CENNS events, we then sample from this distribution.

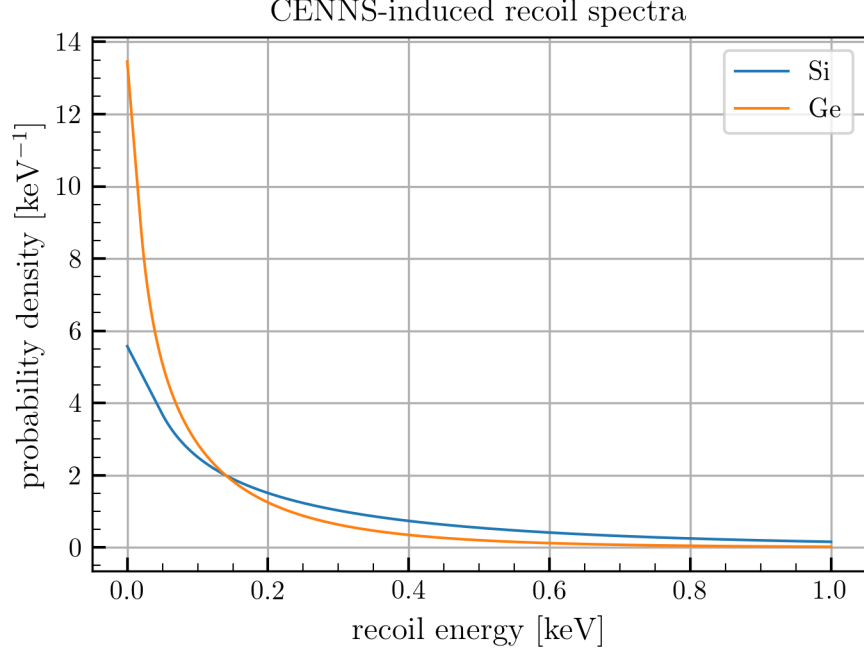


Figure 2.4: CENNS-induced recoil PDFs for silicon and germanium

2.6.2 Simulating samples of events

With the true recoil spectrum of CENNS events calculated, all the pieces are now in place to simulate samples of collected data.

2.6.2.1 CENNS

Simulated samples of CENNS events are drawn from the PDFs shown in Figure 2.4. This is accomplished by numerically calculating the cumulative distribution function (CDF) of the distributions using trapezoidal integration. To be explicit, for PDF data $(E_{r,i}, \rho_{\nu,i})$ with i going from 1 to N , the number of grid points, elements of the array of CDF values c_j are:

$$c_j = \sum_{i=2}^j \frac{1}{2} (\rho_{\nu,i-1} + \rho_{\nu,i}) (E_{r,i} - E_{r,i-1}) = c_{j-1} + \frac{1}{2} (\rho_{\nu,j-1} + \rho_{\nu,j}) (E_{r,j} - E_{r,j-1}) \quad (2.6.2)$$

for $j = 2$ to N . $c_1 = 0$ by definition. To avoid trouble with numerical error associated with this procedure, we manually set $c_N = 1$. This ensures any randomly-generated values larger than the calculated value of c_N are correctly handled. The error associated with this step is only $\sim 10^{-14}$ %, but is a reassuring safeguard.

We now randomly generate floats in $[0, 1)$. For each random value x_k , with k going from 1 to N_ν , the number of CENNS events in the sample, we find i such that $c_i \leq x_k < c_{i+1}$. We then interpolate between the neighboring points to calculate an energy E_k :

$$E_k = E_{r,i} + \frac{x_k - c_i}{c_{i+1} - c_i} (E_{r,i-1} - E_{r,i}) \quad (2.6.3)$$

which yields a set of N_ν energies $\{E_k\}$ distributed according to the density $\rho_\nu(E)$: our simulated sample of true recoil energies for CENNS events.

Sampling uniformly on $[0, 1)$ and calculating the inverse of the CDF is a common trick for sampling from arbitrary distributions. It works because the density of samples is proportional to the inverse slope of the transformation: assume we randomly generate values x with density $\rho_x(x) = 1$. Now let $c^{-1}(x)$ be a smooth function giving the inverse cumulative distribution function, and let $\rho_E(E)$ be the density over the transformed variable $E = c^{-1}(x)$. The probability of a value landing in an infinitesimal width dx about x is $\rho_x(x)dx$. The same must be true about the probability of landing in some region of width dE about $E = c^{-1}(x)$: $\rho_x(x)dx = \rho_E(E)dE$. Thus, $\rho_E(E) = \rho_x(x) \frac{dx}{dE} = \frac{dx}{dE}$ since $\rho_x(x) = 1$. But $x = c(E)$, so $\frac{dx}{dE} = \frac{dc}{dE} = \rho_\nu(E)$, since the CDF is the antiderivative of the PDF. So $\rho_E(E) = \rho_\nu(E)$ is the desired density.

The linear interpolation in (2.6.3) implicitly makes the assumption that the true PDF is a piecewise continuous sequence of line segments connected to the calculated points $(E_{r,i}, \rho_{\nu,i})$. Based on the fine spacing of the energy grid we don't expect samples of (at maximum) $O(10^4)$ generated according to this distribution to differ substantially from a smooth version of the same distribution (e.g., a cubic spline). We made the same assumption both when we calculated the CDF and when we normalized R_ν into ρ_ν by using trapezoidal integration. This approximation will be made often throughout the remainder of this chapter and the next. So long as the grid spacing remains fine enough, this will not be an issue.

Once the sample of CENNS-induced recoil energies $\{E_k\}$ has been generated, we generate a sample of measured energies $\{\tilde{E}_k\}$ by adding in gaussian noise with width given by the detector resolution $\sigma(E_k)$ (2.4.2). That is, we generate a set of N_ν values $\{G_k\}$ that are distributed according to a standard normal, and then:

$$\tilde{E}_k = E_k + G_k \sigma(E_k) \quad (2.6.4)$$

2.6.2.2 Captures

As discussed in Section 2.3, the `nrCascadeSim` code generates a sample of capture-induced recoil energies. We sample values from this set with repetition and add gaussian noise to emulate detector resolution analogously to (2.6.4), resulting in a sample of measured capture-induced energies.

2.6.2.3 Background

As mentioned in Section 2.4.3, we add a sample of background events to each simulated sample. For the flat case, the events are uniformly distributed in measured energy, so once a combined sample of measured CENNS and captures events $\{E_\alpha\}$ has been generated, the background events are generated uniformly between $E_{\alpha,\min}$ and $E_{\alpha,\max}$ for the unbinned case and $E_{j=0}$ and $E_{j=J}$ for the binned case, where $E_{j=0}$ and $E_{j=J}$ are the lower and upper limits of all the bins (J bins in total).

For the sloped case, $P_b(E) \propto E^{-0.9}$. The exact PDF for the binned analysis is:

$$P_b(E) = \frac{0.1E^{-0.9}}{E_{j=J}^{0.1} - E_{j=0}^{0.1}} \quad (2.6.5)$$

(the sloped background was not used in any of the unbinned analysis). To sample from this distribution, we sample x uniformly on $[0, 1)$ and transform as:

$$E = [(E_{j=J}^{0.1} - E_{j=0}^{0.1})x + E_{j=0}^{0.1}]^{10} \quad (2.6.6)$$

which is the same trick used to sample CENNS events, except the inverse CDF is calculated exactly.

2.6.3 Calculating measurement PDFs

Once the full sample of CENNS, capture, and background events is generated, we store that data together in a single array as a single “sample” of data to analyze. The next step will be to calculate (and maximize) the likelihood functions.

At this point we need to distinguish between what we call “true PDFs” $\rho_k(E_r)$, which are PDFs over true recoil energies and do not account for detector effects at all, and “measurement PDFs” $P_k(E)$, which are PDFs over measured energies, equal to the convolution of the true PDFs with normal distributions G with widths given by the resolution function $\sigma(E)$ (2.4.1):

$$\begin{aligned}
P_k(E) &= \int \rho_k(E_r) G(E|E_r, \sigma(E_r)) dE_r \\
&= \frac{1}{\sqrt{2\pi}} \int_0^\infty \frac{\rho_k(E_r)}{\sqrt{\sigma_0^2 + CE_r}} \exp\left[-\frac{(E - E_r)^2}{2\sigma_0^2 + 2CE_r}\right] dE_r
\end{aligned} \tag{2.6.7}$$

where we introduced the notation

$$G(x|\mu, \Delta) = \frac{1}{\sqrt{2\pi\Delta}} \exp\left[-\frac{1}{2\Delta^2}(x - \mu)^2\right] \tag{2.6.8}$$

for a normalized gaussian with mean μ and variance Δ^2 . The $P_k(E)$ are the PDFs appearing in the unbinned likelihood function (2.5.1), and the $A_{k,j}$ appearing in the binned likelihood function (2.5.5) are the integrals of $P_k(E)$ over each bin j :

$$A_{k,j} = \int_{E_j}^{E_{j+1}} P_k(E) dE \tag{2.6.9}$$

We generate samples of CENNS and capture events with densities $P_k(E_r)$ by sampling from $\rho_k(E_r)$ and adding gaussian noise to each sample point. However, we need to calculate the actual *value* of the measurement PDFs (without using data from a particular sample) in order to calculate the likelihood functions.

2.6.3.1 CENNS

To calculate the measurement PDF of CENNS events, we approximate the integral (2.6.7) numerically by approximating the CENNS distribution $\rho_\nu(E)dE$ as a set of finite but small areas $A_i = \frac{1}{2}(\rho_{\nu,i} + \rho_{\nu,i+1})(E_{r,i+1} - E_{r,i})$ and associated energies $E_{A,i} = \frac{1}{2}(E_{r,i} + E_{r,i+1})$ based on the tabulated $(E_{r,i}, \rho_{\nu,i})$ data plotted in Figure 2.4. $P_\nu(E)$ is then approximated as a sum over these areas,

$$\begin{aligned}
P_\nu(E) &= \sum_{i=1}^{N-1} A_i G(E|E_{A,i}, \sigma(E_{A,i})) \\
&= \frac{1}{\sqrt{2\pi}} \sum_{i=1}^{N-1} \frac{A_i}{\sqrt{\sigma_0^2 + CE_{A,i}}} \exp\left[-\frac{(E - E_{A,i})^2}{2\sigma_0^2 + 2CE_{A,i}}\right]
\end{aligned} \tag{2.6.10}$$

where N is the number of points in the $(E_{r,i}, \rho_{\nu,i})$ data.

To calculate the $A_{\nu,j}$, $P_\nu(E)$ is evaluated at each of the E_j and the trapezoid-approximated area under $P_\nu(E)$ is calculated:

$$A_{\nu,j} = \frac{1}{2}(P_\nu(E_j) + P_\nu(E_{j+1}))(E_{j+1} - E_j) \quad (2.6.11)$$

2.6.3.2 Captures

For the capture PDF, we use the result that, inside an integral, we can approximate $\rho_c(E)$ as a sum of delta functions. For some N_c data points $E_{rc,i}$ distributed according to $\rho_c(E)$, then inside an integral,

$$\lim_{N_c \rightarrow \infty} \frac{1}{N_c} \sum_{i=1}^{N_c} \delta(E - E_{rc,i}) = \rho_c(E) \quad (2.6.12)$$

Plugging this in to (2.6.7) (and now merely taking N_c to be very large) yields:

$$\begin{aligned} P_c(E) &= \int \frac{1}{N_c} \sum_{i=1}^{N_c} \delta(E_r - E_{rc,i}) G(E|E_r, \sigma(E_r)) dE_r \\ &= \frac{1}{N_c} \sum_{i=1}^{N_c} G(E|E_{rc,i}, \sigma(E_{rc,i})) \\ &= \frac{1}{\sqrt{2\pi}N_c} \sum_{i=1}^{N_c} \frac{1}{\sqrt{\sigma_0^2 + CE_{rc,i}}} \exp \left[-\frac{(E - E_{rc,i})^2}{2\sigma_0^2 + 2CE_{rc,i}} \right] \end{aligned} \quad (2.6.13)$$

We use the sample of recoil energies generated by `nrCascadeSim` as our sample $\{E_{rc,i}\}$.

However, the calculation of the measurement PDF as given above is extremely slow for the large samples considered in the unbinned analysis. Thus, instead of calculating (2.6.13) for every energy in every simulated sample for the unbinned analysis, once a resolution $\sigma(E)$ has been chosen, the measurement PDF $P_c(E_k)$ is evaluated at a grid of energies $\{E_k\}$ consisting of 2,500 points spaced evenly between a lower bound of $E_{rc,i,\min} - 10\sigma(E_{rc,i,\min})$ and an upper bound of either $E_{rc,i,\max} + 10\sigma(E_{rc,i,\max})$ or 6 keV, whichever is larger. These $\geq 10\sigma$ bounds on the expected range of measured capture energies (which also easily contains the expected range of measured CENNS event energies) ensures that the calculated grid of $P_c(E_k)$ values contains all measured energies in the simulated samples with that resolution. The value

$P_c(E_i)$ at an energy in the sample E_i is then calculated by linear interpolation of the nearest points on $P_c(E_k)$.

For the binned analysis, the calculation of (2.6.13) at the bin edges $\{E_j\}$ is much faster (the number of bins is the same approximate size as the $\{E_k\}$ energy grid (see Section 2.7.2), so there would be no time save with calculating on this grid). The $A_{c,j}$ are calculated in the same way as the $A_{\nu,j}$ (2.6.11).

2.6.3.3 Background

The flat-background measurement PDF is just

$$P_b(E) = \begin{cases} \frac{1}{E_{\max} - E_{\min}}, & E_{\min} \leq E \leq E_{\max} \\ 0, & \text{otherwise} \end{cases} \quad (2.6.14)$$

that is, a uniform distribution between the minimum and maximum energies, which are either the minimum and maximum energies in the sample $E_{\alpha,\min}$ and $E_{\alpha,\max}$ or the edges of the highest and lowest bins $E_{j=0}$ and $E_{j=J}$ for unbinned or binned analyses, respectively. The $A_{b,j}$ are proportional to the bin widths, $A_{b,j} = (E_{j+1} - E_j)/(E_{j=J} - E_{j=0})$.

For the sloped case, to calculate $A_{b,j}$ we integrate (2.6.5) over each bin:

$$A_{b,j} = \frac{E_{j+1}^{0.1} - E_j^{0.1}}{E_{j=J}^{0.1} - E_{j=0}^{0.1}} \quad (2.6.15)$$

2.6.4 Calculation of Likelihood Function

The likelihood functions were not calculated as written in (2.5.1), (2.5.4), (2.5.5), or (2.5.8). The exponential factor $e^{-n_{\text{total}}}$ alone for any reasonable guesses for the $\{n_k\}$ drives the function to zero because of numerical underflow. The smallest integer exponential allowed by numpy's `exp()` function is `exp(-744)`, which returns `1e-323`. `exp(-745)` returns `0.0`. Evaluating the likelihood function on the log scale would eliminate this trouble. Also, since we're only interested in the ratios of likelihoods over the same sample, we can avoid calculating the $N!$ and $C_j!$ factors altogether, avoiding either additional computational troubles or approximations for the factorial. Thus, we calculate the quantities L and L' for the unbinned analysis:

$$L = -\ln \mathcal{L} - \ln(N!) \quad (2.6.16a)$$

$$L' = -\ln \mathcal{L}' - \ln(N!) \quad (2.6.16b)$$

and for the binned analysis:

$$L = -\ln \mathcal{L} - \sum_j \ln(C_j!) \quad (2.6.17a)$$

$$L' = -\ln \mathcal{L}' - \sum_j \ln(C_j!) \quad (2.6.17b)$$

These yield expressions that are much more numerically stable to calculate. For the unbinned analysis:

$$L = n_{\text{total}} - \sum_{i=1}^N \ln [n_\nu P_\nu(E_i) + n_c P_c(E_i) + n_b P_b(E_i)] \quad (2.6.18a)$$

$$L' = n_c + n_b - \sum_{i=1}^N \ln [n_c P_c(E_i) + n_b P_b(E_i)] \quad (2.6.18b)$$

and for the binned analysis:

$$L = n_{\text{total}} - \sum_j C_j \ln [n_\nu A_{\nu,j} + n_c A_{c,j} + n_b A_{b,j}] \quad (2.6.19a)$$

$$L' = n_c + n_b - \sum_j C_j \ln [n'_c A_{c,j} + n'_b A_{b,j}] \quad (2.6.19b)$$

We then calculate L_1 as the minimum value of L and L_2 as the minimum of L' . We would then calculate $\chi_0^2 = 2 \ln(\mathcal{L}_1/\mathcal{L}_2)$ as

$$\chi_0^2 = 2(L_2 - L_1) \quad (2.6.20)$$

The numerical optimization of L and L' are performed using `scipy.optimize.minimize` in Python.

2.7 Results

The groundwork has now been laid to simulate measured samples of all three types of events – CENNS, capture, and background – in some environmental conditions (neutron flux and detector resolution) and perform a statistical analysis on the resulting dataset to determine how confidently a reactor CENNS measurement can be made in those conditions. All that remains is to repeat this analysis for a variety of thermal neutron fluxes (to see how many neutrons can be present before the CENNS signal is drowned out) and detector resolutions (to see what improvements need be made to detector technologies in order to succeed in making the measurement), and we will have our results: a map of what conditions need to be met in order for a reactor CENNS measurement to be made.

These results are presented in this section. The confidence Z of a CENNS measurement is calculated for different combinations of baseline resolution σ_0 , effective resolution σ_{eff} , and ambient thermal neutron flux (corresponding to different numbers of capture events N_c in each generated sample). The range of thermal neutron fluxes considered was from $2.7 \times 10^{-7} \text{ cm}^{-2} \text{ s}^{-1}$ to $2.7 \times 10^{-3} \text{ cm}^{-2} \text{ s}^{-1}$, corresponding to ~ 3000 to 3×10^7 capture events in silicon and $\sim 16,000$ to 1.6×10^8 events in germanium (see Table 2.3). This range of fluxes was chosen after a few data runs to cover the region of interest for this investigation, i.e., the region where it goes from being impossible to distinguish CENNS events to being possible. This section will also compare the binned and unbinned analyses described in Section 2.5, and show that the results are similar enough that one can be swapped out for the other.

2.7.1 Unbinned analysis

For the unbinned analysis, effective resolutions were probed between 1 eV and 50 eV for baseline resolutions of 1 eV, 5 eV, and 10 eV in silicon (unbinned analysis in Ge was not completed at the time the switch to the binned analysis was made). These baselines were chosen to cover up to, and slightly beyond, the current field-leading low-threshold detector performances (c.f., Table 2.1).

Figure 2.5 shows results in silicon for baseline $\sigma_0 = 1 \text{ eV}$. The significance was calculated on a 25×25 grid of equally-spaced resolutions and logarithmically-spaced fluxes. Two reference flux levels are shown as horizontal gray lines. The dashed line marks the IEEE standard sea level thermal neutron flux, $4 \text{ cm}^{-2} \text{ hr}^{-1}$ [2]. The dotted gray line marks $6.52 \times 10^{-4} \text{ cm}^{-2} \text{ s}^{-1}$, the reactogenic thermal neutron flux measured at the MINER facility, $5.8 \times 10^7 \text{ cm}^{-2} \text{ s}^{-1}$ [79], extrapolated out to 10 m from the reactor core,¹⁹ and then reduced by a factor of 10^9 . These two lines correspond to approximately 13,000,000 and 7,500,000 capture events in Si, and 63,000,000 and 37,000,000 in Ge. The black curve marked “ 5σ ” is the

¹⁹It was estimated from Figure 12 of [79] that the measurements were taken at a distance of 1.06 m from the core, and propagation was done assuming a simple $1/r^2$ reduction in flux with distance r .

$Z = 5$ contour line for this data after smoothing by 4 iterations through a Jacobi relaxation scheme (see [135], eq. (8.22)). This contour roughly delineates the point below which the CENNS component of the data can be distinguished at the 5σ significance level in an exposure of 100 kg yr.

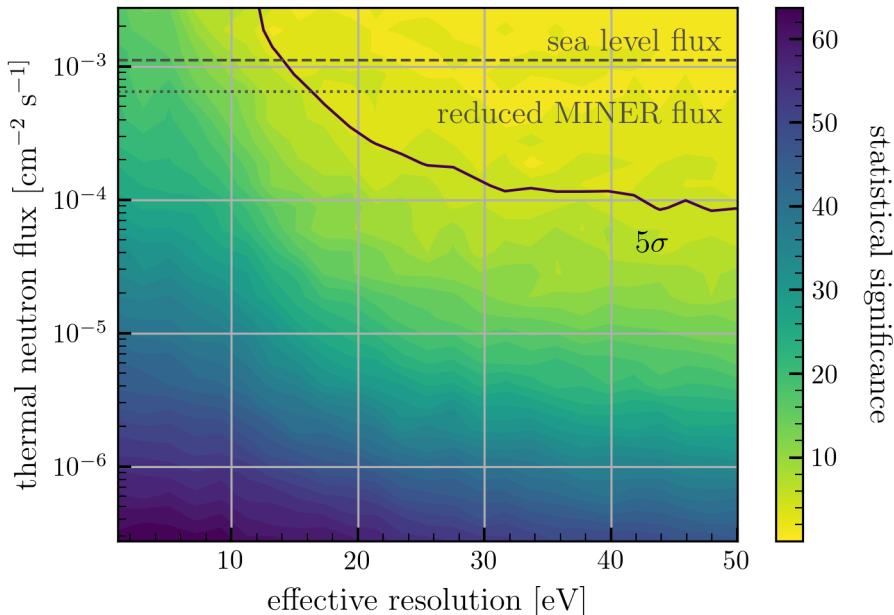


Figure 2.5: Results of unbinned analysis for $\sigma_0 = 1$ eV in silicon. Dashed and dotted gray lines mark standard sea level flux and reported thermal neutron flux at MINER facility reduced by a factor of 10^9 , respectively. Black line marked “ 5σ ” represents the $Z = 5$ contour line (after smoothing)

Unsurprisingly, the significance of a CENNS measurement grows as the ambient thermal neutron flux decreases and the detector resolution improves. This plot also indicates that the ambient thermal neutron flux must be reduced by considerable amounts (greater than nine orders of magnitude) from typical reactor-adjacent fluxes by shielding or other reduction methods in order to reach 5σ significance in 100 kg yr.

Plots showing a few examples of maximum-likelihood fits with and without CENNS are shown in Figure 2.6. The black points show histograms of generated data with error bars (horizontal errors bars indicate the width of bins, vertical error bars represent statistical error in the bin counts (see Section 3.10.5)). The blue curves represent scaled measurement PDFs $n_{\text{total}}P_{\text{true}}$ for the fit maximized to $\mathcal{L}(P_{\text{true}}(E))$ from (2.5.3). The dashed blue curves are the contribution of CENNS events to the blue curves. The orange curves represent the fits to \mathcal{L}' , i.e., the best fit without a CENNS component. The lower panels show zoomed-in views of the regions in red boxes in the top row. The significance of each CENNS observation is written in the top corner of each plot, blue if larger than 5 and red otherwise.

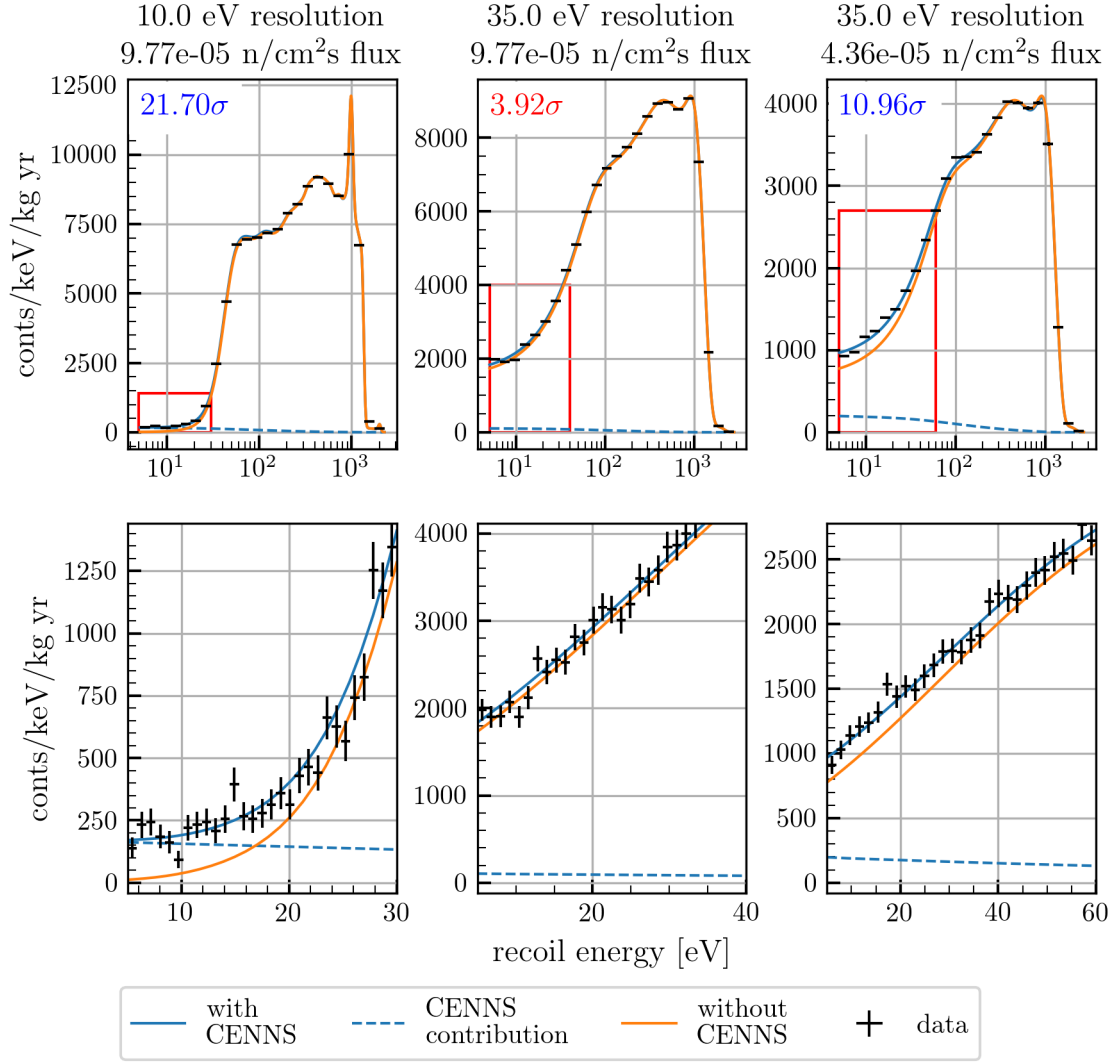


Figure 2.6: Three example fits using the unbinned likelihood function in Si for a baseline resolution of 1 eV. Lower panes show zoomed-in views of red boxed regions.

The left and middle plots show a higher thermal neutron flux, $9.77 \times 10^{-5} \text{ cm}^{-2} \text{ s}^{-1}$, corresponding to $\sim 1,120,000$ capture events. The right plot shows a lower flux, $4.36 \times 10^{-6} \text{ cm}^{-2} \text{ s}^{-1}$, corresponding to $\sim 500,000$ capture events. The leftmost plot has an effective resolution of 10 eV, and the middle and right plots have an effective resolution of 35 eV. The middle plot has a Z value of only 3.92, indicating the CENNS component has not been measured at high significance. The plots on either side show the two methods for discerning the CENNS signal: either improve resolution so resolution-smear capture events contribute less at the extreme low-energy region where CENNS events dominate (left), or decrease the thermal neutron flux enough that the small number of CENNS events is significant compared to the number of capture events (right).

Similar “landscapes” of Z -values were calculated for 5 eV and 10 eV baselines. The resulting 5σ contours are plotted in Figure 2.7. Once again, these lines represent approximate thresholds above which a confident CENNS measurement is not possible in 100 kyr. Plots of the full landscapes for $\sigma_0 = 5$ eV and 10 eV are given in Appendix A.

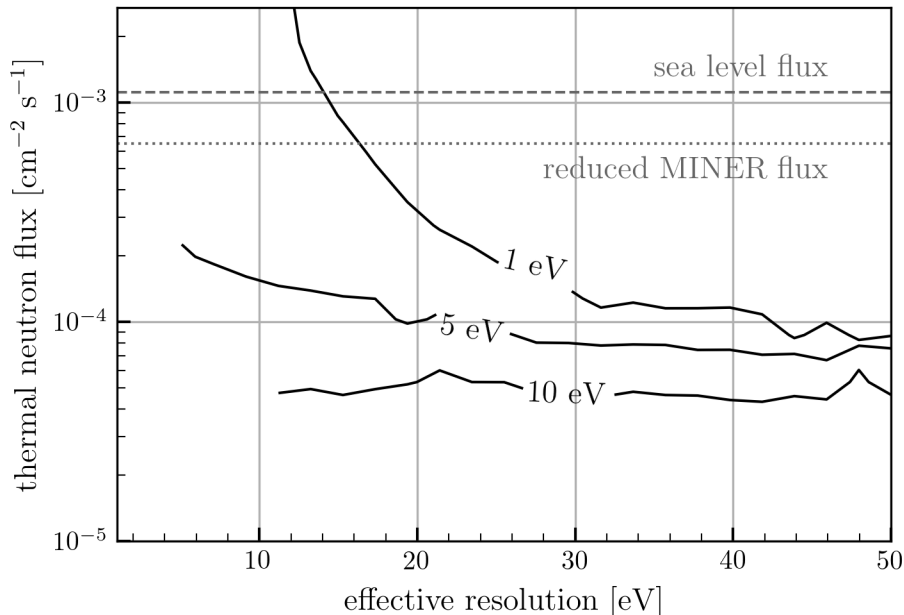


Figure 2.7: Resulting 5σ contours in unbinned analyses for 1 eV, 5 eV, and 10 eV baseline resolutions in Si

As can be seen, increasing baseline resolutions causes the requirements for measuring CENNS to move toward lower fluxes. For lower baseline resolutions, the CENNS signal can be detected in substantially higher fluxes, but worse baseline resolutions make it more difficult to detect the CENNS signal at a given flux. Also, the slopes of these 5σ contours decrease as the baseline resolution goes up, meaning that at higher baseline resolutions, changing the effective resolution (i.e., changing the coefficient C in (2.4.1), which gives the scaling of detector resolution with energy) doesn’t change sensitivity to CENNS as much. Achieving finer resolutions has diminishing returns unless the baseline resolution can be improved.

2.7.2 Comparing binned and unbinned methods

As mentioned in Section 2.5, it was found that the unbinned analysis was extremely slow, while an alternative analysis using a binned likelihood function yielded extremely similar results, while being some three orders of magnitude faster. This section will directly compare the results of binned and unbinned analyses, to demonstrate the suitability in swapping one method out for the other in favor of the faster one.

2.7.2.1 Comparing landscapes

The binned and unbinned analyses were compared for the case of a 5 eV baseline in silicon. A side-by-side comparison of the Z landscapes is shown in Figure 2.8.

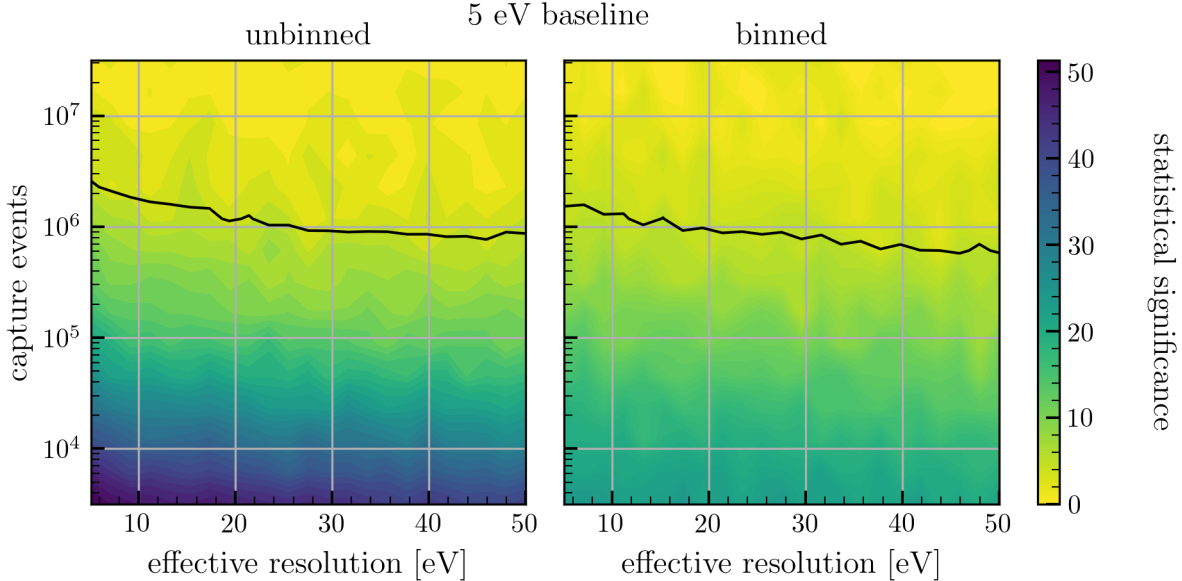


Figure 2.8: Comparison of binned (left) and unbinned (right) Z landscapes for $\sigma_0 = 5$ eV in silicon

Visually, these two results are very hard to distinguish from each other for more than $\sim 10^5$ capture events. Importantly, the 5σ contour is in very nearly the same location in both plots. It is thus reasonable to suspect that we present essentially the same information using the binned analysis rather than the costly unbinned version. The next subsections investigate this possibility in more detail. For posterity, similar comparisons for 1 eV and 10 eV baselines are shown in Appendix B.

2.7.2.2 Binning methods

Before further investigations were made into whether the binned analysis can be aptly replaced by the unbinned analysis, the actual choice of binning must be made. The “binned” analyses in the previous section and in Appendix B use 3,000 logarithmically-spaced bins between threshold and 3 keV (this will end up being the binning method we use in future sections as well). For now, we consider four different binnings: “3k log” is the binning just described. “5k log” consists of 5,000 logarithmically-spaced bins. “0.25 eV” and “0.5 eV” bins are linear binnings with bin widths of 0.25 and 0.5 eV, respectively. All binnings considered extend from threshold to 3 keV.

To assess how similarly these binnings behaved, ten points in the landscape of the 5 eV baseline data were selected arbitrarily. Samples were generated and likelihood fits calculated 150 times for all bin-

nings at each point. Figure 2.9 shows the resulting histograms of Z values for one of these ten points. The Z value calculated with the unbinned analysis is plotted as a black dotted line.

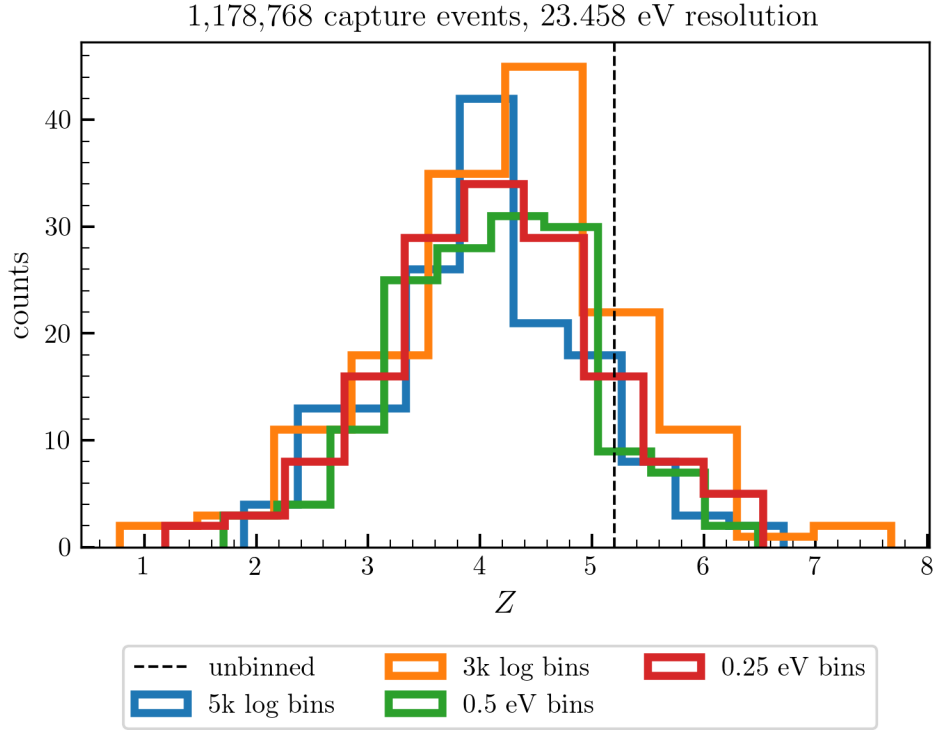


Figure 2.9: Histograms of generated Z values for ~ 1.2 M capture events with an effective resolution of 23.5 eV for the four different binnings. The Z value calculated with the unbinned methods is shown as a vertical dashed black line

It can be seen that the distributions of Z values are visually in very good agreement with each other, and in moderately good agreement with the unbinned value. The same agreement is true for all ten points selected for testing. Since most of the distributions appear fairly normal, we quantify this agreement by calculating a Z -score (not to be confused with the actual Z values calculated by the likelihood ratio test) for all pairs of binnings at a given point, $Z = |m_1 - m_2|/\sqrt{s_1 s_2}$ for samples with means m_i and standard deviations s_i . The average and maximum scores at each of the ten selected points are shown in Table 2.4. Note the last four rows correspond to the four corners of the surveyed landscape for $\sigma_0 = 5$ eV.

Table 2.4: Summary of Z scores for variation between distributions of calculated significances for four binnings for ten surveyed points in landscape

| Capture events | Resolution [eV] | Avg. Z score (P -value) | Max Z score (P -value) |
|----------------|-----------------|------------------------------|-----------------------------|
| 84,834 | 7.125 | 0.0535 (95.7%) | 0.1166 (90.7%) |
| 2,275,845 | 7.125 | 0.0302 (97.6%) | 0.0760 (93.9%) |
| 22,758 | 21.417 | 0.0834 (93.4%) | 0.1990 (84.2%) |
| 22,758 | 23.458 | 0.0892 (92.9%) | 0.2312 (81.7%) |
| 1,178,768 | 23.458 | 0.0664 (94.7%) | 0.1742 (86.2%) |
| 84,834 | 13.25 | 0.0305 (97.6%) | 0.0678 (94.6%) |
| 3,162 | 5.083 | 0.0882 (93.0%) | 0.2326 (81.6%) |
| 31,622,776 | 5.083 | 0.0632 (95.0%) | 0.1423 (88.7%) |
| 3,162 | 50 | 0.0550 (95.6%) | 0.1325 (89.5%) |
| 31,622,776 | 50 | 0.0237 (98.1%) | 0.0614 (95.1%) |

It can be seen that the worst disagreement between any two binnings was $Z = 0.2326$, with a P -value of 81.6%, still firmly in the realm of agreement between the distributions. The overall average, over all pairs of binnings at the same resolution and number of capture events, is $Z = 0.078$, corresponding to a P -value of 93.8%. Given this information, we can therefore expect that all four of the binnings tested behave essentially the same.

Note that we use the modified Z test here and not a typical two-sample t -test because we are only interested in how our different samples *overlap*, that is, how consistent the *distributions* are with each other, rather than wanting to know how likely it is that the distributions are exactly the same. In fact, we *expect* some systematic variation between the distributions, since they come from slightly different methods that retain slightly different information about the simulated samples. We merely want to see how substantially the two distributions overlap with each other, to assess how similar any two given results will be, i.e., whether the expected difference between two different binning methods is larger than the expected variation of an individual binning method. We find that the difference between binning methods is generally much smaller than variation within a single binning method.

The 3k log binning was chosen going forward for being more efficient than the binning methods with more points. It was also found that the logarithmic binnings were slightly more consistent in finding the true optimized likelihoods at higher fluxes (probably due to retaining more information at very low energies).

Before we move on, it will be beneficial to quickly comment on expected variation of the binned likelihood methods. The standard deviations of each sample of 150 significances calculated for all ten points in each of the four binnings are shown in histogram in 2.10. The same histogram broken up by binning method is shown in Figure B.2 in Appendix B.

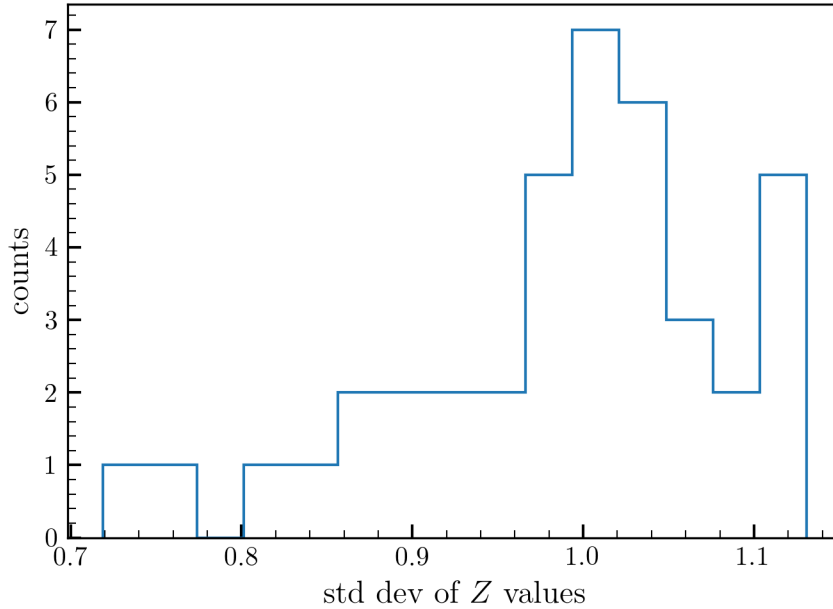


Figure 2.10: Standard deviations of all 40 generated samples of Z values (confidence values) with all different binning methods. The average standard deviation was 0.989

The mean standard deviation in all 40 samples of 150 Z values was 0.989. Thus a reasonable expectation for the uncertainty in any single Z value is ± 1 .

2.7.2.3 Comparing distributions

To compare the binned and unbinned calculations, we can compare the distribution of significances from the 3k log binning to the value yielded in the unbinned analysis (i.e., the dotted line in Figure 2.9). Z scores were calculated for the unbinned value compared to the distribution of significances yielded with the 3k log binning. The resulting values are given in Table 2.5.

Table 2.5: Z scores for unbinned significances compared with distribution of significances calculated with 3k log binning.

| Capture events | Resolution [eV] | Z score | P -value |
|----------------|-----------------|-----------|------------|
| 84,834 | 7.125 | 0.5946 | 55.21% |
| 2,275,845 | 7.125 | 1.5381 | 12.40% |
| 22,758 | 21.417 | 0.6527 | 51.39% |
| 22,758 | 23.458 | 1.3365 | 18.14% |
| 1,178,768 | 23.458 | 0.8912 | 37.28% |
| 84,834 | 13.25 | 1.7277 | 8.40% |
| 3,162 | 5.083 | 0.8275 | 40.80% |
| 31,622,776 | 5.083 | 0.4787 | 63.22% |
| 3,162 | 50 | 1.1746 | 24.01% |
| 31,622,776 | 50 | 0.9287 | 35.30% |

The highest disagreement between binned and unbinned was $Z \approx 1.7$ with a P -value of only 8.4%, which is not great agreement. However, one would expect in a sample of this size to encounter a lower bound of P -values on the order of 10%, which is exactly what we see. The rest of the P values show better agreement. Thus we do not find this data sufficient to indicate that the binned and unbinned methods are substantially different. Similar Z -score tests for the other binning methods yielded similar results.

2.7.2.4 Comparing contours

To more precisely assess how the switch to a binned analysis affected our most important results, the 5σ contours plotted in Figure 2.7, we directly compare the contours yielded with each method. To facilitate this, a new set of Z landscape data was calculated using the unbinned analysis for $\sigma_0 = 5$ eV, which we call the “dense unbinned data,” consisting of 75 values of effective resolution between 5 and 50 eV, and 10 values of thermal neutron flux between $\sim 2.8 \times 10^{-6}$ and $\sim 6.5 \times 10^{-4} \text{ cm}^{-2} \text{ s}^{-1}$ (between about 31,600 and 6.31M capture events). This data is plotted side-by-side with the original unbinned 5 eV baseline data in Figure 2.11.

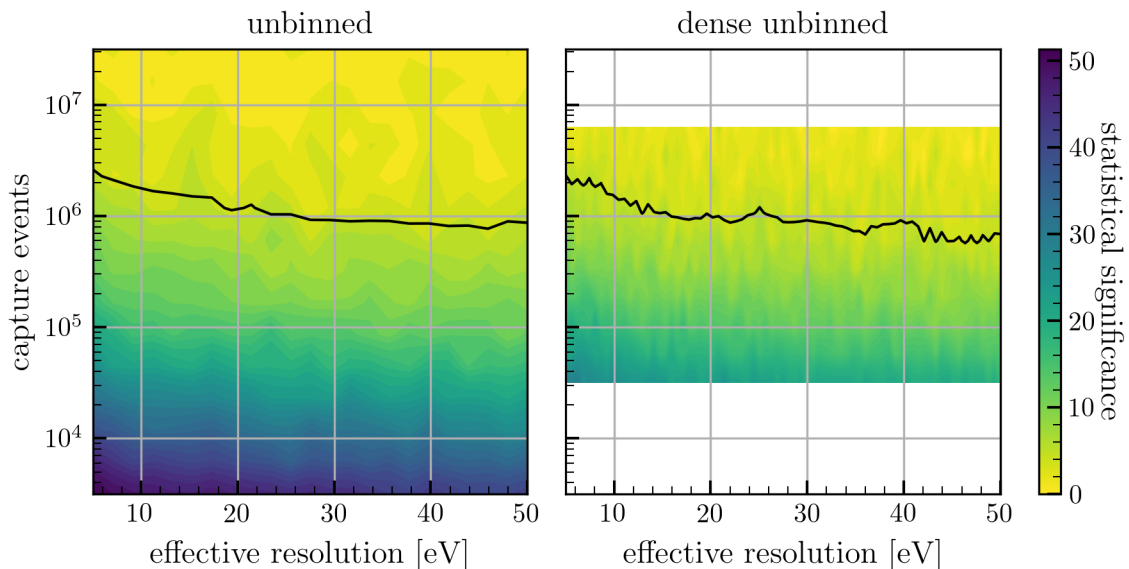


Figure 2.11: Comparison of original unbinned Z landscape data ($\sigma_0 = 5$ eV) and “dense unbinned” data, evaluated on a denser grid of points

Both contours have been smoothed by four iterations through a Jacobi relaxation scheme. It should be noted that the jagged appearance of the dense unbinned contour is largely due to the fact that since there are more points on the evaluated grid of effective resolutions, the noise is higher-frequency. The Jacobi relaxation scheme has some difficulty smoothing out noise with wavelength similar to double the grid spacing, so this noise persists through the smoothing procedure, and since there are more points in the

dense grid, there are more opportunities for such a sawtooth pattern to form (see Figure B.3 in Appendix B).

We can compare the variation of our unbinned and binned contours relative to the dense unbinned contour. As a first comparison, the two unbinned contours and the contour yielded by the 3k log binning are plotted on top of each other in Figure 2.12.

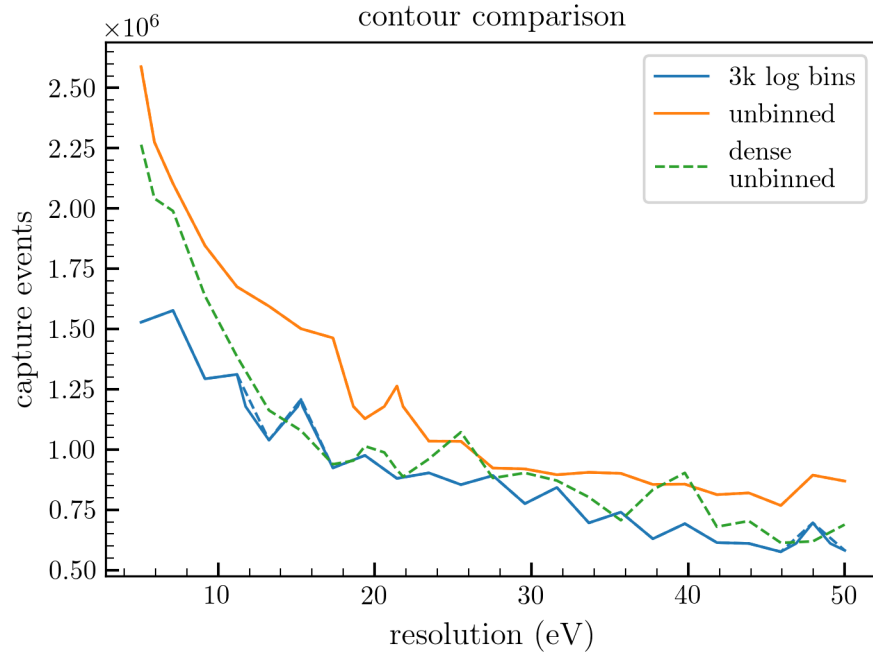


Figure 2.12: 5σ contours for unbinned, dense unbinned, and 3k log binned data

Once again, the contours in this figure have been relaxed four times (smoothed by four iterations through the Jacobi relaxation scheme). Figure B.4 in Appendix B shows the four contours before smoothing. Visually, the contours are all in fairly good agreement here.

A slightly easier-to-decipher indication of how the unbinned and binned contours compare to the dense unbinned contour is given in Figure 2.13.

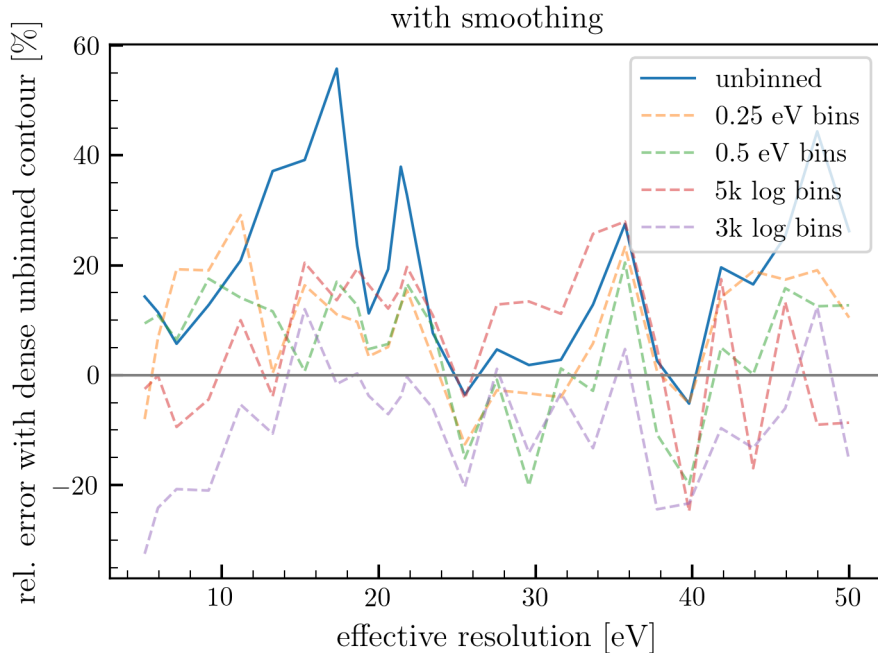


Figure 2.13: Relative difference in unbidden and binned contours from dense unbidden contour

Once again, a plot without smoothing is given in Appendix B (Figure B.5). Note that in this plot, positive values mean that the indicated contour is at higher capture events than the dense unbidden contour. It can be seen in this figure that both unbidden and binned contours vary quite a bit about the dense unbidden contour. The amount of variation in the unbidden contour is of comparable magnitude to the binned contours.

To be more precise about what is plotted here, the height of each contour is linearly interpolated to the exact points at which the dense unbidden contour is plotted. Then, for each array of $y_{c,i}$ values giving the height of contour c at point i , and \hat{y}_i giving the height of the dense unbidden contour, Figure 2.13 shows $dy_i \equiv (y_{c,i} - \hat{y}_i)/\hat{y}_i$. The scaled variance of each contour about the dense unbidden contour is listed in Table 2.6. This is the quantity

$$\frac{100}{N-1} \sum_{i=1}^N dy_i^2 \quad (2.7.1)$$

is the scaled variance of the dy_i about zero. The factor of 100 is included so that values are $O(1)$. What is important are their relative values, which can be seen are very similar, and in fact are smaller for the binned methods than the unbidden method, which was calculated in exactly the same way as the dense unbidden data. For the same contours without smoothing, the variance of the binned methods is likewise

of similar magnitude as the variance of the unbinned contour (see Table B.2 in Appendix B). The scaled variance of the unbinned data is a measure of how much the 5σ contour varies purely due to randomness in generated samples of events. The binned methods all give results well within this variation. Based on this, we go forward with the assumption that the binned methods, and in particular the 3k log binning, are suitably similar to the unbinned method to be appropriate replacements.

Table 2.6: Variance about the dense unbinned contour for the other contours plotted in Figure 2.13

| Binning | Scaled variance |
|--------------|-----------------|
| unbinned | 5.988 |
| 0.25 eV bins | 1.830 |
| 0.5 eV bins | 1.569 |
| 5k log bins | 2.259 |
| 3k log bins | 2.146 |

2.7.3 Binned analysis

A few results of the binned analysis with flat background in silicon have already been shown in the previous section. This section will summarize the rest of the results for flat, sloped, and combination backgrounds in both silicon and germanium.

A sample of maximum likelihood (ML) fits with all three background models is given in Appendix C. The 5σ contours resulting from the binned analysis in Si and Ge are plotted in Figures 2.14, 2.15, and 2.16 for the three different background models surveyed. Figure 2.17 shows these contours plotted on top of each other. Some brief discussion follows.

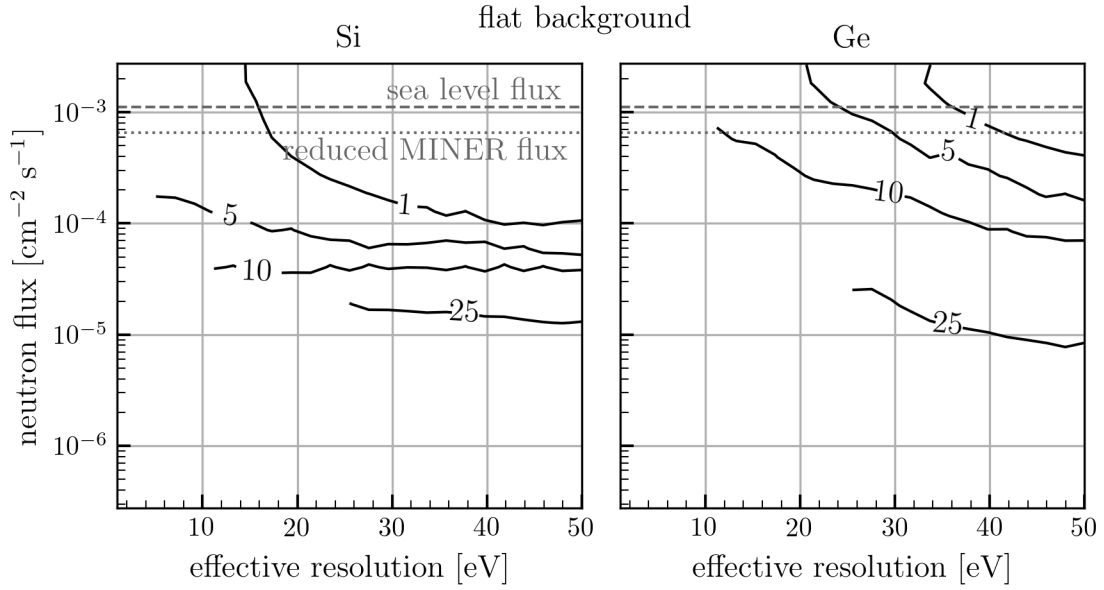


Figure 2.14: 5σ contours for flat background model in Si and Ge. Inline labels on the contours give the baseline resolution in eV.

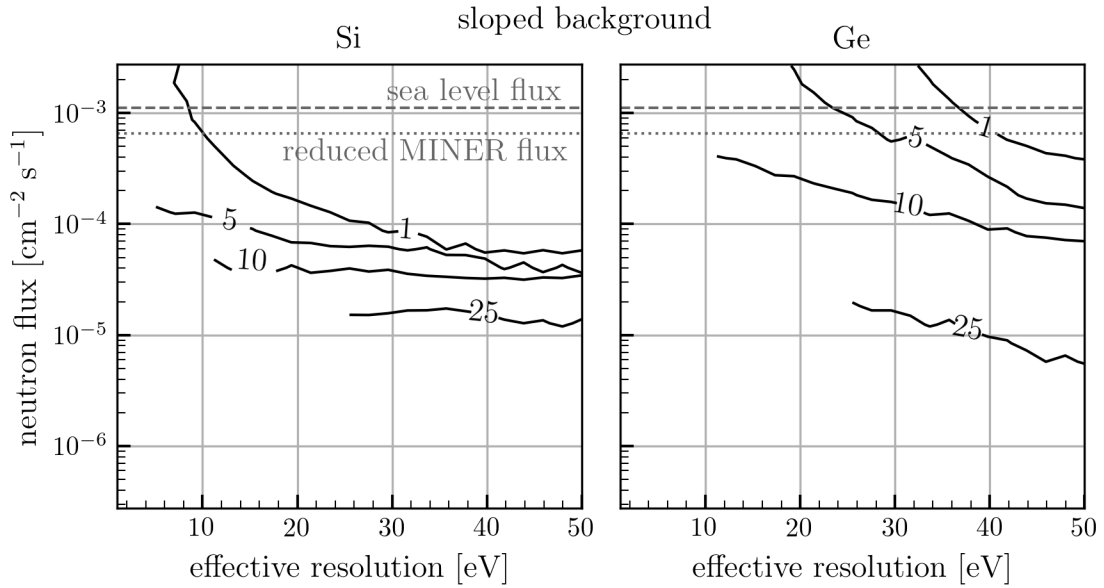


Figure 2.15: 5σ contours for sloped background model in Si and Ge. Inline labels of contours give baseline resolution in eV

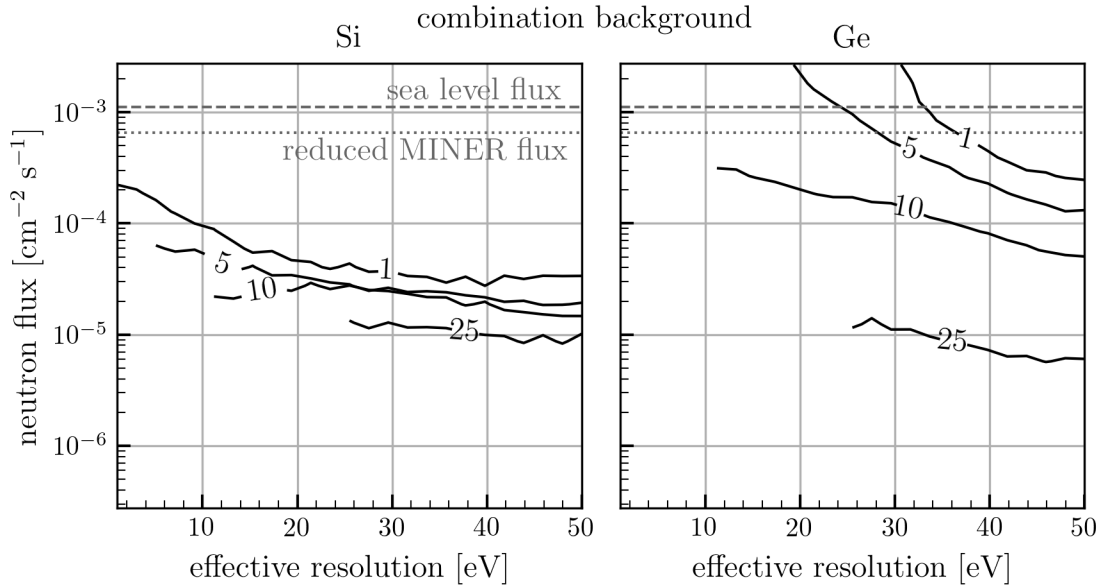


Figure 2.16: 5σ contours for combination background in Si and Ge. Inline labels of contours give baseline resolution in eV

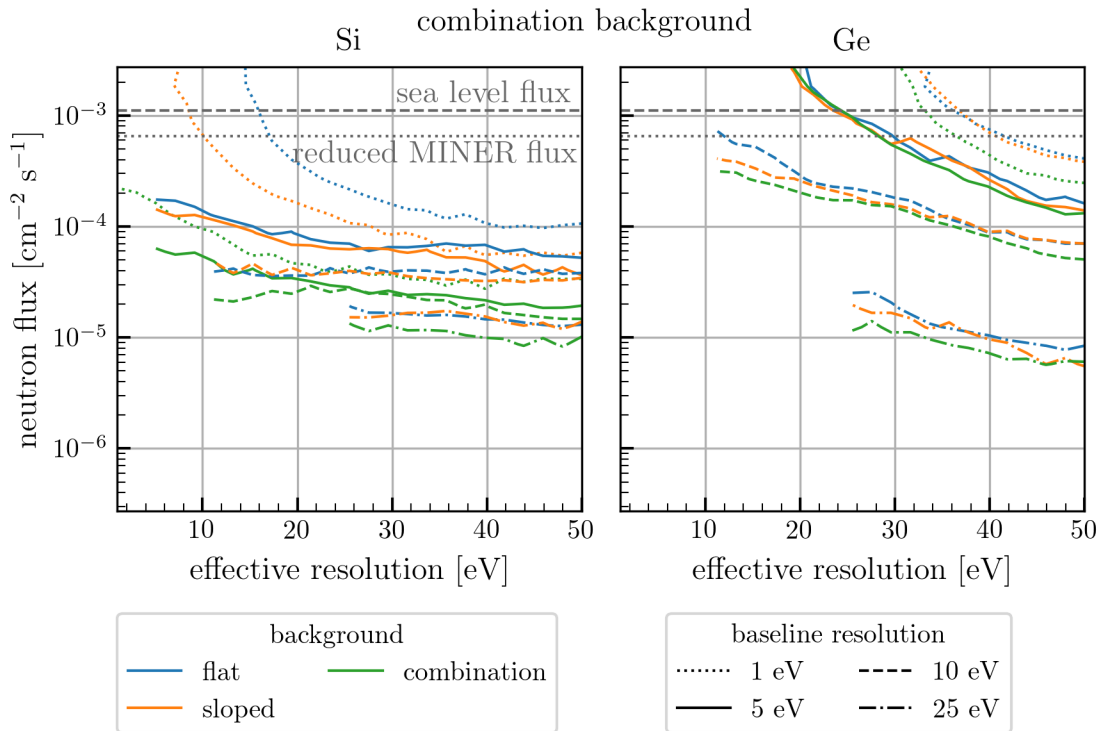


Figure 2.17: Summary of all 5σ contours for the different background models (blue, orange, and green) and baseline resolutions (dotted, solid, dashed, and dot/dashed lines)

It can be seen in this last plot that, unsurprisingly, the combination background requires the lowest thermal neutron fluxes to achieve 5σ significance. However, it should also be noted that, despite fairly wide differences in the background models, the criteria that need to be met for a 5σ CENNS measurement are extremely similar for a given baseline resolution. On the one hand, this highlights that the influence of neutron-capture backgrounds is largely unaffected by the presence, or absence, of other types of background, so long as those other backgrounds are of similar magnitude to the CENNS signal. This starts being less true as detector baseline resolution improves, however, and at eV-scale baselines additional backgrounds can make a substantial difference. We should highlight, though, that the background models considered here are intended to emulate forms of background that cannot be reduced, normalized, or vetoed. The wider set of possible backgrounds generally fall outside of these categories, and background reductions by vetoes or by normalizing to rates outside the primary region of interest for CENNS can generally bring these backgrounds down to levels and forms more similar to what is considered here. Therefore, we expect these results to be highly applicable to CENNS searches at reactors in general, and care should be taken to ensure neutron backgrounds are comparable to the limits indicated by these results.

2.8 Capture Veto

We have shown in the last section that there are fairly strict limits on the maximum thermal neutron fluxes that will allow a 5σ CENNS measurement in 100 kg yr exposure. However, up to this point we have ignored what we expect to be one of the most effective ways besides shielding of reducing the effects of neutron-capture-induced backgrounds: vetoing capture events.

During neutron captures, the capturing nuclei end up in excited energy states, and as they fall back to their ground state they emit $O(\text{MeV})$ gammas. By detecting the gamma(s) emitted in a capture event, it is possible to veto the nuclear recoil(s) caused by the capture. This idea is not unheard of. Detecting the gammas emitted during neutron capture has been proposed in the context of dark matter direct detection experiments as a way to detect any neutrons entering/leaving the detector [136, 137]. However, the idea in these proposals is to capture any neutrons leaving the detector in boron-doped scintillating material after scattering in the primary detector volume, rather than to use the gamma measurements to veto the capture events themselves.²⁰

Active neutron vetoes have not commonly been proposed in the context of CENNS searches. The experiment at the Dresden-II reactor has used a plastic-scintillator-based active veto for fast neutron scatterers [90], but these materials are only sensitive to higher-energy ($\gtrsim 10$ keV) neutrons, which cause keV-

²⁰Note boron often comes up when talking about neutron capturing/shielding because it has an exceptionally large neutron capture cross section, and is extremely effective at increasing the stopping/capturing power of neutron shields and scintillators [138].

scale proton recoils in the scintillator [139]. For the most part, reactor CENNS experiments rely on passive neutron shielding, e.g., polyethylene [87, 96] and borated (boron-doped) polyethylene [84, 89, 94, 103]. Active vetoes in CENNS searches are predominantly used to veto cosmogenic muons, for the most part using plastic scintillator panels [89, 96, 103], though cryogenic-detector-based methods have also been proposed [94]. However, it’s not totally unheard of to use solid-state semiconductor detectors to detect capture-induced gammas. CONRAD, a germanium-based gamma detector used by the CONUS collaboration to characterize *in situ* backgrounds at the KBR reactor plant, has measured several germanium deexcitation (i.e., post-capture) lines in the ~ 100 keV range [140].

The measurement of capture-induced gammas can be used to veto capture-induced nuclear recoils. We can model this veto process by assuming that, if an emitted gamma is absorbed somewhere else in the detector, that event can be vetoed. For some probability p of vetoing, we can model the effects as a reduction in the effective thermal neutron flux, $I_{\text{effective}} = (1 - p)I_{\text{actual}}$. Recall that the probability of an interaction is $p = 1 - e^{-\Sigma d}$, where Σ is the macroscopic cross section and d is the distance travelled by the gamma. We use the same gamma-cascade data used by `nrCascadeSim` to collect the most common emitted gamma energies, E_{ij} , (energy of the j^{th} gamma emitted along the i^{th} cascade) along with the corresponding probabilities P_i of cascade i . We calculate the cross section Σ_{ij} at E_{ij} by linearly interpolating gamma/silicon and gamma/germanium cross section data from the XCOM database [141]. We parameterize in terms of \bar{d} , the average distance a gamma must travel before leaving the detector, and we arrive at the following formula for the total effective flux reduction:

$$\frac{I_{\text{effective}}}{I_{\text{actual}}} = \sum_i P_i \exp \left(-\bar{d} \sum_j \Sigma_{ij} \right) \quad (2.8.1)$$

Note that we sum the Σ_{ij} along each cascade together, counting a veto as succeeding if any of the gammas emitted during a cascade is detected. Table 2.7 lists the effective flux reductions for several values of \bar{d} . It can be seen that for moderately-sized detectors, a substantial portion of capture events can be vetoed, particularly in germanium. It should be noted that detector resolution and threshold generally deteriorate with increasing size, but the benefits of scaling up the detector may be large.

To parameterize instead by detector mass, we calculate \bar{d} for a 1 cm cube using MC methods (analogous to the ones used in Section 3.6.1), which yields a value of

Table 2.7: Expected effective thermal neutron flux reduction (2.8.1) in silicon and germanium detectors as a function of \bar{d}

| \bar{d} (cm) | Si | Ge |
|----------------|------------------------|------------------------|
| 0.1 | 0.9823 | 0.8181 |
| 0.5 | 0.9151 | 0.5972 |
| 1 | 0.8382 | 0.442 |
| 5 | 0.4267 | 0.07027 |
| 10 | 0.1937 | 0.01251 |
| 20 | 0.04538 | 0.001166 |
| 50 | 0.001747 | 7.313×10^{-6} |
| 100 | 7.119×10^{-5} | 1.917×10^{-9} |

$$\bar{d} \approx 0.4547 \pm 0.0001 \text{ cm} \tag{2.8.2}$$

For different cubic detectors, \bar{d} scales linearly with the side length. Table 2.8 shows effective flux reductions for cubic detectors of different masses up to 10^4 kg.

Table 2.8: Effective flux reduction (2.8.1) for cubic silicon and germanium detectors as a function of mass

| Mass | Silicon | Germanium |
|-----------|-----------|------------------------|
| 0.1 g | 0.9721 | 0.7995 |
| 0.5 g | 0.9528 | 0.7371 |
| 1 g | 0.9409 | 0.7056 |
| 10 g | 0.8774 | 0.5745 |
| 100 g | 0.7562 | 0.3931 |
| 500 g | 0.6232 | 0.2515 |
| 1 kg | 0.5532 | 0.1944 |
| 2 kg | 0.477 | 0.1432 |
| 100 kg | 0.08053 | 0.006878 |
| 1000 kg | 0.007651 | 0.0003935 |
| 10^4 kg | 0.0003413 | 2.672×10^{-6} |

2.9 Discussion

This chapter has endeavored to show approximately what conditions need to be met in order to measure CENNS in the vicinity of a nuclear reactor, specifically in reference to the influence of thermal neutron capture backgrounds. Generic detectors composed of silicon and germanium have been considered with a range of baseline resolutions, effective resolutions, and in a number of ambient thermal neutron fluxes.

A few more points bear discussing, especially as regards the ability to extend these results to a wider range of experimental situations. Some discussion will be given to the relative merits of silicon and germanium. Major uncertainties in this analysis will be described.

2.9.1 Scaling laws

There are a few main experimental parameters that were held fixed in this analysis that generally will vary in almost all experimental situations: the reactor thermal power and the exposure time of the experiment. Both of these things will change the total numbers of events in a given sample, and so it will be beneficial to look at the approximate scaling of the significance of a CENNS measurement with the sample size.

Once again, the binned log-likelihood is proportional to L (2.6.19a):

$$L = n_{\text{total}} - \sum_j C_j \ln [n_\nu A_{\nu,j} + n_c A_{c,j} + n_b A_{b,j}] \quad (2.9.1)$$

Consider doubling the sample size, i.e., collecting two of every data point in the original sample. Then every C_j is doubled, and the fit numbers $\{n_k\}$ of each event are also doubled. The scaled negative log likelihood becomes:

$$\begin{aligned} L_{\text{new}} &= 2n_{\text{total}} - \sum_j 2C_j \ln [2n_\nu A_{\nu,j} + 2n_c A_{c,j} + 2n_b A_{b,j}] \\ &= 2n_{\text{total}} - \sum_j (2C_j \ln [n_\nu A_{\nu,j} + n_c A_{c,j} + n_b A_{b,j}] + 2C_j \ln 2) \\ &= 2L - 2 \ln 2 \sum_j C_j = 2L - 2N \ln 2 \end{aligned} \quad (2.9.2)$$

Similarly, we expect L' to become $2L' - 2N \ln 2$. The significance, $Z = \sqrt{2(L_2 - L_1)}$, then becomes $\sqrt{2(2L_2 - 2N \ln 2 - 2L_1 + 2N \ln 2)} = \sqrt{2}Z$. So the statistical significance of a CENNS measurement in an exposure Q , assuming the sample is large enough to dampen out statistical noise, scales as $Q^{1/2}$ (since Q is proportional to the number of events of all types).

We can apply this to other reactors by noting that the neutrino emission rate of a reactor scales linearly with the thermal power. So, for a reactor with thermal power P_{th} MW (note our assumed reactor had a thermal power of ≈ 1 MW) and an exposure time of $(100 \text{ kg yr})/P_{th}$, our results at a thermal neutron flux I will give exactly the same results in a flux of $P_{th} \times I$ (this yields the exact same number

of CENNS and capture events as our data). To extrapolate to different different distances r from the reactor core, just replace the thermal power P_{th} in MW with $P_{th} \times ((10 \text{ m})/r)^2$ in the formulas above. For example, for detector deployed 10 m from the ~ 3 GW Dresden-II reactor in an ambient thermal neutron flux of $0.25 \text{ cm}^{-2} \text{ s}^{-1}$ (value estimated on-site [90]), our results directly apply to an exposure time of $\sim 12.2 \text{ kg days}$ at a flux of $8.33 \times 10^{-5} \text{ cm}^{-2} \text{ s}^{-1}$, i.e., a 5σ CENNS measurement can be made in a 10-eV-baseline germanium detector with an effective resolution lower than $\approx 40 \text{ eV}$.

2.9.2 Silicon vs. germanium

The results of comparing silicon and germanium are very interesting. For most cases, the germanium far outperforms the silicon, due to the larger sample of CENNS events taken. The actual relative number of CENNS events is smaller in germanium, 3.3 CENNS events in Ge for every one in Si, and 4.9 capture events, but the increased number of CENNS events total makes high-statistics measurements possible.

However, the results in germanium change much more dramatically as a function of the detector resolution, both the effective resolution (slopes of the contours) and the baseline resolution (distance between the contours). Changing resolution has a much more drastic effect in germanium. We hypothesize two causes for this. The first is that the capture spectrum in Si is largely flat above $\sim 50 \text{ eV}$, while for Ge the capture spectrum slopes upward until the large peaks near $\sim 300 \text{ eV}$ (see Figure 2.3). So, for coarser resolutions, more of the capture spectrum in Ge gets “spread out” to the lower energies where the CENNS signal is. Secondly, the CENNS spectrum in Ge is more sharply peaked at low energy (see Figure 2.4). Thus, for coarser baseline resolutions, which cause higher energy thresholds, comparatively more CENNS events are cut off by the energy threshold in Ge than in Si. Thus, at coarse resolutions it is likely best to use silicon detectors, but at finer resolutions germanium is preferable.

2.9.3 Uncertainties

The last point that we will mention is sources of uncertainty. One major source of uncertainty in our results is in the reactor neutrino spectrum described in Section 2.2.2.2. Many large systematic uncertainties remain in this spectrum (see, e.g., [106, 111, 112]), and some disagreements between the model used and measurements, e.g., those taken at the Daya Bay nuclear reactor complex [121] are well-known. More recent work has shown promise in resolving the discrepancy [142], though uncertainties remain high. Some preliminary work comparing results using both neutrino spectra found systematic differences, though a full analysis using the Daya Bay data was not pursued.

Another source of uncertainty is the possibility of major contributions to the capture spectrum from missing cascades in the `nrCascadeSim` code, particularly in Ge. The set of cascades in Ge used comprise all the major high-probability cascades, and the probability of any one missing cascade is at maximum 0.005% – however, only approximately 27% of all possible cascades are accounted for in Ge (in code version 1.4.6), compared to $\sim 95\%$ in Si. Taken together these missing cascades may cause a substantial departure from the Ge spectrum used, though it is likely that the spectral difference from the spectrum used is small. Missing cascades all likely involve transitions through densely-populated energy bands of the germanium nuclei at higher energy (and with short lifetimes), followed by transitions directly to ground, which would cause a relatively flat, mostly higher-energy contribution to the spectrum. The most significant part of the capture spectrum for our purposes is the low-energy portion, so we don't expect these missing cascades to substantially change our results.

We expect the dominant source of error in our results to be statistical. As was shown in Section 2.7.2, the uncertainty in any individual calculated Z value is approximately 1. For the position of the contours, we saw that their vertical positions (corresponding to neutron flux) can vary due to statistical effects by as much as 60%. This is expected to be the main source of error in our results, and so a constant $\sim 60\%$ vertical error bar can aptly be applied to our results.

CHAPTER III

DARK MATTER DIRECT DETECTION

This chapter outlines work developing a semianalytical method for characterizing the neutron backgrounds to dark matter detector calibrations at the NEXUS underground facility.

Dark matter direct-detection experiments have been underway for decades, still without success. As detector technologies improve, the importance of detector calibration increases, and background characterization is absolutely essential to deciphering the data collected. This chapter will be devoted to a method for characterizing neutron backgrounds in a shallow (~ 100 m) underground facility called the NEXUS facility. A generic neutron flux spectrum will be assumed based on available data and some basic physical assumptions. A semianalytical simulation of the HVeV detectors will be presented.

Almost all studies that involve simulating neutron backgrounds to both CENNS and DM searches use MC methods to simulate both neutron fluxes and detector response (e.g., [76, 79, 83, 87, 105, 143]). The most commonly used such MC tool is Geant4 [144, 145], a many-use toolkit for simulating particle transport through matter. According to Scopus, the original Geant4 publication has been cited over 17,000 times since its publication in 2003 [146]. However, MC tools like Geant4 become extremely inefficient when simulating low-probability events like interactions with neutrons in low-flux environments [147]. There are a number of advanced Monte Carlo methods like splitting, importance sampling, and forward flux sampling that might help efficiency [147, 148], but implementing them is difficult and usually must be finely tailored to a specific application. The other option is to forego MC methods entirely, and attempt to approximate detector response using purely analytical methods.

The tack taken in this chapter is somewhere between these extremes. The semianalytical approach described here begins with analytical methods to estimate the rates of interactions between ambient neutrons and the detector, which does not require expensive particle-tracking and collision simulations. From there, the response of the detector, i.e., how the information about collisions in the detector propagates to the readout systems, are simulated via MC methods. This sort of mixed approach combines the benefit of calculating high-accuracy collision (recoil) rates even for high-rarity events, but allows for complex models of detector response that cannot be encoded analytically. There is no surprising physics in this methodology, yet as far as I am aware this is the only example of such an approach in the literature. This chapter should demonstrate that this sort of methodology is a straightforward and viable method for calculating detector response to neutrons (and other particles), and should open the door for similar background studies and studies that involve measuring components of the neutron spectrum directly and then calculating the detector response semianalytically.

Our semianalytical method is summarized in Figure 3.1. The ambient neutron flux is convoluted with the scatter and capture cross sections analytically (i.e., (1.4.1)) to yield the spectrum of scatter-induced recoil energies and the total rate of capture events. Here we switch to MC methods. A sample of scatter-induced recoil energies is generated from the calculated spectrum and a sample of capture-induced recoil energies is taken from `nrCascadeSim`. The ionization produced by each recoil event is simulated according to a specified ionization model. This then allows the calculation of the resulting spectrum of neutron-induced phonon energies as measured in the detector.

Section 3.1 will give a brief overview of WIMP dark matter and WIMP detection. The SuperCDMS collaboration will be introduced in Section 3.2. The NEXUS facility will be introduced and described. In Section 3.3 the HVeV detectors will be described. The model ambient neutron spectrum will be introduced in Section 3.4. The calculation of event rates and recoil spectra by analytical convolution will be given in Section 3.5, and Section 3.6 will outline the treatment of multiple scatters. Section 3.7 will introduce the ionization model used. In Section 3.8, the simulation procedure will be described. Section 3.9 will give the results and Section 3.10 will describe sources of error in the final spectrum. Section 3.11 will give concluding remarks

3.1 Dark Matter Direct Detection

“Direct detection” of dark matter refers to the measurement of DM interactions with atomic matter in detectors. Current direct detection experiments can mostly be categorized based on the dark matter model they are searching for. These models include undiscovered types of neutrinos, hypothesized particle types called axions, and several particle candidates residing in an extension of the standard model based around “supersymmetry,” a hypothesized set of matching fermions for every known boson and matching bosons for every known fermion. The DM model of interest here is that of weakly interacting massive particles (WIMPs), a broad class of non-baryonic massive particles which only interact with normal matter at rates comparable to or smaller than the weak scale.

3.1.1 WIMP Dark Matter

WIMPs are one of the oldest and most popular categories of dark matter hypothesis. As a proposal for a missing particle somewhere in the standard model, they are extremely well-motivated and well backed up theoretically. Depending on how vague one is in defining the WIMP category, the properties of WIMPs are those that one almost necessarily arrives at as a result of accounting for all the evidence regarding dark matter. We briefly outline these evidential steps below.

First, by definition DM cannot interact by the electromagnetic interaction. Interaction by electromagnetism is the emission or absorption of light - since dark matter is “dark,” it cannot couple to this

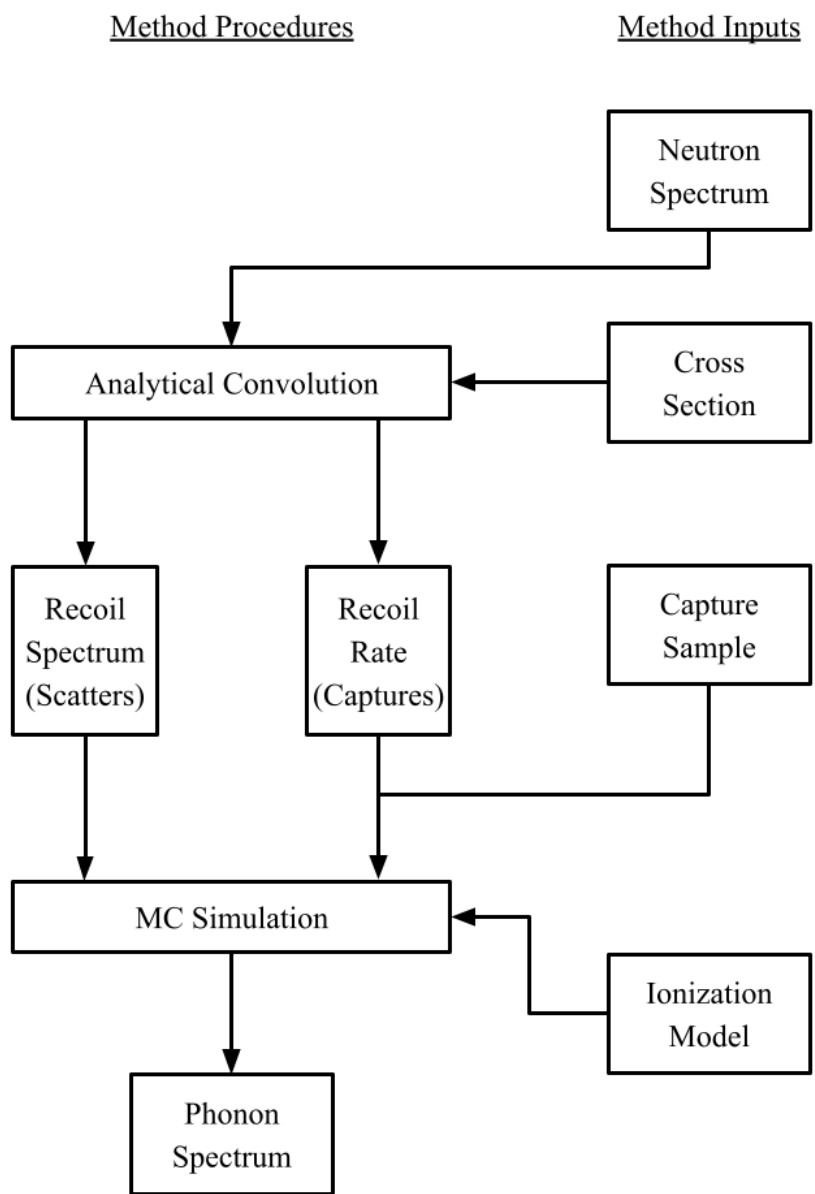


Figure 3.1: Flow chart summarizing semianalytical method used in this chapter to calculate neutron-induced phonon spectrum

interaction at all. This means it must be electrically neutral, with negligible magnetic moment. Second, it cannot interact via the strong force. With almost any nonzero strong coupling, head-on collisions with cosmic ray protons and alpha particles would leave visible signatures in the form of gamma rays.

Thirdly, DM cannot be baryonic (composed of an odd number of quarks, e.g., protons or neutrons). Constraints on the amount of baryonic matter in the universe come from calculations of Big Bang nucleosynthesis (BBN), the process of light nuclei ($Z \lesssim 4$) formation during the Big Bang. Calculation of the rates of BBN gives an estimate for the total amount of primordial (relic from the Big Bang) baryonic matter in the universe. Measured values of luminous matter agree with estimates for the total amount of baryonic matter, leaving very little room for relic baryonic dark matter [149].

Next, dark matter must be *cold*. The “temperature” of a population of relic dark matter refers to its velocity distribution shortly after the Big Bang. Very roughly, if the mass of the DM particle is much smaller than the mean energy of the relic population of particles (set by the temperature of the universe when those particles formed and remained stable (“freeze out”) as the universe cooled following the Big Bang), the velocity of those particles will be ultrarelativistic (“hot dark matter”), and the distribution of velocities will be shaped quite differently than if the mass is much larger than the temperature at freeze-out (“cold dark matter”). Simulations (e.g., [23]) show that cold dark matter models are very successful in predicting the scale and structure of matter in the universe, i.e., distribution into galaxies, galaxy clusters, and superclusters. On the other hand, hot dark matter results in the suppression of structures on the scale of galaxies. Spatial variations in matter density that go on to be responsible for clustering of matter are suppressed on galactic scales by the larger velocities of the hot DM particles. The DM particles must be colder, and the particles slower-moving, so that spatial variations can form and deepen and the types of galaxies we observe today can form. For standard weak-coupling particles, this result provides a rough constraint on the mass of DM particles to $\gtrsim 10$ eV. Importantly, this rules out standard model neutrinos.

The next set of constraints come in the form of constraints on the self-interaction cross section of the DM particles. Two things need to be true: first, the amount of DM in the early universe must be small enough so that the structures we observe in the universe today can form in the way they did, and the amount of DM in the universe today must be large enough to account for all the missing matter. Thus, constraints can be put on the rates at which DM particles collide and annihilate with each other and at which they spontaneously decay (an early work is [150], a more recent work is [151]). The estimated interaction rates are small, consistent with weak force interactions. This immediately suggests that DM particles couple to the weak interaction or another interaction with a similar energy scale.

Together, these considerations suggest DM must be a nonbaryonic particle with self-interactions at the weak scale or smaller, and mass large enough so that the population of DM at freeze out is cold. This

is the basic WIMP definition. However, it should be noted that the “WIMP” category has changed somewhat since its first definition. Some of the most stringent constraints on DM properties come from detection efforts searching for these classical WIMPs, both direct (e.g., [152, 153]) and indirect (e.g., [154]). The possible parameter space of the “WIMP” category, which traditionally consisted of particle masses between $\sim\text{GeV}$ and TeV scales, has been reduced substantially by experiments, motivating a widening of the search area. Many WIMPs considered today are lighter, and belong in slightly different spots in extensions of the standard model [155, 156], such as dark photons [157, 158]. This new category of particles is often informally denoted as “light” dark matter (LDM), though here we will continue to use the phrase “WIMP.” Where classical WIMPs are in many ways the “shortest leap” to meeting all the criteria required by the original evidence, new light WIMP models are further removed from normal matter, e.g., “scalar” DM [159] or “secluded” DM [160]. But despite the many ways that these light WIMPs differ from their classical predecessors, many of the same experimental practices can be used to detect them [161, 162], e.g., [163] and [164].

3.1.2 Detecting WIMPs

Very briefly, it will be beneficial to make explicit the tenets of DM direct detection.

The primary interaction between DM and normal matter that we will focus on is DM-nucleon coupling (interactions between DM particles and protons/neutrons), a set of interactions that causes nuclear recoils. Goodman and Witten [165] were the first to suggest that the detectors proposed by Drukier and Stodolsky [72] for detecting neutrino-nucleus interactions can be used to detect the NRs caused by dark matter. Since both types of events cause low-energy NRs, all the experimental practices applied to CENNS detection can also be applied to DM detection, and vice-versa. For example, Singh et al. [103] analyzed TEXONO data to put constraints on super-light WIMP-nucleon cross sections, and Lopez-Asamar [166] has proposed using the SuperCDMS detectors described in Section 3.3 to detect CENNS events caused by solar neutrinos. In addition, nearly all of the detector types described in Section 2.2 have been or are currently being used in direct detection efforts, including CCDs (e.g., [167, 168]), dual-phase scintillators (e.g., [152, 153, 169]), and calorimeters (e.g., [130, 170, 171]), the latter of which will be the focus of this chapter.

The generic expected energy spectrum of DM-induced nuclear recoils is a featureless falling exponential [172]:

$$\frac{dR}{dE_r} = \frac{R_0}{E_0 r} e^{-E_r/E_0 r} \quad (3.1.1)$$

where dR/dE_r is the event rate per unit energy, E_r is the recoil energy, R_0 is the total event rate, E_0 is the most probable incident kinetic energy of the DM particles, and r is the unitless factor $4M_\chi M_A/(M_\chi + M_A)^2$, for DM mass M_χ and nuclear mass M_A .

The total rate R_0 (in tru) is typically written as a function of the local dark matter density ρ_χ , cross section \mathcal{O}_χ , and the velocity of the Earth with respect to the bulk dark matter halo v_0 :

$$R_0 = \frac{\mathcal{O}_\chi \rho_\chi v_0}{M_\chi M_A} \quad (3.1.2)$$

The factor $\rho_\chi v_0/M_\chi$ is the particle flux (particles per unit area per unit time). The factor of $1/M_A$ normalizes the rate per unit of detector mass. Note also that the cross section \mathcal{O}_χ should scale approximately as A^2 .²¹ Typical estimates for the local DM halo density are $\rho_\chi \approx 0.42 \text{ GeV cm}^{-3}$ [173].

The velocity of the Earth with respect to the galactic halo v_0 is on average the velocity of the Solar System around the galactic center, something like 232 km/s.²² The Earth's velocity oscillates over the course of the year as it orbits the Sun, causing a yearly modulation in the total DM rate - maximum in June, minimum in December. Looking for this modulation in the DM signal is an effective way to increase the significance of a measurement [177, 178]. For a per-nucleon cross section of 10^{-41} cm^2 and a mass of 0.5 GeV, (3.1.2) corresponds to an interaction rate with silicon of $\sim 0.03 \text{ events kg}^{-1} \text{ day}^{-1}$.

3.2 SuperCDMS

The Super Cryogenic Dark Matter Search (SuperCDMS) is an international collaboration searching for WIMP dark matter. The current phase of the experiment, SuperCDMS SNOLAB, is centered at the SNOLAB facility in Creighton Mine in Sudbury, Ontario. SNOLAB is an extension of the Sudbury Neutrino Observatory (SNO), a deep-underground ($\sim 6 \text{ kmwe}$) research laboratory with 5,000 m² of clean room laboratory space [179].²³ SNO was, along with the Super-Kamiokande experiment [180, 181], one of the first to confirm the process of neutrino oscillations from solar neutrinos [182, 183] (see also the review [184]). It benefits from one of the largest overburdens of any underground laboratory on the planet (see,

²¹Technically, the cross section goes as $(g_p Z + g_n N)^2$ for some coupling constants g_p and g_n for protons and neutrons and atomic and neutron numbers Z and N , but for large nuclei the ratio Z/A is approximately constant so the overall scaling is approximately $\sim A^2$

²²This quoted value is the International Astronomical Union (IAU)'s recommended value for the local circular velocity, 220 km/s [174] plus the Sun's velocity in that direction relative to the circularly-orbiting reference frame, $\sim 12 \text{ km/s}$, as reported by [175]. There are substantial uncertainties in these values, particularly to the circular velocity, though the literature tends to agree on the use of these values [176].

²³See also <https://www.snolab.ca/about/about-snolab/>

e.g., the labs referenced in [185]), making it one of the lowest-background laboratory environments on the planet.

The cryogenic dark matter search (CDMS) has a decades-long history in DM direct detection. SuperCDMS descends from the CDMS [186–189], CDMS-II [190–192], SuperCDMS Soudan [163, 193], and CDMSlite [130] experiments in the Soudan Mine in Minnesota. Taken together these represent one of the largest experimental campaigns on the planet in the search for dark matter.²⁴ Current published plans for the SuperCDMS SNOLAB phase involve the deployment of some 20+ kg worth of cryogenic semiconductor crystal calorimeters, with a planned 5 years of operating time [105, 194, 195].

The entire SuperCDMS collaboration involves 29 institutions in 7 different countries, all contributing different functions.²⁵ SLAC National Accelerator Laboratory is responsible for the detector payload (meaning fabrication, etc. of all the detector pieces). From SLAC, the detector components go to Fermi National Accelerator Laboratory (FNAL, or FermiLab), where the cryogenics apparatus and shielding are developed. Operations at FNAL are the focus of this chapter.

3.2.1 The NEXUS facility

The Northwestern Experimental Underground Site at Fermilab (NEXUS@FNAL) is an underground facility situated in the MINOS cavern at FNAL, 107 m (300 mwe) below Batavia, Illinois [196, 197]. For the past few years, NEXUS has been home to several CDMS HV detectors, with the aim of calibrating the detectors and characterizing sources of background in them.

3.3 The HVeV Detectors

The SuperCDMS SNOLAB experiment will utilize two types of cryogenic detectors, both with Ge and Si versions. The iZIP (interleaved Z-sensitive Ionization and Phonon) detectors are more sensitive to intermediate mass DM. These detectors collect both ionization and heat information from energy deposits, allowing discrimination between ER and NR events (ER events produce much more charge compared to NRs for the same amount of heat deposited) [143]. On the other hand, the HV (high-voltage) detectors do not discriminate between ER and NR events, and focus only on measuring heat deposits. However, they have much lower energy thresholds, and are more sensitive to lighter ($\lesssim 5$ GeV) dark matter particles.

The HV detectors' low thresholds come from the process of phonon amplification in the semiconductor crystals during operation. When a nucleus recoils, its energy is carried into the surrounding crystal through two main avenues: heat and ionization. Heat is carried away by quantized units of vibrational energy called *phonons*, which for the most part propagate through the crystal without dissi-

²⁴Note the papers referenced are far from an exhaustive list

²⁵See <https://supercdms.slac.stanford.edu/collaboration>

pating [198]. In addition, scattering between the nucleus and surrounding valence electrons can ionize those electrons, creating e/h pairs. A high-voltage bias is applied across the crystal (hence the name, HV), which pushes the ionized e^- and h^+ in opposite directions through the crystal, creating yet more phonons by the Neganov-Trofimov-Luke (NTL) phonon amplification effect [199, 200]. Roughly, as the ionized particles propagate through the crystal, they collide with other electrons, creating yet more phonons (“Luke phonons,” or “NTL phonons”). The total energy emitted as Luke phonons is the work done on the e/h pair by the bias voltage, eV_b , where e is the elementary charge and V_b is the bias voltage across the detector.

The Luke phonons and prompt phonons, the phonons produced directly by the recoil, propagate through the crystal, reflecting off the sides, until they come into contact with aluminum fins deposited on the upper face of the crystal. A portion of the phonons are transmitted into the aluminum fins, which are part of components called QETs: quantum-trap-assisted electrothermal-feedback transition edge sensors [201]. The phonons are efficiently directed into a thin tungsten film held right around its superconducting transition temperature (a “transition edge sensor,” TES), where the resistivity of the tungsten changes rapidly as a function of temperature. The phonons transmitted by the aluminum fins thermalize (dissipate) into the tungsten, increasing its temperature, so its resistance changes. A current signal is monitored constantly through the TES; when this resistance change occurs, the current drops suddenly, which can be read off and used to measure the energy deposited into the QET, which is then in turn used to determine the energy of the initial NR.

This operating principle was first used in CDMSlite iZIP detectors, where the standard iZIP detectors were biased at higher-than-normal voltage (50-80 V) [130]. The first versions of the current generation of Si HV detectors were 100 mm diameter cylinders, 33.3 mm thick, and weighed 0.61 kg, with baseline energy resolution ~ 5 eV [105]. However, recent work has examined differing detector sizes in Si detectors. One investigation found cylindrical detectors 70%-120% larger had some promise in maintaining acceptable thresholds while increasing detector payload [202], but the greatest advancements have occurred by decreasing detector size. An energy resolution of 14 eV was demonstrated on a 1 cm^2 by 4 mm crystal weighing 0.93 g [203]. Subsequent improvements with a crystal only 1 mm thick gave an energy resolution of only 3 eV at a much smaller voltage bias of 50 V [204]. Early DM results using these detectors show field-leading constraints on light and superlight (dark photon) DM with extremely short exposures, operating in surface environments with very low shielding [171, 205]. The physics reach of these electronvolt-

resolution HV (HVeV) detectors is extremely large, and their development is a high priority. Beyond DM searches, these detectors also have applications in solid state physics [206] and neutrino science [68, 166].

3.3.1 HVeV development

Analysis for calibration runs of the HVeV detectors is currently underway at NEXUS. They have yet to characterize the neutron backgrounds at NEXUS, and they have not characterized thermal-neutron backgrounds at SNOLAB. The rest of this chapter will be devoted to the simulation of neutron-induced events in the HVeV detectors in the NEXUS facility, in an effort to begin shedding some light on which portion of the observed background events in that facility are produced by neutrons.

3.4 Neutron Spectrum in NEXUS

Ambient backgrounds have been a limiting factor in DM searches since the experiments of Ahlen et al. [207] and Caldwell et al. [208] in the late 80's.²⁶ In underground facilities, neutrons are a major component of the backgrounds [105, 185, 209–212]. Neutrons are particularly difficult to deal with, as they produce NRs phenomenologically identical to the NRs produced by scattering WIMPs. This section describes our model for the ambient thermal neutron flux in the NEXUS facility, that will be used to ultimately predict the neutron-induced background signal in the HVeV detectors.

A rudimentary model of radiogenic neutron flux was developed based on unpublished simulations of fast neutrons in SNOLAB by Rob Calkins [213]. The data provided by Dr. Calkins included unnormalized emission spectra from uranium and thorium impurities in shotcrete (spray-on concrete, material used in construction of SNOLAB) and norite rock (magnesium and iron rich igneous rock) surrounding the lab. This data is plotted in Figure 3.2. It was simulated using *SuperSim*, a set of software programs and data built on top of Geant4 for the SuperCDMS collaboration (see [105] for a description of the physics lists utilized in SuperSim).

²⁶See [12], pg. 24

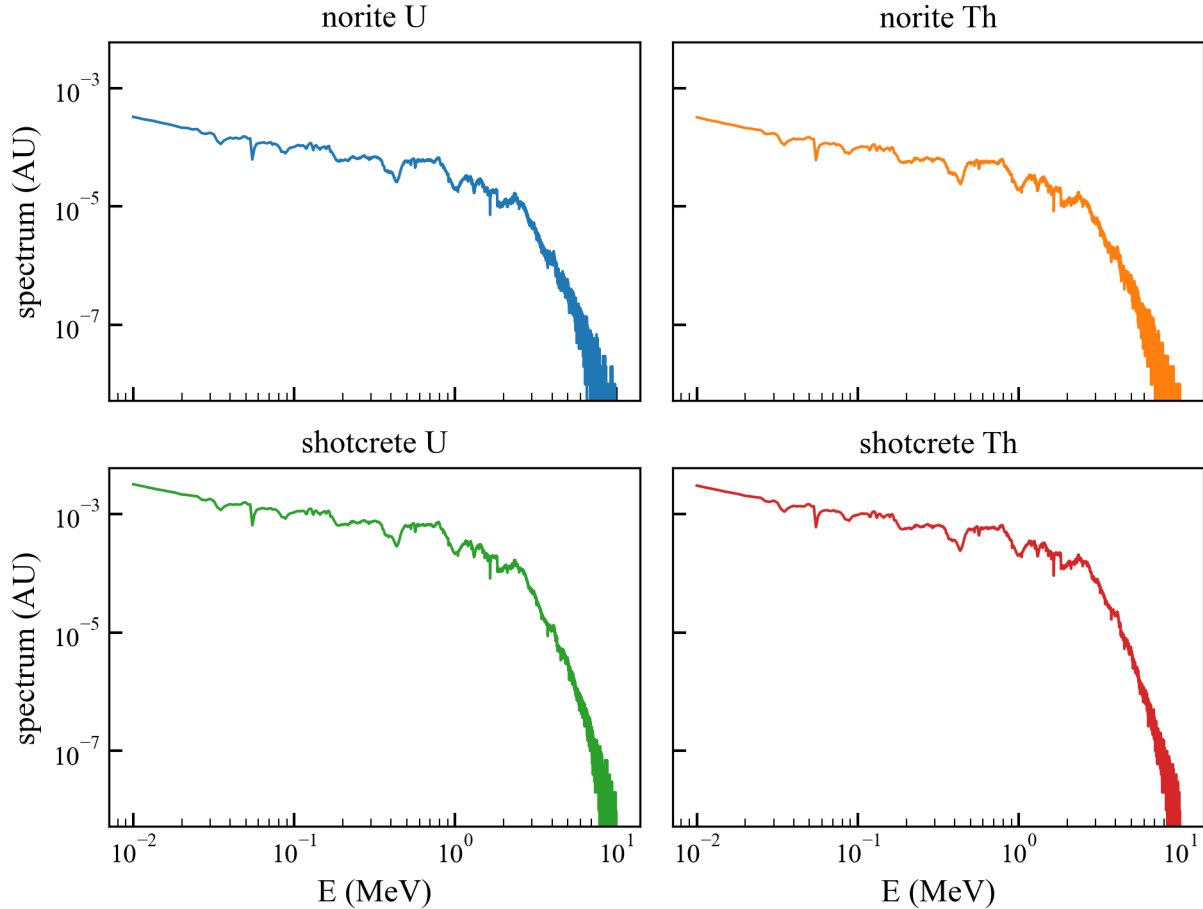


Figure 3.2: Unnormalized radiogenic fast neutron fluxes simulated in the SNOLAB geometry (provided by R. Calkins)

The relative contributions of uranium and thorium are estimated from measurements of their relative abundance in rock samples taken around SNOLAB using a Ge gamma detector, as documented in an internal SNOLAB report by Lawson [214]. Similar values are given by Tiwari [215] in public conference slides. These are listed in Table 3.1.

Table 3.1: Abundances of radioactive isotopes in rock and concrete at SNOLAB reported by D. Tiwari

| Material | Uranium (ppm) | Thorium (ppm) |
|-----------|---------------|---------------|
| Norite | 1.3 | 6.5 |
| Shotcrete | 2.46 | 15.24 |

It was assumed that shotcrete and norite contribute equally to the neutron flux inside the lab (that is, a radioactive particle in either the norite or the shotcrete is equally likely to contribute neutrons to the ambient flux). The overall fast flux is normalized to $4000 \text{ neutrons m}^{-2} \text{ day}^{-1}$ ($\approx 4.63 \times 10^{-6} \text{ cm}^{-2} \text{ s}^{-1}$), the value given in the SNOLAB user’s handbook for fast neutron flux [216]. Note that “fast” here extends

down to energies as low as 10 keV. The resulting combined fast flux spectrum was extrapolated down to thermal energies by fitting a line to the log-log spectrum data below 20 keV. The resulting power-law fit $I(E)$ is:

$$I(E) = (2.477 \times 10^{-9})E^{-0.564} \quad (3.4.1)$$

where E is in eV and the flux I is in $\text{cm}^{-2} \text{s}^{-1} \text{eV}^{-1}$. The combined fast flux spectrum is plotted with the power law fit in Figure 3.3.

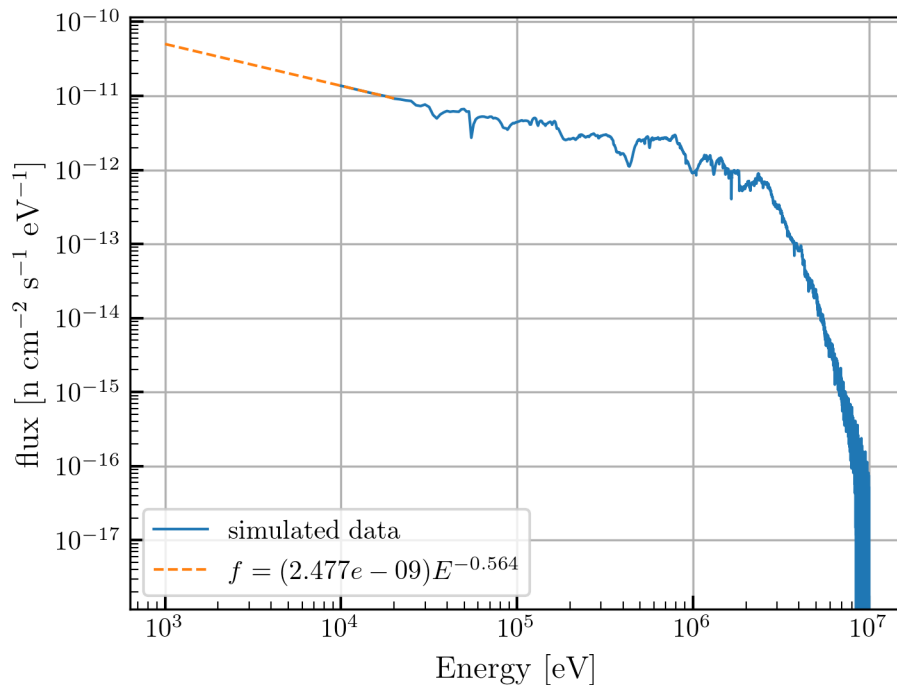


Figure 3.3: Total radiogenic fast neutron flux spectrum (blue) and fitted power-law (orange)

This power-law fit is merged with the presumed neutron distribution at thermal energies. Fully thermalized neutrons are expected to behave analogously to a gas in thermal equilibrium at room temperature, and so their kinetic energies follow a Maxwell-Boltzman distribution [217]:

$$\rho(E) = 2\sqrt{\frac{E}{\pi}} \left(\frac{1}{kT}\right)^{3/2} \exp\left(-\frac{E}{kT}\right) \quad (3.4.2)$$

where E is the kinetic energy, T is the temperature, and k is the Boltzmann constant. The spectrum is assumed to be in equilibrium, so the rate of fast-neutron production balances neutron thermalization, which brings neutrons from high energies to thermal energies, and this in turn is in balance with the rate of neutron capture on various materials in the lab, which removes thermal neutrons from the system.²⁷ If on average it takes t_1 seconds for a fast neutron to thermalize, and t_2 seconds for a thermal neutron to be captured, then on average there will be t_2/t_1 thermal neutrons for every fast neutron (the neutrons spend t_2/t_1 as much time at thermal energies than at fast energies). The thermalization time is assumed to be $30 \mu\text{s}$, the value of total thermalization time measured by Moeller and Sjostrand [219] for fast neutrons in water (note also that Moeller and Sjostrand’s results are consistent with the assumption of Maxwell-Boltzmann-distributed thermal energies). The average capture time is taken to be $200 \mu\text{s}$, in good agreement with several recent measurements of the average neutron capture time in heavy water, e.g., Anderson et al. [220] ($202.35 \pm 0.87 \mu\text{s}$) and Zhang et al. [221] ($202.6 \pm 3.7 \mu\text{s}$). This results in a total thermal neutron flux of $\sim 27,000 \text{ n m}^{-2} \text{ day}^{-1}$ ($3.1 \times 10^{-5} \text{ n cm}^{-2} \text{ s}^{-1}$). For room temperature ($T = 298 \text{ K}$), the thermal distribution begins sloping up near $E \approx 0.15 \text{ eV}$, so this is where we cut off the extrapolated power-law fit (3.4.1).

The resulting neutron spectrum is plotted in Figure 3.4. This is our assumed ambient neutron flux in the NEXUS facility. The maximum energy included is $\approx 10 \text{ MeV}$, and it goes down to a minimum value of 10^{-4} eV . The total neutron flux is $\approx 30,900 \text{ neutrons m}^{-2} \text{ day}^{-1}$ ($3.58 \times 10^{-5} \text{ neutrons cm}^{-2} \text{ s}^{-1}$). This is about 50% higher than measurements of total neutron flux made in the underground Kamioka Observatory [209], an underground facility with similar overburden.

²⁷Neutron decay is assumed negligible on the time scales in question here, as the neutron half-life is on the order of 15 minutes [218]

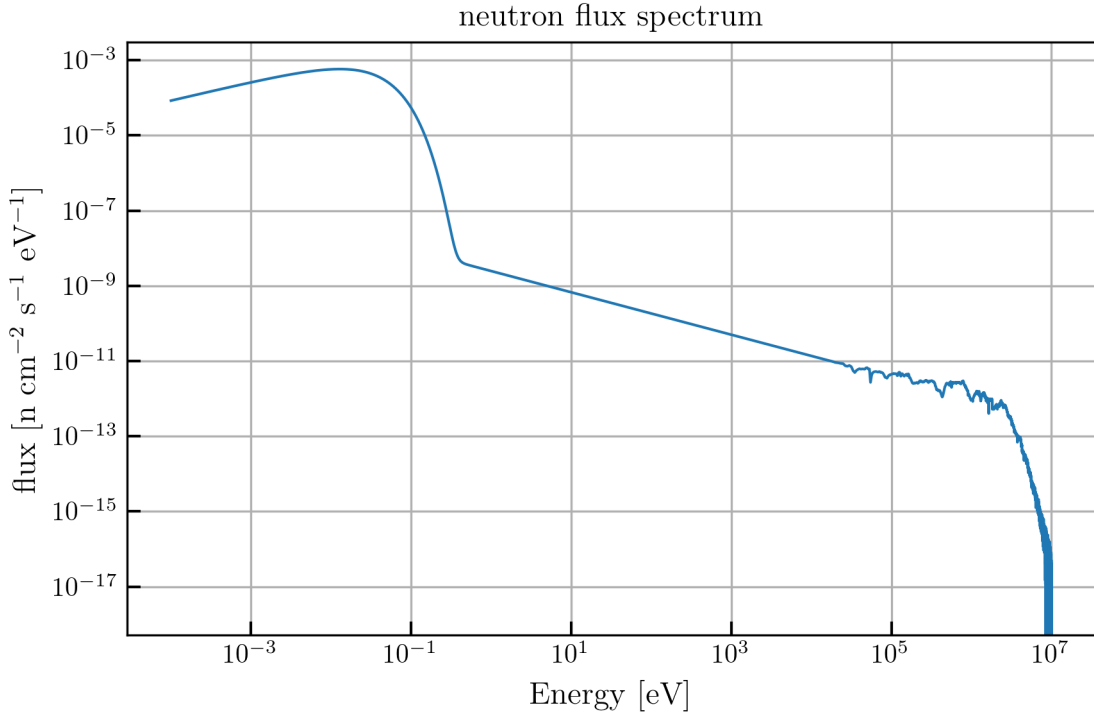


Figure 3.4: Model ambient neutron flux spectrum at NEXUS

3.5 Calculation of Event Rates and Spectra

Once we have a model for the ambient neutron flux (Figure 3.4), we can calculate the rate of neutron captures and the spectrum of scatter-induced recoil events in the silicon of the HVeV detectors by analytical means. These will be the results of this section (see Figure 3.1).

3.5.1 Captures

Ambient neutrons will interact with the HVeV detectors in two ways: captures and scatters. The method for calculating the capture-induced recoil spectrum here is identical to the method used in the previous chapter, which is simply to use the dedicated software `nrCascadeSim` [124] (see Section 2.3.1). A sample of capture events is generated using `nrCascadeSim` and will be used in the “MC Simulation” phase of the procedure, Section 3.8. However, we must calculate the rate of capture events based on our ambient neutron flux model. To do this, the neutron flux below $E = 5$ eV is considered to contribute equally to the capture rate. Integrating the neutron flux below 5 eV results in a total capture rate of ≈ 9.79 captures $\text{kg}^{-1} \text{day}^{-1}$.

3.5.2 Scatters

This section describe the analytical convolution used to calculate the scatter-induced recoil spectrum due to the neutron flux spectrum calculated in Section 3.4 and plotted in Figure 3.4. In analogy with (2.6.1), the rate $n(E_r)$ (in dru) of nuclear recoils with energy E_r is:

$$n(E_r) = \frac{1}{m_{Si}} \int_0^\infty I(E_n) \sigma(E_r, E_n) dE_n \quad (3.5.1)$$

where m_{Si} is the mass of a silicon nucleus, $I(E_n)$ is the flux of incident neutrons with energy E_n , and $\sigma(E_r, E_n)$ is the elastic scatter cross section of silicon.

This integral can be approximated as a trapezoidal sum over tabulated energy/spectrum neutron flux data $(E_{n,i}, I_i)$ (data arrays of length N , i.e., what is plotted in Figure 3.4):

$$\begin{aligned} n(E_r) &= \frac{1}{2m_{Si}} \sum_{i=0}^{N-2} [I_i \sigma(E_r, E_{n,i}) + I_{i+1} \sigma(E_r, E_{n,i+1})] (E_{n,i+1} - E_{n,i}) \\ &= \frac{1}{2m_{Si}} \left[I_0 \sigma(E_r, E_{n,0}) (E_{n,1} - E_{n,0}) \right. \\ &\quad \left. + I_{N-1} \sigma(E_r, E_{n,N-1}) (E_{n,N-1} - E_{n,N-2}) \right. \\ &\quad \left. + \sum_{i=1}^{N-2} I_i \sigma(E_r, E_{n,i}) (E_{n,i+1} - E_{n,i-1}) \right] \end{aligned} \quad (3.5.2)$$

The cross section data is taken from ENDF (Evaluated Nuclear Data File) data files [222]. In the ENDF files, the differential cross sections σ are represented as:

$$\sigma(\mu, E_n) = \frac{\mathcal{O}(E_n)}{2\pi} f(\mu, E_n) \quad (3.5.3)$$

where μ is the cosine of the center-of-mass-frame scattering angle and f is a probability distribution over μ , normalized such that

$$\int_{-1}^1 f(\mu, E_n) d\mu = 1 \quad (3.5.4)$$

$\mathcal{O}(E_n)$ is the total (angle-integrated) cross section, given in file 3 of the ENDF tapes. These are plotted in Appendix D. Interpolation laws are given directly, so values at arbitrary $E_{n,i}$ can be calculated. The values of $f(\mu, E_n)$ are given in file 4 of the ENDF tapes, and are read in using the `ENDFtk` code [223]. The rest of the data is read directly using evaluated plot files from the ENDF web interface or by reading the files directly in python [224].

The conversion between recoil energy E_r and μ is:

$$E_r = \alpha E_n (1 - \mu) \quad (3.5.5a)$$

$$\mu = 1 - \frac{E_r}{\alpha E_n} \quad (3.5.5b)$$

where $\alpha = 2A/(A + 1)^2$ for mass number A . So $f(\mu, E_n)$ is translated into a distribution over recoil energies $f(E_r, E_n)$ as:

$$f(E_r, E_n) = \frac{f(\mu, E_n)}{\alpha E_n} \quad (3.5.6)$$

so that now

$$\int_0^{2\alpha E_n} f(E_r, E_n) dE_r = 1 \quad (3.5.7)$$

where the maximum recoil energy for a given neutron energy is $2\alpha E_n$.

Interpolation laws for the $f(\mu, E_n)$ are also given in file 4 of the ENDF tape, so values of f at arbitrary μ and, hence, arbitrary E_r , can also be calculated. For Si, all interpolation laws are linear.

Thus, the spectrum can be calculated as:

$$\begin{aligned} n(E_r) = \frac{1}{4\pi\alpha m_{Si}} & \left[\frac{1}{E_{n,0}} I_0 \mathcal{O}(E_{n,0}) f(\mu_0, E_{n,0}) (E_{n,1} - E_{n,0}) \right. \\ & + \frac{1}{E_{n,N-1}} I_{N-1} \mathcal{O}(E_{n,N-1}) f(\mu_{N-1}, E_{n,N-1}) (E_{n,N-1} - E_{n,N-2}) \\ & \left. + \sum_{i=1}^{N-2} \frac{1}{E_{n,i}} I_i \mathcal{O}(E_{n,i}) f(\mu_i, E_{n,i}) (E_{n,i+1} - E_{n,i-1}) \right] \end{aligned} \quad (3.5.8)$$

where $\mu_i = 1 - E_r/\alpha E_{n,i}$ if $E_r < 2\alpha E_{n,i}$ and zero otherwise.

We evaluate the dru spectrum $n(E_r)$ on an energy grid of 15,000 values between 10^{-15} eV and 1.33 MeV (the maximum recoil energy that a 10 MeV neutron can cause in ^{28}Si). This extremely low lower bound is used to avoid spectral distortion of the low-energy signal that can happen when cutting off the evaluation at higher energies. The resulting recoil spectrum is plotted in Figure 3.5. The total scatter rate is 146.1 scatters $\text{kg}^{-1} \text{day}^{-1}$.

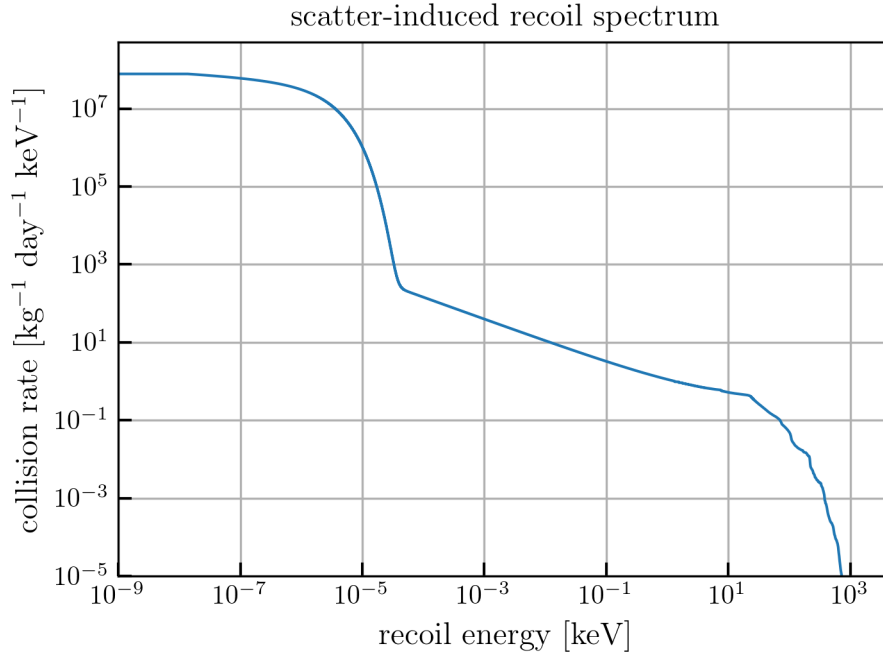


Figure 3.5: Neutron-scatter-induced recoil spectrum calculated via (3.5.8). The expected scatter rate is $146.1 \text{ kg}^{-1} \text{ day}^{-1}$. The spectrum continues almost completely flat down to the minimum energy, and drops nearly vertically to zero above one MeV.

3.6 Treatment of Multiple Scatters

The previous section introduced analytical methods to calculate recoil spectra and rates for neutron-induced events. However, those treatments did not account for the possibility that a neutron may interact more than once in the detector. This section introduces an analytical method for calculating the rates of scatter events associated with neutrons that scatter more than one time in the detector (“multiple scatters”). The next section does the same for captures. These two sections will conclude the “Analytical Convolution” step of Figure 3.1.

As stated before, the differential interaction rate per particle dr of incident neutrons in some energy bin centered at E_n with width dE_n that cause recoils in some energy bin of width dE_r centered at a recoil energy E_r is:

$$dr = I(E_n)\sigma(E_r, E_n)dE_r dE_n \quad (3.6.1)$$

where $I(E_n)$ is the incident neutron flux and $\sigma(E_r, E_n)$ is the elastic scatter cross section of the atoms in the detector.

We can parameterize this in terms of the energy of the neutrons *after* the scatter, $E'_n = E_n - E_r$:

$$dr = I(E_n)\sigma(E_n - E'_n, E_n)dE'_ndE_n \quad (3.6.2)$$

If we integrate over all incident neutron energies, we can then calculate $r(E'_n)$, the rate (per unit energy) at which neutrons scatter off of a detector particle and leave with a given energy E'_n :

$$r(E'_n) = \int_{E'_n}^{\infty} I(E_n)\sigma(E_n - E'_n, E_n)dE_n \quad (3.6.3)$$

where note the lower bound of the integration is $E_n = E'_n$, below which it is impossible for a neutron to have energy E'_n post-scatter.

We now treat each particle in the detector as a neutron emitter. Given some (approximately) spatially-uniform incident neutron flux, every so often a neutron will scatter off a detector atom, dropping from energy E_n to E'_n , appearing as though the atom emitted a neutron with energy E'_n in a random direction. Since this $r(E'_n)$ is then the total ‘emission rate’ from each atom, then the flux $i'(E'_n)$ of neutrons ‘emitted’ by the atom is

$$i'(E'_n) = \frac{r(E'_n)}{4\pi\varrho^2} \quad (3.6.4)$$

where ϱ is the distance from the emitter. The total flux $I'(E'_n, \mathbf{x})$ at a location \mathbf{x} is then $i'(E'_n)$ integrated over all the atoms in the detector:

$$I'(E'_n, \mathbf{x}) = \rho_n \int_V \frac{r(E'_n)}{4\pi|\mathbf{x} - \mathbf{x}'|^2} d\mathbf{x}' \quad (3.6.5)$$

where $\rho_n = N/V$ is the number density of atoms in the detector.

This “second flux” of neutrons will cause yet more scatters in the detector (and captures, see next section). In order to calculate the rate of these second scatters, we use a formula proportional to (3.5.1) for the rate per unit energy $N(E_r)$ of (first-) scatters in the detector that cause recoils of energy E_r :

$$N(E_r) = N \int_0^\infty I(E_n) \sigma(E_r, E_n) dE_n \quad (3.6.6)$$

As written, this equation assumes a spatially uniform neutron flux density $I(E_n)$. However, if the neutron flux did vary with position \mathbf{x} , i.e., $I = I(E_n, \mathbf{x})$, we would now need to integrate over the volume V of the detector:

$$N(E_r) = \rho_n \int_0^\infty \sigma(E_r, E_n) \int_V I(E_n, \mathbf{x}) d^3\mathbf{x} dE_n \quad (3.6.7)$$

We can plug in our second flux $I'(E_n, \mathbf{x})$ to get the rate per unit energy of second scatters $N_2(E_r)$:

$$\begin{aligned} N_2(E_r) &= \rho_n \int_0^\infty \sigma(E_r, E_n) \int_V I'(E_n, \mathbf{x}) d^3\mathbf{x} dE_n \\ &= \rho_n^2 \int_0^\infty \sigma(E_r, E_n) r(E_n) dE_n \iint \frac{1}{4\pi|\mathbf{x} - \mathbf{x}'|^2} d^3\mathbf{x}' d^3\mathbf{x} \\ &= \rho_n \left[\frac{1}{V} \iint \frac{1}{4\pi|\mathbf{x} - \mathbf{x}'|^2} d^3\mathbf{x}' d^3\mathbf{x} \right] N \int_0^\infty \sigma(E_r, E_n) r(E_n) dE_n \end{aligned} \quad (3.6.8)$$

where in the last line we've separated out the term in brackets as the only part of this expression that depends on the detector geometry. As written, this quantity is a length which we call the ‘‘characteristic length’’ ℓ , roughly equal to the thickness of a disk with radius $2|\mathbf{x} - \mathbf{x}'|$ and volume V , averaged over all pairs of points $(\mathbf{x}, \mathbf{x}')$ in the detector. This integral is nontrivial to evaluate (see Appendix E), but numerical evaluation for the HVeV dimensions given in [205] (1 cm \times 1 cm \times 4 mm) yields a value of 0.307784 cm.

With this, we can define an effective ‘‘second flux’’ of neutrons, $I_2(E_n)$:

$$I_2(E'_n) \equiv \rho_n \ell r(E'_n) = \rho_n \ell \int_{E'_n}^\infty I(E_n) \sigma(E_n - E'_n, E_n) dE_n \quad (3.6.9)$$

and the rate of second scatters takes a familiar form:

$$N_2(E_r) = N \int_0^\infty I_2(E_n) \sigma(E_r, E_n) dE_n \quad (3.6.10)$$

We can generalize this result to the i^{th} scatter by realizing the i^{th} flux only depends on the $(i - 1)^{\text{th}}$ flux. The rate of i^{th} scatters $N_i(E_r)$ is:

$$N_i(E_r) = N \int_0^\infty I_i(E_n) \sigma(E_r, E_n) dE_n \quad (3.6.11)$$

where $I_i(E_n)$ is the “ i^{th} flux:”

$$I_i(E_n) = \rho_n \ell \int_{E_n}^\infty I_{i-1}(E'_n) \sigma(E'_n - E_n, E'_n) dE'_n \quad (3.6.12)$$

for $i > 1$, and $I_1(E_n)$ is the original ambient neutron flux $I(E_n)$.

For a medium with multiple isotopes j with cross sections σ_j and isotopic abundances p_j , we need a sum:

$$I_i(E'_n) = \rho_n \ell \sum_j p_j \int_{E'_n}^\infty I_{i-1}(E_n) \sigma_j(E_n - E'_n, E_n) dE_n \quad (3.6.13a)$$

$$N_i(E_r) = N \sum_j p_j \int_0^\infty I_i(E_n) \sigma_j(E_r, E_n) dE_n \quad (3.6.13b)$$

The total resulting scatter spectrum can then just be calculated the usual way using an effective flux $I_{eff}(E_n) = \sum_i I_i(E_n)$.

The first six i^{th} fluxes $I_i(E_n)$ are plotted in Figure 3.6. Each successive set of fluxes is reduced by a factor of ~ 50 . It can also be seen that the spectrum is skewed toward lower energies at higher i . Note that the sharp drop in the flux spectrum at 10 keV is caused by numerical issues at a discontinuous change in the density of points on the neutron-energy grid. The effect of this instability is a $\sim 0.04\%$ underestimation of the rate, and is neglected. It does not appreciably change the resulting recoil spectrum shape (tested via manually “fixing” the discontinuity). The tooth-shaped dip near 100 keV, on the other hand, can be explained by physical reasons. There is a wide resonance trough in the cross section near this energy, which causes a sharp drop in particle interactions in this neighborhood (see Appendix D).

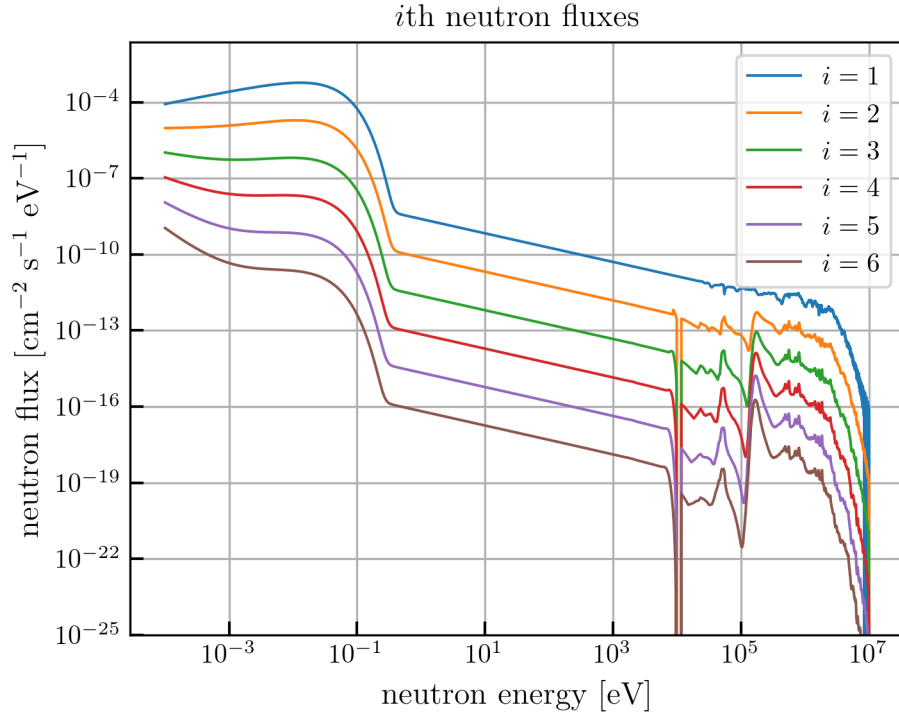


Figure 3.6: First six i^{th} fluxes $I_i(E_n)$.

The i^{th} recoil spectra $N_i(E_r)$ corresponding to these flux spectra are plotted in Figure 3.7. Once again, each spectrum is scaled by about 10^{-2} and skewed slightly toward lower energies. Note the total resulting fluxes and recoil spectrum are visually indistinguishable from the first scatter flux/recoil spectrum. Table 3.2 gives the total i^{th} scatter rates and the proportion of incident scatters. The first five subsequent scatters ($i = 2$ to 6) add approximately 3.83% to the total scatter rate. Beyond $i = 6$, the effects become smaller than one part in 2×10^7 and are neglected.

Table 3.2: Total i^{th} scatter rates up to $i = 6$. Proportions of the initial incident scattering rate given in the third column

| i | Scatter rate [$\text{kg}^{-1} \text{ day}^{-1}$] | Percent of first scatters |
|-------|--|---------------------------|
| 1 | 146.09 | 100.0000% |
| 2 | 5.3344 | 3.6515% |
| 3 | 0.24166 | 0.1654% |
| 4 | 0.014646 | 0.0100% |
| 5 | 0.0011013 | 0.0008% |
| 6 | 8.9144e-05 | 0.0001% |
| total | 151.68 | 103.8277% |

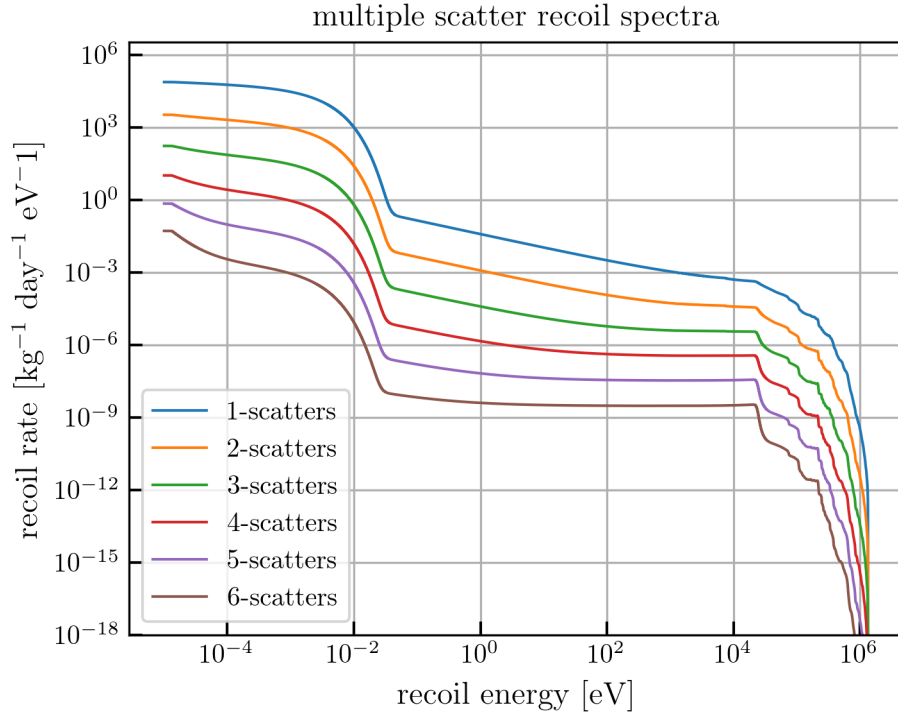


Figure 3.7: Recoil energy spectra for first six scatters.

3.6.1 Capture as second interaction

A process related to that of multiple scatters is where a post-scatter neutron is then captured by a silicon atom (“second captures”). In this section, the rate of second- and beyond captures will be calculated. This is the final step in the “Analytical Convolution” phase of Figure 3.1.

Calculating the rate of second captures is simpler than the calculation of second (and beyond) scatters since the neutron capture cross section only depends weakly on the neutron energy and so can be treated as a constant. The average capture cross section of Si was given in Section 2.3 as 0.171 barns. The corresponding macroscopic cross section Σ is 0.0085 cm^{-1} .

The probability that a thermal neutron passing a distance Δx through the detector is captured is $1 - e^{-\Sigma\Delta x}$. To calculate the rate that neutrons are captured after scattering, we then just need to calculate the average value of $1 - e^{-\Sigma\Delta x}$ for all initial points inside the detector and all possible (assumed straight-line) outgoing trajectories. We perform a direct Monte Carlo (MC) simulation of this process by randomly generating 10^7 positions and trajectories in the detector volume. To simplify calculations, the length Δx

of each outgoing straight-line path was calculated by a simple stepping algorithm accurate to the nearest 10^{-15} cm.²⁸ The resulting probability of capturing is

$$p = 0.24889\% \pm 0.00008\% \quad (3.6.14)$$

The uncertainty in this value is calculated via the formula for uncertainty in a Monte-Carlo integral given by [225]:

$$\int f dV = V \langle f \rangle \pm V \sqrt{\frac{\langle f^2 \rangle - \langle f \rangle^2}{N}} \quad (3.6.15)$$

where the angle brackets denote the average over the MC sample, and N is the number of points in the sample.

Note that since the probabilities in question are so low, several approximations yield effectively identical results. The different approximate formulas are given in Table 3.3, along with the resulting values for an MC sample of 10^7 events. Once again, the angle brackets denote arithmetic mean over the generated sample of positions/trajectories. Absolute uncertainties are given in parentheses in the middle column. It can be seen the values are all extremely similar, differing only in the sixth decimal place. Note the second row uses the same approximation as was used in Section 2.8 for the probabilities of gamma anticoincidence vetoes (there $\langle \Delta x \rangle$ was referred to as \bar{d}). Note also that the calculated value of $\langle \Delta x \rangle$ was ≈ 0.2937 cm.

Table 3.3: Comparison of methods for calculating the probability of second captures

| Formula | Value (%) |
|--|------------|
| $\langle 1 - \exp(-\Sigma \Delta x) \rangle$ | 0.24889(8) |
| $1 - \exp(-\Sigma \langle \Delta x \rangle)$ | 0.24916(8) |
| $\Sigma \langle \Delta x \rangle$ | 0.24947(8) |

Thus, approximately 0.25% of neutrons leaving scatters with thermal energies will be captured. The total capture rate per particle is

²⁸The algorithm involves the steps: (1) step along path (2) check if still inside detector (3) if so, step again (4) if not, step back and halve step length (5) repeat

$$\begin{aligned}
& \int_0^{5 \text{ eV}} \left[I(E_n) \mathcal{O}_c + 10^{-3} \sum_{i=1}^{\infty} \left(\int_{E_n}^{\infty} I_i(E'_n) \sigma(E'_n - E_n, E'_n) dE'_n \right) \right] dE_n \\
& = \int_0^{5 \text{ eV}} \left[I(E_n) \mathcal{O}_c + (2.5 \times 10^{-3}) \sum_{i=2}^{\infty} \frac{I_i(E_n)}{\rho_n \ell} \right] dE_n
\end{aligned} \tag{3.6.16}$$

where \mathcal{O}_c is the total capture cross section, and the $I_i(E_n)$ are the i^{th} fluxes defined in the previous section. Note $E = 5 \text{ eV}$ was the maximum energy considered to contribute to the capture rate in Section 3.5.1. As with scatters, we neglect $i > 6$ (terms beyond $i = 6$ contribute less than one part in 9×10^8 to the capture rate). This yields a modified capture rate of $10.087 \text{ captures kg}^{-1} \text{ day}^{-1}$, a 2.983% increase.

Table 3.4: i^{th} capture rates and rates relative to initial capture rate

| i | Capture rate [$\text{kg}^{-1} \text{ day}^{-1}$] | Percent original |
|----------|--|------------------|
| original | 9.7946 | 100.0000% |
| 2 | 0.28315 | 2.8909% |
| 3 | 0.0087262 | 0.0891% |
| 4 | 0.00027232 | 0.0028% |
| 5 | 8.6962e-06 | 0.0001% |
| 6 | 2.9016e-07 | 0.0000% |
| total | 10.087 | 102.9828% |

3.7 Ionization Model

This section presents the ionization model used to approximate HVeV detector response to a given recoil spectrum. The ionization model will give the probability distribution for the number of e/h pairs produced by a recoil of a given energy. While the HVeV detectors don't measure this ionization directly, the process of NTL phonon amplification makes the process of ionization, particularly at low energies, extremely important for predicting detector response to a given spectrum of recoil energies. The ionization model will allow us to convert a sample of recoil energies into a sample of ionizations (numbers of produced e/h pairs), allowing a prediction for the energy spectrum measured by the detector.

Unlike the calculation of the recoil spectrum outlined in the previous two sections, this ionization model relies on MC methods. Once the recoil spectrum has been calculated, recoil events are sampled and the ionization caused by each event is calculated. A detailed description of the simulation process is given in Section 3.8.

The model described in this section is referred to as the Alig-Lindhard (AL) model, and combines two separate models of ionization in semiconductors from the literature, the Lindhard model and the Alig model. These models are described briefly below.

3.7.1 Lindhard model

The *Lindhard model* [226] is one of the most widely-used models of ionization in the literature. Published in 1963, it was one of the first theoretical treatments of “damage effects” (a generic term for the consequences of collisions in an atomic lattice) that considered the relative amounts of energy transferred to electrons and to nuclei. This thus represents one of the first “ionization models” in the literature.

This model is derived using approximate general formulas for cross sections in arbitrary materials. Integral formulas describing the distributions of arbitrary physical quantities averaged over a set of possible collisions are derived, and successive approximations applied to allow evaluation of the integral formulas. These approximations are:

- (A) Recoiling electrons do not transfer energy into atomic nuclei; once energy is transferred to the electron system, it stays there
- (B) The atomic binding energy ($O(\text{eV})$) is negligible compared to typical energies transferred to the atomic lattice
- (C) Energy transferred to the electrons is small compared to the final energy of the incident particle
- (D) Nuclear and electronic collisions are uncorrelated, and the overlap between electron/nucleus and electron/electron interactions is small
- (E) The energy lost to atomic collision by the incident particle is small compared to its initial energy

They calculate solutions to approximations (D) and (E) for the yield numerically, and approximate the asymptotic behavior of approximation (D) with an analytic function of the form given below. The yield Y_L is the proportion of energy given to electrons, E_r is the initial recoil energy, Z is the atomic number, and k is a constant of proportionality appearing in the nucleus-nucleus cross section. The value of k is taken to be 0.15, approximately the theoretical value for silicon (used by, e.g., [227]). The model equations are:

$$Y_L(E_r) = \frac{kg(\epsilon)}{1 + kg(\epsilon)} \quad (3.7.1a)$$

$$g(\epsilon) = 3\epsilon^{0.15} + 0.7\epsilon^{0.6} + \epsilon \quad (3.7.1b)$$

$$\epsilon(E_r) = 11.5Z^{-7/3}E_r \quad (3.7.1c)$$

where in the last equation, E_r is in keV. This form for $g(\epsilon)$ is given by [172] as a good fit for Lindhard's numerical calculation of the function. This form is commonly used in the literature, see, e.g., [126, 228–230].

For a recoil energy E_r , the electron-equivalent energy is $E_{ee} = E_r Y_L(E_r)$. The number of e/h pairs produced n_{eh} is related to this energy by the constant ϵ_γ , the average energy required to ionize a single e/h pair: $n_{eh} = E_{ee}/\epsilon_\gamma$. A value of $\epsilon_\gamma = 3.8$ eV is common in the literature (see, e.g., [130, 171, 203, 206]), though this value has been measured to fluctuate with temperature and recoil energy (see [231]).

Figure 3.8 shows the Lindhard ionization energy $E_{ee} = E_r Y_L(E_r)$ as a function of recoil energy E_r . It can be seen that Y_L increases slowly from zero to about 0.2 at a recoil energy of 1 keV.

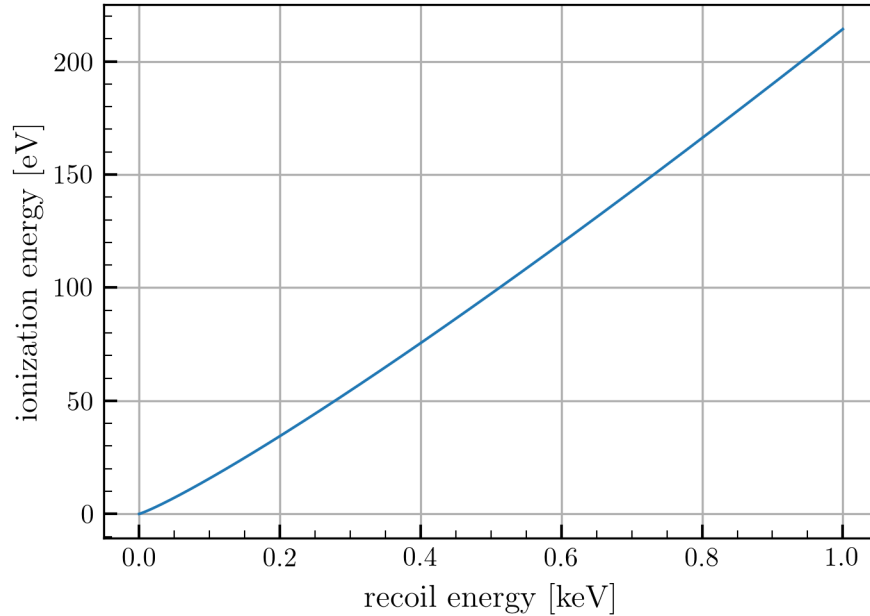


Figure 3.8: Ionization energy vs. recoil energy according to the Lindhard model with $k = 0.15$

The Lindhard model also gives predictions for the variance in the ionization yield as a function of energy. A common way to parameterize this variance is through the *Fano factor*, defined as the ratio

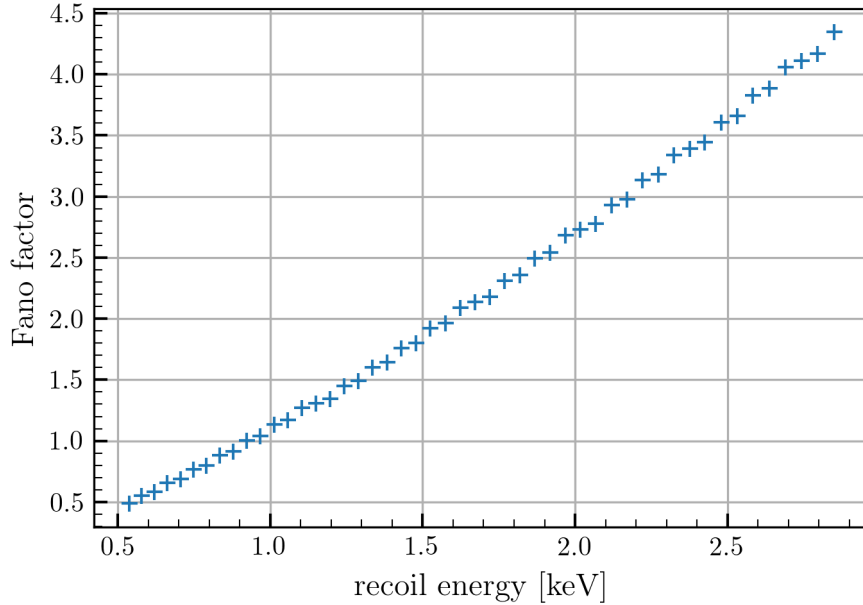


Figure 3.9: Fano factor vs recoil energy data extracted from Lindhard model approximation (D) (provided by A. Villano)

of the true variance σ_n^2 in the number of e/h pairs produced to the variance expected from a Poisson-distributed process (which is just the mean, \bar{n}):

$$F = \frac{\sigma_n^2}{\bar{n}} \quad (3.7.2)$$

The Fano factor gives a measure of the inherent variability associated with generic collision-induced ionizations. The Lindhard-model calculations of the variance in Y_L for approximation (D) are given in Figure 7 in [226]. It is possible to scrape this data visually using a tool such as DataThief [232] and from it calculate the Fano factor. Data retrieved this way was provided by Anthony Villano. The data is shown in Figure 3.9.

The Lindhard model has been shown to agree with experiment at moderately high energy [233–236]. However, more recent measurements show a breakdown in accuracy at lower (sub-keV_{ee}) energies [126, 227, 237–240]. There are several proposed reasons for this breakdown, mostly involving the approximations (A)–(E). In particular, (B) though (E) are valid of higher-velocity incident particles, but stop holding at lower energies. A slightly-modified model was proposed by [229] to correct approximation (B) and account for the atomic binding energy, and a generalization allowing k to vary with energy was used by [126], both with moderate improvement to the low-energy accuracy. However, these alternative models are

still in stages of infancy. Furthermore, average and variance data about the ionization yield is not sufficient to simulate the production of e/h pairs, particularly at lower energies. A more complete description is required.

3.7.2 Alig model

In order to fully simulate the ionization of individual e/h pairs, we need an ionization model that gives full distribution information. One such model is the *Alig model* [241], a statistical model for the ionizing power of ballistic (high-energy) electrons in semiconductors developed in 1980. Its main premise is that a fast-moving electron traversing a semiconductor scatters against other electrons in two ways: either it hits an electron hard enough to ionize (“scattering by ionization”, “impact ionization”) or it doesn’t, and the impact energy is dissipated in the form of phonons (“phonon scattering,” “scattering by phonon production,” “producing phonons,” etc.).²⁹

The Alig model calculates two sets of probability distributions. The first, denoted $P_m(E)$, gives the probability that an incident electron of energy E will produce m phonons before scattering by ionization. The second is denoted $p_n(E)$ and is the probability that an electron of energy E will eventually be the cause of n ionized e/h pairs. This is the distribution of interest, that allows for the simulation of e/h pair production due to an incident electron of a given energy.

The authors make a few starting assumptions in developing the model. First is that functionally, electrons and holes can be treated identically. This is an important leap, as it allows for a recursive construction of the mechanics that is central to the model. Second, the band structure of the semiconductor is taken to be parabolic and isotropic above and below the band gap (the gap in energies between valence and conduction energy levels), i.e., that electrons in valence and conduction bands can move in any direction equally and that their energy scales as the square of their momentum. Essentially, this means the electrons are treated as free particles. The density of states of a free particle with energy E is:

$$\rho(E) = \left(\frac{V}{2\pi^2}\right) \left(\frac{2m}{\hbar^2}\right)^{3/2} \sqrt{E} \quad (3.7.3)$$

where V is the total volume of the semiconductor and m is the (vacuum) mass of the electron. This approximation eliminates small corrections due to limiting electrons and holes to a discrete set of states, and

²⁹Alig and collaborators don’t technically specify that the initial incident particle need be an electron. However, several assumptions made in the treatment assume charge, mass, cross section., etc., of the incident particle are the same as the electrons and holes. Thus, we consider the model to apply to incident ballistic electrons.

greatly simplifies calculations. Related, it is also assumed that all states not forbidden by energy conservation are equally accessible.

It is also assumed that initial and final trajectories are uncorrelated, so the momenta of particles following any scatter are equally distributed over 4π steradians (this is called the “random- k ” approximation; this is almost, but not quite, the approach recommended by [242] for reasons of computational efficiency). This technically allows for momentum conservation to be violated in individual scattering events, but on average this effect should not be appreciable. The authors specify that the more important place to account for momentum conservation is in the calculation of the threshold energies for ionization events (see (3.7.14) below).

Last, it is assumed that the phonons produced by collisions are monoenergetic optical phonons, that is, all the phonons have the same energy $\hbar\omega_0$ and, as opposed to acoustic phonons, they do not dissipate. This approximation is generally justified at most energies and in large ambient electric fields, as is the case here, though may begin to break down at lower energies [198].

The model begins by considering the rate at which the incident electron scatters by either process. The rate $\gamma(E)$ of scattering by ionization is

$$\begin{aligned}\gamma(E) &= \frac{2\pi}{\hbar} \frac{\Delta}{V} |M|^2 \int dE_e \int dE_h \rho(E_e) \rho(E_h) \rho(E - E_g - E_e - E_h) \\ &= \frac{2\pi}{\hbar} |M|^2 \frac{V^2 \Delta}{8\pi^6} \left(\frac{2m}{\hbar^2}\right)^{9/2} \frac{2\pi(E - E_g)^{7/2}}{105}\end{aligned}\tag{3.7.4}$$

for $E > E_{th}$, the minimum energy required to ionize (if $E < E_{th}$, $\gamma(E) = 0$). Here, M is the matrix element of the Coulomb interaction,³⁰ Δ is the volume per electronic state, and V is the total volume of the semiconductor. E_g is the band gap energy, in silicon taken to be 1.17 eV [243]. The subscripts e and h denote the ionized electron and hole, respectively, and the integration takes place over the region $E_e + E_h \leq E - E_g$. The value of the integral can be interpreted as the total number of final states of the combined incident particle/electron/hole system that has a total energy of $E - E_g$.

³⁰For the uninitiated, a “matrix element” in quantum mechanics is a measure of how strongly an interaction influences a transition from one state to another. Very roughly, the matrix element of an interaction measures the magnitude of the final state projected onto the interacted-with initial state (the initial state operated on by the potential energy operator of the interaction).

On the other hand, the rate of phonon scattering $\gamma'(E)$ is:

$$\begin{aligned}\gamma'(E) &= \frac{2\pi}{\hbar} |M'|^2 \rho(E - \hbar\omega_0) \\ &= \frac{2\pi}{\hbar} |M'|^2 \frac{V}{2\pi^2} \left(\frac{2m}{\hbar^2}\right)^{3/2} \sqrt{E - \hbar\omega_0}\end{aligned}\tag{3.7.5}$$

where M' is the matrix element for phonon scattering.

Based on the relative rates of each interaction, we can calculate the probability of either interaction happening first. The probability that the incident particle scatters by ionization first, which is just $P_0(E)$, is

$$P_0(E) = \frac{\gamma(E)}{\gamma(E) + \gamma'(E)} = [1 + \gamma'(E)/\gamma(E)]^{-1}\tag{3.7.6}$$

The probability that the particle produces m phonons and then scatters by ionization is

$$P_m(E) = [1 - P_0(E)] P_{m-1}(E - \hbar\omega_0)\tag{3.7.7}$$

that is, the probability that the particle produces a phonon first $[1 - P_0(E)]$ times the probability the particle, now with energy $E - \hbar\omega_0$, creates $(m - 1)$ more phonons before scattering by ionization, $P_{m-1}(E - \hbar\omega_0)$.

To calculate $P_0(E)$, the ratio $\gamma'(E)/\gamma(E)$ is parameterized as:

$$\frac{\gamma'(E)}{\gamma(E)} = A \frac{105}{2\pi} \frac{(E - \hbar\omega_0)^{1/2}}{(E - E_g)^{7/2}}\tag{3.7.8}$$

where the parameter A is defined as:

$$A = \frac{|M'|^2}{|M|^2} \frac{4\pi^4}{V\Delta} \left(\frac{\hbar^2}{2m}\right)^3\tag{3.7.9}$$

and is assumed to be a constant. An order-of-magnitude estimate of A based on the approximate magnitude of the matrix elements [244, 245] yields a value of $O(1)$ eV. They fit a value of $A = 5.2 \text{ eV}^3$ based on the resulting pair-creation energies in silicon (ϵ_γ).

The sum of $P_m(E)$ over all m is the probability that the particle creates any number of phonons before scattering by ionization. The residual probability is the odds that the particle never scatters by ionization at all, $p_0(E)$:

$$p_0(E) = 1 - \sum_{m=0}^{\infty} P_m(E) \quad (3.7.10)$$

Now, in order to produce n e/h pairs, either a particle produces a phonon first (with probability $[1 - P_0(E)]$) and then goes on to produce n e/h pairs (with probability $p_n(E - \hbar\omega_0)$), or the particle creates an e/h pair first (probability $P_0(E)$), and the three resulting particles will go on to produce a total of $(n - 1)$ further e/h pairs. The probability of this latter occurrence is the ratio of the rate of ionizations where all the ionized particles produce $(n - 1)$ e/h pairs to the total ionization rate,

$$\frac{\gamma_{n-1}(E)}{\gamma(E)} \quad (3.7.11)$$

where $\gamma_{n-1}(E)$ is the rate of scattering by ionization reduced by the probability the final particles produce $(n - 1)$ e/h pairs:

$$\begin{aligned} \gamma_{n-1}(E) = & \\ \frac{2\pi}{\hbar} \frac{\Delta}{V} |M|^2 \sum_{i,j} \int dE_e \int dE_h \rho(E_e) \rho(E_h) \rho(E - E_g - E_e - E_h) p_i(E_e) p_j(E_h) p_{n-1-i-j}(E_f) & \end{aligned} \quad (3.7.12)$$

(c.f. eq. (3.7.4)). The sum over i runs from 0 to $(n - 1)$, and the sum over j runs from 0 to $(n - 1 - i)$. The ratio $\gamma_{n-1}(E)/\gamma(E)$ can be calculated as:

$$\frac{\gamma_{n-1}(E)}{\gamma(E)} = \frac{105}{2\pi(E - E_g)^{7/2}} \int dE_e \int dE_h \sqrt{E_e E_h (E - E_g - E_e - E_h)} \sum_{i,j} p_i(E_e) p_j(E_h) p_{n-1-i-j}(E_f) \quad (3.7.13)$$

$\gamma_{n-1}(E)$ is zero below a threshold energy $E_{th,n}$, calculated as:

$$E_{th,n} = 5E_{th,n-1} + 2E_g - 4\sqrt{E_{th,n-1}^2 + \frac{1}{2}E_g E_{th,n-1}} \quad (3.7.14)$$

with $E_{th,1} = E_{th}$ (mentioned above) equal to $3E_g/2$. This set of threshold energies accounts for both required energy conservation and momentum conservation during an ionizing collision.

The probability an incident particle creates n pairs is then

$$p_n(E) = P_0(E) \frac{\gamma_{n-1}(E)}{\gamma(E)} + [1 - P_0(E)]p_n(E - \hbar\omega_0) \quad (3.7.15)$$

This formula was implemented in a C++ script to evaluate $p_n(E)$ on an energy grid E_k of energies spaced evenly by $\hbar\omega_0$ from 0 to 189 eV (k from 0 to 2,999), for n up to 75.³¹ Several methods were tried to evaluate the integral (3.7.13). The first involved a simple rectangular integration on an evenly-spaced grid of points in the (E_e, E_h) plane (a square grid cut in half on the diagonal).³² However, it was found this method converged extremely slowly and required $\sim 300,000$ points to approximate the integrals with sufficient precision. On the other hand, direct Monte Carlo (MC) integration converged extremely quickly, reaching satisfactory convergence with only 2,500 points. Note that the calculation of the $p_n(E)$ is $O(N^3 K N_{eval})$ where N_{eval} is the number of points used in evaluating the integral (3.7.13), K is the number of energy values E_k , and N is the maximum value of n .

Figures 3.10 and 3.11 show the calculated values of $p_n(E)$. Figure 3.10 is the first few pair production probability peaks, $p_n(E)$, as a function of E , and Figure 3.11 is a heatmap of the full pair-production data calculated.

³¹The first implementation was in a Jupyter notebook, but it was found the C++ implementation was several orders of magnitude faster

³²An earlier method, that used the evaluated energy points E_k as the grid points, is not worth mentioning.

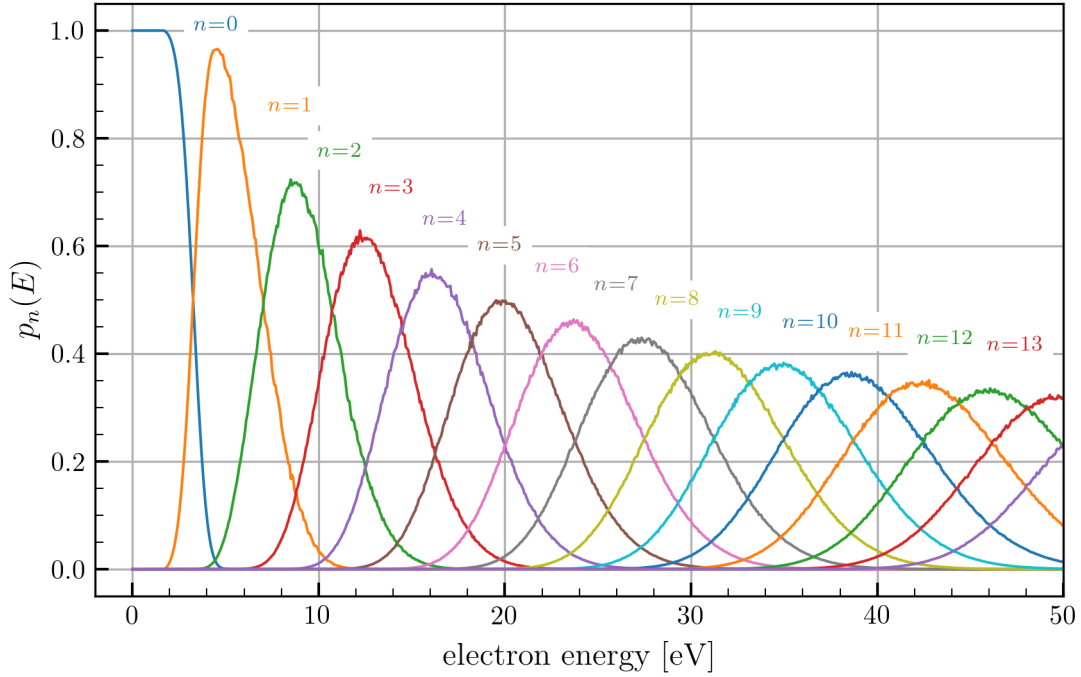


Figure 3.10: First several pair-production probability curves $p_n(E)$ from the Alig model

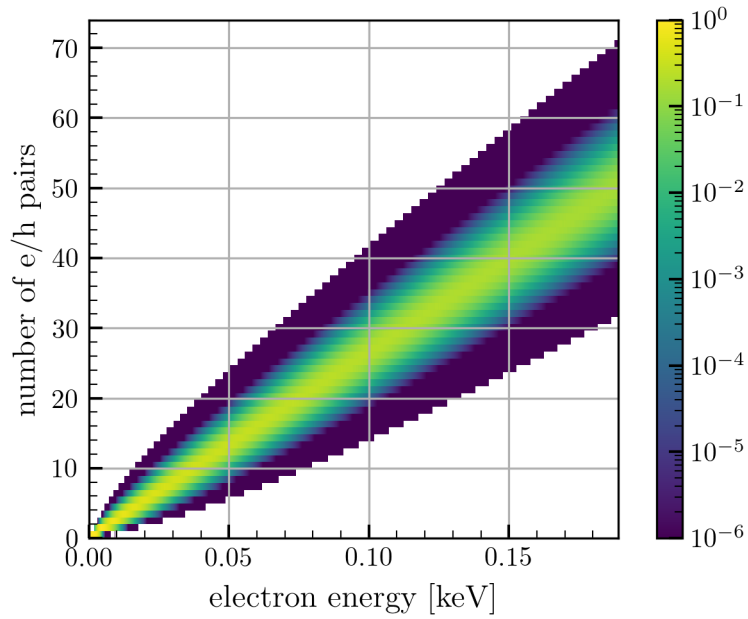


Figure 3.11: Full Alig-model e/h pair production probability data $p_n(E)$, evaluated at 3,000 energies between 0 and 189 eV for n up to 75. Values smaller than 10^{-6} have been masked out.

Figures 3.12 and 3.13 illustrate the convergence of the MC and grid-based methods. Figure 3.12 shows $p_n(E)$ vs E data calculated with both the MC and the grid method. The grid method curves ap-

proach the MC-calculated curves slowly as the number of points on the grid increases. Figure 3.13 shows the gradual convergence of the grid-based method more clearly. The quantity plotted is $p_{n,MC}(E) - p_{n,m}(E)$, where $p_{n,MC}(E)$ is $p_n(E)$ calculated using a MC method with 25,000 points (25kMC), and $p_{n,m}(E)$ is $p_n(E)$ calculated with method m . The grid-based methods are all systematically smaller than the MC methods, while the 2,500-point MC method is not significantly different from the 25kMC method at the 90% level. This 90% value is calculated by fitting a gaussian to the 25kMC data for each value of n and calculating the variance of the 25kMC data about the fitted gaussian. The variance of the other data sets about the fitted gaussian are also calculated, and a Z -value is calculated as

$$Z = \frac{\langle \Delta p_m \rangle}{\sqrt{\sigma_m \sigma_{MC}}} \quad (3.7.16)$$

where Δp_m is the difference between the $p_{n,m}(E)$ data (calculated with method m) and the gaussian fitted to the 25kMC data, σ_m is the standard deviation of the Δp_m and σ_{MC} is the standard deviation of the Δp_{25kMC} data. The angle brackets denote an arithmetic mean. This is a very rough Z-test estimate, and the largest associated P -value for the 2,500-point MC data (for $n \leq 13$, beyond which the fits become much less reliable³³) is $\sim 7\%$. In contrast, the 70×70 grid data reached 94% and the 750×750 grid data reached 47%. The 25kMC data itself had a peak value of 14%.

³³Note the convergence-testing data was only calculated for energies up to 50 eV and n up to 25

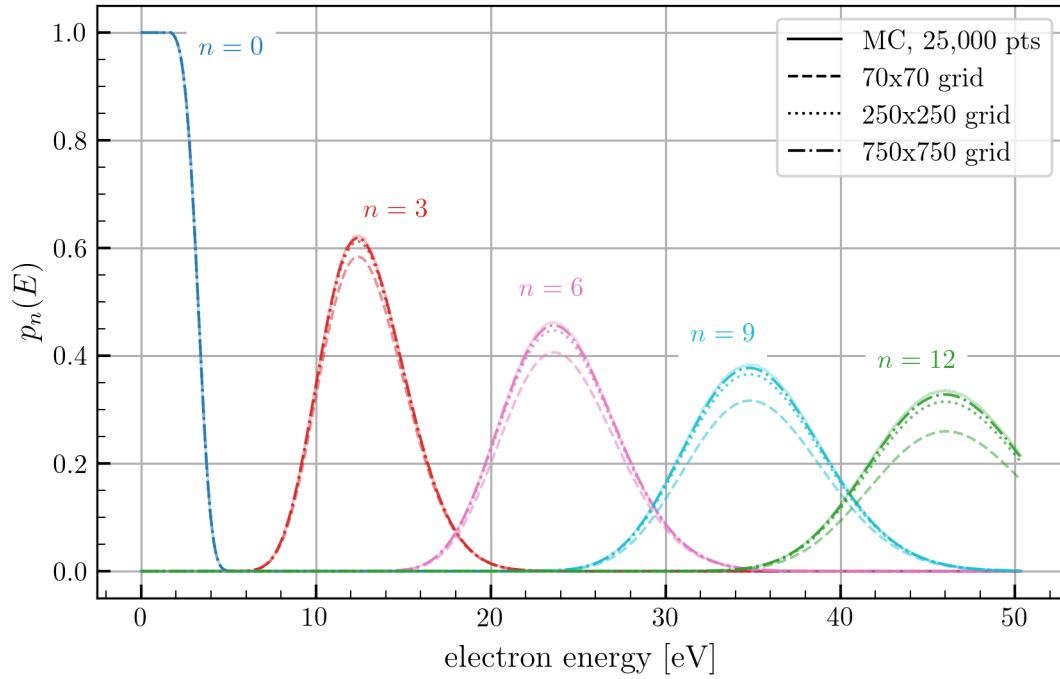


Figure 3.12: Alig model probabilities for $n = 0, 3, 6,$ and 9 calculated by several integration methods. Even on a 750×750 grid, the values are noticeably and systematically smaller than the MC method. Discrepancies are negligible for $n = 0$ and worsen with growing n . Note the 25kMC curve is semi-transparent

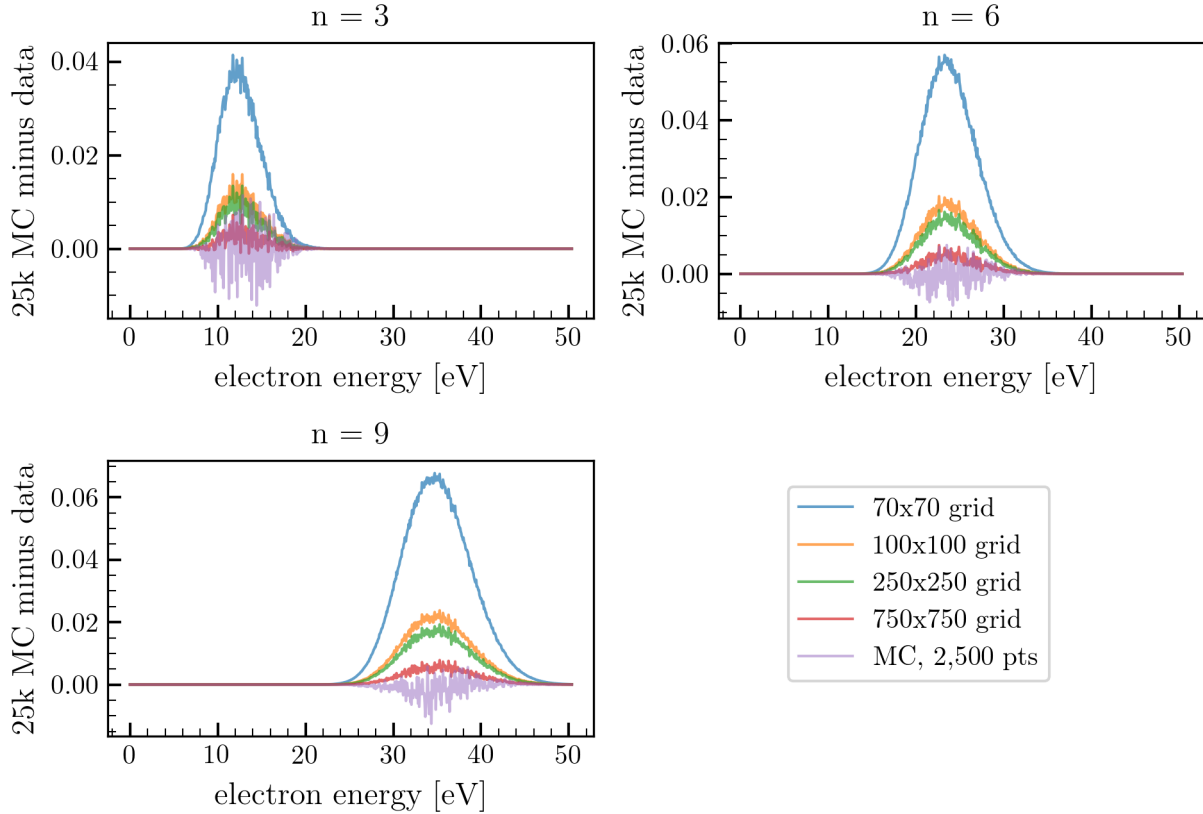


Figure 3.13: The difference between Alig-model peaks calculated by MC method with 25,000 points vs. several other integration methods. Grid-based methods converged very slowly, but the MC method with 2,500 is consistent with the 25,000-point MC method up to statistical fluctuations at the 90% level

Note for all the integration methods discussed above, the values of $p_n(E)$ at evaluated points ($E_e, E_h, E_g - E_e - E_h$) were calculated by linear interpolation of the nearest points on the energy grid E_k .

3.7.3 Putting it together: the Alig-Lindhard model

The combined Alig-Lindhard (AL) model presented here combines the distribution information from the Alig model with the yield information from the Lindhard model. The model can be stated very succinctly: we treat a recoiling nucleus as an “effective electron” in the Alig model with a reduced effective energy given by the Lindhard ionization yield. That is, for a recoil energy E_r , the probability distribution $\hat{p}_n(E_r)$ for producing n e/h pairs is:

$$\hat{p}_n(E_r) = p_n(E_r Y_L(E_r)) \quad (3.7.17)$$

with $p_n(E)$ from the Alig model and $Y_L(E)$ from the Lindhard model.

To calculate values for a particular recoil energy, we interpolate to $E_r Y_L(E_r)$ from the nearest energy values on the energy grid E_k . A few resulting pair-probability distributions $\hat{p}_n(E_r)$ as a function of n are plotted in Figure 3.14

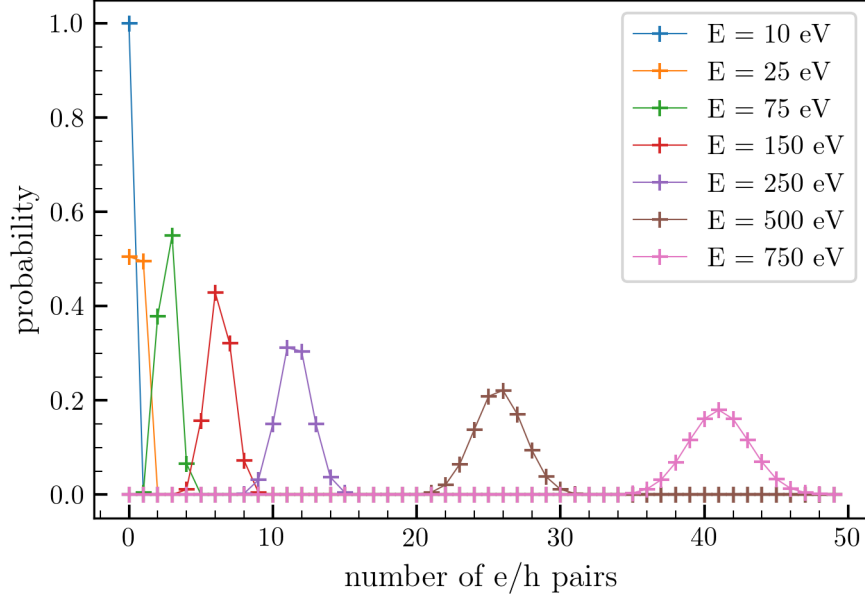


Figure 3.14: Distributions $\hat{p}_n = \hat{p}_n(E_r)$ for several recoil energies

3.7.3.1 Higher-energy recoils

This method works for recoil energies below ≈ 896 eV. Above that, $E_r Y_L(E_r)$ is larger than the upper bound of the energy grid used to calculate the $p_n(E)$, 189 eV. However, at higher energies the Alig model distributions $p_n(E)$ begin to take a Gaussian form (see Appendix F). Therefore, we can approximate the \hat{p}_n as Gaussians with means given by the Lindhard value $E_r Y_L(E_r)/\epsilon_\gamma$. However, we cannot use the variances suggested by the Alig model gaussian fits, as they correspond to the constant electron Fano factor, while for nuclear recoils the Fano factor is expected to increase with increasing energy. Thus we use the Lindhard-model Fano factor data plotted in Figure 3.9. A resulting heatmap of $\hat{p}_n(E_r)$ for recoil energies up to 2 keV is shown in Figure 3.15. The average e/h pairs produced, $E_r Y_L(E_r)/\epsilon_\gamma$, is plotted as a red curve.

The transition between the evaluated $p_n(E)$ data and the Gaussian approximation is obvious in Figure 3.15. The width of the distributions \hat{p}_n increases discontinuously. We expect that the Lindhard Fano factor used for $E_r > 896$ eV is more accurate than the Fano factor resulting at energies below 896 eV. This represents a systematic underestimation of the Fano factor at those lower recoil energies. This is discussed further in Section 3.10.7

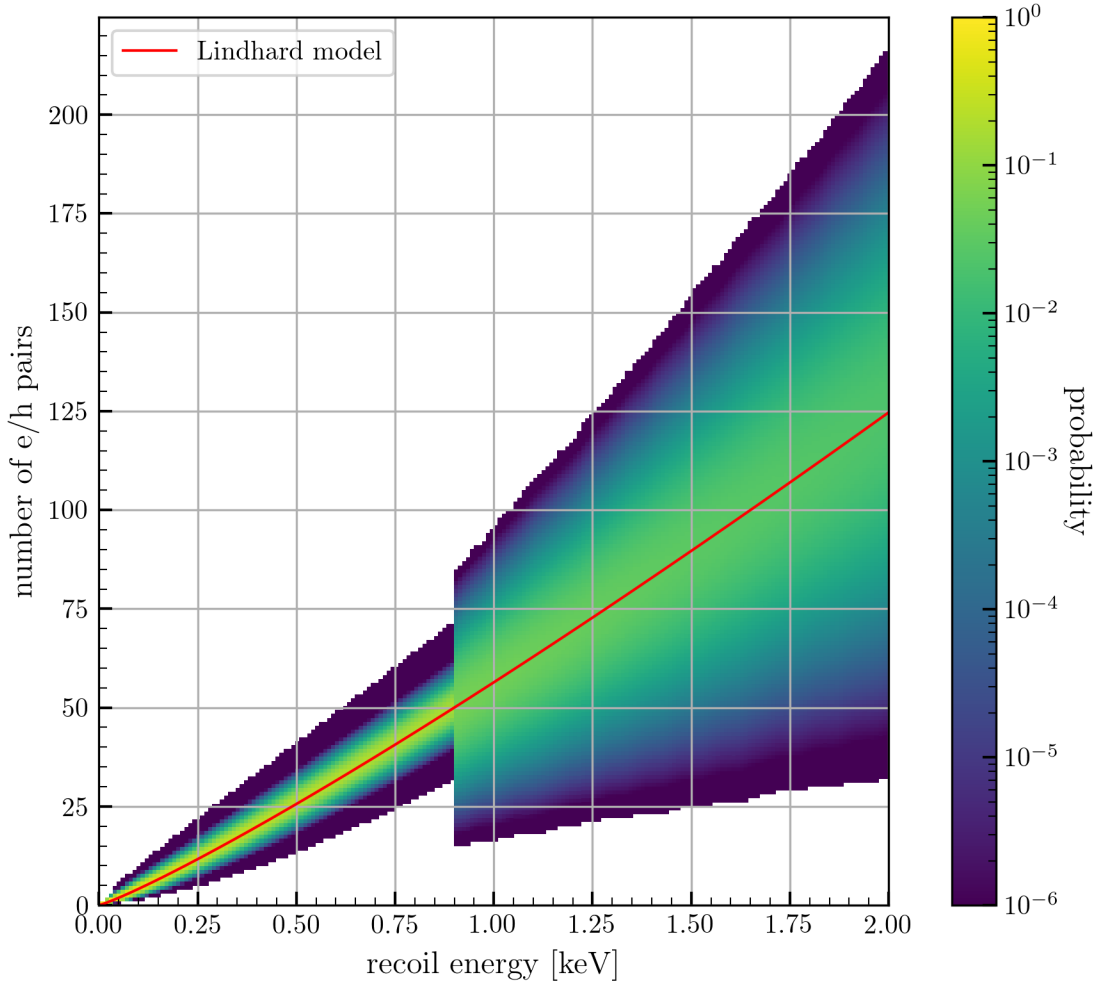


Figure 3.15: Heatmap of AL model e/h pair creation probabilities $\hat{p}_n(E_r)$ for recoil energies up to 2 keV. Values smaller than 10^{-6} have been masked out. The red line marks the average number of e/h pairs predicted by the Lindhard model

3.7.4 Comparison with IMPACT data

Measurements of ionization yield in silicon have recently been taken using HVeV detectors at Triangle Universities Nuclear Laboratory (TUNL) as part of the Ionization Measurement with Phonons At Cryogenic Temperatures (IMPACT) experiment [239, 240]. The published data surveys recoils as low as 100 eV, to date the lowest-energy measurement of ionization yield in silicon in the literature.

The e/h pair production distribution data was scraped using DataThief from Figure 2 in the results published on the arXiv [240]. Visual comparison between ionization distributions predicted by the AL model and this IMPACT data is given in Figure 3.16. Note the energies given in the IMPACT plots were converted into e/h pair counts simply by dividing by the voltage, 100 V. Note the IMPACT data contains two sets of data at 220 eV, using two different sets of detectors (“near” and “far”).

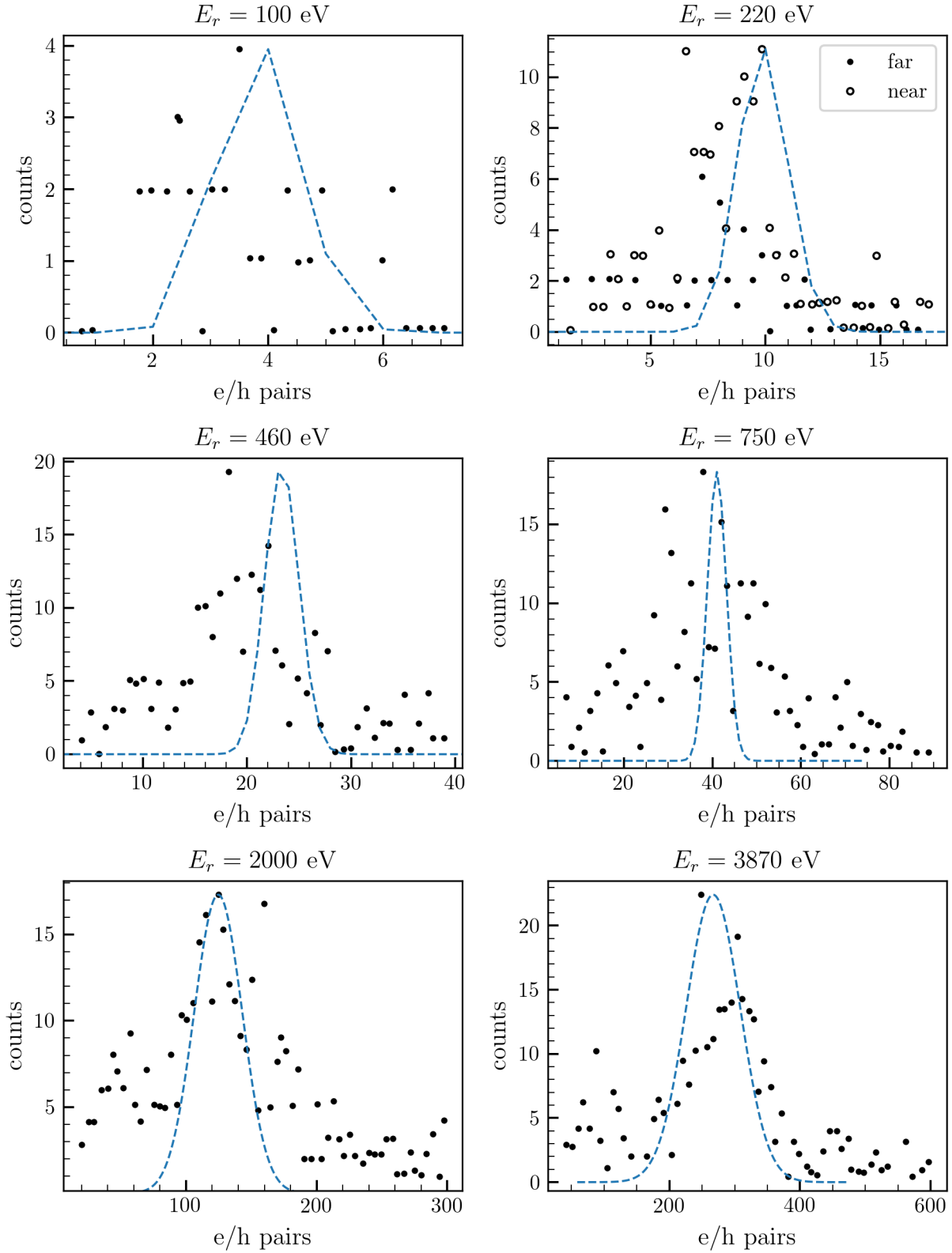


Figure 3.16: Comparison of AL model (dashed curves) with IMPACT data (black circles)

The AL model curves are normalized arbitrarily to the height of the highest peak in the IMPACT data. The AL model matches mildly well. It can be seen that at lower energies, the AL model tends to overestimate the ionization yield, and it underestimates the Fano factor consistently at all energies. Overall, however, the two sets match reasonably well. See Section 3.10.7 for a discussion of these errors.

3.8 Simulation Procedure

At this point, the recoil spectrum of scatter events and the rate of capture events have been calculated analytically. We also have our ionization model, which can be used to simulate the charge produced by a recoil of a given energy, and from there the total phonon energy produced by the event (what is measured by the HVEV detectors) can be calculated. We can thus complete our prediction of the neutron-induced spectrum of events in the detectors by MC methods.

First, sets of recoil energies induced by captures and scatters are sampled from their respective recoil distributions. A sample of $\sim 10^7$ capture events is generated using `nrCascadeSim` ver. 1.0.6, as described in Section 2.3.1. A set of scatter events of the same size is sampled from the recoil distribution plotted in Figure 3.5 (technically, events are drawn from the sum of the six spectra plotted in Figure 3.7, though this is visually indistinguishable from Figure 3.5). The method for generating this sample is analogous to the method used in Section 2.6.2.1 to generate CENNS events from tabulated spectrum data.

For each generated recoil energy $E_{r,i}$ in the set $\{E_{r,i}\}$, the number of ionized e/h pairs produced by that recoil is generated according to the ionization model $\hat{p}_n(E_{r,i})$ described in the last section. The average ionization energy $E_{ee,i} = E_{r,i}Y_L(E_{r,i})$ is calculated. If $E_{ee,i} \leq E_{k,\max} \approx 189$ eV (the maximum energy on the evaluated grid $\{E_k\}$ for the Alig model e/h pair probabilities $p_n(E)$, see Section 3.7.2), then the values $\hat{p}_n(E_{r,i})$ are calculated by linearly interpolating from the nearest values on the energy grid $p_n(E_k)$ to $p_n(E_{ee,i})$. If not, and $E_{ee,i}$ is beyond the range of evaluated energies, the Gaussian approximation is used. That is, the $\hat{p}_n(E_{r,i})$ are approximated as:

$$\hat{p}_n(E) \propto \exp\left[-\frac{(n - \bar{n})^2}{2F_i\bar{n}}\right] \quad (3.8.1)$$

where $\bar{n} = E_{ee,i}/\epsilon_\gamma$ is the average number of e/h pairs created and F_i is the value of the Fano factor at $E_{r,i}$, calculated by linear interpolation of the data plotted in Figure 3.9. The \hat{p}_n are normalized between $n = \left\lceil \bar{n} - 5\sqrt{F_i\bar{n}} \right\rceil$ and $n = \left\lceil \bar{n} + 5\sqrt{F_i\bar{n}} \right\rceil$ (inclusive).

As mentioned in Section 3.3, each ionized e/h pair emits an amount of energy equal to eV_b in the form of NTL phonons, where e is the elementary charge and V_b is the bias voltage. A typical operating

voltage for the HVeV detectors is 100 V [205], which we take to be the bias voltage here. Assuming the phonon and charge collection efficiencies are 100% (see Section 3.10.8), then the total phonon energy \tilde{E}_p is

$$\tilde{E}_p = E_r + n_{eh}eV_b \quad (3.8.2)$$

We lastly add gaussian-distributed noise of width $\sigma_0 = 3$ eV to account for the effects of baseline detector resolution (the same baseline resolution demonstrated by [204] and [205], and slightly worse than that demonstrated by [206]). So the actual measured phonon energy E_p is calculated as $E_p = \tilde{E}_p + \sigma_0 G$, where G is a standard-normal random variate. Note the Fano variance in n_{eh} implemented in the ionization model accounts for the dominant term in the coefficient C in the resolution model used in the last chapter (2.4.1). For the region where a gaussian model was used for the ionization, this is thus an identical resolution model to (2.4.1) with $C = F\epsilon_\gamma$.

The resulting sample of measured total phonon energies $\{E_{p,i}\}$ is of interest to us. This sample is binned into 5 eV bins and histogram counts are stored to disk, and each histogram is normalized by the calculated total event rates, 10.09 captures $\text{kg}^{-1} \text{day}^{-1}$ and 151.68 scatters $\text{kg}^{-1} \text{day}^{-1}$. The resulting spectra are given in the next section.

3.9 Results

3.9.1 Generated samples

Histograms of the generated samples of scatters and captures are shown in Figure 3.17 up to 1 keV. For reference, around 81% of scatter events and 9.5% of generated capture events lie in this range.

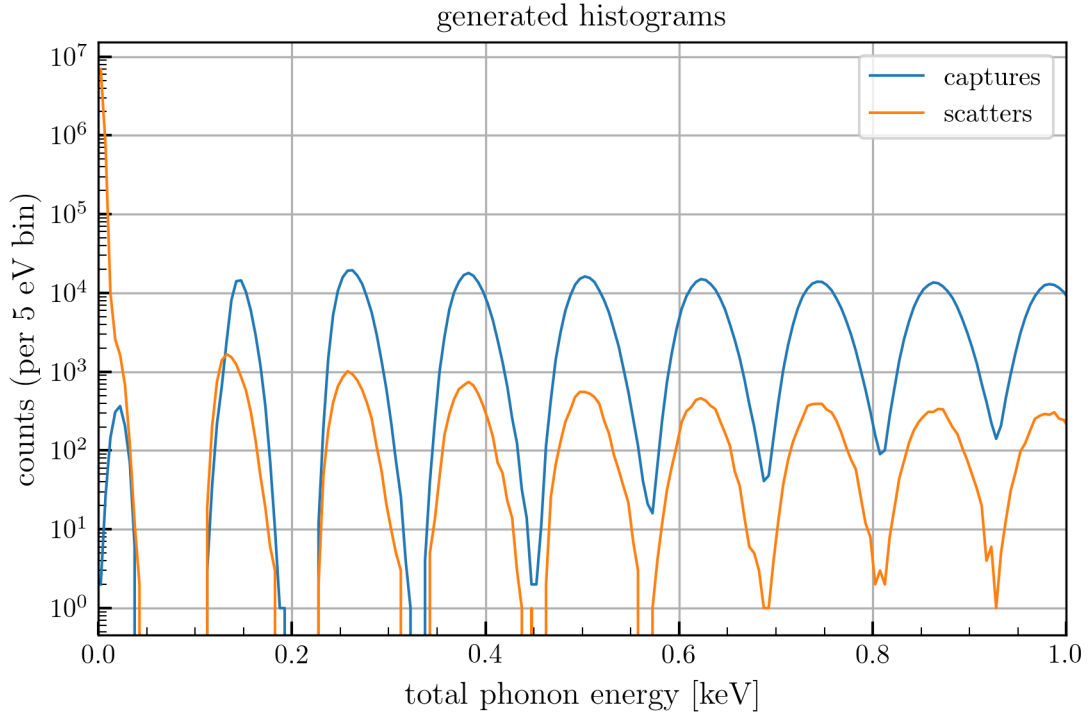


Figure 3.17: Histogram of generated phonon energies for scatters and captures up to 1 keV

3.9.2 Total event rates

The histograms in Figure 3.17 were renormalized by their respective event rates, 10.09 captures $\text{kg}^{-1} \text{day}^{-1}$ and 151.68 scatters $\text{kg}^{-1} \text{day}^{-1}$. Figure 3.18 shows the normalized spectrum for each type of event. The total neutron-induced spectrum, including both types of event, is shown in Figure 3.19. Figure 3.19 also shows the total uncertainty in the spectrum (see Section 3.10) shaded in transparent blue. The total neutron-induced event rate below 1 keV is 68.61 ± 13.52 (syst.) ± 0.07 (stat.) $\text{kg}^{-1} \text{day}^{-1}$.

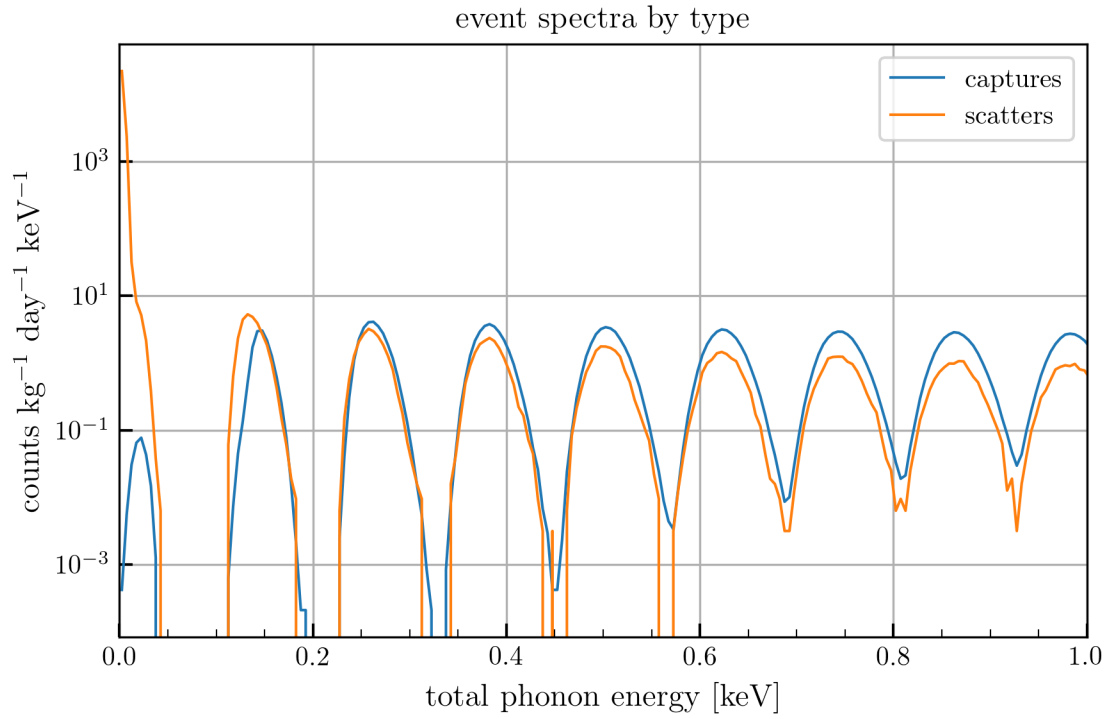


Figure 3.18: Neutron-induced event spectra by type

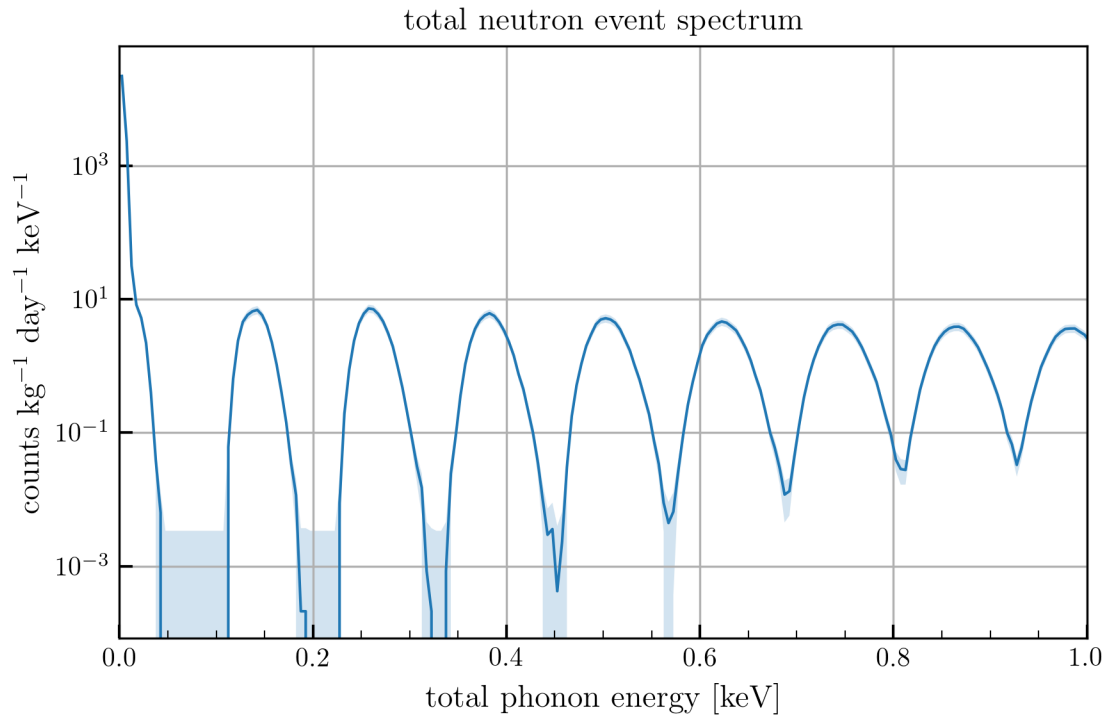


Figure 3.19: Total neutron-induced phonon energy spectrum (solid blue) with uncertainties (transparent blue shading). See Section 3.10 for description of error sources

The spectrum is clearly divided into distinct, rounded peaks, spaced approximately 120 eV apart. For the first few, the peaks are completely disjoint. Higher-energy peaks begin to overlap by around 400 eV. These peaks correspond exactly to the number of e/h pairs produced. The spectrum broken up by charge produced is shown in Figure 3.20. The rate of events in each peak, along with the peak positions and widths, are listed in Table 3.5. Nearly all low-energy events are caused by scatters, while captures become the dominant source of neutron events around the second e/h pair peak.

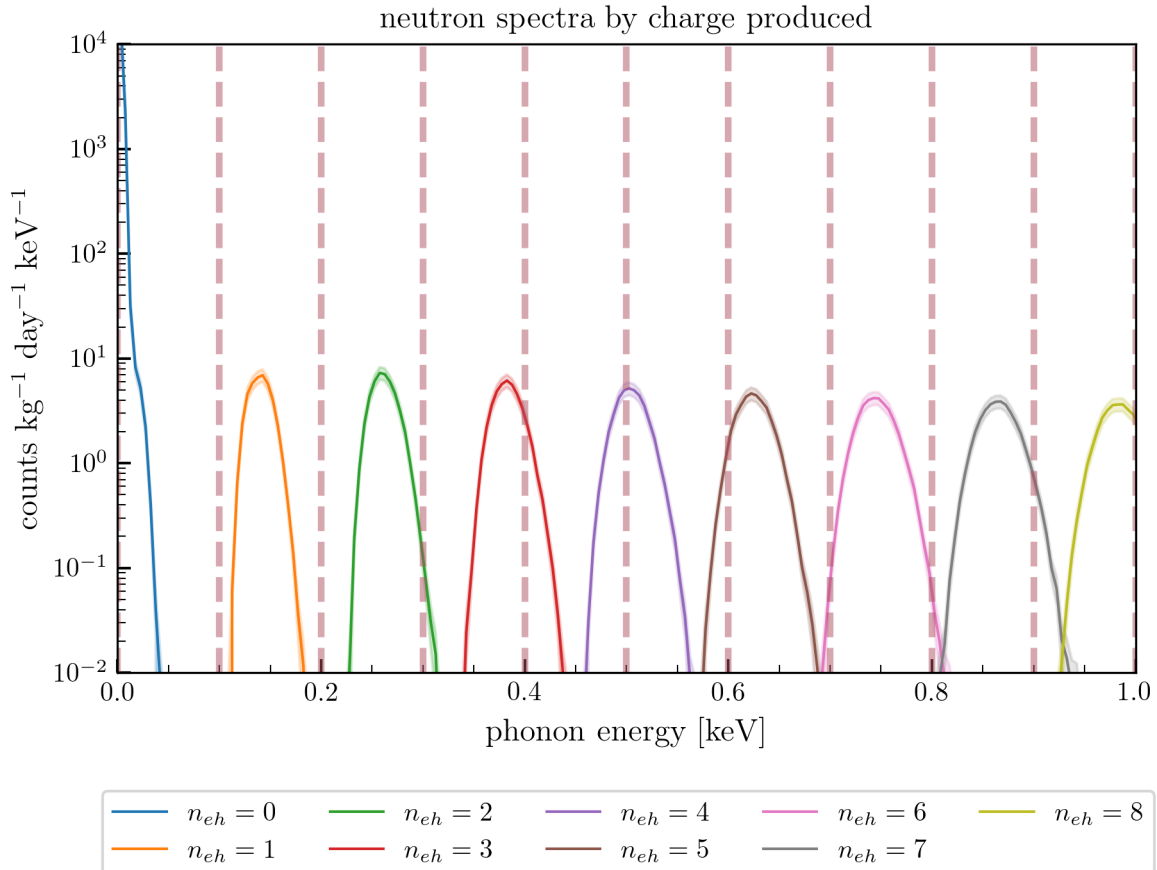


Figure 3.20: Neutron spectra by amount of charge produced. Red dotted lines correspond to the NTL phonon energy produced by an integer amount of charge

Table 3.5: Event rates by type in and peak positions of each e/h pair peak. All rates in $\text{kg}^{-1} \text{ day}^{-1}$. Uncertainties listed are systematics, then statistics (see Section 3.10). Note the errors listed in the peak position column are not uncertainties in the peak positions, but are the standard deviation of each peak about the listed mean

| n_{eh} | Peak Position [eV] | Scatter rate | Capture rate | Total |
|----------|--------------------|-------------------------------|-----------------------------|-------------------------------|
| 0 | 3.00 ± 1.58 | $67.065 \pm 13.327 \pm 0.027$ | $0.001 \pm 0.000 \pm 0.000$ | $67.066 \pm 13.327 \pm 0.027$ |
| 1 | 140.39 ± 10.99 | $0.139 \pm 0.017 \pm 0.008$ | $0.064 \pm 0.008 \pm 0.001$ | $0.203 \pm 0.025 \pm 0.009$ |
| 2 | 261.97 ± 12.43 | $0.100 \pm 0.013 \pm 0.008$ | $0.128 \pm 0.015 \pm 0.001$ | $0.229 \pm 0.028 \pm 0.009$ |
| 3 | 383.51 ± 14.08 | $0.081 \pm 0.011 \pm 0.008$ | $0.133 \pm 0.016 \pm 0.002$ | $0.214 \pm 0.026 \pm 0.009$ |
| 4 | 504.82 ± 15.39 | $0.070 \pm 0.009 \pm 0.007$ | $0.133 \pm 0.016 \pm 0.002$ | $0.203 \pm 0.025 \pm 0.009$ |
| 5 | 625.26 ± 16.50 | $0.060 \pm 0.008 \pm 0.007$ | $0.132 \pm 0.016 \pm 0.002$ | $0.192 \pm 0.024 \pm 0.009$ |
| 6 | 745.75 ± 17.63 | $0.057 \pm 0.008 \pm 0.007$ | $0.132 \pm 0.016 \pm 0.002$ | $0.189 \pm 0.023 \pm 0.009$ |
| 7 | 865.73 ± 18.58 | $0.050 \pm 0.007 \pm 0.007$ | $0.133 \pm 0.016 \pm 0.002$ | $0.183 \pm 0.023 \pm 0.009$ |
| 8 | 985.09 ± 19.41 | $0.048 \pm 0.007 \pm 0.007$ | $0.134 \pm 0.016 \pm 0.002$ | $0.182 \pm 0.022 \pm 0.009$ |

3.10 Error Estimation

This section describes sources of error in the final neutron-induced event spectrum plotted in Figure 3.19. There are two main categories of error, systematic and statistical. Systematic uncertainties arise from uncertainties in physical quantities or errors in model approximations. Statistical uncertainties arise because of Monte Carlo processes' reliance on discrete, randomly generated data.

The next few sections outline significant sources of systematic error. Section 3.10.4 outlines a novel procedure for propagating these systematic uncertainties through a Monte Carlo process. Section 3.10.5 describes the quantification of statistical errors. Section 3.10.6 will outline a few sources of error that were found negligible. Section 3.10.7 discusses the errors specifically associated with the ionization model and 3.10.8 will discuss the assumption of 100% detector efficiency. Section 3.10.9 describes errors associated with incorrect assumptions made regarding actual HVeV detector deployment. A summary is given in Section 3.10.10. Figure 3.27 at the end of the chapter shows all the major uncertainty sources.

3.10.1 Neutron spectrum

The systematic uncertainties associated with the neutron spectrum are large because of the extremely oversimplified assumptions made in calculating it. This systematic will come to dominate the uncertainties in the final spectrum almost no matter what assumptions we make about it. As a rough lower-bound estimate, we assume a static 10% uncertainty in the neutron spectrum. Unsurprisingly, this will result in a flat $\approx 10\%$ uncertainty in the neutron-induced phonon spectrum in the end (see Figure 3.27). The actual errors in the neutron spectrum are likely much larger, though it is difficult to estimate the true magnitude. Levels of radioactive material in the rocks and building material surrounding the NEXUS

facility could be entirely different than those found at SNOLAB, and the overall neutron flux could be wildly different.

In addition, this analysis has ignored cosmogenic neutrons. For backgrounds at the relatively shallow (~ 300 mwe) NEXUS facility, the cosmogenic flux is expected to be non-negligible. In 2014 the flux of fast cosmogenic neutrons was measured to be $1.5 \times 10^{-6} \text{ cm}^{-2} \text{ s}^{-1}$ in the MINOS cavern [246], which is near a third of the fast radiogenic neutron flux estimated in Section 3.4. Unfortunately, a complete characterization of the effects of a cosmogenic component to the neutron flux at NEXUS would require a much more involved analysis. It is probably reasonable to expect the shape of the thermal and intermediate components of the spectrum not to change much, but the overall flux would likely increase by 30-40% (assuming the radiogenic flux levels in NEXUS are similar to the SNOLAB values).

However, it should be noted that the estimated errors associated with uncertainty in the neutron spectrum have more to do with the overall normalization of the spectrum than the shape. A study of phonon collection efficiency in CDMS-II detectors [230] found that varying the shape of the incident neutron spectrum had fairly small effects on the resulting spectrum of recoil energies. Our errors are probably larger than the ones considered there, and their analysis included several layers of shielding that the incident neutron flux had to pass through, but it should be remembered that the elastic-scattering total cross sections in silicon at low energy are largely featureless (see Figure D.1), resulting in a substantial smoothing-out of features in the neutron spectrum. Thus variations in the shape of the neutron spectrum due to differing radiogenic sources or a cosmogenic component are not expected to contribute to the final uncertainties as much as variation in the total neutron flux and the ratio of thermal to fast neutron fluxes.

3.10.2 Cross sections

The event cross sections are measured quantities, and therefore carry associated uncertainties.

The average capture cross section in silicon is given by the EGAF database as 0.171 ± 0.003 barns [128]. This uncertainty of $\approx 1.75\%$ causes an uncertainty of the same magnitude in the overall capture event rate, and causes a flat 1.75% uncertainty in the capture-induced recoil spectrum.

Uncertainties in the elastic scatter cross section are summarized in file 33 of the ENDF data tapes (see [224], Ch. 33). ENDF uncertainty data is generally scattered in multiple places throughout the data tapes. This is done to avoid redundancy, as many types of data contained in the tapes are combinations of the other types of data. The elastic scatter cross sections (reaction number $MT = 2$) are a combination of the total cross section ($MT = 1$) and the inelastic cross section ($MT = 3$) data (and, in some energy ranges, the capture cross section data, $MT = 102$). Thus, the uncertainty in the elastic cross sections can be calculated from the uncertainty in these other quantities. The full uncertainty data in the elastic scat-

ter cross sections for silicon requires reading data from some 33 different subsections of the file 33 tapes for ^{28}Si , ^{29}Si , and ^{30}Si , and 17 additional tapes containing cross section data. The resulting relative uncertainty in the cross sections are plotted in Figure 3.21 (see also the cross sections plotted with error bars in Figure D.1 in Appendix D).

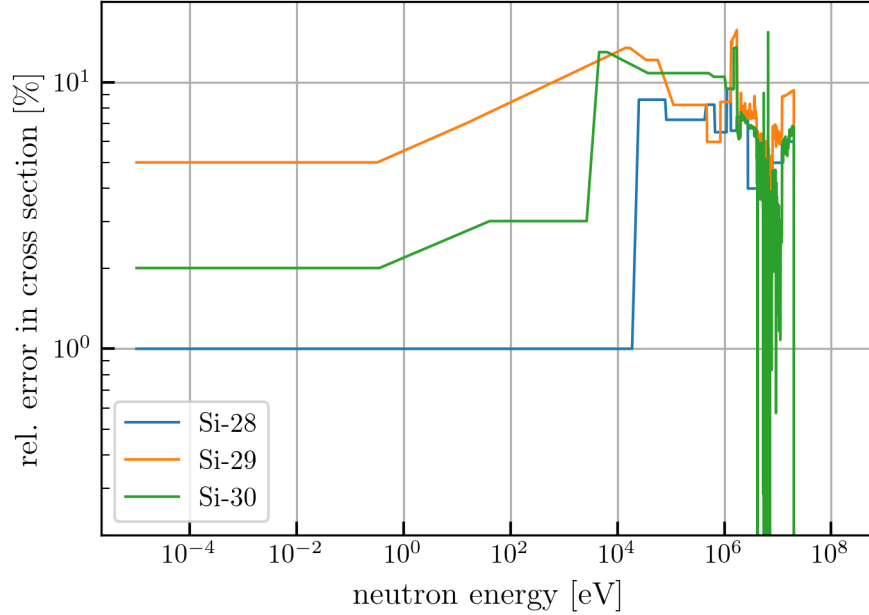


Figure 3.21: Relative error in the elastic scatter cross section data for silicon from ENDF database

To calculate the effect on the scatter-induced recoil spectrum, note that the spectrum (3.5.8) is linear in the cross section. We can just replace the data $\mathcal{O}(E_n)$ with the uncertainties $\partial\mathcal{O}(E_n)$ in that equation to calculate the uncertainty caused in the resulting recoil spectrum.

3.10.3 Inelastic scatters

Throughout this treatment, we've neglected inelastic scatters entirely. In these scatters, which are more significant at higher energies, kinetic energy is lost to the nucleus, which is excited to an elevated energy state in the collision.

In general, the treatment of inelastic scatters is extremely complicated, and would add a substantial amount to the computational effort required to calculate the recoil spectrum in Section 3.5. Thus these interactions were ignored completely in our models. We can estimate the influence of this neglect by considering the inelastic scatter cross section \mathcal{O}_{non} as an uncertainty in the elastic cross section \mathcal{O}_{el} , i.e., $\mathcal{O}_{tot} = \mathcal{O}_{el} + \mathcal{O}_{non} \approx \mathcal{O}_{el} \pm \partial\mathcal{O}_{el}$, valid for $\mathcal{O}_{non} \ll \mathcal{O}_{el}$.

Technically, this method for approximating the uncertainty causes some spectral distortion on the resulting error distribution. An elastic contribution to the interaction rate concentrates all events at

a single total final energy, whereas an inelastic contribution smears out its interactions over a range of possible final energies, depending on the elevated energy state of the nucleus. Thus, adding a small component of possible inelastic interactions to the cross section will add slightly more events at lower energies and slightly fewer events at higher energies. However, this effect is expected to be small given first, the already small corrections caused by this addition, and second because true inelastic corrections would add the same total integrated correction as considering the inelastic cross section to be an uncertainty on the elastic cross section.

The total cross sections of elastic and inelastic interactions in silicon are plotted in Figure 3.22. It can be seen the inelastic cross sections are several orders of magnitude smaller than the elastic cross sections until $O(\text{MeV})$ energies. Since most neutrons in the model spectrum presented in Section 3.4 have energies below the MeV scale, neglecting inelastic scatters does not contribute much to the errors. For neutron distributions with higher ultra-fast fluxes, this approximation will lose accuracy.

Figure 3.27 shows that for most energies of interest, these corrections are on the order of 0.1%. The total correction to the rate is $\approx 8.7\%$, though the vast majority of these missing events fall in the zero e/h pair peak at extremely low energies, far below threshold in the HVeV detectors.³⁴

3.10.4 Propagating systematic uncertainties through MC process

While it may be possible to analytically propagate uncertainties through the ionization model presented in Section 3.7, it will in general not be possible for an arbitrary Monte Carlo-based ionization model, and in either case it will be extremely computationally expensive. A simpler approach taking advantage of the MC calculations already done is possible, to propagate uncertainty in the recoil spectrum $f(E_r)$ forward to the phonon spectrum, $g(E_p)$.

Consider an arbitrary ionization model defined by some transfer function $T = T(E_r, E_p)$ which takes recoil energies into phonon energies. The phonon spectrum can then be represented as:

$$g(E_p) = \int f(E_r)T(E_r, E_p)dE_r \quad (3.10.1)$$

Given some uncertainty in the recoil spectrum, $\partial f(E_r)$, then the resulting uncertainty in the phonon spectrum will be

³⁴It should probably be mentioned that the detector threshold has been completely ignored in this analysis. This is so that any analysis in the future can truncate the spectrum where their threshold is, and not be limited by our choice of threshold here.

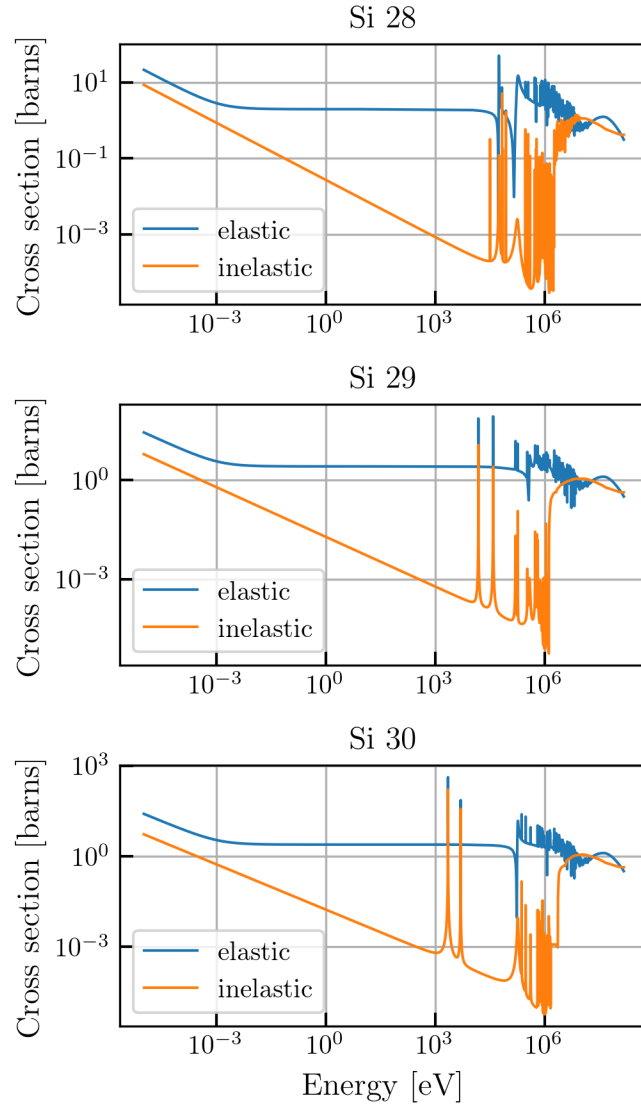


Figure 3.22: Elastic and inelastic cross sections for the isotopes of silicon

$$\partial g(E_p) = \int_0^\infty \partial f(E_r) T(E_r, E_p) dE_r \quad (3.10.2)$$

Now, we consider some case where the form of T is not known. The transfer is represented as some non-analytical process on a generated set of N recoil energies $\{E_i\}$, and the result is a phonon spectrum that takes the form of a histogram g_j over bins j :

$$\begin{aligned}
g_j &= \int_{\text{bin } j} g(E_p) dE_p \\
&= \sum_{i: \tilde{E}_p(E_i) \in \text{bin } j} 1
\end{aligned} \tag{3.10.3}$$

where the function $\tilde{E}_p(E_i)$ is a function that takes in the recoil energy E_i and spits out the phonon energy $\tilde{E}_p(E_i)$. The transfer function is then $T(E_r, E_p) \propto \delta(E_p - \tilde{E}_p(E_i))$. If we call the integral of the recoil spectrum $F = \int f(E_r) dE_r$, then we can write

$$f(E_r) = \frac{F}{N} \sum_i \delta(E_r - E_i) \tag{3.10.4}$$

where the $\{E_i\}$ are distributed according to $f(E_r)$. We can see that $T(E_i, E_p) = (N/F)\delta(E_p - \tilde{E}_p(E_i))$.

Assume $E_i < E_{i+1}$. Also define the function $E(I)$, which parameterizes the $\{E_i\}$ so that $E(i/N) = E_i$. Note here that the $\{E_i\}$ are uniformly spaced between zero and one over I , and distributed according to $f(E_r)$ over $E(I)$. So $dI = \frac{1}{N} di = \frac{1}{F} f(E) dE$.

Going to the $N \rightarrow \infty$ limit, we can instead write $f(E_r)$ as an integral:

$$\begin{aligned}
f(E_r) &= F \int \delta(E_r - E(I)) dI \\
&= \int f(E) \delta(E_r - E) dE
\end{aligned} \tag{3.10.5}$$

Note the second line is true definitionally. We thus see that the correct way to translate between sums and integrals as $N \rightarrow \infty$ is $\sum_i \rightarrow \int di = N \int dI$.

We now express $\partial f(E_r)$ on the basis of delta functions centered at the $\{E_i\}$ (a basis for any function whose support is a subset of the support of $f(E_r)$):

$$\partial f(E_r) = \frac{F}{N} \sum_i \Delta_i \delta(E_r - E_i) \tag{3.10.6}$$

where the coefficients Δ_i must be determined.

Now, by definition

$$\begin{aligned}\partial f(E_r) &= \int \partial f(E) \delta(E_r - E) dE \\ &= F \int \frac{\partial f(E)}{f(E)} \delta(E_r - E(I)) dI\end{aligned}\tag{3.10.7}$$

Going back to a sum,

$$\partial f(E_r) = \frac{F}{N} \sum_i \frac{\partial f(E_i)}{f(E_i)} \delta(E_r - E_i)\tag{3.10.8}$$

and we see that the coefficients

$$\Delta_i = \frac{\partial f(E_i)}{f(E_i)}\tag{3.10.9}$$

are the relative uncertainty in f at E_i .

Further, note the uncertainty in the histogram of bin j , ∂g_j , is:

$$\begin{aligned}\partial g_j &= \int_{\text{bin } j} \partial g(E_p) dE_p \\ &= \int_{\text{bin } j} \sum_i \Delta_i \delta(E_p - \tilde{E}_p(E_i)) dE_p \\ &= \sum_{i: \tilde{E}_p(E_i) \in \text{bin } j} \Delta_i\end{aligned}\tag{3.10.10}$$

Thus the uncertainty in the phonon spectrum can be calculated by associating each simulated recoil event with the relative uncertainty in the recoil spectrum at that event's energy, and counting up all of the uncertainties in each bin of phonon energy the same way the events are counted to get the phonon spectrum in the first place.

3.10.5 Statistical uncertainties

Estimation of statistical uncertainties associated with a Monte Carlo process is generic for any analysis involving counting the number of generated points that satisfy certain conditions (in our case, the condition being whether or not an event is in a given energy bin).

If the MC process obeys some true probability distribution p_j , where j represents a given condition (i.e., being in bin j), then the number k_j of generated points (events) that satisfy the condition after generating N total points is distributed according to the binomial distribution,

$$\binom{N}{k_j} p_j^{k_j} (1 - p_j)^{N - k_j} \quad (3.10.11)$$

Given some generated sample with k_j points that satisfy j out of N total, the uncertainty ∂p_j in p_j is:

$$\partial p_j = \sqrt{\frac{(k_j + 1)(N - k_j + 1)}{(N + 2)^2(N + 3)}} \quad (3.10.12)$$

The quantity of interest to us, the “true” height of the histogram in bin j , is Np_j , with uncertainty $N\partial p_j$.

3.10.6 Negligible sources of error

Several sources of error were found to be negligible, but bear mentioning.

3.10.6.1 Uncertainties in multiple scatters, second captures

Uncertainties associated with second- and higher scatters and captures were all neglected, since their contributions to the final event rate are suppressed by factors $O(10^{-2})$.

3.10.6.2 Numerical errors

In an extensive numerical analytical procedure like the one used here (particularly in Sections 3.5 and 3.6), numerical errors can accumulate. One of the most serious sources of numerical errors came in the evaluation of the angular terms in the elastic scatter cross sections. We assess this error accumulation by calculating the total scatter rate R two ways:

$$R = \int dE_r \int dE_n I(E_n) \sigma(E_r, E_n) \quad (3.10.13)$$

If we perform the integration over recoil energy E_r first, the cross section becomes the total cross section,

$$R = \int dE_n \mathcal{O}(E_n) I(E_n) \quad (3.10.14)$$

and R can be calculated directly without considering the angular terms in the cross section. On the other hand, the integral over E_n gives the differential interaction rate $r(E_r)$ (equal to $n(E_r)$ (3.5.8) multiplied by the silicon nuclear mass):

$$R = \int dE_r r(E_r) \quad (3.10.15)$$

The total scatter rate was calculated both ways, and the relative error between the two values was $\approx 5 \times 10^{-6}$, which we neglect compared to our other sources of error.

Other sources of numerical error were found to be smaller. For example, the choice of recoil energy grid was found to vary the total rate by $\approx 4 \times 10^{-6}$ by doubling and halving the number of points in the grid. Extending the energy grid to much higher/much lower energies came with a similar error.

3.10.6.3 Overlapping samples

One source of error in our physical assumptions is the assumption of perfect additivity of the cross sections for capture and scatter (i.e., we calculate the rates independently and add them together). Technically, the two rates are coupled together - a neutron cannot do both at once.

Consider two probabilistic processes. Process 1 occurs with independent probability p and process 2 occurs with independent probability q , meaning that if process 2 could not occur, then process 1 occurs p of the time, and similarly for process 2. However, if it is possible for both processes to occur on the same population of events, the actual probabilities will be slightly lower than p and q because the population available to undergo a process is decreased by the number of population members that undergo the other process.

To calculate the true probabilities p_1 and p_2 , note first that p_3 , the probability that neither process occurs, is $p_3 = (1 - p)(1 - q)$. Note also that the relative rates of each process are in ratio p/q . Then, we have that the relative proportion of process 1 events to the total events that undergo either process is

$$\frac{p}{p + q} = \frac{p_1}{p_1 + p_2} \quad (3.10.16)$$

But $p_1 + p_2 = 1 - p_3 = p + q - pq$, thus:

$$p_1 = \frac{p}{p+q}(p+q-pq) = p - \frac{p^2q}{p+q} \quad (3.10.17)$$

and similarly,

$$p_2 = q - \frac{pq^2}{p+q} \quad (3.10.18)$$

In both cases, the relative correction is $pq/(p+q)$, which is $\sim \min(p, q)$ when the two probabilities have very different magnitudes.

To calculate the true probabilities here, we then need to calculate the “independent probability” p and q of either a capture or a scatter event. In general, the probability of an interaction with a macroscopic cross section Σ when travelling a small distance dx is just Σdx . We can approximate the “distance” that a particle must travel through a semiconductor to interact with a single nucleus by considering each nucleus to reside in some cube of side length l . We must have that $1/l^3 = \rho_n$, the number density. Thus $l = \rho_n^{-1/3}$. But since $\Sigma = \rho_n \mathcal{O}$, then the probability of an interaction is:

$$p_{\text{interaction}} = \rho_n^{2/3} \mathcal{O} \quad (3.10.19)$$

Note that $\rho_n^{-2/3}$ is an area, approximately the ‘geometrical area’ of each nucleus (the area of the faces of each cube containing a single nucleus). The probabilities of interaction are the ratio of this geometric area with the cross sectional area \mathcal{O} . In silicon, the geometric area is $\approx 7.37 \times 10^{-16} \text{ cm}^2 = 7.37 \times 10^8$ barns.

For a non-constant cross section, we average \mathcal{O} over the flux spectrum $I(E)$:

$$\begin{aligned} p_{\text{interaction}} &= \rho_n^{2/3} \frac{1}{\int I(E) dE} \int \mathcal{O}(E) I(E) dE \\ &= \rho_n^{2/3} \frac{R}{I_{\text{tot}}} \end{aligned} \quad (3.10.20)$$

where R is the interaction rate per particle and I_{tot} is the total particle flux (particles per unit time per unit area).

For captures, (3.10.19) yields a probability of 2.3×10^{-10} . For scatters, the total interaction rate is $7.89 \times 10^{-29} \text{ s}^{-1}$ and the total neutron flux is $3.58 \times 10^{-5} \text{ neutrons cm}^{-2} \text{ s}^{-1}$. This gives a total interaction probability of 3.0×10^{-9} . The relative correction term is then 2.155×10^{-10} , safely negligible.

3.10.7 Ionization model

The Alig-Lindhard ionization model introduced in Section 3.7 has several main deficiencies that should be mentioned in connection with errors or uncertainties in the final neutron spectrum. The choice of ionization model does not affect the overall normalization of the neutron phonon spectrum, but it seriously affects the shape.

First, the AL model does not resolve the discrepancy between the Lindhard model and recent measurements of ionization yield, as discussed in Section 3.7.1. To conform to those measurements, yields should be smaller at low energies, meaning fewer events in higher e/h pair peaks. Rates below 1 keV are likely slightly higher than predicted here, as fewer events produce enough charge to reach $> 1 \text{ keV}$. It is difficult to estimate the true errors, as measurements only go as low as 100 eV [240], and testing modifications to the distribution of e/h pairs is highly dependent on how the probabilities are modified. Tests rescaling probabilities linearly with n to lower the yield by 10% found that peak probabilities changed by as much as 115% in the first ten e/h pair peaks.

In addition, the AL ionization model underestimates the Fano factor consistently (see Figure 3.16). The true spectrum likely has wider peaks than plotted in Figure 3.19, with more overlap. In addition, the QET phonon energy resolution (non-Fano resolution effects) was modelled as a constant baseline detector resolution, $\sigma_0 = 3 \text{ eV}$. A more realistic model should include some energy dependence, which will cause additional asymmetric broadening of the e/h pair peaks.

It should also be noted that spectral uncertainties are harder to decouple from statistical uncertainties because of how the statistical uncertainties depend on the height of the spectrum in each bin. In addition, the only way to directly assess the uncertainty associated with the ionization model would be to test alternatives, and at this stage no satisfactory alternatives are available. Simple modifications based on lowering the threshold between the Alig-model probabilities and the gaussian approximation fail due to the gaussian approximation being invalid at low-enough energies to have an effect in the region of interest (at $E_r \sim 200 \text{ eV}$, where n_{eh} is on average 9, the Fano factor data in Figure 3.9 yields a standard deviation of 2, meaning there's only 4.5σ to $n_{eh} < 0$, leaving a non-negligible proportion of events in impossible territory).

Some modifications to the AL model, such as a more careful treatment of the “equivalent electron” may yield better results. However, it is desirable to find an ionization model that does not rely directly

on the Lindhard model, despite its good results at high energy. More detailed investigations of possible modifications to the Alig model and other ionization models should be undertaken. A brief investigation looking to parameterize nuclear interactions in an analogous way to the Alig model treatment for electrons found that assumptions made in the original model should be revisited, such as scattering by acoustic phonons and the free-particle approximation. More work needs to be done.

3.10.8 Detector efficiency

A related, but distinct, effect to assumptions made in the ionization model is the assumption of 100% charge and phonon collection efficiency in the detector. In reality, both charge and phonon collection will not be 100% efficient processes. Some portion of the phonons produced in the detector won't make it to the QET, and the produced charge doesn't necessarily produce all the NTL phonons (3.8.2) says they should. A modified formula for the collected phonon energy E_p (3.8.2) is (see, e.g., [105, 204]):

$$E_p = \epsilon_p E_r + \epsilon_L \epsilon_Q n_{eh} e V_b \quad (3.10.21)$$

where ϵ_Q is the charge collection efficiency, and ϵ_p and ϵ_L are the phonon collection efficiencies for prompt and NTL (Luke) phonons, respectively.

3.10.8.1 Phonon collection efficiencies

The phonon collection efficiencies ϵ_p and ϵ_L give the proportion of energy in the form of phonons, E_r in prompt phonons (ϵ_p) and $\epsilon_Q n_{eh} e V_b$ in NTL phonons (ϵ_L), that reach the QETs.³⁵ Both ϵ_p and ϵ_L are expected to be extremely low at low energies, and grow rapidly to maximum at $O(\text{eV})$ energies, e.g., as measured by [230] during calibration of CDMS-II Ge detectors. After the peak, they are effectively constant for higher energies. In addition, ϵ_L has been measured in HVeV detectors to be nearly independent of applied voltage to within 1% [203].

Loss mechanisms for phonons are described by [242]. A substantial fraction, related to the coverage of aluminum film deposited on the detector (part of QET components), are lost due to transmission into inactive components or, after transmission into the active aluminum QET components, have insufficient energy to be transferred into the tungsten TES. For early QET technologies, about 40% of trans-

³⁵Note there is generally a third type of phonon at play, so-called “recombination phonons,” which form during charge recombination at the electrodes of the detector. However, the HVeV detectors achieve high-field conditions through the use of contact-free electrodes, demonstrated to minimize leakage currents [202], and so charges are expected to accumulate at the surface of the detector, rather than recombine and create phonons. More on this charge accumulation in the next section.

ferred phonons were lost in this latter way [201, 247]. Another major loss, especially for initial low-energy ($\lesssim 10$ eV) NRs, is scattering of phonons into two lower-energy phonons (“anharmonic decay”) in the bulk of the detector, by scattering off of impurities and mass defects (crystal defects) in the crystal. Energy loss rates during reflections off the edges of the crystal are nonzero but extremely low. Total measured phonon loss rates at the crystal surface in iZIP detectors were $\sim 0.1\%$ per interaction [248], and it’s reasonable to expect similar rates in the HVeV detectors.

An important detail to note is that reconstructing event energies from output signals in these detectors is generally impossible from first principles. These detectors all go through a calibration stage using events of *known* energy, e.g., events induced by optical lasers [171, 203, 204] (HVeV), X-rays from electron capture on ^{55}Fe [204, 249] (HVeV, CPD³⁶), ^{57}Co [204] (HVeV), and ^{71}Ge [130] (CDMSlite iZIP), and monoenergetic neutrons from ^{252}Cf and radiation from electron capture on ^{133}Ba [163, 191, 192, 230] (CDMS-II ZIP,³⁷ iZIP). Note the gamma calibration, i.e., with lasers or electron captures, calibrates ERs, while the ^{252}Cf neutron source calibrates NRs (and both are used in ZIP and iZIP detectors to calibrate both ionization and phonon channels). In HV detectors, ER calibration normalizes the value of ϵ_L so that ERs, where the ionization yield is unity, are measured with the correct energy. Thus we can consider ϵ_L to be unity.³⁸

ϵ_p and ϵ_L are generally treated as identical, but [230] investigated the differences by looking at the differences in collection of ER and NR events in CDMS-II silicon ZIP detectors, and found $\epsilon_p/\epsilon_L \approx 0.95$. This has a small effect on our results. Because of the high operating voltage V_b , resulting in NTL phonon energies of several hundred eV, a 5% change in the deposited NR energy (change of $O(10)$ eV for the highest-energy recoils) causes a $\sim 1\%$ (max $\sim 2\%$) shift in the overall measured energy for events in higher e/h pair peaks (in the 0 e/h pair peak the change is 5%, as all of the deposited energy comes from prompt phonons).

The effect of this disparity in phonon efficiencies is shown in Figure 3.23. The blue spectrum shows our original neutron spectrum from Figure 3.19. The orange spectrum shows the resulting spectrum with $\epsilon_p = 95\%$. To better illustrate how ϵ_p less than unity affects the spectrum, the extreme case of $\epsilon_p = 50\%$ is plotted in green. From this curve, it’s easier to see that the effect of $\epsilon_p < 1$ is to shift higher e/h pair peaks toward lower energies and make them slightly narrower.

³⁶CPD = Cryogenic PhotoDetector, a gamma detector developed by [250]

³⁷The ZIP detectors are an earlier iteration of the current iZIP detectors, which leave out the “interleaved” part. Rather than having the phonon sensors and charge-detecting electrodes interleaved over each face, they have two electrodes covering one face and four phonon detectors covering the other face [251]

³⁸Actual measured values of ϵ_L are typically fairly small, in the realm of 5% [203] to 27% [204]. Large uncertainties in these values are incurred because of uncertainties in electronics and readout systems, hence the need for careful calibration in the first place.

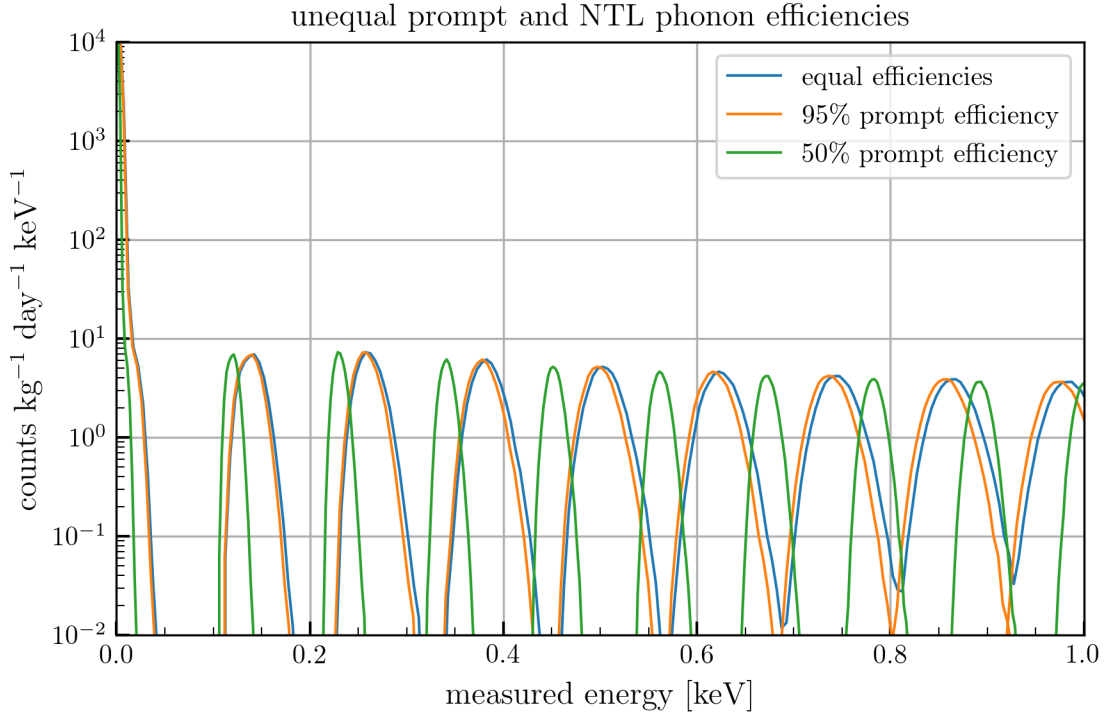


Figure 3.23: Effect of differing prompt and NTL phonon collection efficiencies. Plot shows original (equal) data and 95% prompt efficiency. The unrealistic case of 50% prompt efficiency is included to better illustrate the effects of $\epsilon_p < 1$

We can see that the effect is extremely small for the realistic $\epsilon_p = 0.95$ spectrum. It should also be noted that incorporating this effect does not substantially contribute to event rates between the e/h pair peaks, as is the case for imperfect charge collection efficiency. For nonzero e/h pair peaks, energies are shifted by $\sim 1\%$ (closer to 2% for energies on the high-energy side of the first two e/h pair peaks).

Note that to calculate the above spectra, all events in each bin in Figure 3.19 are treated identically as having an energy equal to the center of the bin. This treatment, of treating bins rather than events, will also be used in the following section.

3.10.8.2 Charge collection efficiency

The charge collection efficiency ϵ_Q is a measure of what proportion of the theoretical phonon energy due to freed charges, $n_{eh}eV_b$, is actually released as NTL phonons. As with the phonon collection efficiencies, ϵ_Q is expected to be small at low energies and rise rapidly to maximum. The position of this steep rise is generally at slightly higher energies than the rise of the phonon efficiencies, and is one of the limiting criteria for determining the energy threshold of the detector. However, unlike the phonon collection efficiency, ϵ_Q is expected to vary with event energy, and is generally smaller for events occurring on or near the surface of the detector [105]. Past analyses have often assumed ϵ_Q to be very close to one

for recoils in the bulk of earlier CDMS detectors. However, data taken with the HVeV detectors indicates $\epsilon_Q < 1$ [171, 203, 205, 206]. The presence of events in between e/h pair peaks in laser calibration data is evidence of imperfect charge collection. Quantization into the pair peaks is caused by discrete charge numbers n_{eh} , so events between the peaks indicates non-integer amount of charge.

As an illustration, public SNOLAB HVeV Run 2 laser calibration data [252] that accompanied ref. [205] is plotted in Figure 3.24 in 5 eV bins. The peaks were delineated by eye at the boundaries of the bins, as shown by the red bands. Counting the events between peaks reveals that approximately 13.3% of events were affected by imperfect charge collection.

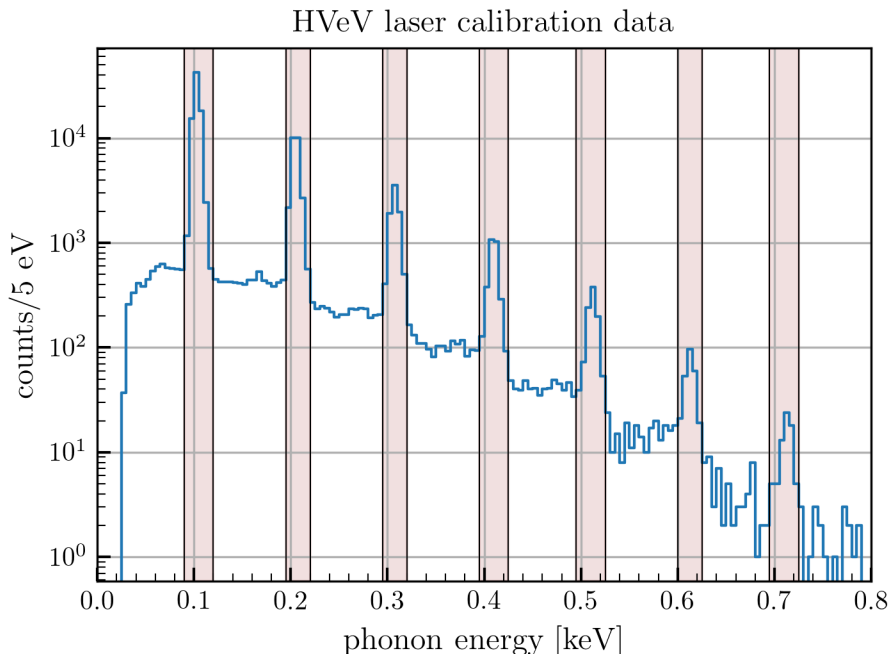


Figure 3.24: Laser calibration data from SNOLAB HVeV Run 2. Red bands indicate estimated peak locations to calculate rate of in-between peak events (13.3%)

Several processes can lead to non-integer amounts of charge collection. [204] found that leakage current, current spontaneously induced in high-field conditions by freeing charges from impurities in the semiconductor crystal, was likely responsible for most of the between-peak events found in [171], and demonstrated that this effect could be reduced using contact-free electrodes as described above. However, other work has measured three other processes causing “fill-in” in the HVeV detectors: subgap infrared (SGIR) photons, impact ionization (II), and charge trapping (CT) [205, 206, 253]. SGIR radiation is a laser-induced phenomenon that has been shown to be mitigated using upgraded components and shielding [171], so we do not need to worry about it here. Two other processes contribute: surface [202, 204] and bulk [130] charge accumulation.

Impact ionization (II) occurs when charge carriers traversing the detector scatter off of impurity states in the semiconductor and free additional charges, which traverse some fraction of the detector width, depositing some fraction z/l_z of eV_b , where $l_z = 4$ mm is the width of the detector and z is the distance traversed by the impacted charge. This serves to increase the value of ϵ_Q . The opposite process is charge trapping (CT), where a charge carrier is trapped by a vacant impurity state, thus reducing ϵ_Q . Note the probabilities of II and CT are in general different for electrons and holes, each proportional to the density of acceptor and donor impurity states respectively, but in the high-purity Si HVeV detectors, the rates are very similar [253].

There are essentially two mechanisms where charge trapping can occur. First, charges can be trapped during *drift*, while propagating across the detector material under the influence of the bias field. If this is the case, the efficiency ϵ_Q should vary approximately as $1/l_z$ [254]. Second, charges can be trapped in the initial charge cloud that is produced during the recoil event. In this case, the dependence on the detector thickness is negligible, and mainly depends on the magnitude of the bias voltage. Also, this will cause discrete changes in energy deposits, as these charges have no chance to produce NTL phonons.

Charge trapping effects in ERs were studied by Penn et al. [254] for the original CDMS Si detectors in a range of bias voltages and detector thicknesses. They found that both effects are significant, though they do not estimate relative magnitudes. Mast et al. [202] found that trapping in the initial cloud is dominant for detectors less than a few cm thick, and estimate typical drift trapping lengths (inverse macroscopic cross sections, Σ^{-1}) of ≈ 2 cm in Si. More recently, rates of charge trapping and impact ionization in HVeV were estimated by Amaral et al. [205] and Ponce et al. [253] based on the model described by Ponce et al. [255]. The earlier paper exposed the detector to 650 nm light under a ± 140 V bias [253]. They calibrated leakage current rates by normalizing to non-laser-correlated events, and fit values of $P_{CT} = 0.713 \pm 0.093\%$ and $P_{II} = 1.576 \pm 0.110\%$. The later paper, which published LDM limits from a surface lab at Northwestern University [205], used (632 nm) laser calibration data at 100 V to fit $P_{CT} = 11 \pm 3\%$ and $P_{II} = 2^{+3}_{-2}\%$ using the same model.

We use the same model, the “flat model” [255], to roughly estimate the effect of nonzero CT and II rates on the neutron-induced spectrum. This model gives the probability distribution ${}^{(m)}h(x)$ for the NTL-energy x (in units of eV_b) given off by the ionization of m charge carriers. It neglects multiple impact ionizations and considers any CT/II probabilities independent of the other charges produced. It approximates the energy deposited by a charge that is either trapped or impact-ionized as depositing energy uniformly between $x = 0$ and $x = 1$ (hence “flat”). The model has two free parameters: P_{CT} and P_{II} . The probability distribution ${}^{(m)}h(x)$ can be written as:

$$\begin{aligned}
{}^{(m)}h(x) &= P_1^m \delta(x - m) + mP_1^{m-1} P_{CT} \Theta(x - m + 1) \Theta(m - x) \\
&+ mP_1^{m-1} P_{II} \Theta(x - m) \Theta(m + 1 - x) \\
&+ \sum_{i=0}^{m-2} \sum_{j=0}^{m-i} \frac{m! P_1^i P_{CT}^j P_{II}^{m-i-j}}{i! j! (m-i-j)!} f_{IH}(x - m + j | m - i)
\end{aligned} \tag{3.10.22}$$

where $\Theta(x)$ is the Heavyside function and $P_1 \equiv 1 - P_{CT} - P_{II}$. The first term represents all m charges neither trapping nor impact ionizing. The next two represent either one charge trapping or impact ionizing and the other $m - 1$ doing neither. Note that because of the Heavyside functions, these essentially constitute flat plateaus extending to $m - 1$ and $m + 1$. The summation encompasses all other combinations of CT and II. In the sum, i represents the number that neither trap nor ionize, j is the number that trap, and $m - i - j$ is the number that impact ionize. The large fraction is the probability of that combination of i , j , and $m - i - j$ events of each type. The distribution $f_{IH}(x|n)$ is the Irwin-Hall distribution [256, 257], which gives the distribution of the sum of n uniform random deviates – i.e., the amount of charge in addition to $m - j$, the minimum possible for that combo, that is produced by $m - i$ random amounts of charge (j of which are trapped, $m - i - j$ of which are freed). The Irwin-Hall distribution takes the form:

$$f_{IH}(x|n) = \frac{1}{(n-1)!} \sum_{k=0}^n \binom{n}{k} (x-k)^{n-1} \Theta(x-k) \Theta(n-x) \tag{3.10.23}$$

Effects of the flat trapping model with the values of P_{CT} and P_{II} measured by [253] and [205] are shown in Figure 3.25.

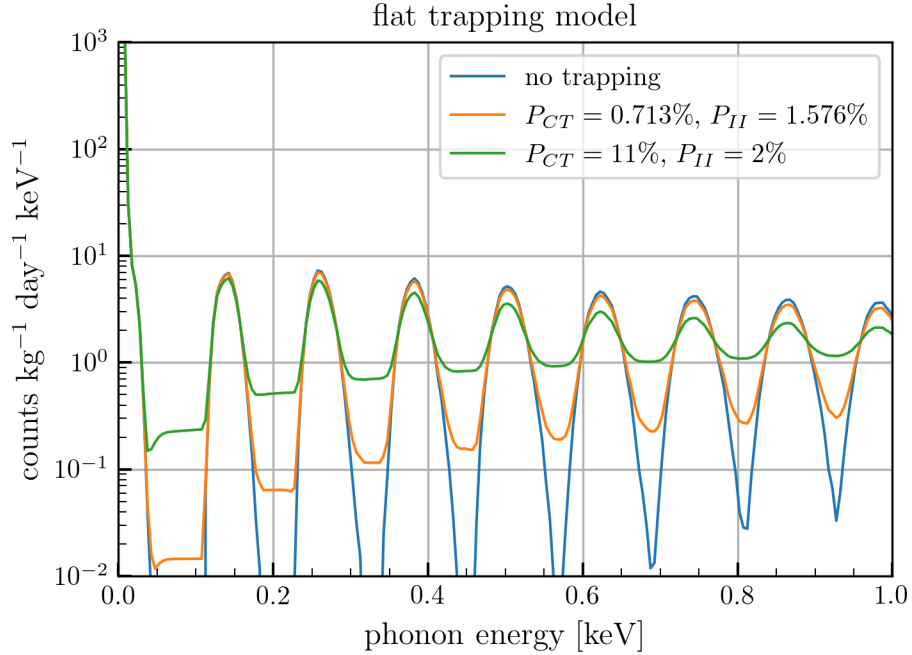


Figure 3.25: Spectrum of neutron-induced events with charge trapping and impact ionization as per flat trapping model

A simplified model of drift trapping was also implemented by assuming a constant macroscopic trapping “cross section” Σ (inverse drift trapping length) with the probability distribution,

$$\rho(z) = \Sigma e^{-\Sigma z} \quad (3.10.24)$$

where once again z is the distance travelled through the detector, and the NTL energy is $eV_b(z/l_z)$, where l_z is the width of the detector. This drift trapping model was implemented by simulating 15,000 e/h pairs released at random positions in the detector and propagated according to (3.10.24) for each bin of events in the neutron spectrum (Figure 3.19). Results are shown in Figure 3.26. (Note $\Sigma = 0.5 \text{ cm}^{-1}$ is consistent with the findings of [202]).

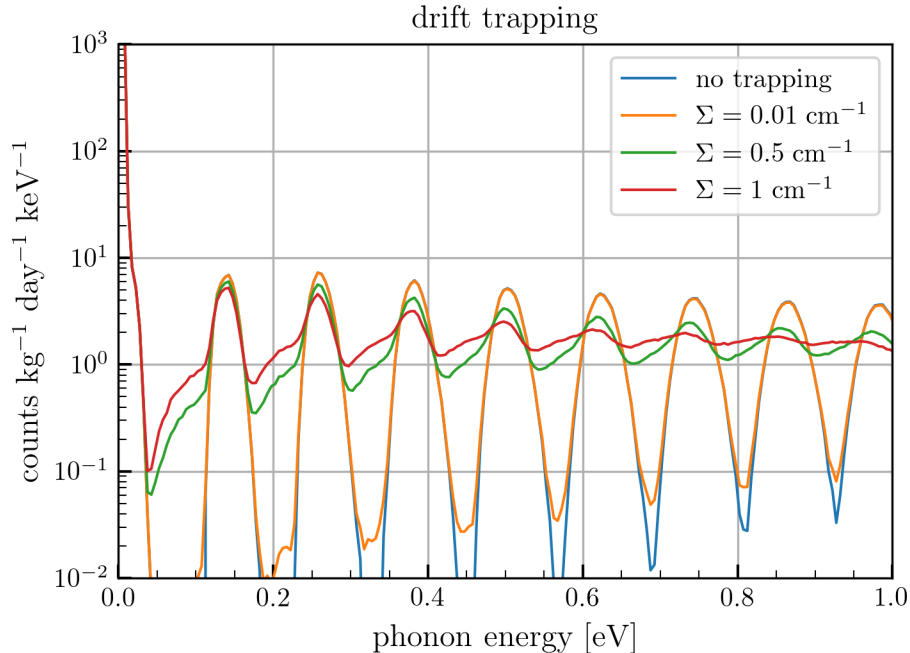


Figure 3.26: Effect of simple drift trapping model

For both trapping/impact ionization models, event spectra are filled in between the e/h pair peaks. Because impact ionization is generally less common than trapping, the fill-in between events is generally asymmetric. Fill-in between the first pair peak and the zero pair peak is generally much lower, especially at lower energies, as the fill-in only comes from trapping of low-charge events. The fill-in from drift trapping is more sloped than for the flat trapping model.

The last point about charge collection efficiency that needs to be mentioned is charge accumulation. Both forms of charge accumulation, bulk and surface, result from natural operation of the detector. Bulk charge accumulation occurs as a direct result of charge trapping. Immediately after cooling, impurity states in the semiconductor will be unoccupied, but will slowly fill as charges are trapped, thus charging the bulk of the detector. This process has been described in first-generation CDMS detectors [258], CDM-Slite detectors [130], and current-generation prototypes [202]. This accumulating bulk charge will have two main effects. First, charge trapping will generally decrease, as there are fewer vacant impurities open to trap, leading to an increase in ϵ_Q [254]. However, the accumulated charge will also create a “counter-bias” that works against the applied bias field, effectively decreasing V_b . The same effect happens with surface charge accumulation. For a detector using contact-free electrodes, charge carriers moving through the detector reach the edge of the semiconductor crystal and have nowhere to go, and so accumulate on the surface of the detector. A counter-bias builds up exactly analogous to a capacitor with capacitance $\epsilon_0 A/d$, where A is the cross-sectional area of the detector (1 cm^2) and d is the total vacuum gap width [202].

In both cases, bulk and surface charge accumulation, the counter-bias serves to effectively reduce the bias voltage V_b . The main effect this has on the spectrum is to linearly shift the e/h pair peaks. Hong et al. [204] reported particularly major charge accumulation during ^{57}Co X-ray calibration due to the relatively large rate of charge generation in short periods of time. They observed counter-bias accumulating at a rate of 0.2 V/hr. This is a fairly extreme case, and charge accumulation is expected to be much slower in most other situations. Both types of charge accumulation can be eliminated (“neutralized”) by grounding the detector and either irradiating at high intensity (“flashing,” e.g., [130, 171, 202, 253]) or by warming the detector to ~ 20 K (“baking,” e.g., [204]).

3.10.8.3 Other types of efficiencies

Other types of efficiencies relevant in the operation of an HVeV-type detector are generally concerned with data postprocessing and analysis, particularly cut efficiencies in the selection/rejection of events for inclusion in the analysis sample. Agnese et al. [230] identify efficiencies associated with two types of data quality cuts: the chi-squared cut, which involves pulse-shape discrimination to select events that sufficiently resemble single-particle collisions, and fiducial volume cuts, which seek to discriminate between events occurring close to the surface of the detector, which are more likely to be unwanted backgrounds, and events occurring in the bulk of the detector. The chi-squared cut efficiency is basically constant above threshold, and can largely be ignored. There is some energy dependence to the fiducial volume cuts (at higher energies, the cut efficiency decreases as larger energy deposits at the surface are harder to distinguish from bulk events). Other cuts include rejecting data based on proximity to other events, events occurring where the baseline (standard-operation, absence-of-an-event) signal had non-negligible variation, or where the temperature of the detector was too far from the nominal operating temperature. Amaral et al. [205] report an overall data quality cut efficiency nearly constant $> 90\%$ above 100 eV, falling to $\sim 40\%$ at lower energies. We thus expect this type of efficiency to cause an overall constant renormalization of the event spectrum, with energy-dependent effects mainly affecting the zero e/h pair peak, which is below most realistic thresholds anyway. Thus we can ignore this class of detector efficiencies.

3.10.9 Miscellaneous Errors

A number of other sources of error have been pointed out by members of the SuperCDMS Analysis group, and are of particular relevance to members of the collaboration seeking to use/adapt these results.

3.10.9.1 Detector shielding and neutron attenuation

This analysis has ignored the neutron-reducing effects of the fridge systems and additional shielding deployed around the HVeV detectors. The actual flux through the detector will be lower than our results, with a comparatively larger thermal component due to neutron attenuation (energy loss) while passing through the additional layers of material. Assuming a dedicated passive neutron shield of 50 cm of polyethylene (PE), a reduction on the order of 10^6 would be expected (e.g., as reported for the shielding setup used at CDMS-II Soudan [187]). Without a dedicated neutron shield, typical reduction is on the order of 5 – 60%.³⁹

3.10.9.2 Event timing and timing resolution

A possibly significant source of errors in the treatment of multiple scatters is the finite timing resolution of the HVeV detectors. In Section 3.6, the second (and third, and so on) time a neutron scattered in the detector was treated as a completely separate event. However, in practice, the detectors have a finite timing resolution, and for all but the lowest-energy ($\lesssim 0.1$ eV) neutrons, two successive scatters by the same neutron would follow too quickly after each other to be differentiated by the detector readout systems. The correct treatment of these scatters is to add the energy and the ionization of the individual scatters together into a single output event, rather than counting as two separate events of lower energy. As mentioned in Section 3.10.6.1, we’ve largely neglected uncertainties associated with second- and further scatters, but with this discussion in mind the $\sim 4\%$ of events that take the form of second- and higher scatters and captures are not added to the overall rate, but will contribute to changing the shape of the spectrum.

3.10.10 Summary of errors

Relative uncertainties in the final neutron-induced phonon spectrum are shown in Figure 3.27 by source. Note the statistics uncertainties reach as high as $\sim 2000\%$ where the neutron spectrum is extremely small (note also that this plot masks out bins where the neutron spectrum has zero magnitude).

The total contributions to uncertainty in the neutron-induced event rate are given in Table 3.6. Integrals of the different uncertainty spectra only extend to 1 keV. Values given are relative to the total neutron-induced event rate in that region, $64.41 \text{ kg}^{-1} \text{ day}^{-1}$. The absolute uncertainties from statistics and systematics are plotted in Figure 3.28.

³⁹Assuming the dominant neutron attenuator is the copper box surrounding the detectors within the fridge, with a mass density of 8.96 g/cm^3 , thickness ~ 1 cm, and cross section between 1 and 10 barns (c.f., plotted cross sections in the ENDF web portal, <https://www-nds.iaea.org/exfor/endl.htm> [222]).

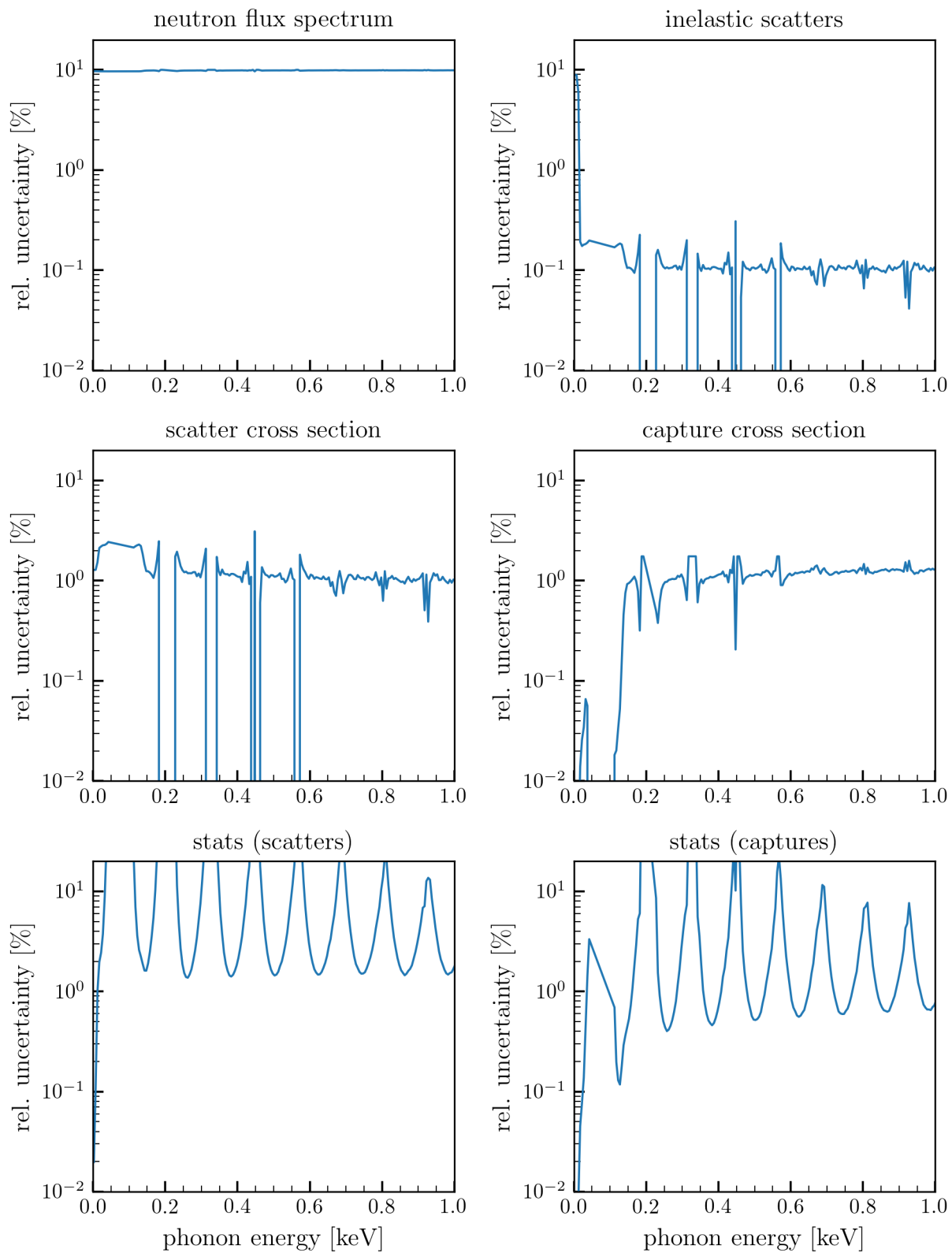


Figure 3.27: Uncertainties relative to the final total neutron-induced phonon spectrum by source

Table 3.6: Integrated uncertainties in the total neutron-induced event rate over the region of interest (≤ 1 keV)

| Source | Abs. Uncertainty [$\text{kg}^{-1} \text{ day}^{-1}$] | Rel. Uncertainty [%] |
|-----------------------|--|----------------------|
| neutron flux spectrum | 6.652 | 9.695 |
| inelastic scatters | 5.969 | 8.699 |
| scatter cross section | 0.879 | 1.280 |
| capture cross section | 0.017 | 0.024 |
| stats (scatters) | 0.060 | 0.087 |
| stats (captures) | 0.011 | 0.016 |

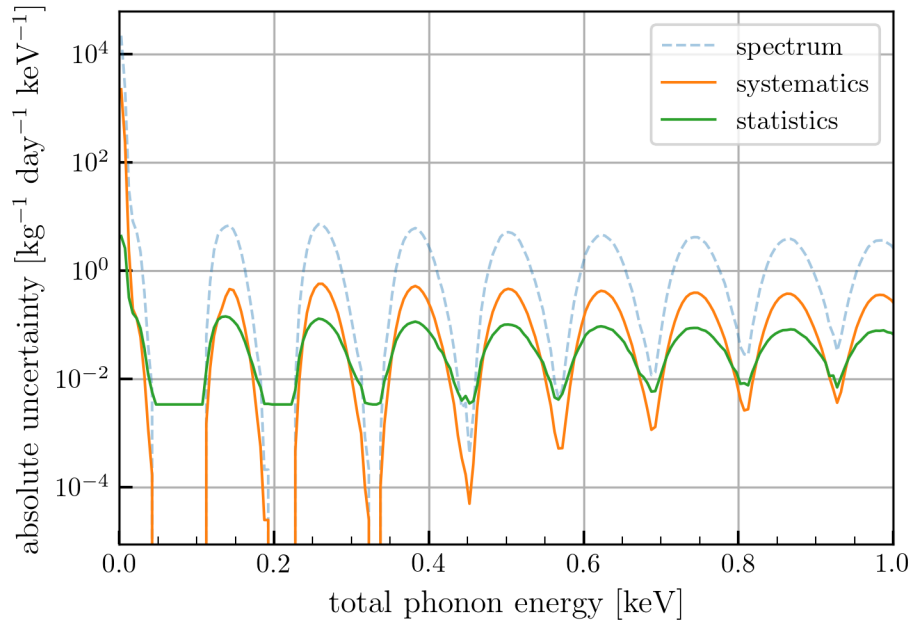


Figure 3.28: Absolute uncertainties due to systematic uncertainties and statistical uncertainties associated with MC procedure. Original neutron spectrum plotted in dashed blue for reference.

3.11 Discussion

In this chapter a model for neutron-induced backgrounds in SuperCDMS HVeV detectors has been developed using a novel semianalytical approach. A model of ambient radiogenic neutron fluxes was constructed using simulations of fast neutrons in the SNOLAB geometry and assuming a Maxwell-Boltzmann distribution for thermal neutrons. The spectrum of elastic-scatter-induced recoils, including multiple scatters, was calculated with analytical methods. An ionization model was introduced combining the Lindhard and Alig models. The neutron-induced spectrum was found to be highly clustered into rounded peaks spaced by ≈ 120 eV. The total rate below 1 keV was $68.61 \text{ kg}^{-1} \text{ day}^{-1}$.

The dominant errors in the neutron-induced spectrum were from uncertainty in the ambient neutron flux spectrum. A more accurate ionization model and a model incorporating charge collection efficiency of the detector could also substantially change the shape of the spectrum. The analysis did also not account for shielding materials surrounding the detector, nor the finite timing resolution of the HVeV detectors.

The primary value in this treatment is not the predicted neutron spectrum itself, as substantial uncertainties in its size and shape remain. Rather, it is our hope that the presentation of a novel method for calculating this spectrum, which does not rely on top-to-bottom simulations, will benefit future work in this vein. The semianalytical method presented allows one to partition the computation into distinct steps – simulation of the neutron spectrum, calculation of the collision rate, and simulation of the detector response – such that accumulating statistical errors can be kept to a minimum. Each step requiring simulation can be taken using results from the previous steps, and only requires modeling a brief part of the processes of particle production, propagation, and interaction. The probabilities of the simulated particles reaching the “endpoint” of each individual step are much larger than the probabilities for simulated particles to contribute to the final neutron-induced event spectrum in the detector. Thus statistical errors are kept much lower. In addition, individual steps can be revisited or modified to update or improve methods, without re-running from the beginning.

CHAPTER IV

CONCLUSIONS

The previous two chapters have investigated different aspects of neutron-induced backgrounds in searches for coherent-elastic neutrino-nucleus scatter (CENNS) and dark matter (DM). In these rare-event searches, where the events of interest are low-energy nuclear recoils, neutrons represent a substantial background that produces nuclear recoils indistinguishable from the events of interest.

The second chapter focused on CENNS searches using nuclear reactor antineutrinos. Thermal reactorogenic neutrons can drown out the CENNS signal by radiative capture on detector nuclei. In that chapter, the collection of datasets of CENNS, capture, and additional background events were simulated and analyzed for what level of ambient thermal neutron flux was necessary to make a high-significance measurement of CENNS with a detector with different energy resolutions.

The third chapter centered on the neutron-induced background in the HVeV detectors used by the SuperCDMS Collaboration for DM searches. A new semianalytical method for the computation of the neutron signal was presented. A neutron model based on simulations of fast neutron flux at SNOLAB was described. The resulting scatter recoil spectrum was calculated, including neutrons which undergo multiple interactions in the detector. The detector response was simulated using a new ionization model.

4.1 Main Takeaways

The central theme of this work is that neutrons represent a substantial background to searches for rare events that cause nuclear recoils, but the correct mitigation, analysis, or technology can overcome them. For CENNS searches, typical reactor-adjacent thermal neutron fluxes should be reduced by several orders of magnitude in order to measure CENNS at high significance, but making improvements to detector resolution can greatly help reach those targets. For DM searches, characterizing neutron backgrounds with the semianalytical methods presented can efficiently and accurately predict the neutron-induced signal in cryogenic silicon detectors.

For the most part, the detector resolution and thermal neutron flux requirements to detect CENNS are independent of a small amount of “other” backgrounds for today’s detectors. The baseline resolution is the most important individual determinant of whether a significant CENNS measurement can be made, but the effective resolution becomes more important as the baseline resolution gets finer. For the best detector resolutions available today ($\sigma_0 \sim 5$ eV), typical ambient thermal neutron fluxes should be reduced to about 10% of the standard sea level thermal neutron flux for a significant measurement in 100 kg yr deployment 10 m from a MW nuclear reactor. Germanium detectors are generally more sensitive to the CENNS signal, but do worse than silicon with coarser resolution.

For underground DM searches, methods combining simulation and analytical methods can be used to predict neutron-induced backgrounds in cryogenic silicon detectors. Such a prediction can be used to better constrain DM interaction rates and to search for a DM signal. Based on an approximate model of radiogenic neutrons and an ionization model combining the models of Alig and Lindhard, the neutron signal is expected to be separated into distinct rounded e/h pair peaks, with an approximate rate of 0.2 events $\text{kg}^{-1} \text{day}^{-1}$ each in the first few e/h pair peaks (and a rate of $\approx 67.1 \text{ kg}^{-1} \text{day}^{-1}$ in the zero e/h pair peak). The uncertainties in the semianalytical method were shown to be dominated by systematic uncertainties, particularly in the neutron flux spectrum.

4.2 Where To Go From Here?

There are many ways to carry the work from the last two chapters forward. Several improvements or adaptations of the work can be made immediately to make this work more useful.

For the CENNS work, further investigation of how the confidence of a measurement varies as a function of flux and resolution would be interesting, to determine empirical formulas for the required exposure or thermal flux for a particular case. Further investigations of neutron capture effects on CENNS searches should also expand to incorporate more realistic models of other radiogenic and cosmogenic backgrounds, especially elastic scatters with fast radiogenic neutrons. Modelling thermal fluxes in different shielding configurations can also yield valuable insight into what sorts of shielding are effective in shielding against both fast and slow neutrons.

For the work on neutron backgrounds at NEXUS, several improvements should be prioritized. Incorporating the detector timing resolution is one such modification. Likewise, analysis including a cosmogenic component to the neutron flux (or at minimum a better assessment of the uncertainty associated with the neutron flux in general) should be done in the near future. Including the effects of passive shielding elements in the detectors and attenuation of neutrons through fridge components should also be completed as soon as possible.

Slightly more involved analysis involving better simulation of the neutron spectrum, and in particular, analysis of the thermalization of neutrons and the form of the thermal part of the spectrum, can be done to minimize uncertainties in the neutron-induced event spectrum. It is also of great interest to the community to construct improved models of ionization in low-energy nuclear recoils, which agree with the newest experimental data. Such a model would eliminate a considerable part of the uncertainties in the shape of the spectrum.

REFERENCES

- ¹Z. Bell et al., “Neutron detection with cryogenics and semiconductors”, [physica status solidi \(c\) **2**, 1592–1605 \(2005\)](#).
- ²J. Dirk et al., “Terrestrial thermal neutrons”, [IEEE Transactions on Nuclear Science **50**, 2060–2064 \(2003\)](#).
- ³V. Kudryavtsev, P. Zakhary, and B. Easeman, “Neutron production in (α, n) reactions”, [Nuclear Instruments and Methods in Physics Research Section A: Accelerators, Spectrometers, Detectors and Associated Equipment **972**, 164095 \(2020\)](#).
- ⁴W. Pauli, *Open letter to the group of radioactive people at the Gauverein meeting in Tübinge*, <http://www.math.utah.edu/~beebe/talks/2015/qtm/pdf/pauli-1930-ltc.pdf>, Translated by Kurt Riesselmann, Dec. 4, 1930.
- ⁵A. D. Franklin and A. D. Marino, *Are there really neutrinos?: an evidential history*, 2nd ed. (CRC Press, 2020).
- ⁶F. Reines and C. L. Cowan, “Detection of the free neutrino”, [Phys. Rev. **92**, 830–831 \(1953\)](#).
- ⁷C. L. Cowan et al., “Detection of the free neutrino: a confirmation”, [Science **124**, 103–104 \(1956\)](#).
- ⁸F. Couchot et al., “Cosmological constraints on the neutrino mass including systematic uncertainties”, [Astronomy & Astrophysics **606**, A104 \(2017\)](#).
- ⁹M. Aker et al. (The KATRIN Collaboration), “Direct neutrino-mass measurement with sub-electronvolt sensitivity”, [Nature Physics **18**, 160–166 \(2022\)](#).
- ¹⁰A. Ianni, “Solar neutrinos and the solar model”, [Physics of the Dark Universe **4**, DARK TAUP2013, 44–49 \(2014\)](#).
- ¹¹A. Oralbaev, M. Skorokhvatov, and O. Titov, “The inverse beta decay: a study of cross section”, [Journal of Physics: Conference Series **675**, 012003 \(2016\)](#).
- ¹²G. Bertone and D. Hooper, “History of dark matter”, [Rev. Mod. Phys. **90**, 045002 \(2018\)](#).
- ¹³L. Roszkowski, E. M. Sessolo, and S. Trojanowski, “WIMP dark matter candidates and searches—current status and future prospects”, [Reports on Progress in Physics **81**, 066201 \(2018\)](#).
- ¹⁴E. Hubble and M. L. Humason, “The Velocity-Distance Relation among Extra-Galactic Nebulae”, [The Astrophysical Journal **74**, 43 \(1931\)](#).
- ¹⁵F. Zwicky, “Republication of: the redshift of extragalactic nebulae”, [General Relativity and Gravitation **41**, 207–224 \(2009\)](#), originally published: F. Zwicky, “Die Rotverschiebung von extragalaktischen Nebeln”, *Helv. Phys. Acta* **6**, 110–127 (1933).
- ¹⁶J. Ehlers, “Editorial note to: F. Zwicky the redshift of extragalactic nebulae”, [General Relativity and Gravitation **41**, 203–206 \(2009\)](#).
- ¹⁷V. C. Rubin and J. Ford W. Kent, “Rotation of the Andromeda Nebula from a Spectroscopic Survey of Emission Regions”, [The Astrophysical Journal **159**, 379 \(1970\)](#).
- ¹⁸I. S. Chandrasekhar, “The Time of Relaxation of Stellar Systems.”, [The Astrophysical Journal **93**, 285 \(1941\)](#).
- ¹⁹W. H. Press and P. Schechter, “Formation of Galaxies and Clusters of Galaxies by Self-Similar Gravitational Condensation”, [Astrophysical Journal **187**, 425–438 \(1974\)](#).
- ²⁰M. Davis, J. Huchra, D. W. Latham, and J. Tonry, “A survey of galaxy redshifts. II. The large scale space distribution.”, [Astrophysical Journal **253**, 423–445 \(1982\)](#).
- ²¹Ade, P. A. R. et al. (Planck Collaboration), “Planck 2013 results. XVI. cosmological parameters”, [A&A **571**, A16 \(2014\)](#).
- ²²N. Aghanim et al., “Planck 2018 results”, [Astronomy & Astrophysics **641**, A5 \(2020\)](#).
- ²³G. R. Blumenthal, S. M. Faber, J. R. Primack, and M. J. Rees, “Formation of galaxies and large-scale structure with cold dark matter”, [Nature **311**, 517–525 \(1984\)](#).

- ²⁴V. Springel et al., “Simulations of the formation, evolution and clustering of galaxies and quasars”, *Nature* **435**, 629–636 (2005).
- ²⁵M. Boylan-Kolchin et al., “Resolving cosmic structure formation with the Millennium-II Simulation”, *Monthly Notices of the Royal Astronomical Society* **398**, 1150–1164 (2009).
- ²⁶R. E. Angulo et al., “Scaling relations for galaxy clusters in the Millennium-XXL simulation”, *Monthly Notices of the Royal Astronomical Society* **426**, 2046–2062 (2012).
- ²⁷D. Clowe et al., “A direct empirical proof of the existence of dark matter*”, *The Astrophysical Journal* **648**, L109 (2006).
- ²⁸P. A. Zyla et al. (Particle Data Group), “Review of Particle Physics”, *Progress of Theoretical and Experimental Physics* **2020**, 083C01, 10.1093/ptep/ptaa104 (2020).
- ²⁹A. J. Biffi, A. Gevorgian, K. Harris, and A. N. Villano, *Critical background for CEvNS measurements at reactors*, under review; <https://arxiv.org/abs/2212.14148>, 2022.
- ³⁰D. Z. Freedman, “Coherent effects of a weak neutral current”, *Phys. Rev. D* **9**, 1389–1392 (1974).
- ³¹D. Baxter et al., “Coherent elastic neutrino-nucleus scattering at the European Spallation Source”, *Journal of High Energy Physics* **2020**, 10.1007/jhep02(2020)123 (2020).
- ³²X. Qian and J.-C. Peng, “Physics with reactor neutrinos”, *Reports on Progress in Physics* **82**, 036201 (2019).
- ³³B. Cañas, E. Garcés, O. Miranda, and A. Parada, “Future perspectives for a weak mixing angle measurement in coherent elastic neutrino nucleus scattering experiments”, *Physics Letters B* **784**, 159–162 (2018).
- ³⁴M. Cadeddu and F. Dordei, “Reinterpreting the weak mixing angle from atomic parity violation in view of the Cs neutron rms radius measurement from COHERENT”, *Phys. Rev. D* **99**, 033010 (2019).
- ³⁵X.-R. Huang and L.-W. Chen, “Neutron skin in CsI and low-energy effective weak mixing angle from COHERENT data”, *Phys. Rev. D* **100**, 071301 (2019).
- ³⁶D. Papoulias and T. Kosmas, “COHERENT constraints to conventional and exotic neutrino physics”, *Physical Review D* **97**, 10.1103/physrevd.97.033003 (2018).
- ³⁷J. Billard, J. Johnston, and B. J. Kavanagh, “Prospects for exploring new physics in coherent elastic neutrino-nucleus scattering”, *Journal of Cosmology and Astroparticle Physics* **2018**, 016–016 (2018).
- ³⁸O. G. Miranda, D. K. Papoulias, M. Tórtola, and J. W. F. Valle, “Probing neutrino transition magnetic moments with coherent elastic neutrino-nucleus scattering”, *Journal of High Energy Physics* **2019**, 10.1007/jhep07(2019)103 (2019).
- ³⁹H. Bonet et al., “First upper limits on neutrino electromagnetic properties from the CONUS experiment”, *The European Physical Journal C* **82**, 10.1140/epjc/s10052-022-10722-1 (2022).
- ⁴⁰D. Papoulias, “COHERENT constraints after the COHERENT-2020 quenching factor measurement”, *Physical Review D* **102**, 10.1103/physrevd.102.113004 (2020).
- ⁴¹M. Cadeddu et al., “Neutrino charge radii from COHERENT elastic neutrino-nucleus scattering”, *Physical Review D* **98**, 10.1103/physrevd.98.113010 (2018).
- ⁴²P. Coloma, I. Esteban, M. Gonzalez-Garcia, and J. Menéndez, “Determining the nuclear neutron distribution from coherent elastic neutrino-nucleus scattering: current results and future prospects”, *Journal of High Energy Physics* **2020**, 10.1007/JHEP08(2020)030 (2020).
- ⁴³M. Cadeddu, C. Giunti, Y. Li, and Y. Zhang, “Average CsI neutron density distribution from COHERENT data”, *Physical Review Letters* **120**, 10.1103/physrevlett.120.072501 (2018).
- ⁴⁴E. Ciuffoli, J. Evslin, Q. Fu, and J. Tang, “Extracting nuclear form factors with coherent neutrino scattering”, *Physical Review D* **97**, 10.1103/physrevd.97.113003 (2018).
- ⁴⁵D. Papoulias et al., “Constraining nuclear physics parameters with current and future COHERENT data”, *Physics Letters B* **800**, 135133 (2020).

- ⁴⁶M. Cadeddu et al., “Neutrino, electroweak, and nuclear physics from COHERENT elastic neutrino-nucleus scattering with refined quenching factor”, *Physical Review D* **101**, 10.1103/physrevd.101.033004 (2020).
- ⁴⁷C. Blanco, D. Hooper, and P. Machado, “Constraining sterile neutrino interpretations of the LSND and MiniBooNE anomalies with coherent neutrino scattering experiments”, *Physical Review D* **101**, 10.1103/physrevd.101.075051 (2020).
- ⁴⁸T. Kosmas, D. Papoulias, M. Tórtola, and J. Valle, “Probing light sterile neutrino signatures at reactor and spallation neutron source neutrino experiments”, *Physical Review D* **96**, 10.1103/physrevd.96.063013 (2017).
- ⁴⁹B. Dutta et al., “Sensitivity to oscillation with a sterile fourth generation neutrino from ultralow threshold neutrino-nucleus coherent scattering”, *Phys. Rev. D* **94**, 093002 (2016).
- ⁵⁰S.-F. Ge and I. M. Shoemaker, “Constraining photon portal dark matter with TEXONO and COHERENT data”, *Journal of High Energy Physics* **2018**, 10.1007/jhep11(2018)066 (2018).
- ⁵¹V. Brdar, W. Rodejohann, and X.-J. Xu, “Producing a new fermion in coherent elastic neutrino-nucleus scattering: from neutrino mass to dark matter”, *Journal of High Energy Physics* **2018**, 10.1007/jhep12(2018)024 (2018).
- ⁵²B. Dutta et al., “Dark matter signals from timing spectra at neutrino experiments”, *Physical Review Letters* **124**, 10.1103/physrevlett.124.121802 (2020).
- ⁵³C. Giunti, “General COHERENT constraints on neutrino nonstandard interactions”, *Physical Review D* **101**, 10.1103/physrevd.101.035039 (2020).
- ⁵⁴I. M. Shoemaker, “COHERENT search strategy for beyond standard model neutrino interactions”, *Physical Review D* **95**, 10.1103/physrevd.95.115028 (2017).
- ⁵⁵B. Dutta, R. Mahapatra, L. E. Strigari, and J. W. Walker, “Sensitivity to Z -prime and nonstandard neutrino interactions from ultralow threshold neutrino-nucleus coherent scattering”, *Phys. Rev. D* **93**, 10.1103/PhysRevD.93.013015 (2016).
- ⁵⁶P. Coloma, M. Gonzalez-Garcia, M. Maltoni, and T. Schwetz, “COHERENT enlightenment of the neutrino dark side”, *Physical Review D* **96**, 10.1103/physrevd.96.115007 (2017).
- ⁵⁷J. B. Dent et al., “Probing light mediators at ultralow threshold energies with coherent elastic neutrino-nucleus scattering”, *Physical Review D* **96**, 10.1103/physrevd.96.095007 (2017).
- ⁵⁸J. Liao and D. Marfatia, “COHERENT constraints on nonstandard neutrino interactions”, *Physics Letters B* **775**, 54–57 (2017).
- ⁵⁹J. B. Dent et al., “Accelerator and reactor complementarity in coherent neutrino-nucleus scattering”, *Physical Review D* **97**, 10.1103/physrevd.97.035009 (2018).
- ⁶⁰Y. Farzan, M. Lindner, W. Rodejohann, and X.-J. Xu, “Probing neutrino coupling to a light scalar with coherent neutrino scattering”, *Journal of High Energy Physics* **2018**, 10.1007/jhep05(2018)066 (2018).
- ⁶¹M. Abdullah et al., “Coherent elastic neutrino nucleus scattering as a probe of a Z' through kinetic and mass mixing effects”, *Physical Review D* **98**, 10.1103/physrevd.98.015005 (2018).
- ⁶²I. Esteban et al., “Updated constraints on non-standard interactions from global analysis of oscillation data”, *Journal of High Energy Physics* **2018**, 10.1007/jhep08(2018)180 (2018).
- ⁶³D. A. Sierra, V. D. Romeri, and N. Rojas, “COHERENT analysis of neutrino generalized interactions”, *Physical Review D* **98**, 10.1103/physrevd.98.075018 (2018).
- ⁶⁴T. Lasserre and H. W. Sobel, “Reactor neutrinos”, *Comptes Rendus Physique* **6**, Neutrino physics, 749–757 (2005).
- ⁶⁵Y. Kim, “Detection of antineutrinos for reactor monitoring”, *Nuclear Engineering and Technology* **48**, 285–292 (2016).
- ⁶⁶A. Bernstein et al., “Colloquium: neutrino detectors as tools for nuclear security”, *Rev. Mod. Phys.* **92**, 011003 (2020).

- ⁶⁷M. Bowen and P. Huber, “Reactor neutrino applications and coherent elastic neutrino nucleus scattering”, *Physical Review D* **102**, 10.1103/physrevd.102.053008 (2020).
- ⁶⁸B. Dutta and L. E. Strigari, “Neutrino physics with dark matter detectors”, *Annual Review of Nuclear and Particle Science* **69**, 137–161 (2019).
- ⁶⁹D. Z. Freedman, D. N. Schramm, and D. L. Tubbs, “The weak neutral current and its effects in stellar collapse”, *Annual Review of Nuclear Science* **27**, 167–207 (1977).
- ⁷⁰J. R. Wilson, “Coherent neutrino scattering and stellar collapse”, *Phys. Rev. Lett.* **32**, 849–852 (1974).
- ⁷¹F. Suekane, “Weinberg angle”, in *Quantum oscillations: a simple principle underlying important aspects of physics* (Springer International Publishing, Cham, 2021), pp. 57–71.
- ⁷²A. Drukier and L. Stodolsky, “Principles and applications of a neutral-current detector for neutrino physics and astronomy”, *Phys. Rev. D* **30**, 2295–2309 (1984).
- ⁷³D. Akimov et al., “Observation of coherent elastic neutrino-nucleus scattering”, *Science* **357**, 1123–1126 (2017).
- ⁷⁴E. Tiesinga, P. J. Mohr, D. B. Newell, and B. N. Taylor, *The 2018 CODATA recommended values of the fundamental physical constants (web version 8.1)*, edited by J. Baker, M. Douma, and S. Kotochigova, National Institute of Science and Technology, retrieved via `scipy.constants` python module, version 1.6.2, 2019.
- ⁷⁵S. R. Klein and J. Nystrand, “Exclusive vector meson production in relativistic heavy ion collisions”, *Phys. Rev. C* **60**, 014903 (1999).
- ⁷⁶J. Hakenmüller et al., “Neutron-induced background in the CONUS experiment”, *The European Physical Journal C* **79**, 699 (2019).
- ⁷⁷B. Scholz, “First observation of coherent elastic neutrino-nucleus scattering”, PhD thesis (University of Chicago, Chicago, IL, Dec. 2018).
- ⁷⁸T. A. Mueller et al., “Improved predictions of reactor antineutrino spectra”, *Phys. Rev. C* **83**, 054615 (2011).
- ⁷⁹G. Agnolet et al. (MINER Collaboration), “Background studies for the MINER Coherent Neutrino Scattering reactor experiment”, *Nuclear Instruments and Methods in Physics Research Section A: Accelerators, Spectrometers, Detectors and Associated Equipment* **853**, 53–60 (2017).
- ⁸⁰W. E. Ang, S. Prasad, and R. Mahapatra (MINER Collaboration), “Coherent elastic neutrino nucleus scatter response of semiconductor detectors to nuclear reactor antineutrinos”, *Nuclear Instruments and Methods in Physics Research Section A: Accelerators, Spectrometers, Detectors and Associated Equipment* **1004**, 165342 (2021).
- ⁸¹J. A. Formaggio, E. Figueroa-Feliciano, and A. J. Anderson, “Sterile neutrinos, coherent scattering, and oscillometry measurements with low-temperature bolometers”, *Phys. Rev. D* **85**, 013009 (2012).
- ⁸²J. Billard et al., “Coherent neutrino scattering with low temperature bolometers at Chooz reactor complex”, *Journal of Physics G: Nuclear and Particle Physics* **44**, 105101 (2017).
- ⁸³A. Leder et al., “Unfolding neutron spectrum with Markov Chain Monte Carlo at MIT research reactor with He-3 neutral current detectors”, *Journal of Instrumentation* **13**, P02004–P02004 (2018).
- ⁸⁴G. Beaulieu et al. (Ricochet Collaboration), *Ricochet progress and status*, <https://arxiv.org/abs/2111.06745>, 2021.
- ⁸⁵G. Fernandez Moroni et al., “Charge coupled devices for detection of coherent neutrino-nucleus scattering”, *Phys. Rev. D* **91**, 072001 (2015).
- ⁸⁶A. Aguilar-Arevalo et al. (CONNIE Collaboration), *The CONNIE experiment*, 2016.
- ⁸⁷A. Aguilar-Arevalo et al. (CONNIE Collaboration), “Exploring low-energy neutrino physics with the coherent neutrino nucleus interaction experiment”, *Phys. Rev. D* **100**, 092005 (2019).
- ⁸⁸A. Aguilar-Arevalo et al. (CONNIE Collaboration), “Search for light mediators in the low-energy data of the CONNIE reactor neutrino experiment”, *Journal of High Energy Physics* **2020**, 10.1007/jhep04(2020)054 (2020).

- ⁸⁹H. Bonet et al., “Constraints on elastic neutrino nucleus scattering in the fully coherent regime from the CONUS experiment”, *Physical Review Letters* **126**, 10.1103/physrevlett.126.041804 (2021).
- ⁹⁰J. Colaresi et al., “First results from a search for coherent elastic neutrino-nucleus scattering at a reactor site”, *Phys. Rev. D* **104**, 072003 (2021).
- ⁹¹J. Colaresi et al., “Measurement of coherent elastic neutrino-nucleus scattering from reactor antineutrinos”, *Phys. Rev. Lett.* **129**, 211802 (2022).
- ⁹²R. Strauss et al., “The ν -cleus experiment: a gram-scale fiducial-volume cryogenic detector for the first detection of coherent neutrino–nucleus scattering”, *The European Physical Journal C* **77**, 10.1140/epjc/s10052-017-5068-2 (2017).
- ⁹³R. Strauss et al., “Gram-scale cryogenic calorimeters for rare-event searches”, *Phys. Rev. D* **96**, 022009 (2017).
- ⁹⁴G. Angloher et al., “Exploring CE ν NS with NUCLEUS at the Chooz nuclear power plant”, *The European Physical Journal C* **79**, 1018 (2019).
- ⁹⁵R. Strauss, J. Rothe, F. Petricca, and S. Schönert, “The ν -cleus experiment: gram-scale cryogenic calorimeters for a discovery of coherent neutrino scattering”, *Journal of Physics: Conference Series* **1342**, 012132 (2020).
- ⁹⁶V. Belov et al., “The ν GeN experiment at the Kalinin nuclear power plant”, *Journal of Instrumentation* **10**, P12011 (2015).
- ⁹⁷D. Y. Akimov et al., “The RED-100 two-phase emission detector”, *Instruments and Experimental Techniques* **60**, 175–181 (2017).
- ⁹⁸D. Y. Akimov et al., “Coherent elastic neutrino scattering on atomic nucleus: recently discovered type of low-energy neutrino interaction”, *Physics-Uspekhi* **62**, 166 (2019).
- ⁹⁹D. Akimov et al., “First ground-level laboratory test of the two-phase xenon emission detector RED-100”, *Journal of Instrumentation* **15**, P02020 (2020).
- ¹⁰⁰H. T.-K. Wong, “Taiwan experiment on neutrino – history, status and prospects”, 10.48550/ARXIV.1608.00306 (2016).
- ¹⁰¹L. Singh and H. Wong, “Low energy neutrino physics with sub-keV Ge-detectors at Kuo-Sheng neutrino laboratory”, *Journal of Physics: Conference Series* **888**, 012124 (2017).
- ¹⁰²M. K. Singh et al., “Background rejection of TEXONO experiment to explore the sub-keV energy region with HPGe detector”, *Indian Journal of Physics* **91**, 1277–1291 (2017).
- ¹⁰³M. K. Singh et al., “Constraints on bosonic dark matter with low threshold germanium detector at Kuo-Sheng reactor neutrino laboratory”, *Chinese Journal of Physics* **58**, 63–74 (2019).
- ¹⁰⁴K. Ni, J. Qi, E. Shockley, and Y. Wei, “Sensitivity of a liquid xenon detector to neutrino–nucleus coherent scattering and neutrino magnetic moment from reactor neutrinos”, *Universe* **7**, 10.3390/universe7030054 (2021).
- ¹⁰⁵R. Agnese et al., “Projected sensitivity of the SuperCDMS SNOLAB experiment”, *Physical Review D* **95**, 10.1103/physrevd.95.082002 (2017).
- ¹⁰⁶A. C. Hayes and P. Vogel, “Reactor neutrino spectra”, *Annual Review of Nuclear and Particle Science* **66**, 219–244 (2016).
- ¹⁰⁷F. von Feilitzsch, A. Hahn, and K. Schreckenbach, “Experimental beta-spectra from ^{239}Pu and ^{235}U thermal neutron fission products and their correlated antineutrino spectra”, *Physics Letters B* **118**, 162–166 (1982).
- ¹⁰⁸K. Schreckenbach, G. Colvin, W. Gelletly, and F. Von Feilitzsch, “Determination of the antineutrino spectrum from ^{235}U thermal neutron fission products up to 9.5 MeV”, *Physics Letters B* **160**, 325–330 (1985).
- ¹⁰⁹A. Hahn et al., “Antineutrino spectra from ^{241}Pu and ^{239}Pu thermal neutron fission products”, *Physics Letters B* **218**, 365–368 (1989).

- ¹¹⁰N. Haag et al., “Experimental determination of the antineutrino spectrum of the fission products of ^{238}U ”, *Phys. Rev. Lett.* **112**, 122501 (2014).
- ¹¹¹P. Vogel, “Conversion of electron spectrum associated with fission into the antineutrino spectrum”, *Phys. Rev. C* **76**, 025504 (2007).
- ¹¹²A. C. Hayes et al., “Systematic uncertainties in the analysis of the reactor neutrino anomaly”, *Phys. Rev. Lett.* **112**, 202501 (2014).
- ¹¹³J. F. Briesmeister et al., *MCNPTM—A General Monte Carlo N-Particle Transport Code*, tech. rep. LA-13709-M, Code Version 4C (Los Alamos National Laboratory, Los Alamos, NM, USA, Dec. 2000).
- ¹¹⁴J. Tuli, “Evaluated nuclear structure data file”, *Nuclear Instruments and Methods in Physics Research Section A: Accelerators, Spectrometers, Detectors and Associated Equipment* **369**, 506–510 (1996).
- ¹¹⁵O. Tengblad et al., “Integral $\bar{\nu}$ -spectra derived from experimental β -spectra of individual fission products”, *Nuclear Physics A* **503**, 136–160 (1989).
- ¹¹⁶G. Rudstam et al., “Beta and gamma spectra of short-lived fission products”, *Atomic Data and Nuclear Data Tables* **45**, 239–320 (1990).
- ¹¹⁷S. Borg et al., “On-line separation of isotopes at a reactor in Studsvik (OSIRIS)”, *Nuclear Instruments and Methods* **91**, 109–116 (1971).
- ¹¹⁸J.-i. Katakura, T. Yoshida, K. Oyamatsu, and T. Tachibana, *JENDL fission product decay data file 2000*, tech. rep. JAERI-1343 (Japan Atomic Energy Research Institution, Japan, 2001).
- ¹¹⁹K. Takahashi, M. Yamada, and T. Kondoh, “Beta-decay half-lives calculated on the gross theory”, *Atomic Data and Nuclear Data Tables* **12**, 101–142 (1973).
- ¹²⁰J. Hardy, L. Carraz, B. Jonson, and P. Hansen, “The essential decay of pandemonium: a demonstration of errors in complex beta-decay schemes”, *Physics Letters B* **71**, 307–310 (1977).
- ¹²¹F. P. An et al., “Improved measurement of the reactor antineutrino flux and spectrum at Daya Bay”, *Chinese Physics C* **41**, 013002 (2017).
- ¹²²P. Vogel and J. Engel, “Neutrino electromagnetic form factors”, *Phys. Rev. D* **39**, 3378–3383 (1989).
- ¹²³M. Jalali, M. R. Abdi, and M. Mostajaboddavati, “Reactor power measurement by gamma and neutron radiation in heavy water zero power reactor (HWZPR)”, *Annals of Nuclear Energy* **57**, 368–374 (2013).
- ¹²⁴A. N. Villano, K. Harris, and S. Brown, “nrCascadeSim - a simulation tool for nuclear recoil cascades resulting from neutron capture”, *Journal of Open Source Software* **7**, 3993 (2022).
- ¹²⁵R. Agnese et al. (SuperCDMS Collaboration), “Search for low-mass dark matter with CDMSlite using a profile likelihood fit”, *Phys. Rev. D* **99**, 062001 (2019).
- ¹²⁶M. F. Albakry et al. (SuperCDMS Collaboration), “Ionization yield measurement in a germanium CDMSlite detector using photo-neutron sources”, *Phys. Rev. D* **105**, 122002 (2022).
- ¹²⁷R. B. Firestone et al., “The evaluated gamma-ray activation file (EGAF)”, *AIP Conference Proceedings* **769**, 219–224 (2005).
- ¹²⁸S. F. Mughabghab, *Thermal neutron capture cross sections resonance integrals and g-factors*, tech. rep. INDC(NDS)-440 (International Atomic Energy Agency, Brookhaven National Laboratory, Upton, NY, Feb. 2003).
- ¹²⁹J. Billard, E. Figueroa-Feliciano, and L. Strigari, “Implication of neutrino backgrounds on the reach of next generation dark matter direct detection experiments”, *Physical Review D* **89**, 10.1103/physrevd.89.023524 (2014).
- ¹³⁰R. Agnese et al. (SuperCDMS Collaboration), “Low-mass dark matter search with CDMSlite”, *Phys. Rev. D* **97**, 022002 (2018).
- ¹³¹S. S. Wilks, “The Large-Sample Distribution of the Likelihood Ratio for Testing Composite Hypotheses”, *Annals Math. Statist.* **9**, 60–62 (1938).
- ¹³²J. R. Taylor, *An introduction to error analysis: the study of uncertainties in physical measurements*, 2nd ed. (University Science Books, Sausalito, California, 1997).

- ¹³³G. Cowan, K. Cranmer, E. Gross, and O. Vitells, “Asymptotic formulae for likelihood-based tests of new physics”, *The European Physical Journal C* **71**, 10.1140/epjc/s10052-011-1554-0 (2011).
- ¹³⁴National Nuclear Data Center, Brookhaven National Laboratory, *NuDat (Nuclear Structure and Decay Data)*, Mar. 2008.
- ¹³⁵A. L. Garcia, *Numerical methods for physics*, 2nd ed., revised (Alejandro L. Garcia, 2015).
- ¹³⁶A. Wright, P. Mosteiro, B. Loer, and F. Calaprice, “A highly efficient neutron veto for dark matter experiments”, *Nuclear Instruments and Methods in Physics Research Section A: Accelerators, Spectrometers, Detectors and Associated Equipment* **644**, 18–26 (2011).
- ¹³⁷R. Calkins and B. Loer (SuperCDMS Collaboration), “Prototyping an Active Neutron Veto for SuperCDMS”, *AIP Conf. Proc.* **1672**, edited by J. L. Orrell, 140002 (2015).
- ¹³⁸M. Z. Nurazila, Y. Hafizal, and M. A. M. Harun, “Neutron attenuation and mechanical properties of polymer composites filled with boron carbide particles”, *IOP Conference Series: Materials Science and Engineering* **785**, 012005 (2020).
- ¹³⁹C. Awe et al., “Liquid scintillator response to proton recoils in the 10–100 keV range”, *Phys. Rev. C* **98**, 045802 (2018).
- ¹⁴⁰J. Hakenmüller and G. Heusser, “CONRAD — a low level germanium test detector for the CONUS experiment”, *Applied Radiation and Isotopes* **194**, 110669 (2023).
- ¹⁴¹M. J. Berger et al., *XCOM: photon cross section database*, <http://physics.nist.gov/xcom>, published by the National Institute of Standards and Technology (NIST), Gaithersburg, MD. Accessed 2021-12-08., 2010.
- ¹⁴²M. Estienne et al., “Updated summation model: an improved agreement with the daya bay antineutrino fluxes”, *Phys. Rev. Lett.* **123**, 022502 (2019).
- ¹⁴³R. Calkins (SuperCDMS Collaboration), “The SuperCDMS Soudan high threshold WIMP search and the planned SuperCDMS SNOLAB experiment”, *J. Phys. Conf. Ser.* **718**, 042009 (2016).
- ¹⁴⁴S. Agostinelli et al., “Geant4—a simulation toolkit”, *Nuclear Instruments and Methods in Physics Research Section A: Accelerators, Spectrometers, Detectors and Associated Equipment* **506**, 250–303 (2003).
- ¹⁴⁵G. Collaboration, *Geant4 physics reference manual rev 6.0* (2021).
- ¹⁴⁶Elsevier, *Scopus preview*, <https://www.scopus.com/home.uri>, Accessed March 2, 2023.
- ¹⁴⁷J. L. Beck and K. M. Zuev, “Rare-event simulation”, in *Handbook of uncertainty quantification* (Spring International Publishing, Switzerland, 2015).
- ¹⁴⁸R. J. Allen, C. Valeriani, and P. R. ten Wolde, “Forward flux sampling for rare event simulations”, *Journal of Physics: Condensed Matter* **21**, 463102 (2009).
- ¹⁴⁹D. Tytler, J. M. O’Meara, N. Suzuki, and D. Lubin, “Review of Big Bang nucleosynthesis and primordial abundances”, *Physica Scripta* **T85**, 12 (2000).
- ¹⁵⁰G. Steigman and M. S. Turner, “Cosmological constraints on the properties of weakly interacting massive particles”, *Nuclear Physics B* **253**, 375–386 (1985).
- ¹⁵¹S. W. Randall et al., “Constraints on the self-interaction cross section of dark matter from numerical simulations of the merging galaxy cluster 1E 0657–56”, *The Astrophysical Journal* **679**, 1173 (2008).
- ¹⁵²E. Aprile et al. (XENON Collaboration), “First dark matter search results from the XENON1T experiment”, *Phys. Rev. Lett.* **119**, 181301 (2017).
- ¹⁵³D. S. Akerib et al. (LUX Collaboration), “Results from a search for dark matter in the complete LUX exposure”, *Phys. Rev. Lett.* **118**, 021303 (2017).
- ¹⁵⁴A. Albert et al., “Searching for dark matter annihilation in recently discovered Milky Way satellites with FERMI-LAT”, *The Astrophysical Journal* **834**, 110 (2017).
- ¹⁵⁵B. Holdom, “Two U(1)’s and ϵ charge shifts”, *Physics Letters B* **166**, 196–198 (1986).
- ¹⁵⁶P. Galison and A. Manohar, “Two Z’s or not two Z’s?”, *Physics Letters B* **136**, 279–283 (1984).

- ¹⁵⁷R. Essig, J. Mardon, and T. Volansky, “Direct detection of sub-GeV dark matter”, *Phys. Rev. D* **85**, 076007 (2012).
- ¹⁵⁸J. Alexander et al., *Dark Sectors 2016 Workshop: Community Report*, 2016.
- ¹⁵⁹C. Boehm and P. Fayet, “Scalar dark matter candidates”, *Nuclear Physics B* **683**, 219–263 (2004).
- ¹⁶⁰M. Pospelov, A. Ritz, and M. Voloshin, “Secluded WIMP dark matter”, *Physics Letters B* **662**, 53–61 (2008).
- ¹⁶¹H. An, M. Pospelov, J. Pradler, and A. Ritz, “Direct detection constraints on dark photon dark matter”, *Physics Letters B* **747**, 331–338 (2015).
- ¹⁶²E. Izaguirre, G. Krnjaic, P. Schuster, and N. Toro, “Analyzing the discovery potential for light dark matter”, *Phys. Rev. Lett.* **115**, 251301 (2015).
- ¹⁶³T. Aralis et al. (SuperCDMS Collaboration), “Constraints on dark photons and axionlike particles from the SuperCDMS Soudan experiment”, *Phys. Rev. D* **101**, [Erratum: *Phys.Rev.D* 103, 039901 (2021)], 052008 (2020).
- ¹⁶⁴R. Essig et al., “Direct detection of sub-GeV dark matter with semiconductor targets”, *Journal of High Energy Physics* **2016**, 46 (2016).
- ¹⁶⁵M. W. Goodman and E. Witten, “Detectability of certain dark-matter candidates”, *Phys. Rev. D* **31**, 3059–3063 (1985).
- ¹⁶⁶E. Lopez-Asamar (SuperCDMS Collaboration), “SuperCDMS SNOLAB: status and prospects for measuring the coherent neutrino scattering”, *J. Phys. Conf. Ser.* **1216**, edited by J. Learned, 012020 (2019).
- ¹⁶⁷A. Aguilar-Arevalo et al. (DAMIC Collaboration), “Results on low-mass weakly interacting massive particles from an 11 kg d target exposure of DAMIC at SNOLAB”, *Phys. Rev. Lett.* **125**, 241803 (2020).
- ¹⁶⁸M. Crisler et al., “SENSEI: first direct-detection constraints on sub-GeV dark matter from a surface run”, *Physical Review Letters* **121**, 10.1103/physrevlett.121.061803 (2018).
- ¹⁶⁹E. Aprile et al., “The xenon1t dark matter experiment”, English, *The European Physical Journal C - Particles and Fields* **77**, Article (2017).
- ¹⁷⁰G. Angloher et al., “Results on light dark matter particles with a low-threshold CRESST-II detector”, *The European Physical Journal C* **76**, 25 (2016).
- ¹⁷¹R. Agnese et al. (SuperCDMS Collaboration), “First dark matter constraints from a SuperCDMS single-charge sensitive detector”, *Phys. Rev. Lett.* **121**, [Erratum: *Phys.Rev.Lett.* 122, 069901 (2019)], 051301 (2018).
- ¹⁷²J. Lewin and P. Smith, “Review of mathematics, numerical factors, and corrections for dark matter experiments based on elastic nuclear recoil”, *Astroparticle Physics* **6**, 87–112 (1996).
- ¹⁷³M. Pato, F. Iocco, and G. Bertone, “Dynamical constraints on the dark matter distribution in the Milky Way”, *Journal of Cosmology and Astroparticle Physics* **2015**, 001 (2015).
- ¹⁷⁴F. J. Kerr and D. Lynden-Bell, “Review of galactic constants”, *Monthly Notices of the Royal Astronomical Society* **221**, 1023–1038 (1986).
- ¹⁷⁵R. Schönrich, J. Binney, and W. Dehnen, “Local kinematics and the local standard of rest”, *Monthly Notices of the Royal Astronomical Society* **403**, 1829–1833 (2010).
- ¹⁷⁶P. J. McMillan and J. J. Binney, “The uncertainty in Galactic parameters”, *Monthly Notices of the Royal Astronomical Society* **402**, 934–940 (2010).
- ¹⁷⁷A. K. Drukier, K. Freese, and D. N. Spergel, “Detecting cold dark-matter candidates”, *Phys. Rev. D* **33**, 3495–3508 (1986).
- ¹⁷⁸K. Freese, M. Lisanti, and C. Savage, “Colloquium: annual modulation of dark matter”, *Rev. Mod. Phys.* **85**, 1561–1581 (2013).
- ¹⁷⁹F. Duncan, A. Noble, and D. Sinclair, “The construction and anticipated science of snolab”, *Annual Review of Nuclear and Particle Science* **60**, 163–180 (2010).

- ¹⁸⁰S. Fukuda et al. (Super-Kamiokande Collaboration), “Solar ^8B and hep neutrino measurements from 1258 days of Super-Kamiokande data”, *Phys. Rev. Lett.* **86**, 5651–5655 (2001).
- ¹⁸¹J. Hosaka et al. (Super-Kamiokande Collaboration), “Solar neutrino measurements in Super-Kamiokande-I”, *Phys. Rev. D* **73**, 112001 (2006).
- ¹⁸²Q. R. Ahmad et al. (SNO Collaboration), “Measurement of the rate of $\nu_e + d \rightarrow p + p + e^-$ interactions produced by ^8B solar neutrinos at the Sudbury Neutrino Observatory”, *Phys. Rev. Lett.* **87**, 071301 (2001).
- ¹⁸³Q. R. Ahmad et al. (SNO Collaboration), “Direct evidence for neutrino flavor transformation from neutral-current interactions in the Sudbury Neutrino Observatory”, *Phys. Rev. Lett.* **89**, 011301 (2002).
- ¹⁸⁴N. Jelley, A. B. McDonald, and R. H. Robertson, “The Sudbury Neutrino Observatory”, *Annual Review of Nuclear and Particle Science* **59**, 431–465 (2009).
- ¹⁸⁵D.-M. Mei and A. Hime, “Muon-induced background study for underground laboratories”, *Phys. Rev. D* **73**, 053004 (2006).
- ¹⁸⁶D. S. Akerib et al. (CDMS Collaboration), “First results from the cryogenic dark matter search in the Soudan underground laboratory”, *Phys. Rev. Lett.* **93**, 211301 (2004).
- ¹⁸⁷D. S. Akerib et al. (CDMS Collaboration), “Exclusion limits on the WIMP-nucleon cross section from the first run of the cryogenic dark matter search in the Soudan underground laboratory”, *Phys. Rev. D* **72**, 052009 (2005).
- ¹⁸⁸D. S. Akerib et al., *Limits on spin-dependent wimp-nucleon interactions from the cryogenic dark matter search*, tech. rep. FERMILAB-PUB-05-454-E (Fermi National Accelerator Lab (FNAL), Batavia, IL, Sept. 2005).
- ¹⁸⁹D. S. Akerib et al. (CDMS Collaboration), “Limits on spin-independent wimp-nucleon interactions from the two-tower run of the cryogenic dark matter search”, *Phys. Rev. Lett.* **96**, 011302 (2006).
- ¹⁹⁰CDMS Collaboration, “Dark matter search results from the cdms ii experiment”, *Science* **327**, 1619–1621 (2010).
- ¹⁹¹R. Agnese et al. (CDMS Collaboration), “Silicon detector dark matter results from the final exposure of CDMS II”, *Phys. Rev. Lett.* **111**, 251301 (2013).
- ¹⁹²R. Agnese et al. (SuperCDMS Collaboration), “Improved wimp-search reach of the cdms ii germanium data”, *Phys. Rev. D* **92**, 072003 (2015).
- ¹⁹³R. Agnese et al. (SuperCDMS Collaboration), “Results from the super cryogenic dark matter search experiment at Soudan”, *Phys. Rev. Lett.* **120**, 061802 (2018).
- ¹⁹⁴W. Rau (SuperCDMS Collaboration), “SuperCDMS SNOLAB - status and plans”, *J. Phys. Conf. Ser.* **1342**, edited by K. Clark et al., 012077 (2020).
- ¹⁹⁵M. F. Albakry et al. (SuperCDMS Collaboration), “A strategy for low-mass dark matter searches with cryogenic detectors in the SuperCDMS SNOLAB facility”, in 2022 Snowmass Summer Study (Mar. 2022).
- ¹⁹⁶N. Mast, *NEXUS@FNAL status and plans*, tech. rep. FERMILAB-SLIDES-20-059-V (Fermi National Accelerator Laboratory, Batavia, IL, 2020).
- ¹⁹⁷F. D. E. Company, *NuMI tunnels and halls: geotechnical baseline report*, tech. rep. Attachment to Exhibit A, Contract 6-7-4 (Fermi National Accelerator Laboratory, Batavia, IL, Aug. 1999).
- ¹⁹⁸C. Jacoboni and L. Reggiani, “The monte carlo method for the solution of charge transport in semiconductors with applications to covalent materials”, *Rev. Mod. Phys.* **55**, 645–705 (1983).
- ¹⁹⁹P. Luke et al., “Calorimetric ionization detector”, *Nuclear Instruments and Methods in Physics Research Section A: Accelerators, Spectrometers, Detectors and Associated Equipment* **289**, 406–409 (1990).
- ²⁰⁰B. Neganov and V. Trofimov, “Colorimetric method measuring ionizing radiation”, *Otkryt. Izobret* **146**, 53 (1985).
- ²⁰¹K. D. Irwin et al., “A quasiparticle-trap-assisted transition-edge sensor for phonon-mediated particle detection”, *Review of Scientific Instruments* **66**, 5322–5326 (1995).

- ²⁰²N. Mast et al., “Performance of the first 150 mm diameter cryogenic silicon ionization detectors with contact-free electrodes”, *Nuclear Instruments and Methods in Physics Research Section A: Accelerators, Spectrometers, Detectors and Associated Equipment* **904**, 15–22 (2018).
- ²⁰³R. K. Romani et al., “Thermal detection of single e-h pairs in a biased silicon crystal detector”, *Applied Physics Letters* **112**, 043501 (2018).
- ²⁰⁴Z. Hong et al., “Single electron–hole pair sensitive silicon detector with surface event discrimination”, *Nuclear Instruments and Methods in Physics Research Section A: Accelerators, Spectrometers, Detectors and Associated Equipment* **963**, 163757 (2020).
- ²⁰⁵D. W. Amaral et al., “Constraints on low-mass, relic dark matter candidates from a surface-operated supercdms single-charge sensitive detector”, *Phys. Rev. D* **102**, 091101 (2020).
- ²⁰⁶R. Ren et al., “Design and characterization of a phonon-mediated cryogenic particle detector with an eV-scale threshold and 100 keV-scale dynamic range”, *Phys. Rev. D* **104**, 032010 (2021).
- ²⁰⁷S. Ahlen et al., “Limits on cold dark matter candidates from an ultralow background germanium spectrometer”, *Physics Letters B* **195**, 603–608 (1987).
- ²⁰⁸D. O. Caldwell et al., “Laboratory limits on galactic cold dark matter”, *Phys. Rev. Lett.* **61**, 510–513 (1988).
- ²⁰⁹K. Mizukoshi et al., “Measurement of ambient neutrons in an underground laboratory at the Kamioka Observatory”, *Progress of Theoretical and Experimental Physics* **2018**, 123C01, 10.1093/ptep/pty133 (2018).
- ²¹⁰B. Aharmim et al., “Cosmogenic neutron production at the Sudbury Neutrino Observatory”, *Physical Review D* **100**, 10.1103/physrevd.100.112005 (2019).
- ²¹¹Y. S. Yoon, J. Kim, and H. Park, “Neutron background measurement for rare event search experiments in the YangYang underground laboratory”, *Astroparticle Physics* **126**, 102533 (2021).
- ²¹²J. A. Formaggio and C. Martoff, “Backgrounds to sensitive experiments underground”, *Annual Review of Nuclear and Particle Science* **54**, 361–412 (2004).
- ²¹³R. Calkins, *Snolab cavern neutron flux spectra*, unpublished, 2015.
- ²¹⁴I. T. Lawson, *Analysis of rock samples from the new laboratory*, tech. rep. SNOLAB-STR-2007-003 (SNOLAB, Creighton Mine, Ontario, Dec. 2005).
- ²¹⁵D. Tiwari, *Characterizing the snolab radiation environment*, https://indico.cern.ch/event/776181/contributions/3349456/attachments/1855267/3047005/DT_CAP2019.pdf, Conference presentation, 2019.
- ²¹⁶*SNOLAB user’s handbook*, Internal documentation. (see also [215]), Creighton Mine, Ontario, June 2006.
- ²¹⁷F. Reif, *Fundamentals of statistical and thermal physics* (McGraw-Hill, 1965).
- ²¹⁸F. E. Wietfeldt and G. L. Greene, “Colloquium: the neutron lifetime”, *Rev. Mod. Phys.* **83**, 1173–1192 (2011).
- ²¹⁹E. Moeller and N. G. Sjostrand, *Measurement of the slowing-down and thermalization time of neutrons in water*, tech. rep. AE-125, NUCLEAR PHYSICS AND RADIATION PHYSICS (Aktiebolaget Atomenergi, Sweden, 1963), p. 58.
- ²²⁰M. R. Anderson et al. (The SNO+ Collaboration), “Measurement of neutron-proton capture in the SNO+ water phase”, *Phys. Rev. C* **102**, 014002 (2020).
- ²²¹Y. Zhang et al., “First measurement of radioactive isotope production through cosmic-ray muon spallation in Super-Kamiokande IV”, *Physical Review D* **93**, 10.1103/physrevd.93.012004 (2016).
- ²²²D. Brown et al., “ENDF/B-VIII.0: the 8th major release of the nuclear reaction data library with CIELO-project cross sections, new standards and thermal scattering data”, *Nuclear Data Sheets* **148**, *Special Issue on Nuclear Reaction Data*, 1–142 (2018).
- ²²³W. Haack, J. L. Conlin, A. McCartney, and N. A. Gibson (Los Alamos National Laboratory), *ENDFtk*, <https://github.com/njoy/ENDFtk>, Accessed February 15, 2022, 2022.

- ²²⁴Cross Sections Evaluation Working Group, *ENDF-6 Formats Manual*, tech. rep. BNL-203218-INRE (Brookhaven National Laboratory, Upton, NY, Feb. 2018).
- ²²⁵W. H. Press, S. A. Teukolsky, W. T. Vetterling, and B. P. Flannery, *Numerical recipes in C*, 2nd ed. (Cambridge University Press, 1994).
- ²²⁶J. Lindhard, V. Nielsen, M. Scharff, and P. Thomsen, “Integral equations governing radiation effects. (notes on atomic collisions, III)”, *Kgl. Danske Videnskab., Selskab. Mat. Fys. Medd.* **33** (1963).
- ²²⁷F. Izraelevitch et al., “A measurement of the ionization efficiency of nuclear recoils in silicon”, *Journal of Instrumentation* **12**, P06014 (2017).
- ²²⁸Y. Sarkis, A. Aguilar-Arevalo, and J. C. D’Olivo, “Study of the ionization efficiency for nuclear recoils in pure crystals”, *Physical Review D* **101**, 10.1103/physrevd.101.102001 (2020).
- ²²⁹P. Sorensen, “Atomic limits in the search for galactic dark matter”, *Physical Review D* **91**, 10.1103/physrevd.91.083509 (2015).
- ²³⁰R. Agnese et al. (CDMS Collaboration), “Nuclear-recoil energy scale in CDMS II silicon dark-matter detectors”, *Nuclear Instruments and Methods in Physics Research Section A: Accelerators, Spectrometers, Detectors and Associated Equipment* **905**, 71–81 (2018).
- ²³¹K. Ramanathan and N. Kurinsky, “Ionization yield in silicon for eV-scale electron-recoil processes”, *Phys. Rev. D* **102**, 063026 (2020).
- ²³²B. Tummers, *DataThief III*, <https://datathief.org/>.
- ²³³A. R. Sattler, “Ionization produced by energetic silicon atoms within a silicon lattice”, *Phys. Rev.* **138**, A1815–A1821 (1965).
- ²³⁴G. Gerbier et al., “Measurement of the ionization of slow silicon nuclei in silicon for the calibration of a silicon dark-matter detector”, *Phys. Rev. D* **42**, 3211–3214 (1990).
- ²³⁵P. Zecher et al., “Energy deposition of energetic silicon atoms within a silicon lattice”, *Phys. Rev. A* **41**, 4058–4061 (1990).
- ²³⁶B. L. Dougherty, “Measurements of ionization produced in silicon crystals by low-energy silicon atoms”, *Phys. Rev. A* **45**, 2104–2107 (1992).
- ²³⁷A. E. Chavarria et al., “Measurement of the ionization produced by sub-keV silicon nuclear recoils in a ccd dark matter detector”, *Phys. Rev. D* **94**, 082007 (2016).
- ²³⁸A. N. Villano et al., “First observation of isolated nuclear recoils following neutron capture for dark matter calibration”, *Phys. Rev. D* **105**, 083014 (2022).
- ²³⁹R. Ren, “Ionization yield measurements and low-energy background investigation using a SuperCDMS-HVeV detector”, PhD thesis (Northwestern University, Evanston, Illinois, Dec. 2022).
- ²⁴⁰M. F. Albakry et al., *First measurement of the nuclear-recoil ionization yield in silicon at 100 eV*, <https://doi.org/10.48550/arXiv.2303.02196>, 2023.
- ²⁴¹R. C. Alig, S. Bloom, and C. W. Struck, “Scattering by ionization and phonon emission in semiconductors”, *Phys. Rev. B* **22**, 5565–5582 (1980).
- ²⁴²S. W. Leman, “Invited review article: physics and monte carlo techniques as relevant to cryogenic, phonon, and ionization readout of cryogenic dark matter search radiation detectors”, *The Review of scientific instruments* **83**, 10.1063/1.4747490 (2012).
- ²⁴³K. P. O’Donnell and X. Chen, “Temperature dependence of semiconductor band gaps”, *Applied Physics Letters* **58**, 2924–2926 (1991).
- ²⁴⁴J. Ziman, *Electrons and Phonons: The Theory of Transport Phenomena in Solids* (Oxford University Press, Feb. 2001).
- ²⁴⁵E. O. Kane, “Electron scattering by pair production in silicon”, *Phys. Rev.* **159**, 624–631 (1967).
- ²⁴⁶L. Garrison, “Measurement of neutron and muon fluxes 100 m underground with the SciBath detector”, PhD thesis (Indiana University, Jan. 2014).

- ²⁴⁷M. Kurakado, “Possibility of high resolution detectors using superconducting tunnel junctions”, *Nuclear Instruments and Methods in Physics Research* **196**, 275–277 (1982).
- ²⁴⁸S. Leman et al., “Phonon quasidiffusion in cryogenic dark matter search large germanium detectors”, English (US), *Chinese Journal of Physics* **49**, 349–358 (2011).
- ²⁴⁹I. Alkhatib et al. (SuperCDMS Collaboration), “Light dark matter search with a high-resolution athermal phonon detector operated above ground”, *Phys. Rev. Lett.* **127**, 061801 (2021).
- ²⁵⁰C. W. Fink et al., “Performance of a large area photon detector for rare event search applications”, *Applied Physics Letters* **118**, 022601 (2021).
- ²⁵¹J. Hellmig et al., “The CDMS II z-sensitive ionization and phonon germanium detector”, *Nuclear Instruments and Methods in Physics Research Section A: Accelerators, Spectrometers, Detectors and Associated Equipment* **444**, 308–311 (2000).
- ²⁵²*Public Release of SuperCDMS SNOLAB HVeV Run2 Data*, <https://supercdms.slac.stanford.edu/public-data>, Public release accompanying ref. [205], Jan. 2021.
- ²⁵³F. Ponce et al., “Measuring the impact ionization and charge trapping probabilities in SuperCDMS HVeV phonon sensing detectors”, *Phys. Rev. D* **101**, 031101 (2020).
- ²⁵⁴M. J. Penn et al., “Charge collection and trapping in low-temperature silicon detectors”, *Journal of Applied Physics* **79**, 8179–8186 (1996).
- ²⁵⁵F. Ponce et al., “Modeling of impact ionization and charge trapping in SuperCDMS HVeV detectors”, *Journal of Low Temperature Physics* **199**, 598–605 (2020).
- ²⁵⁶J. O. Irwin, “On the frequency distribution of the means of samples from a population having any law of frequency with finite moments, with special reference to pearson’s type II”, *Biometrika* **19**, 225–239 (1927).
- ²⁵⁷P. Hall, “The distribution of means for samples of size n drawn from a population in which the variate takes values between 0 and 1, all such values being equally probable”, *Biometrika* **19**, 240–245 (1927).
- ²⁵⁸M. J. Penn, B. L. Dougherty, B. Cabrera, and D. L. Sisson, “Simultaneous measurement of phonons and ionization using silicon crystal acoustic detectors”, English, *Nuclear instruments & methods in physics research. Section A, Accelerators, spectrometers, detectors and associated equipment* **364**, 118–123 (1995).
- ²⁵⁹R. C. Alig, “Scattering by ionization and phonon emission in semiconductors. II. Monte Carlo calculations”, *Phys. Rev. B* **27**, 968–977 (1983).
- ²⁶⁰A. Owens, G. Fraser, and K. J. McCarthy, “On the experimental determination of the Fano factor in Si at soft X-ray wavelengths”, *Nuclear Instruments and Methods in Physics Research Section A: Accelerators, Spectrometers, Detectors and Associated Equipment* **491**, 437–443 (2002).

APPENDIX A

Additional data for unbinned CENNS significance analysis

This appendix contains additional data from the unbinned likelihood analysis of the significance of CENNS measurements in silicon described in Section 2.7.1.

Figure A.1 shows significance landscapes (analogous to Figure 2.5) for baseline resolutions of 5 eV (left) and 10 eV (right) in silicon. Black curves denote 5σ contours, as plotted in Figure 2.7. Note the missing data on the left hand side of the 10 eV plot, where points on the evaluated grid would have effective resolutions smaller than the baseline resolution. Note also that at all fluxes, effective resolution has little to no effect on the significance, for both baseline resolutions.

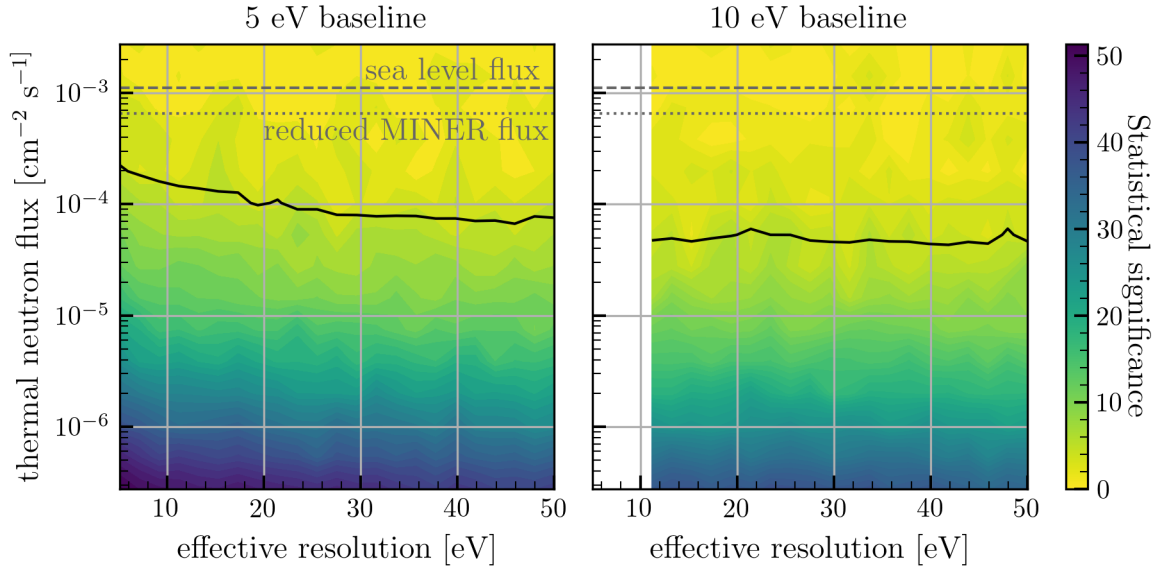


Figure A.1: Full significance landscapes for $\sigma_0 = 5$ eV (left) and 10 eV (right) in Si. Black curves indicate 5σ contours. Gray lines indicating reference fluxes are the same as in Figure 2.5.

APPENDIX B

Supplemental figures on the similarities between binned and unbinned likelihood analyses

This appendix contains extra figures showing the similarities in binned and unbinned analysis results from Section 2.7.2.

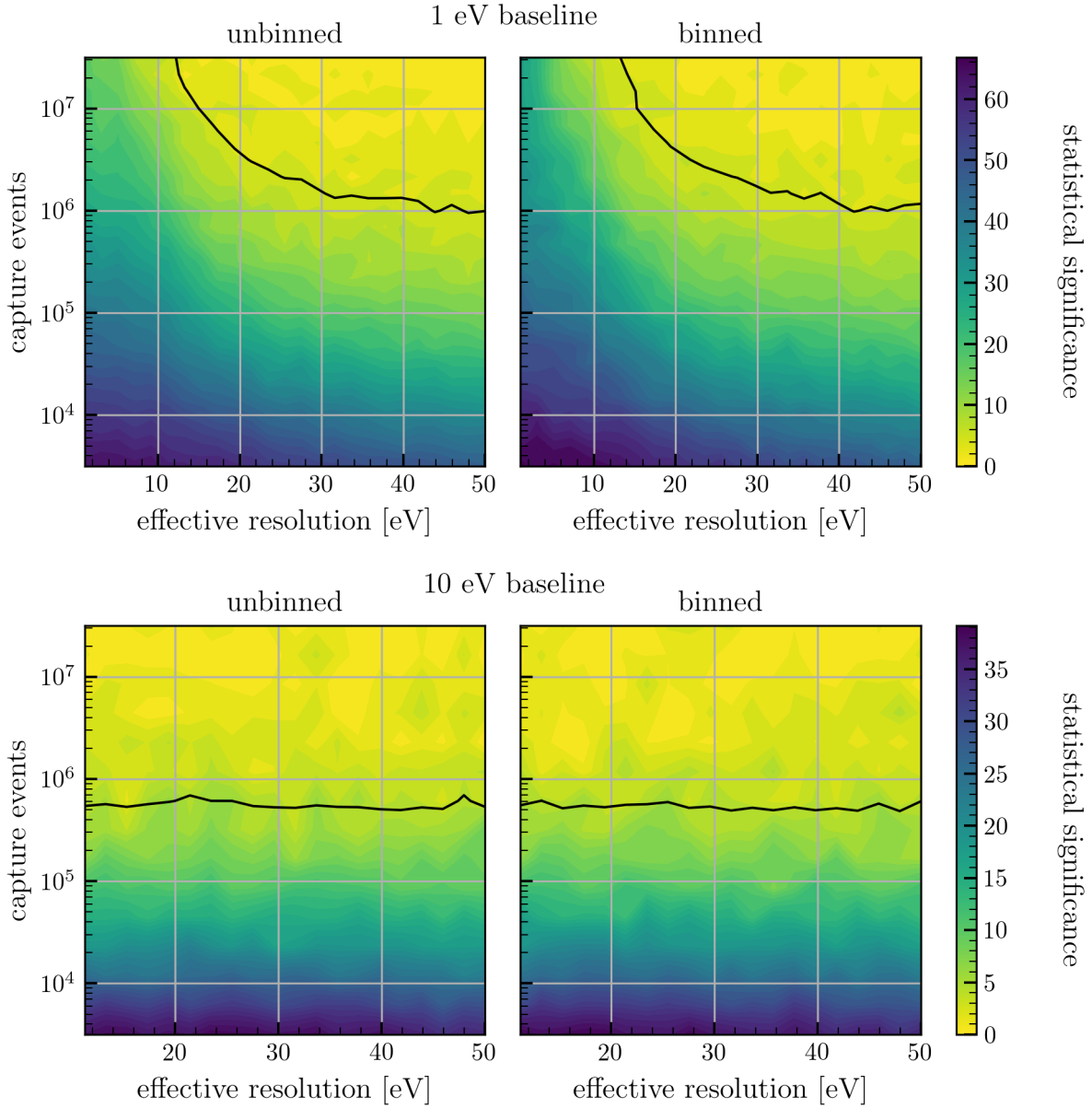


Figure B.1: Side-by-side comparisons analogous to Figure 2.8 for 1 eV and 10 eV baseline resolutions. Behaviors of the other baselines are similar to the 5 eV case

Figure B.1 shows side-by-side visual comparisons analogous to Figure 2.8 of Z landscape plots for 1 eV and 10 eV baseline resolutions. Like the 5 eV baseline data, the landscapes (and in particular the 5σ

contours) are consistent with each other. The unbinned analysis yields extremely similar results to the binned analysis.

Figure B.2 shows the histogram plotted in Figure 2.10 broken up by binning method. The figure shows that there may be some systematic variation between binnings in the variance of calculated Z values (e.g., the 0.25 eV distributions are more consistently close to a width of 1, while the logarithmic binnings are more spread out), though no conclusions can be drawn from this data alone. However, all binnings independently have standard deviations of approximately 1 (means of all four distributions individually are given in Table B.1).

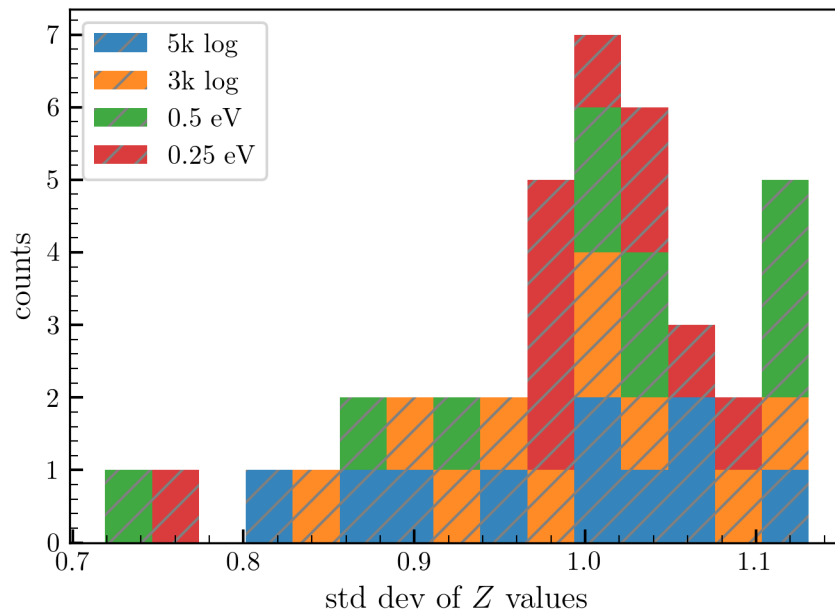


Figure B.2: Histogram shown in Figure 2.10 broken up by binning method

Table B.1: Average standard deviation of Z values for each binning method

| Binning | Avg. std. dev. |
|---------|----------------|
| 5k log | 0.982 |
| 3k log | 0.987 |
| 0.5 eV | 0.997 |
| 0.25 eV | 0.991 |

Figure B.3 shows Z landscape data for the same grid of points as the dense binned data plotted in Figure 2.11. Note the appearance of short lengths of “sawtooth”-like appearance in the 5σ contour, which has been relaxed four times.

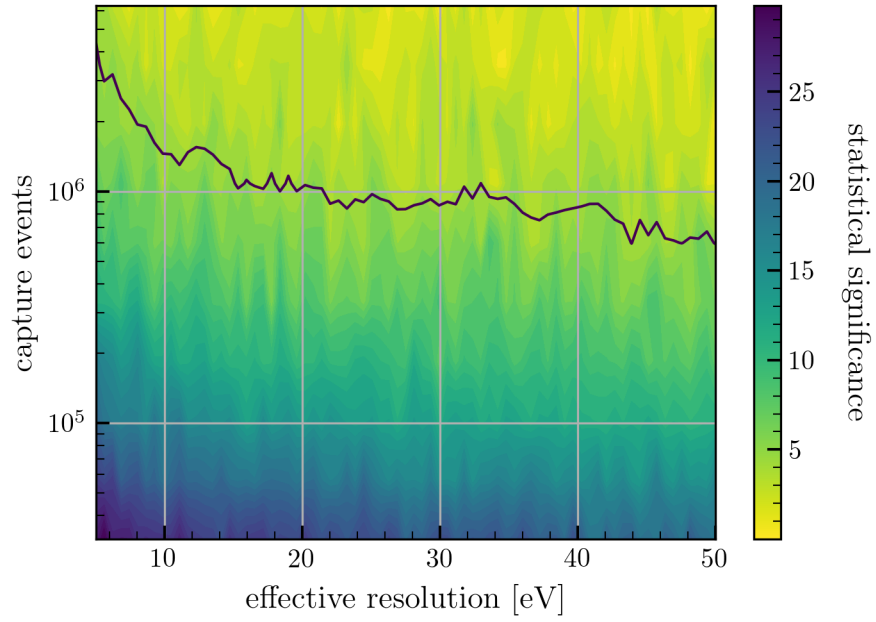


Figure B.3: Z landscape evaluated on the same grid of data points as the dense unbinned data introduced in Section 2.7.2.4

Figure B.4 shows unbinned, dense unbinned, and 3k log binned contours plotted in Figure 2.12 without smoothing.

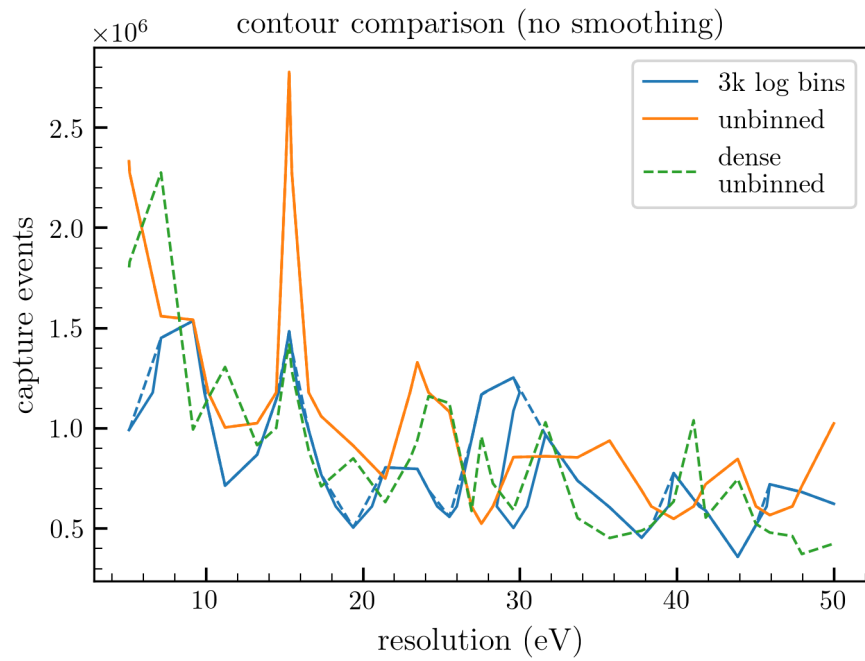


Figure B.4: Unbinned, dense unbinned, and 3k log binned 5σ contours without smoothing

Figure B.5 shows the relative difference between the unbinned and binned contours with the dense unbinned contour before smoothing. Analogous to Figure 2.13.

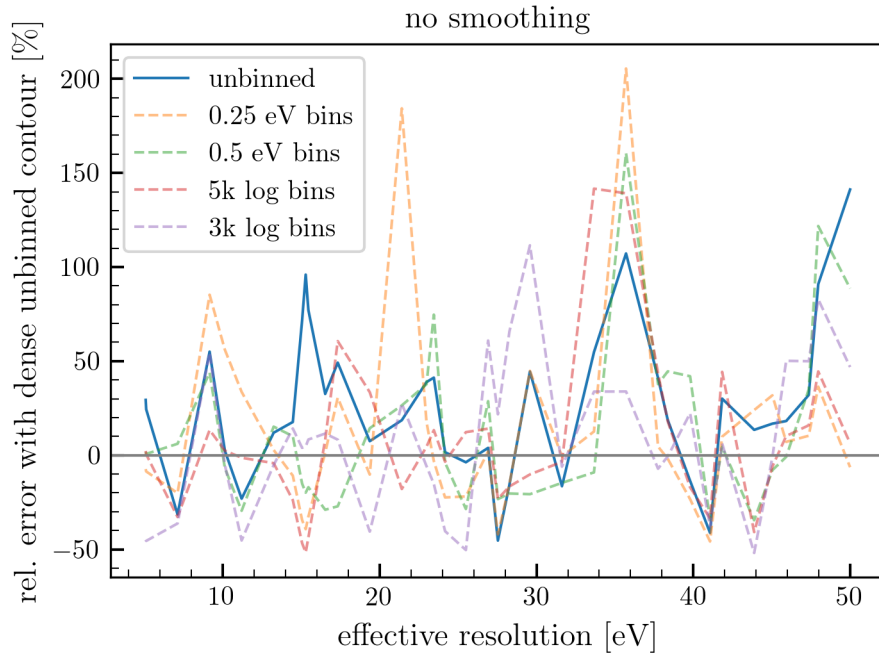


Figure B.5: Relative difference in unbinned and binned contours from dense unbinned contours (analogous to Figure 2.13 without smoothing the contours)

Table B.2 shows the scaled variance (2.7.1) for the unsmoothed contours plotted in Figure B.5.

Compare to scaled variance in the unsmoothed contours, listen in Table 2.6.

Table B.2: Scaled variances of unsmoothed contours

| Binning | Scaled Variance |
|--------------|-----------------|
| unbinned | 24.377 |
| 0.25 eV bins | 29.060 |
| 0.5 eV bins | 20.640 |
| 5k log bins | 17.895 |
| 3k log bins | 16.634 |

APPENDIX C

Sample maximum likelihood fits in binned analysis

This appendix shows sample ML fits used in the binned likelihood analysis, analogous to Figure 2.6, for the different background models used: flat, sloped, and combination. Once again, the black data points are the generated data samples (note the binning shown in this plot is not the binning used in analysis). Solid blue curves represent ML fit curves with a CENNS component, while orange curves represent the ML fit without a CENNS component. The dashed blue curves show the CENNS contribution to the solid blue curves. The second row of each figure shows a zoomed-in view of the boxed region in the figure above it.

For the fits in silicon, the fluxes and effective resolutions in this figure are the same as shown in Figure 2.6. The sigma values are all slightly different than the unbinned values. In the plots for Ge, the flux in the left and middle plots correspond to $\sim 3.16 \times 10^7$ capture events in Ge, and the right corresponds to $\sim 10^7$.

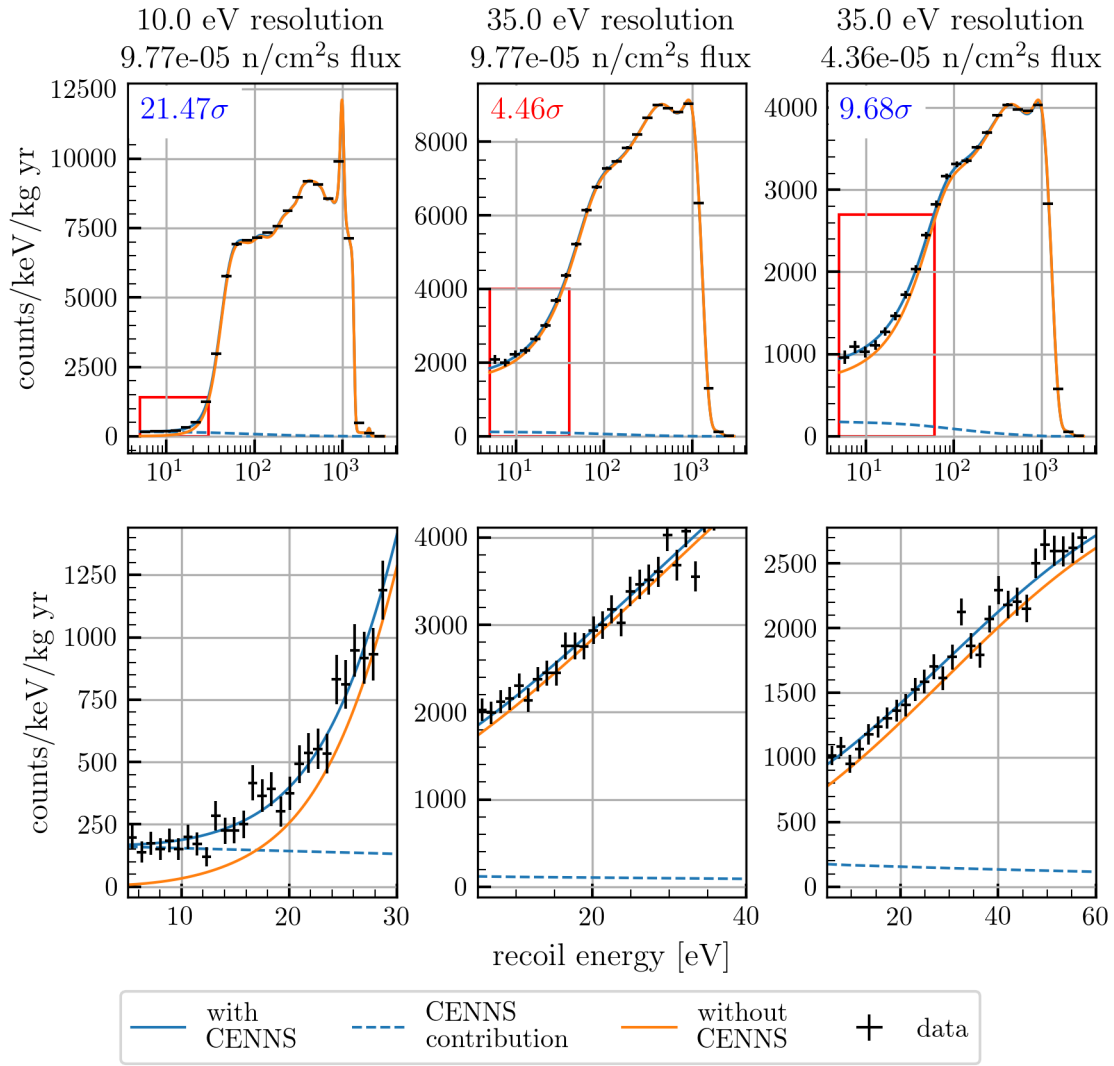


Figure C.1: Sample fits for flat background in Si

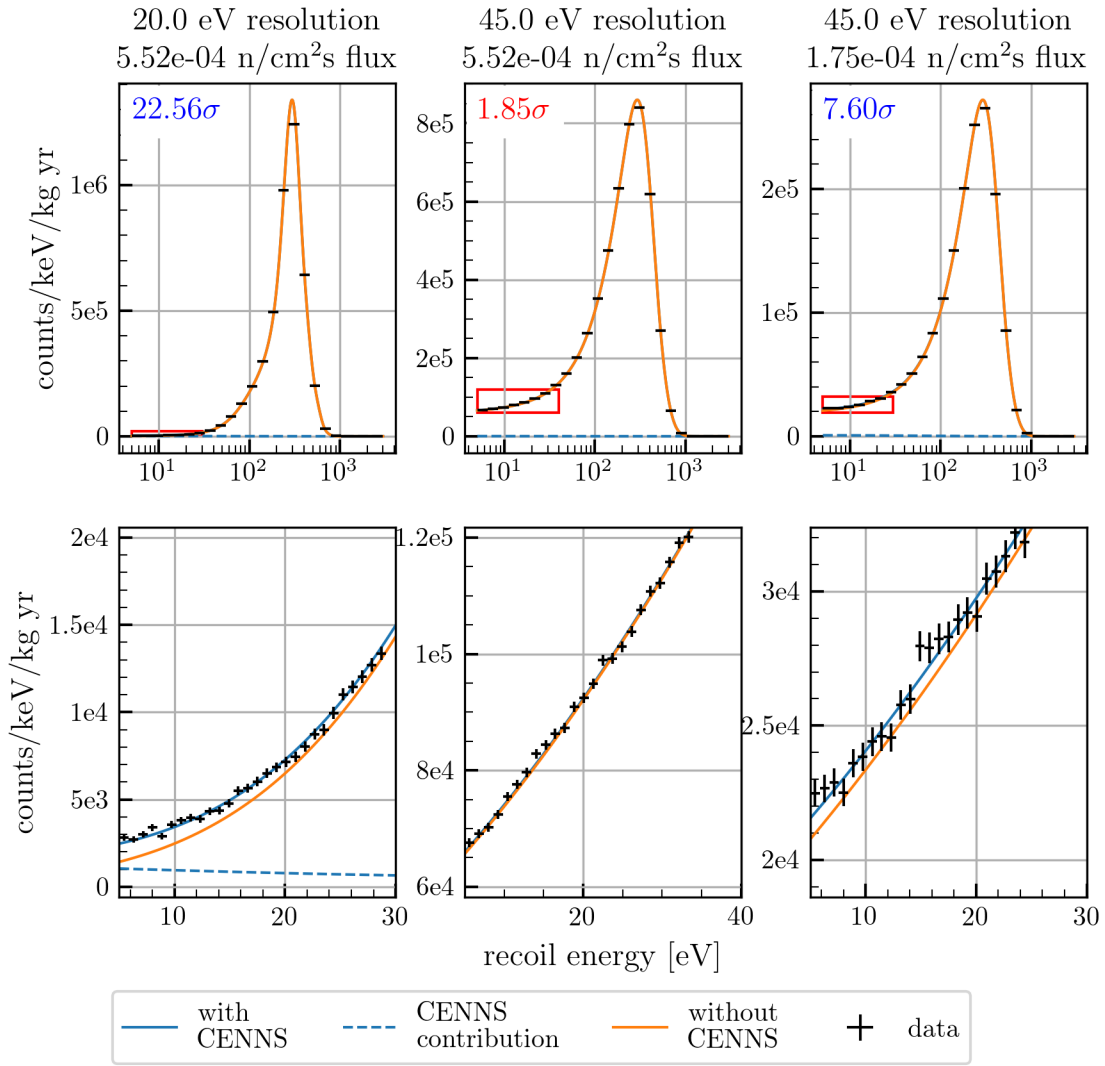


Figure C.2: Sample fits for flat background in Ge

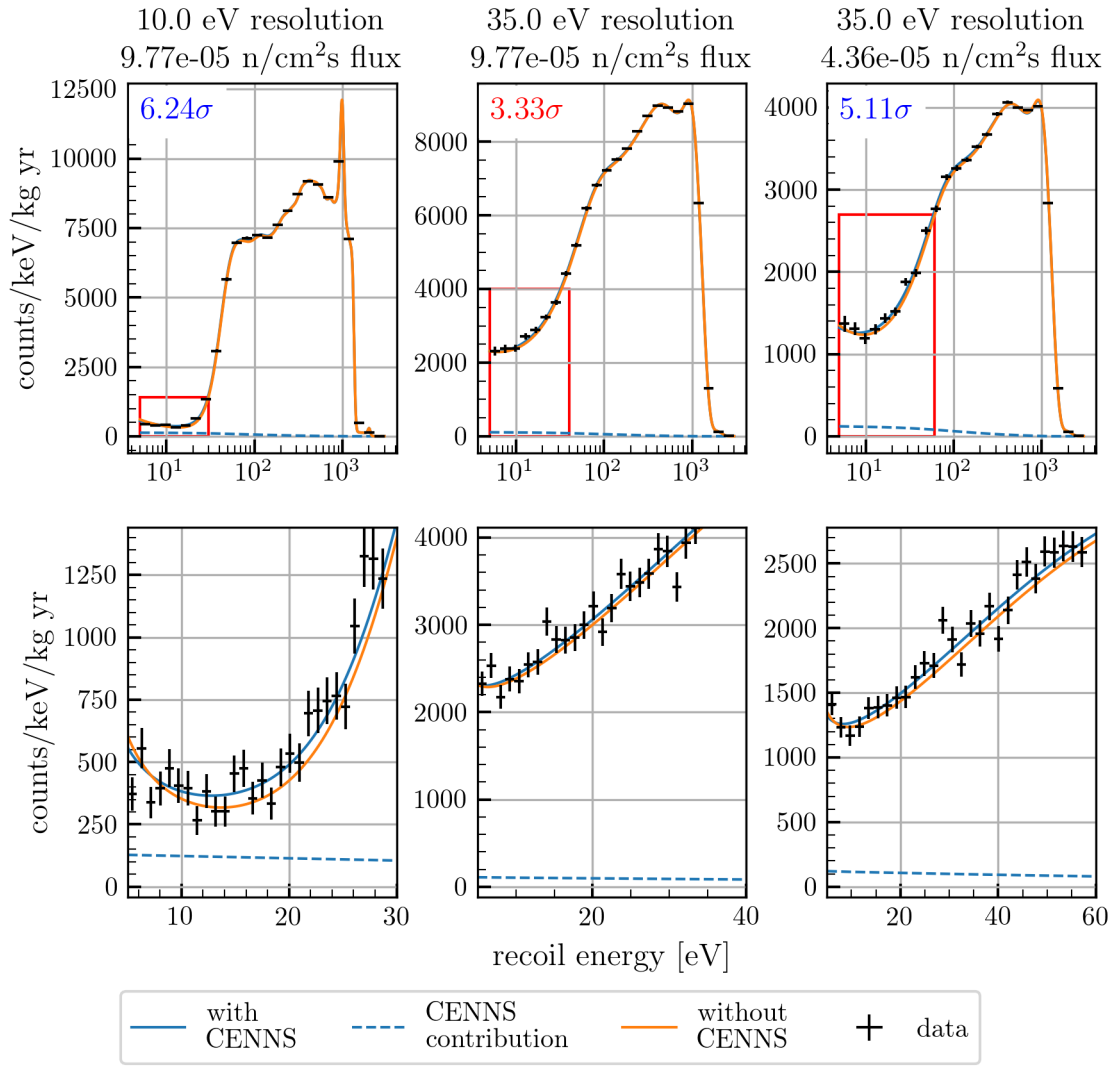


Figure C.3: Sample fits for sloped background in Si

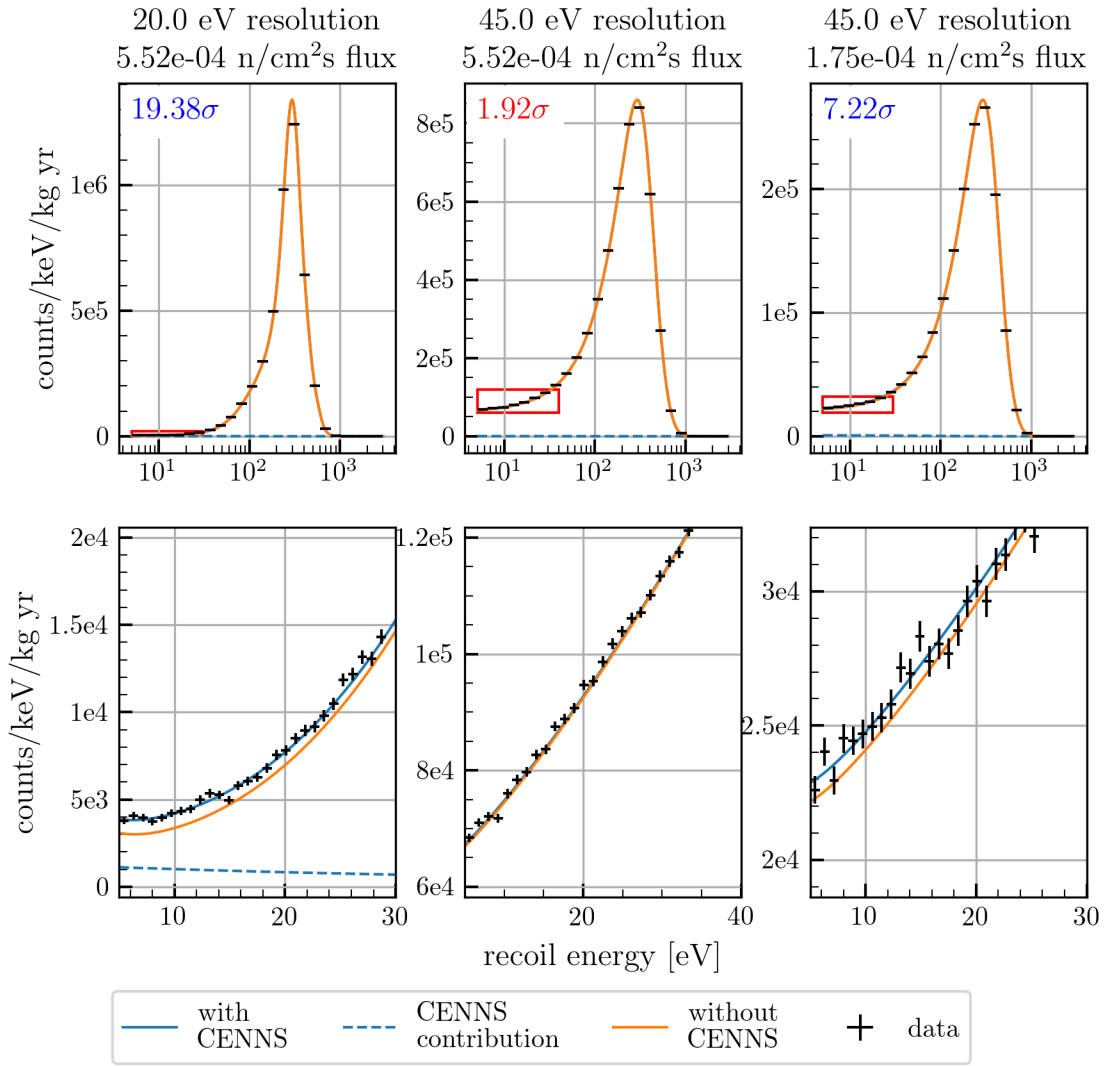


Figure C.4: Sample fits for sloped background in Ge

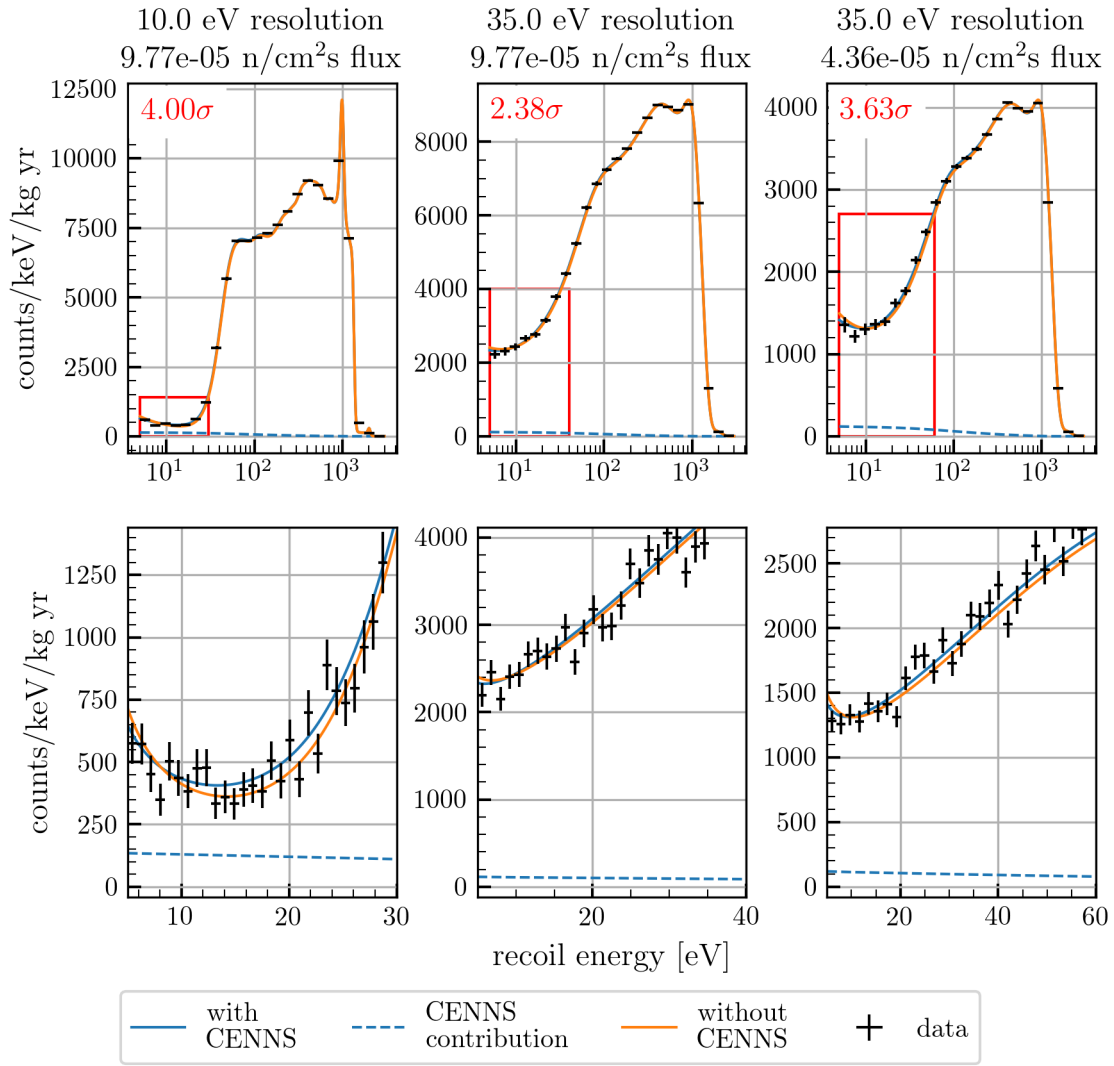


Figure C.5: Sample fits for combination background in Si

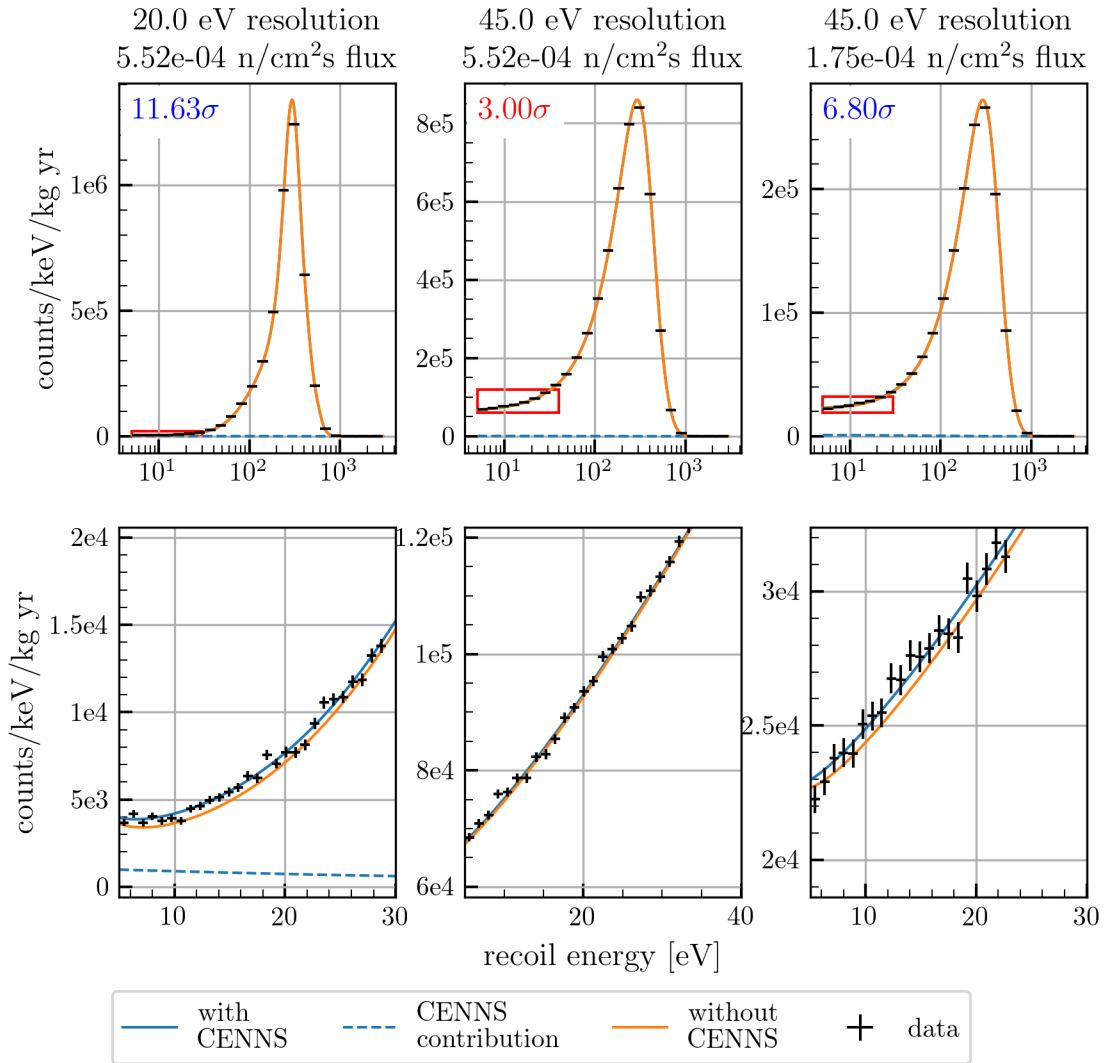


Figure C.6: Sample fits for combination background in Ge

APPENDIX D

Neutron elastic scatter cross sections with silicon

The evaluated neutron elastic-scatter cross sections in silicon are plotted in Figure D.1. Data taken from the ENDF database [222] online interface.⁴⁰ Plots show filled-in 1σ uncertainties in the cross section data, evaluated as described in Section 3.10.2.

⁴⁰See <https://www-nds.iaea.org/exfor/endl.htm>

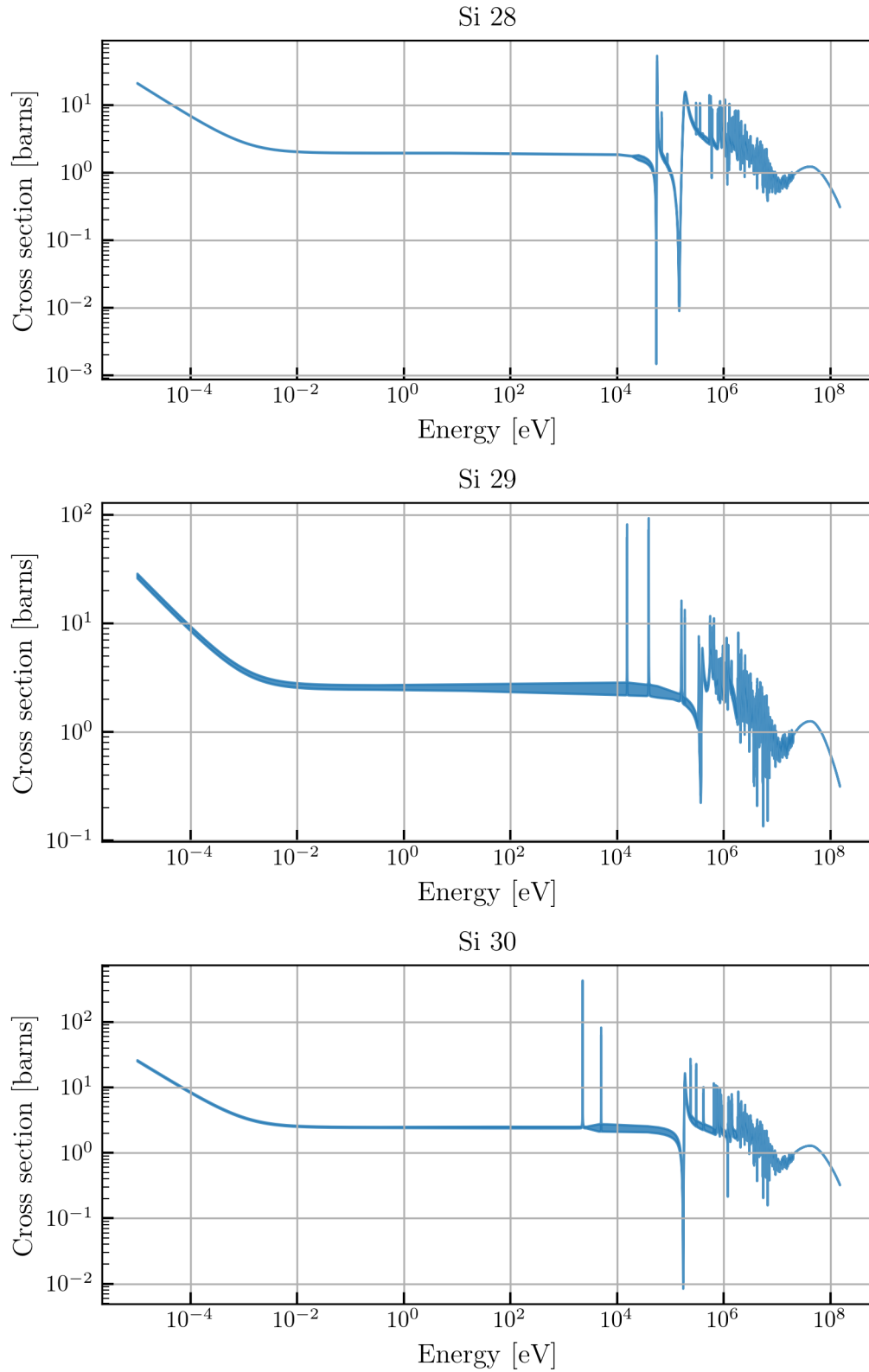


Figure D.1: Neutron elastic-scatter cross sections for silicon. Plots show shaded 1σ confidence intervals. Taken from ENDF/B-VIII.0 database, web interface

APPENDIX E

The characteristic length

In Section 3.6 in connection with the calculation of rates of multiple scattering, we encountered the characteristic length ℓ that depended on the detector geometry. This appendix goes into some detail about the method of its calculation.

Once again, the definition of ℓ is:

$$\ell = \frac{1}{V} \iint \frac{1}{4\pi|\mathbf{x} - \mathbf{x}'|^2} d^3\mathbf{x}' d^3\mathbf{x} \quad (\text{E.1})$$

For a rectangular detector with dimensions $l_x \times l_y \times l_z$, this integral can be expanded in Cartesian coordinates:

$$\ell = \frac{1}{4\pi V} \int_0^{l_x} dx \int_0^{l_x} dx' \int_0^{l_y} dy \int_0^{l_y} dy' \int_0^{l_z} dz \int_0^{l_z} dz' \frac{1}{(x - x')^2 + (y - y')^2 + (z - z')^2} \quad (\text{E.2})$$

However, this integral is not easily evaluated, whether by analytical nor numerical methods. Attempted evaluation of this integral as written by Monte Carlo methods converged extremely slowly. An alternative form of this integral was derived that could be evaluated more easily. This derivation follows.

For now we focus on the integration over one coordinate pair, x and x' (by symmetry, we could just as easily choose y and y' or z and z'). We perform a coordinate transformation to the variables μ and ν :

$$\mu = x + x' \quad (\text{E.3a})$$

$$\nu = x - x' \quad (\text{E.3b})$$

The integrand of (E.2) transforms into these new coordinates trivially. We need to transform the limits of integration and the element of area, $dx dx'$.

The region of integration in (x, x') space is a square of side length l_x with one corner at the origin (left side of Figure E.1). In (ν, μ) space, the square is tilted 45 degrees on its side (right side of Figure E.1). The area of the square in the transformed space is $2l_x^2$, where in the original space it is l_x^2 . So the area element $dx dx' = \frac{1}{2} d\mu d\nu$. The limits of integration can be read off of Figure E.1, yielding:

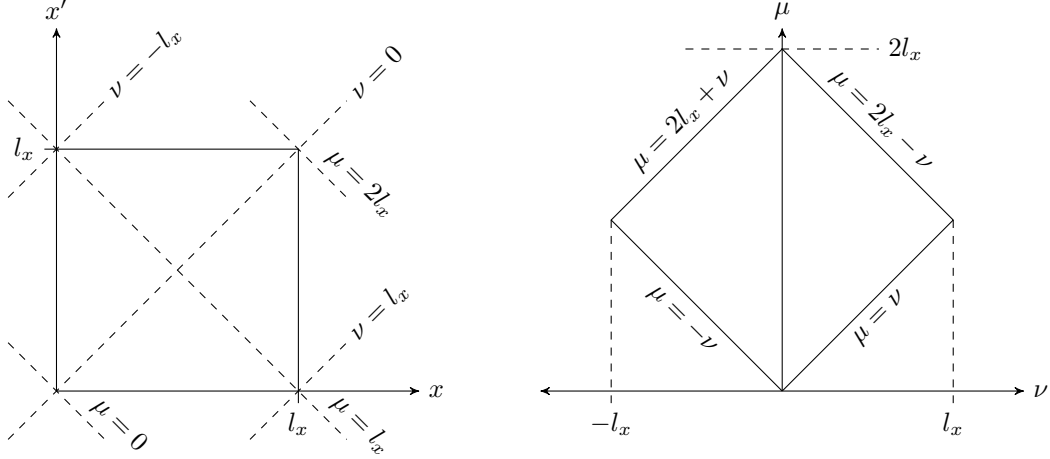


Figure E.1: Schematic of the square region of integration in (x, x') space (left) and (ν, μ) space (right). Equations for the line segments marking the sides of the square in (μ, ν) space are labelled.

$$\int_0^{l_x} dx \int_0^{l_x} dx' \frac{1}{(x-x')^2 + A} = \frac{1}{2} \int_{-l_x}^0 d\nu \int_{-\nu}^{2l_x+\nu} d\mu \frac{1}{\nu^2 + A} + \frac{1}{2} \int_0^{l_x} d\nu \int_{\nu}^{2l_x-\nu} d\mu \frac{1}{\nu^2 + A} \quad (\text{E.4})$$

where we introduced A here as a shorthand for $(y-y')^2 + (z-z')^2$. Notice the two integrals on the right hand side of this equation are identical, which can be seen by exchanging ν for $-\nu$ in either one of them (the integrand is even and the region of integration is symmetric). Thus, we can combine the integrals:

$$\int_0^{l_x} dx \int_0^{l_x} dx' \frac{1}{(x-x')^2 + A} = \int_0^{l_x} d\nu \int_{\nu}^{2l_x-\nu} d\mu \frac{1}{\nu^2 + A} \quad (\text{E.5})$$

The integral over μ follows immediately:

$$\int_0^{l_x} d\nu \int_{\nu}^{2l_x-\nu} d\mu \frac{1}{\nu^2 + A} = 2 \int_0^{l_x} \frac{l_x - \nu}{\nu^2 + A} d\nu \quad (\text{E.6})$$

To go forward, we perform such coordinate transformations for y and z as well, denoting the newly-introduced variables corresponding to each coordinate axis with a subscript. This gives an expression for ℓ :

$$\ell = \frac{2}{\pi V} \int_0^{l_x} d\nu_x \int_0^{l_y} d\nu_y \int_0^{l_z} d\nu_z \frac{(l_x - \nu_x)(l_y - \nu_y)(l_z - \nu_z)}{\nu_x^2 + \nu_y^2 + \nu_z^2} \quad (\text{E.7})$$

From here, the numerical evaluation of this integral is much easier. The `NIntegrate` function in Mathematica successfully estimates the integral to a precision of five decimal places in fewer than 24,000,000 function evaluations using an adaptive Monte Carlo approach (compared to direct Monte Carlo integration of (E.2), which only achieved 2 digits of precision with 50,000,000 function evaluations). Mathematica could not evaluate the original integral.

For detector dimensions of $1 \text{ cm} \times 1 \text{ cm} \times 4 \text{ mm}$, this yields a value of

$$\ell = 0.307784 \text{ cm} \tag{E.8}$$

APPENDIX F

Alig model high-energy, high- n limit

This appendix will derive the asymptotic behavior of the Alig model probabilities $p_n(E)$ (see Section 3.7.2) at high E and large n .

The general formula for $p_n(E)$ is:

$$p_n(E) = P_0(E) \frac{\gamma_{n-1}(E)}{\gamma(E)} + [1 - P_0(E)] p_n(E - \hbar\omega_0) \quad (\text{F.1})$$

The probability the particle scatters by ionization before scattering by phonon emission, $P_0(E)$, is given by

$$P_0(E) = \frac{1}{1 + \gamma'(E)/\gamma(E)} \quad (\text{F.2})$$

where

$$\frac{\gamma'(E)}{\gamma(E)} = A \frac{105(E - \hbar\omega_0)^{1/2}}{2\pi(E - E_g)^{7/2}} \quad (\text{F.3})$$

In the limit when E is very large, $\gamma'(E)/\gamma(E) \sim E^{-3}$ goes to zero, meaning $P_0(E) \rightarrow 1$ and (F.1) becomes:

$$p_n(E) = \frac{\gamma_{n-1}(E)}{\gamma(E)} \quad (\text{F.4})$$

The γ 's are scattering-by-ionization rates, and their ratio can be written:

$$\frac{\gamma_{n-1}(E)}{\gamma(E)} = \frac{\int dE_e \int dE_h \sqrt{E_e E_h E_l} \sum_{p,q} p_p(E_e) p_q(E_h) p_s(E_l)}{\int dE_e \int dE_h \sqrt{E_e E_h E_l}} \quad (\text{F.5})$$

where we've defined the shorthands $E_l \equiv E - E_g - E_e - E_h$ and $s \equiv n - 1 - p - q$. Note that the indices i and j from (3.7.13) have been replaced by p and q .

The denominator D can be evaluated exactly:

$$D \equiv \int dE_e \int dE_h \sqrt{E_e E_h E_l} = \frac{2\pi}{105} (E - E_g)^{7/2} \quad (\text{F.6})$$

Based on visual inspection of calculated values of $p_n(E)$, we now assume that for sufficiently large E and n , $p_n(E)$ takes the form of a gaussian:

$$p_n(E) = a_n \exp \left[-\frac{(E - \eta_n)^2}{2\sigma_n^2} \right] \quad (\text{F.7})$$

with a_n , η_n , and σ_n unknown parameters that depend on n . We will plug this form into (F.4) in hopes of finding a self-consistent form for $p_n(E)$.

We guess the following forms for the parameters:

$$a_n = \frac{k}{\sigma_0 \sqrt{(2n+1)\pi}} \quad (\text{F.8a})$$

$$\eta_n = \eta_0 + nk \quad (\text{F.8b})$$

$$\sigma_n = \sigma_0 \sqrt{n+1/2} \quad (\text{F.8c})$$

for the unknown constants k , σ_0 , and η_0 (σ_0 not to be confused with the model baseline detector phonon resolution).

Define S as the sum appearing in (F.5):

$$\begin{aligned} S &= \sum_{p,q} p_p(E_e) p_q(E_h) p_s(E_l) \\ &= \sum_{p,q} a_p a_q a_s \exp \left[-\frac{(E_e - \eta_p)^2}{2\sigma_p^2} - \frac{(E_h - \eta_q)^2}{2\sigma_q^2} - \frac{(E_l - \eta_s)^2}{2\sigma_s^2} \right] \end{aligned} \quad (\text{F.9})$$

We approximate the summation as an integral, $\sum_p \rightarrow \frac{1}{k} \int d\eta_p$:

$$\begin{aligned} S &\approx \frac{1}{k^2} \int d\eta_p \int d\eta_q a_p a_q a_s \exp \left[-\frac{(E_e - \eta_p)^2}{2\sigma_p^2} - \frac{(E_h - \eta_q)^2}{2\sigma_q^2} - \frac{(E_l - \eta_s)^2}{2\sigma_s^2} \right] \\ &= \frac{1}{k^2} \int d\eta_p \exp \left[-\frac{(E_e - \eta_p)^2}{2\sigma_p^2} \right] \int d\eta_q a_p a_q a_s \\ &\quad \times \exp \left[-\frac{(E_h - \eta_q)^2}{2\sigma_q^2} - \frac{(x + \eta_q)^2}{2\sigma_s^2} \right] \\ &= \frac{a_p a_q a_s}{k^2} \int d\eta_p \exp \left[-\frac{(E_e - \eta_p)^2}{2\sigma_p^2} \right] \int d\eta_q \\ &\quad \times \exp \left\{ -\frac{1}{2} \left[\frac{E_h^2}{\sigma_q^2} + \frac{\eta_q^2}{\sigma_q^2} - \frac{2E_h \eta_q}{\sigma_q^2} + \frac{x^2}{\sigma_s^2} + \frac{\eta_q^2}{\sigma_s^2} + \frac{2x\eta_q}{\sigma_s^2} \right] \right\} \end{aligned} \quad (\text{F.10})$$

where we defined $x \equiv E_l - \eta_s - \eta_q = E_l - 3\eta_0 - (n-1)k + \eta_p$. Based on the observed narrowness of the p_n , we use the saddle-point approximation to treat the gaussians as approximately delta functions, and pull out the a_n from the integral at their value evaluated at the mean values of p , q , and s (barred indices). The values of the barred indices will be returned to later.

For now, the inner integral is:

$$\begin{aligned}
& \int d\eta_q \exp \left\{ -\frac{1}{2} \left[\frac{E_h^2}{\sigma_q^2} + \frac{\eta_q^2}{\sigma_q^2} - \frac{2E_h\eta_q}{\sigma_q^2} + \frac{x^2}{\sigma_s^2} + \frac{\eta_q^2}{\sigma_s^2} + \frac{2x\eta_q}{\sigma_s^2} \right] \right\} \\
&= \exp \left\{ -\frac{1}{2} \left[\frac{E_h^2}{\sigma_q^2} + \frac{x^2}{\sigma_s^2} \right] \right\} \int d\eta_q \exp \left\{ -\frac{1}{2} \left[\frac{\eta_q^2}{\sigma_q^2} - \frac{2E_h\eta_q}{\sigma_q^2} + \frac{\eta_q^2}{\sigma_s^2} + \frac{2x\eta_q}{\sigma_s^2} \right] \right\} \\
&= \exp \left[-\frac{E_h^2}{2\sigma_q^2} - \frac{x^2}{2\sigma_s^2} \right] \int d\eta_q \exp \left\{ -\frac{\eta_q^2}{2} \left[\frac{1}{\sigma_q^2} + \frac{1}{\sigma_s^2} \right] + \left[\frac{E_h}{\sigma_q^2} - \frac{x}{\sigma_s^2} \right] \eta_q \right\} \\
&= \sqrt{2\pi \left(\frac{\sigma_q^2 \sigma_s^2}{\sigma_q^2 + \sigma_s^2} \right)} \exp \left[-\frac{E_h^2}{2\sigma_q^2} - \frac{x^2}{2\sigma_s^2} \right] \exp \left\{ \frac{1}{2} \frac{(E_h \sigma_s^2 - x \sigma_q^2)^2}{\sigma_q^4 \sigma_s^4} \frac{\sigma_q^2 \sigma_s^2}{\sigma_q^2 + \sigma_s^2} \right\}
\end{aligned} \tag{F.11}$$

where in the last line we used the identity

$$\int dx \exp \left[-\frac{1}{2} ax^2 + hx \right] = \sqrt{\frac{2\pi}{a}} \exp \left[\frac{h^2}{2a} \right] \tag{F.12}$$

with $a = (\sigma_q^2 + \sigma_s^2)/\sigma_q^2 \sigma_s^2$ and $h = (E_h \sigma_s^2 - x \sigma_q^2)/\sigma_q^2 \sigma_s^2$. (and note that σ_q and σ_s are also evaluated at average values of q and s from here on). This simplifies further:

$$\begin{aligned}
& \sqrt{2\pi \left(\frac{\sigma_q^2 \sigma_s^2}{\sigma_q^2 + \sigma_s^2} \right)} \exp \left[-\frac{E_h^2}{2\sigma_q^2} - \frac{x^2}{2\sigma_s^2} \right] \exp \left\{ \frac{1}{2} \frac{(E_h \sigma_s^2 - x \sigma_q^2)^2}{\sigma_q^4 \sigma_s^4} \frac{\sigma_q^2 \sigma_s^2}{\sigma_q^2 + \sigma_s^2} \right\} \\
&= \sqrt{2\pi \left(\frac{\sigma_q^2 \sigma_s^2}{\sigma_q^2 + \sigma_s^2} \right)} \exp \left\{ -\frac{1}{2} \left[\frac{E_h^2 \sigma_s^2 + x^2 \sigma_q^2}{\sigma_q^2 \sigma_s^2} \right] \right\} \exp \left\{ \frac{(E_h \sigma_s^2 - x \sigma_q^2)^2}{2\sigma_q^2 \sigma_s^2 (\sigma_q^2 + \sigma_s^2)} \right\} \\
&= \sqrt{2\pi \left(\frac{\sigma_q^2 \sigma_s^2}{\sigma_q^2 + \sigma_s^2} \right)} \exp \left\{ -\frac{1}{2} \left[\frac{E_h^2 \sigma_s^2 + x^2 \sigma_q^2}{\sigma_q^2 \sigma_s^2} - \frac{(E_h \sigma_s^2 - x \sigma_q^2)^2}{\sigma_q^2 \sigma_s^2 (\sigma_q^2 + \sigma_s^2)} \right] \right\} \\
&= \sqrt{2\pi \left(\frac{\sigma_q^2 \sigma_s^2}{\sigma_q^2 + \sigma_s^2} \right)} \exp \left\{ -\frac{1}{2\sigma_q^2 \sigma_s^2} \left[\frac{(E_h^2 \sigma_s^2 + x^2 \sigma_q^2)(\sigma_q^2 + \sigma_s^2)}{\sigma_q^2 + \sigma_s^2} \right. \right. \\
&\quad \left. \left. - \frac{(E_h \sigma_s^2 - x \sigma_q^2)^2}{\sigma_q^2 + \sigma_s^2} \right] \right\} \\
&= \sqrt{2\pi \left(\frac{\sigma_q^2 \sigma_s^2}{\sigma_q^2 + \sigma_s^2} \right)} \exp \left\{ -\frac{1}{2\sigma_q^2 \sigma_s^2 (\sigma_q^2 + \sigma_s^2)} \right. \\
&\quad \left. \times \left[E_h^2 \sigma_s^2 \sigma_q^2 + E_h^2 \sigma_s^4 + x^2 \sigma_q^4 + x^2 \sigma_q^2 \sigma_s^2 - E_h^2 \sigma_s^4 - x^2 \sigma_q^4 + 2E_h x \sigma_q^2 \sigma_s^2 \right] \right\} \\
&= \sqrt{2\pi \left(\frac{\sigma_q^2 \sigma_s^2}{\sigma_q^2 + \sigma_s^2} \right)} \exp \left\{ -\frac{1}{2\sigma_q^2 \sigma_s^2 (\sigma_q^2 + \sigma_s^2)} \right. \\
&\quad \left. \times \left[E_h^2 \sigma_s^2 \sigma_q^2 + x^2 \sigma_q^2 \sigma_s^2 + 2E_h x \sigma_q^2 \sigma_s^2 \right] \right\} \\
&= \sqrt{2\pi \left(\frac{\sigma_q^2 \sigma_s^2}{\sigma_q^2 + \sigma_s^2} \right)} \exp \left\{ -\frac{(E_h + x)^2}{2(\sigma_q^2 + \sigma_s^2)} \right\} \\
&= \sqrt{2\pi \left(\frac{\sigma_q^2 \sigma_s^2}{\sigma_q^2 + \sigma_s^2} \right)} \exp \left\{ -\frac{(y + \eta_p)^2}{2(\sigma_q^2 + \sigma_s^2)} \right\}
\end{aligned} \tag{F.13}$$

where we introduced $y \equiv x + E_h - \eta_p = E - E_g - E_e - 3\eta_0 - (n-1)k$ in the last line. Plugging back into S :

$$S = \frac{a_{\bar{p}} a_{\bar{q}} a_{\bar{s}}}{k^2} \sqrt{2\pi \left(\frac{\sigma_q^2 \sigma_s^2}{\sigma_q^2 + \sigma_s^2} \right)} \int d\eta_p \exp \left[-\frac{(E_e - \eta_p)^2}{2\sigma_p^2} \right] \exp \left[-\frac{(y + \eta_p)^2}{2(\sigma_q^2 + \sigma_s^2)} \right] \tag{F.14}$$

This integral is (introducing the shorthand $\sigma_r^2 \equiv \sigma_q^2 + \sigma_s^2$):

$$\begin{aligned}
& \int d\eta_p \exp \left[-\frac{(E_e - \eta_p)^2}{2\sigma_p^2} \right] \exp \left[-\frac{(y + \eta_p)^2}{2\sigma_r^2} \right] \\
&= \int d\eta_p \exp \left\{ -\frac{1}{2} \left[\frac{E_e^2}{\sigma_p^2} + \frac{\eta_p^2}{\sigma_p^2} - \frac{2E_e\eta_p}{\sigma_p^2} + \frac{y^2}{\sigma_r^2} + \frac{\eta_p^2}{\sigma_r^2} + \frac{2y\eta_p}{\sigma_r^2} \right] \right\} \\
&= \exp \left[-\frac{E_e^2}{2\sigma_p^2} - \frac{y^2}{2\sigma_r^2} \right] \int d\eta_p \exp \left\{ -\frac{\eta_p^2}{2} \left[\frac{1}{\sigma_p^2} + \frac{1}{\sigma_r^2} \right] + \left[\frac{E_e}{\sigma_p^2} - \frac{y}{\sigma_r^2} \right] \eta_p \right\}
\end{aligned} \tag{F.15}$$

Comparison with the second-to-last line of (F.11) shows this equation simplifies to:

$$\begin{aligned}
& \exp \left[-\frac{E_e^2}{2\sigma_p^2} - \frac{y^2}{2\sigma_r^2} \right] \int d\eta_p \exp \left\{ -\frac{\eta_p^2}{2} \left[\frac{1}{\sigma_p^2} + \frac{1}{\sigma_r^2} \right] + \left[\frac{E_e}{\sigma_p^2} - \frac{y}{\sigma_r^2} \right] \eta_p \right\} \\
&= \sqrt{2\pi \left(\frac{\sigma_p^2 \sigma_r^2}{\sigma_p^2 + \sigma_r^2} \right)} \exp \left\{ -\frac{(E_e + y)^2}{2(\sigma_p^2 + \sigma_r^2)} \right\}
\end{aligned} \tag{F.16}$$

So S simplifies to:

$$\begin{aligned}
S &= \frac{a_{\bar{p}} a_{\bar{q}} a_{\bar{s}}}{k^2} \sqrt{2\pi \left(\frac{\sigma_q^2 \sigma_s^2}{\sigma_q^2 + \sigma_s^2} \right)} \int d\eta_p \exp \left[-\frac{(E_e - \eta_p)^2}{2\sigma_p^2} \right] \exp \left[-\frac{(y + \eta_p)^2}{2(\sigma_q^2 + \sigma_s^2)} \right] \\
&= \frac{a_{\bar{p}} a_{\bar{q}} a_{\bar{s}}}{k^2} \sqrt{2\pi \left(\frac{\sigma_q^2 \sigma_s^2}{\sigma_q^2 + \sigma_s^2} \right)} \sqrt{2\pi \left(\frac{\sigma_p^2 \sigma_r^2}{\sigma_p^2 + \sigma_r^2} \right)} \exp \left\{ -\frac{(E_e + y)^2}{2(\sigma_p^2 + \sigma_r^2)} \right\} \\
&= \frac{2\pi a_{\bar{p}} a_{\bar{q}} a_{\bar{s}}}{k^2} \sqrt{\frac{\sigma_p^2 \sigma_q^2 \sigma_s^2}{\sigma_p^2 + \sigma_q^2 + \sigma_s^2}} \exp \left\{ -\frac{(E_e + y)^2}{2(\sigma_p^2 + \sigma_q^2 + \sigma_s^2)} \right\} \\
&= \frac{2\pi a_{\bar{p}} a_{\bar{q}} a_{\bar{s}}}{k^2} \sqrt{\frac{\sigma_p^2 \sigma_q^2 \sigma_s^2}{\sigma_p^2 + \sigma_q^2 + \sigma_s^2}} \exp \left\{ -\frac{A^2}{2(\sigma_p^2 + \sigma_q^2 + \sigma_s^2)} \right\}
\end{aligned} \tag{F.17}$$

where $A \equiv y + E_e = E - E_g - 3\eta_0 - (n-1)k$. At this point we should point out that this expression does not depend on E_e or E_h , and so we can factor S out of the numerator in (F.5), and we'll just get that $p_n(E) = S$.

Now, we simplify (F.17) by using (F.8):

$$\sigma_p^2 + \sigma_q^2 + \sigma_s^2 = \sigma_0^2 \left(p + q + s + \frac{3}{2} \right) = \sigma_0^2 \left(n + \frac{1}{2} \right) = \sigma_n^2 \tag{F.18}$$

and

$$a_{\bar{p}}\sigma_{\bar{p}} = \frac{k}{\sigma_0\sqrt{(2\bar{p}+1)\pi}}\sigma_0\sqrt{\bar{p}+1/2} = \frac{k}{\sqrt{2\pi}} \quad (\text{F.19})$$

and similarly for q and s . This gives:

$$\begin{aligned} p_n(E) &= \left(\frac{2\pi}{k^2}\right) \left(\frac{k^3}{(2\pi)^{3/2}}\right) \left(\frac{1}{\sigma_n}\right) \exp\left[-\frac{A^2}{2\sigma_n^2}\right] \\ &= \frac{k}{\sigma_0\sqrt{(2n+1)\pi}} \exp\left[-\frac{(E-E_g-3\eta_0-(n-1)k)^2}{2\sigma_n^2}\right] \end{aligned} \quad (\text{F.20})$$

if we now assume $A = E - \eta_n = E - \eta_0 - nk$ to conform with our assumed form (F.7), we get $\eta_0 = (k - E_g)/2$:

$$p_n(E) = \frac{k}{\sigma_0\sqrt{(2n+1)\pi}} \exp\left[-\frac{(E-nk-(k-E_g)/2)^2}{(2n+1)\sigma_0^2}\right] \quad (\text{F.21})$$

which provides a two-parameter fit to the entire high-energy, high- n set of Alig model probability distributions. Note also that

$$\begin{aligned} \sum_{n=0}^{\infty} p_n(E) &\approx \frac{1}{k} \int p_n(E) d\eta_n \\ &\approx \frac{1}{k} \int \frac{k}{\sigma_0\sqrt{(2n+1)\pi}} \exp\left[-\frac{(E-\eta_n)^2}{(2n+1)\sigma_0^2}\right] d\eta_n = 1 \end{aligned} \quad (\text{F.22})$$

Thus, the probabilities are correctly normalized over n . Note we held n fixed while integrating over η_n (accurate enough as the gaussians get vanishingly narrow for $E \rightarrow \infty$).

Fit results

The form (F.21) was fit to the $p_n(E_k)$ data calculated in Section 3.7.2 for n . ranging from 8 to 15. The resulting fitted values are $k = 3.7465 \pm 0.0004$ and $\sigma_0 = 1.271 \pm 0.001$ (both in eV).

The fits to Alig pair creation probabilities for $n = 5, 10, 25,$ and 40 are shown in Figure F.1. It can be seen the fits agree with the tabulated data, even far outside the region that was fitted to.

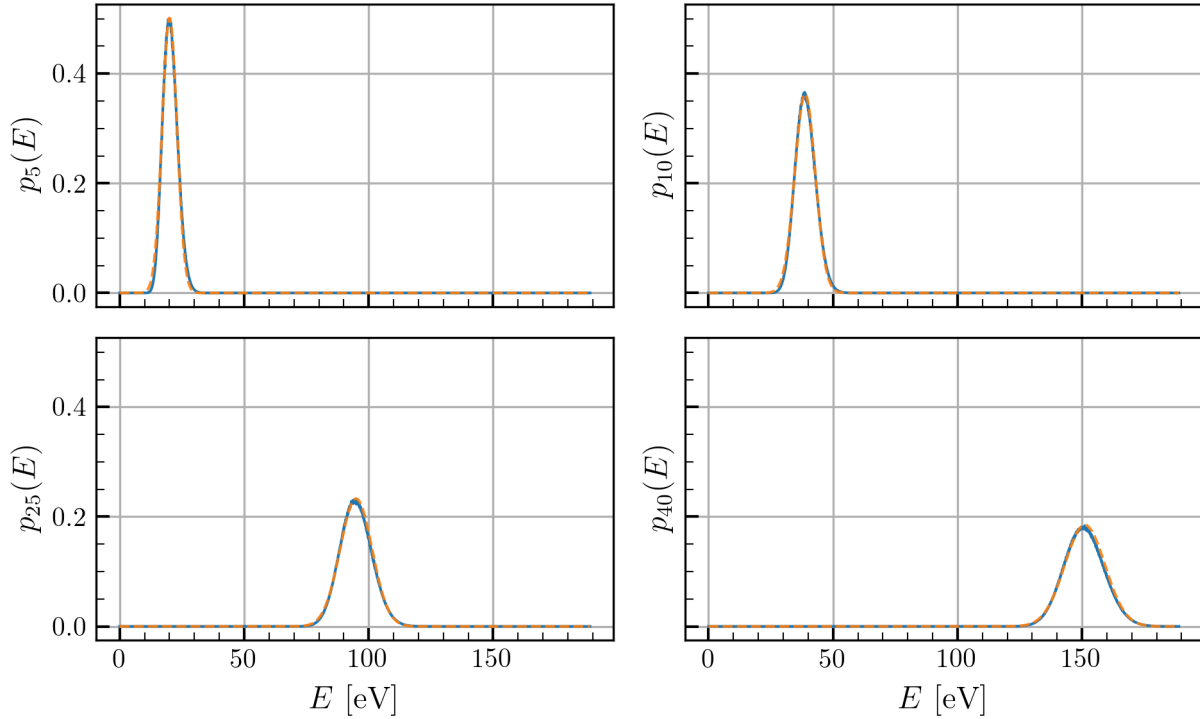


Figure F.1: Results of fit with $k = 3.7465$ and $\sigma_0 = 1.271$ to $n = 5, 10, 25,$ and 40

Properties of the fits

First, it should be noted that the “slope” of the average E -vs- n line, $k = 3.75$, is very close to ϵ_γ . This should not be surprising - they should be the same thing. In fact, Alig and collaborators fitted their value of $A = 5.2 \text{ eV}^3$ (3.7.9) precisely so that this slope would match.

Another thing worth mentioning is this model’s prediction for the electron Fano factor. Once again, the Fano factor is the variance in the number of e/h pairs produced divided by the mean number of pairs produced. Here, we have the variance in n is σ_n^2/k^2 , and the mean is just n . So $F \approx \sigma_n^2/nk^2 \approx \sigma_0^2/k^2 \approx 0.115$. This is close to the value calculated by Alig in their follow-up to the original model [259], but is about 26% lower than the most recently-measured value in silicon [260]. However, the prediction that F is a constant with growing energy is consistent with experiment.